# Multi-physics modeling of cooling of power transformers immersed in a ferrofluid

Sleimane Nasser El Dine

Thèse de doctorat

NNT : 2021UPAST094

université PARIS-SACLAY

# Multiphysics Modeling of Cooling of Power Transformers Immersed in a Ferrofluid

**Thèse de doctorat de l'université Paris-Saclay**

École doctorale n° 575 Electrical, Optical, Bio-Physics and Engineering (EOBE)
Spécialité de doctorat : Génie électrique
Unité de recherche : Université Paris-Saclay, CentraleSupelec, CNRS, Laboratoire de Génie Electrique et Electronique de Paris, 91192, Gif-sur-Yvette, France
Référent : CentraleSupelec

**Thèse présentée et soutenue à Paris-Saclay, le 04/11/2021, par**

**SLEIMANE NASSER EL DINE**

## Composition du Jury

| | |
|---|---|
| **M. Zhuoxiang Ren**<br>Professeur des Universités, Sorbonne Université (GeePs) | Président & Examinateur |
| **M. Abdelkader Benabou**<br>Maître de Conférences HdR, Université de Lille (L2EP) | Rapporteur & Examinateur |
| **M. Didier Trichet**<br>Professeur des Universités, Université de Nantes (IREENA) | Rapporteur & Examinateur |
| **M. Olivier Moreau**<br>Ingénieur Chercheur, EDF R&D (EDF Lab Paris-Saclay) | Examinateur |
| **M. Frédéric Bouillault**<br>Professeur des Universités, Université Paris-Saclay (GeePs) | Invité |

## Direction de la thèse

| | |
|---|---|
| **M. Xavier Mininger**<br>Professeur des Universités, Université Paris-Saclay (GeePs) | Directeur de thèse |
| **Mme Caroline Nore**<br>Professeur des Universités, Université Paris-Saclay (LISN) | Co-Directrice de thèse |

# Remerciements

Le travail faisant l'objet de ce mémoire de thèse a été réalisé au sein du Laboratoire GeePs (Génie électrique et électronique de Paris - Pôle Énergie) rattaché à l'Ecole CentraleSupélec. Je remercie sincèrement Monsieur le Directeur Claude Marchand de m'avoir accueilli dans son laboratoire.
Je voudrais remercier ici mes encadrants qui m'ont aidé à mener à bien ce travail de thèse. Je tiens à exprimer ma grande gratitude à Xavier Mininger et Caroline Nore pour avoir dirigé très judicieusement ce travail et pour m'avoir confié ce sujet de thèse. J'aimerais exprimer ma reconnaissance pour leurs intérêts et leurs disponibilités. Toutes leurs compétences, leurs qualités humaines, leurs optimismes et leurs conseils m'ont été d'un grand soutien au cours de ce travail de thèse. Je les remercie pour toutes leurs aides précieuses. Je remercie mon encadrant durant ma première année de thèse, Frédéric Bouillault dont j'ai pu profiter pleinement de son expérience en modélisation et simulation numérique pour poursuivre mes recherches.
Je tiens à remercier les membres de mon jury de thèse commençant par les rapporteurs, Abdelkader Benabou et Didier Tricher, d'avoir accepté de lire mon manuscrit et de leur intérêt pour mon travail. Merci également aux examinateurs Zhuoxiang Ren et Olivier Moreau pour leur présence et leurs questions à la soutenance.
Je souhaite aussi remercier les permanents du GeePs avec qui j'ai pu avancer mes mesures expérimentales. Je remercie vivement Eric Berthelot pour son soutien, sa disponibilité et son aide toujours importante. Merci aussi à David Alamarguy pour ses conseils de sécurité. Je souhaite exprimer mes sincères remerciements à Madame Sophie Neveu du laboratoire Phenix, pour sa contribution et la réalisation du ferrofluide.
Je voudrais remercier l'ensemble des personnels du GeePs surtout le groupe de calcul scientifique et informatique: Laurent Santandrea, Olivier Hubert et Anthony Guindon. Merci à Adrien Mercier, Guillaume Krebs et Éric Labouré pour leur intérêt, leurs explications et leurs connaissances enrichissantes en électromagnétisme. Je remercie très chaleureusement tous les thésards et les stagiaires qui par leurs conseils, leurs soutiens, et leurs résultats m'ont permis d'y arriver: Raphael Zanella, Amel Nait Djoudi et Nicola Piguemal.
Ce travail de thèse n'aurait pas été couronné de succès sans la merveilleuse ambiance qui a régné au GeePs tout au long de cette période. Je remercie l'ensemble de la famille du GeePs, les doctorants et post-doctorants avec lesquelles j'ai passé de très beaux moments: Nicolas, Tanbir, Guillaume, Cyril, Clément, Shadi, Christine, Luna, Yao, Léo, Koffi, Kokouvic, Sandra, Mohsen, Anas, Anna, Paul.
Enfin, merci à tous mes amis, anciens et nouveaux, pour leurs souhaits, leur soutien et les bons moments. Et pour finir, merci à ma famille, mes parents, mes frères et sœurs, pour leur soutien perpétuel, à qui je dédie ce succès.

# Contents

# Chapter 1

# Introduction

## 1.1 Context and motivations

Power transformers are electromagnetic devices used generally in the electric transmission network to convert the voltage from an electric circuit to another one for effective distribution of the electric power. Transforming power from a level to another one in such devices relies on a ferromagnetic core that exhibits a magnetic induction between two coils created by the alternating current source. Due to the Joule losses dissipated in the coils, the transformer undergoes a hot spot temperature that deteriorates its dielectric properties and may damage its components. In order to maintain the temperature at tolerable values, many transformers are immersed in an insulation liquid that extends their lifetime and retains their dielectric properties. This insulation liquid is most of the time a petroleum oil, particularly in the case of large power transformers.

Mineral oil possesses high thermal conductivity allowing efficient cooling of the transformer but presents drawbacks for the environment in case of leaking accidents. A more "friendly" renewable solution is proposed in several articles [1–3]: some vegetable oils (soy or rapeseed) are considered as insulation liquid for their biodegradability and low inflammability. However, this alternative oil presents a low thermal conductivity comparing to the conventional oil [4] and high dynamic viscosity that unfortunately does not match the researchers' attempts to improve the cooling of these devices. Nevertheless, an improvement of the heat transfer has been observed when adding ferromagnetic nanoparticles to the insulating oil.

Several articles propose using conventional oil seeded with magnetic nanoparticles instead of pure oil. These magnetic nanoparticles, being dispersed inside the oil, create a colloidal suspension with rheological and magnetic properties. Once subjected to the magnetic field of the transformer windings in the presence of a temperature gradient, a thermomagnetic convection can occur in these suspensions and be added to the natural thermal convection. This new phenomenon can improve the heat transfer inside the power transformer to the exterior without resorting to mechanical pumps. The creation of the thermomagnetic convection may also reduce the energy costs used to create a forced convection in some transformers and consequently the generated noise.

Adding magnetic nanoparticles in a conventional oil to enhance the heat transfer process remains a questionable idea. Some published results do not always confirm the ability of the magnetic fluids

to improve the cooling performance of the electromagnetic device. We may ask about the thermomagnetic convection and the conditions that ensure its creation in the magnetic fluid. We cannot be sure that the magnetic body force [5] exerted to the magnetic fluid in thermomagnetic convection always acts in support of the thermo-gravitational buoyancy force or may oppose its work. Moreover, the macroscopic physical properties (thermal conductivity, viscosity, density, heat capacity)) of these fluids are not well known. We have to investigate each of these properties and their effect on the heat transfer process. For instance, adding magnetic nanoparticles in the oil increases the oil viscosity and reduces the velocity of the fluid. Therefore, we wonder whether this increase in the oil viscosity has a negative impact on the rheological properties of the fluid and, therefore, on its cooling efficiency. We should finally conduct a simultaneous experimental and numerical investigation on the cooling performance of the ferrofluid in an actual electromagnetic device to conclude about the relevance of such a solution in improving the heat transfer process.

## 1.2 Objectives

The work proposed in this PhD thesis follows the first collaboration between LiSN (ex-Limsi), Texas A&M University, and GeePs, which main objectives were to propose a numerical model of the magnetoconvection in ferrofluids (PhD thesis of R. Zanella ). The subject of the present thesis addresses the heat transfer process with ferrofluids in power transformers associated with the thermomagnetic convection. This convection describes the heat exchange in the ferrofluid simultaneously subjected to a magnetic field and a temperature gradient. The heat transfer problem associated with the magnetized ferrofluid motion involves a wide variety of physics such as fluid dynamics, heat transfer, and electromagnetism. Coupling these physics together defines the ferrohydrodynamics context. This thesis investigates a complex geometry of power transformers and aims to assess the cooling performance using numerical and experimental approaches. The main objectives of the thesis are listed in the following:

1. To develop a numerical model that describes the thermomagnetic convection with ferrofluids: governing equations, physical properties, boundary conditions.

2. To verify the impact of the thermomagnetic convection in a simplified 2D axisymmetric model of a system representative of a power transformer.

3. To compare the numerical results to measurements conducted on a real experimental setup for the 2D axisymmetric model.

4. To study a complex 3D structure of power transformers and assess the cooling performance using ferrofluid.

## 1.3 Outline

This thesis manuscript is composed of three chapters, with an introduction, a conclusion, and a french summary that summarizes all the results of this research work.

1. **Chapter 2 - Ferrofluids:** we present a state of the art on the ferrofluids: their composition, stability, and applications. Then we introduce the theory of ferrofluid modeling by describing the main ferrohydrodynamic equations. The phenomenon of thermomagnetic convection is detailed, and we report on some numerical and experimental related articles. According to the literature, the effect of oscillating magnetic fields and the impact of magnets on cooling are also presented. We summarize finally the relevant results from the literature on the cooling performance of ferrofluid-immersed power transformers with respect to our objectives.

2. **Chapter 3 - Heat transfer in a heated Solenoid:** We present a combined experimental and numerical approach to assess the cooling process for a heated solenoid immersed in a ferrofluid. We first describe the experimental setup used to verify the thermomagnetic convection impact with ferrofluids. Then we detail the magnetic and thermophysical properties of the solution used to enhance the heat transfer process. The coupling theory is implemented using the finite element method, and the first numerical results are presented. The first set of results considers several expressions of the magnetic force for modeling the thermomagnetic convection, and we conclude about which force should be implemented in the fluid domain. The key part of this chapter is the cross-validation of experimental and numerical results achieved with two different codes (COMSOL and SFEMaNS). We verify the benefit of ferrofluid to enhance the cooling of the immersed solenoid and evaluate the temperature decrease reached in the maximum temperature of the coil. Another important part of this chapter concerns several improvement tests of the thermomagnetic convection realized on the same 2D axisymmetric model. We study the impact of ferrofluid with low Curie temperature of magnetic nanoparticles. In parallel, we show by an experimental/numerical cross-validation the effect of magnets on the heat transfer process in the solenoid system and on its maximum temperature. We also work on the addition of a ferromagnetic core to the coil model that results in lowering the maximum temperature of the coil.

3. **Chapter 4 - Thermomagnetic Convection in Power Transformers:** The first part of this chapter describes the validation of the proposed 3D model of the solenoid system, using some 2D-axisymmetric/3D comparisons. In the next step, we propose a 2D-axisymmetric model of a $40\ \mathrm{kVA}$ simplified power transformer as a first approach for modeling the actual structure of a power transformer. We assess the impact of the thermomagnetic convection added to the effect of changing the material physical properties of the coolant on the heat transfer. We then perform a fully coupled method to study the cooling performance in a 3D structure of a ferrofluid-immersed power transformer using the finite element method. We first describe the design of the 3D non-axisymmetric model. The first challenge of this 3D modeling is to evaluate the magnetic field in the ferrofluid domain that affects the magnetic body force. We perform a time-dependent magnetic calculation to find the most realistic distribution of the magnetic field in the fluid. Next, we seek to obtain the equivalent distribution of the fluid magnetic field with a magnetostatic computation by adjusting the current densities in the transformer coils. Then we couple the resulting magnetic field with the fluid dynamics and the temperature. We study numerically the benefit of using ferrofluid to reduce the maximum temperature in the conductors. We also prospect the evolution of the maximum temperature of the primary winding with different meshes. We finally conclude and present some perspectives.

# Chapter 2

# Ferrofluids

This chapter serves as a literature review of ferrofluids and their role in improving thermal transfer, particularly for the cooling of electromagnetic devices. An overview of ferrofluids -definition, composition, stability, applications- is proposed in the first section. Then, we detail the magnetic modeling of ferrofluids as cited in the literature, considering their magnetic and thermal properties and the associated governing equations. In the third section, thermomagnetic convection is presented as a physical phenomenon able to enhance the heat transfer. In the fourth and fifth sections, the impact of an oscillating magnetic field and supplementary magnets on heat transfer is discussed. Finally, the last section deals with the cooling performances of ferrofluid-based power transformers.

## 2.1 Overview

### 2.1.1 Definition

In 1895, Pierre Curie proved that ferromagnetic materials lose their magnetization when their temperature exceeds a characteristic value, called after him the Curie temperature. Materials then change their ferromagnetic behavior by a paramagnetic one. No substance is known for which the Curie point exceeds its melting point [6, 7]. As a result, a liquid metal does not present significant magnetic properties, and no visible effect is observed when subjected to a magnetic field. Consequently, a magnetic ferrofluid has to be artificially synthesized.
F. Bitter has manufactured the first ferrofluids at the beginning of 1930's. The idea was to increase the Weiss domain observed for the first time in 1907 by the French physicist Pierre Weiss. In 1966, Stephen Papell, a NASA chemist, tried to convert the nonmagnetic rocket fuel into a magnetic one to control it under zero gravity using an external magnetic field. He manufactured, therefore, a combination of magnetite powder $Fe_3O_4$ with Kerosene in the presence of oleic acid. A few years later, R. Rosensweig improved Papell's ferrofluid and set up the ferrofluid corporation with R. Moskowitz [8].
We can distinguish two types of colloidal magnetic suspensions: ferrofluids and magneto-rheological fluids. In a magneto-rheological fluid, *micrometric* magnetic particles are dispersed inside the solution, which confers unique physical properties to the mixture. Each particle is made of several magnetic domains and the global magnetization of the particle is equal to zero. Notably, the fluid viscosity is strongly dependent on the applied magnetic field. Therefore, a magneto-rheological

fluid subjected to a magnetic field changes from a liquid state to a "pastry state" [9].
As mentioned in R. Rosensweig's review [7], a ferrofluid consists of a stable colloidal suspension of monodomain magnetic *nano*particles in a nonmagnetic carrier fluid. The difference in particle size between ferrofluids and magneto-rheological fluids leads to a ferrofluid viscosity less dependent on the magnetic field. Once the ferromagnetic particles are dispersed inside the fluid, a combination of magnetic and rheological properties is acquired for the resultant suspension. This latter becomes sensitive to an external magnetic field (see figure 2.1) [8] and remains flowable in the presence of a magnetic field even in the case of magnetic saturation [6, 9].
Ferrofluid properties are profoundly affected by the thermal Brownian motion of the suspended particles and the magnetic field excitation [6]. The Brownian movement retains the particles suspended in the carrier liquid due to their nanometric size and confers a paramagnetic behavior to the solution [9]. In parallel, when the particles are magnetized, the strong interaction between the fluid molecules and the particles leads to transferring the magnetic interactions from the subdomain particles to the whole fluid.

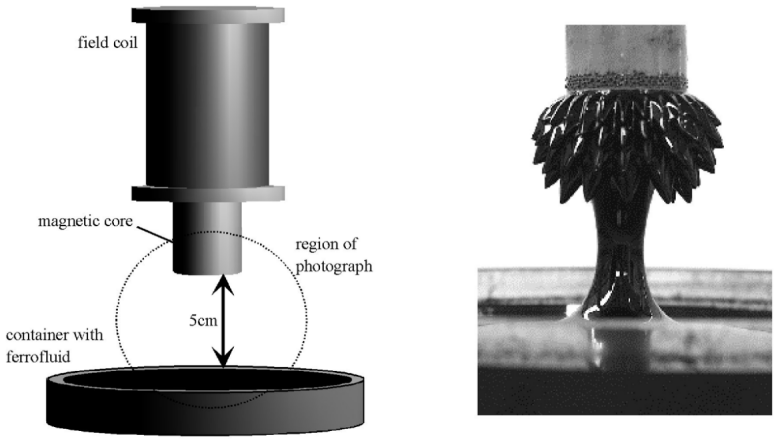


Figure 2.1: Ferrofluid attracted by a magnetic pole. The spike formation results from an interaction between magnetic force, fluid's surface tension, and gravity [10].

### 2.1.2 Composition

The synthesis of a magnetic ferrofluid consists of three essential ingredients: solid magnetic particles, a carrier fluid in which the particles are suspended, and a surfactant located on the particles surface that prevents their accumulation on each other.

#### Magnetic nanoparticles

Only a few material particles can be considered for the ferrofluid synthesis:

- Iron (Fe), cobalt (Co), nickel (Ni), and their alloys (FeNix or FeCox). The advantage of these particles is their high magnetization. However, these particles are rapidly oxidizable, leading to a decrease in their magnetic properties in the solution.

- Magnetic oxides, particularly ferrite particles, are also good candidates for ferrofluid preparation. For instance, we can mention the magnetite $Fe_2O_3$ and the cobalt ferrite $CoFe_2O_4$.

The diameter of suspended particles is usually between 3 and 20 $\mathrm{nm}$. Two principal methods are used to prepare metallic nanoparticles for magnetic colloid preparation: size reduction and precipitation. Size reduction consists of making tiny particles out of big ones by grinding the mass material in a mill for an extended period. The chemical precipitation, i.e., co-precipitation, consists of producing little particles from an initial solution. The size and the form of particles, therefore, depend on the synthesis conditions, particularly the temperature, pH, and the ions metallic ratio [6, 8].

### Carrier liquid

The carrier liquid is a solvent that exists in two forms: organic and polar.
Organic solvents, essentially used in commercial applications, have to be stable with temperature. For instance, aliphatic hydrocarbon ($C_nH_{2n+2}$), carboxylic diester, silicon oil, and polyphenyl ether are the most common.
Polar solvents are principally employed in medical applications.Water and alcohols (Ethanol and Methanol) are the primary examples.
Another example of carrier liquid is mercury, a metallic fluid with high thermal and electrical conductivity. However, mercury presents a high viscosity that is not adapted to our application.

### Surfactant

Another agent is added to the ferrofluid, in addition to the magnetic particles and the carrier fluid, to prevent agglomeration of particles to each other and inhibit their precipitation (see figure 2.2). The surfactant is a solvable dispersal agent that modifies the surface tension of the particles.
In an organic environment, surfactants are composed of a hydrophilic part (high-affinity with particles) and a hydrophobic part (soluble in the solvent). The hydrophilic part settles on the particle, and the hydrophobic one settles on the solvent. Hence, a liquid-solid interface is formed, and the two components are connected.
In a polar environment, the particle is charged. The first layer of surfactant is settled on and makes the particle hydrophobic.The second layer allows the particle to have a polar association with the solvent to make the particle easily soluble [8].

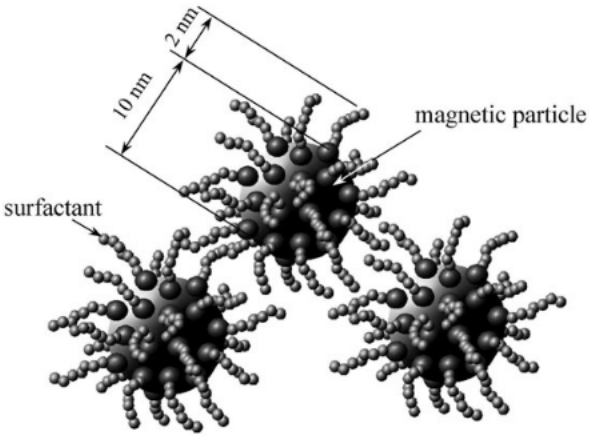


Figure 2.2: Schematic view of the coated particles in a ferrofluid [11].

### 2.1.3 Ferrofluid stability

The stability of a ferrofluid is an important criterion to evaluate if a solution is convenient to be used in fluid applications and research studies. The approach followed in this section is inspired from [6]. In contrast with magneto-rheological fluids, a "good" ferrofluid maintains the homogeneity of dispersion of particles throughout the carrier liquid. Therefore, the following energy terms have to be considered:

- thermal energy = $k_b T$
- magnetic energy = $\mu_0 MHV$
- gravitational energy = $\Delta\rho\, VgL$

where $k_b$ is the Boltzmann's constant in $\mathrm{J.K}^{-1}$, $T$ the absolute temperature in *K*, $\mu_0$ the free space magnetic permeability in $\mathrm{H.m}^{-1}$, $V$ the volume in $\mathrm{m}^3$ of a spherical particle of diameter $d$, $\Delta\rho$ the density variation, $g$ the acceleration of the gravity and $L$ the elevation in the gravitational field in $\mathrm{m}$. The ratio of one term versus another leads to dimensionless numbers that are directly related to the ferrofluid stability.

#### Stability in a magnetic field gradient

Let us consider the case when the magnetic particle is subjected to an external magnetic field: Particles are attracted to the regions of high magnetic field due to the magnetic field gradient, while the thermal energy gives to the particles suspended in the fluid a random motion called Brownian movement that counteracts the magnetic force. Here, the elementary magnetic work required to remove a particle from a zone where a magnetic field **H** exists is given by:

$$\delta W = -\mu_0 M_s \frac{dH}{ds} \tag{2.1}$$

where $ds$ is the instantaneous length. The reversible magnetic work needed to remove a magnetized particle from a point under the magnetic field effect ($\mathbf{H} \neq \mathbf{0}$) to another point outside of this field effect ($\mathbf{H} = \mathbf{0}$) is equal to the magnetic energy and is defined by [6, p. 34]:

$$W = -\int_H^0 (\mu_0 M_s V dH) \approx \mu_0 M H V \tag{2.2}$$

The criterion reflecting the stability of a magnetic particle against segregation in the liquid is given by the ratio of the thermal energy to the magnetic one:

$$\frac{thermal\ energy}{magnetic\ energy} = \frac{k_b T}{\mu_0 M_s H_{max} V} \geq 1 \tag{2.3}$$

where $M_s$ is the magnetization of the ferrofluid at saturation and $H_{max}$ the intensity of the high magnetic field. Substituting $V$ in equation (2.3) by a spherical particle volume ($V = \frac{\pi}{6} d^3$) gives an expression of the maximum size of magnetic particles to limit sedimentation or agglomeration:

$$d \leq \sqrt[3]{\frac{6 k_b T}{\pi \mu_0 M_s H_{max}}} \tag{2.4}$$

The particle size should not reach larger values to remain stable in an intense magnetic field region. This size ranges up to about 10 $\mathrm{nm}$, according to the literature [6].

**Stability against gravitational field**

To retain a homogeneous colloidal and stable suspension, it is also highly recommended that the particle size remains sufficiently small to allow the Brownian movement to overcome the gravitation [8]. While the gravitational field pulls particles downward in a beaker, thermal energy aims to keep them dispersed in the fluid volume against segregation.
As the particles are suspended in the fluid domain, they are subjected to a reduced weight (sum of the gravitational and Archimedes forces):

$$\mathbf{P}_r = (\rho_p - \rho_f) V_p\, \mathbf{g} \tag{2.5}$$

where $\rho_p$ is the density of the particle and $\rho_f$ the density of the fluid. Hence, the stability of ferrofluids depends on the comparison between the thermal agitation, which disperses the particles, and the gravitational potential energy ($E_p = |\mathbf{P}_r| \cdot L$) that a particle acquires with an elevation $L$ in the fluid. Therefore, the stability condition assuming a spherical particle volume is given by [12]:

$$d \leq \sqrt[3]{\frac{6}{\pi} \frac{k_b T}{(\rho_p - \rho_f) g L}} \tag{2.6}$$

**Stability against magnetic agglomeration**

A colloidal ferrofluid contains many magnetic particles dispersed throughout the fluid, and collisions between particles are therefore numerous. Particles are assumed to be monodisperse and not attached to each other. If the particles, i.e., magnetic dipoles, adhere together, a rapid aggregation takes place. The energy needed to separate a pair of particles of diameter $d$ reaches a maximum when the two magnetic dipoles are aligned. The magnetic potential energy of particle 1

in the magnetic field generated by particle 2, i.e., the magnetic dipole interaction energy, is given by [6, p. 16]:

$$E_{dd} = \frac{\mu_0}{4\pi}\left[\frac{\mathbf{m}_1 \cdot \mathbf{m}_2}{|\mathbf{r}_{12}|^3} - \frac{3}{|\mathbf{r}_{12}|^5}(\mathbf{m}_1 \cdot \mathbf{r}_{12}) \cdot (\mathbf{m}_2 \cdot \mathbf{r}_{12})\right] \tag{2.7}$$

where $\mathbf{m}_1$ and $\mathbf{m}_2$ are the magnetic moments in $\mathrm{A.m}^2$ respectively of two magnetized particles, $\mathbf{m}_1 \cdot \mathbf{m}_2 = m^2$ , $(\mathbf{m}_1 \cdot \mathbf{r}_{12}) \cdot (\mathbf{m}_2 \cdot \mathbf{r}_{12}) = m^2 r^2$, with $m = \mu_0 M \pi d^3/6$, and $\mathbf{r}_{12}$ the vector joining the center of these two particles with $|\mathbf{r}_{12}| = r = \delta + d$ as shown in figure (2.3).
The magnetic moment of a random particle is given by:

$$\mathbf{m}_i = \mathbf{M}_i V_{pi} \tag{2.8}$$

where $\mathbf{M}_i$ is the spontaneous magnetization of the particle **i** in $\mathrm{A.m}^{-1}$ and $V_{pi}$ the volume of the same particle in $\mathrm{m}^3$.

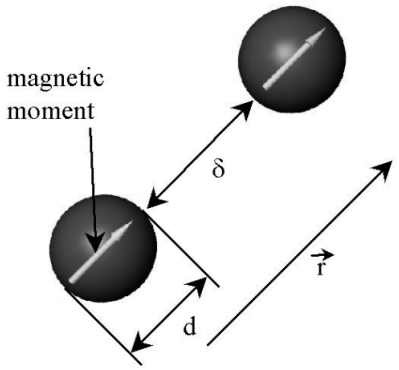


Figure 2.3: Sketch of magnetic dipole-dipole interaction [10].

Considering identical spherical particles, injecting (2.8) into equation (2.7) leads to the following form of the dipole-dipole interaction energy:

$$E_{dd} = \frac{\pi}{72}\mu_0 {M_s}^2 \frac{d^3}{\left(\frac{\delta}{d}+1\right)^3} \tag{2.9}$$

Thus, when the particles get in contact, the interaction energy is minimum, and equation (2.9) is reduced to:

$$E_{dd}^{min} = \frac{\pi}{72}\mu_0 {M_s}^2 d^3 \qquad (\delta = 0) \tag{2.10}$$

This energy has to be compared as before to thermal energy. The thermal motion of particles tends to disrupt the agglomerates with a disruption capacity described by the ratio:

$$\frac{thermal\ energy}{dipole - dipole\ contact\ energy} = \frac{12\ k_b\ T}{\mu_0 {M_s}^2 V} \tag{2.11}$$

Consequently, to avoid aggregation of particles, this ratio must be greater than unity. In parallel,

the magnetic dipole energy interaction must satisfy the stability condition $E_{dd}^{min} < 2k_bT$ (thermal energy of two particles) [9, 13]. The particle size dependence on the temperature and the saturation magnetization is given by:

$$d \leq \sqrt[3]{\frac{144\ k_b\ T}{\pi \mu_0 {M_s}^2}} \tag{2.12}$$

To sum up, the stability and characteristics of ferrofluids depend initially on the suspended particle's properties and the synthesis procedure. One of the main properties that have to be considered is the particle diameter. Practically, it is difficult to synthesize a ferrofluid with a particle size greater than $10\ \mathrm{nm}$. Consequently, particles coated with a surfactant present a total size in the range up to about $15\ \mathrm{nm}$.

### Stability against van der Walls interactions

Even with the above conditions fulfilled, the aggregation of particles cannot be avoided entirely. A second interaction, with an electric origin, called van der Walls interaction, can cause the coagulation of nanoparticles to each other. Let us consider again two spherical nanoparticles of diameter $d$ separated by a distance $\delta$. The van der Walls interaction energy is given according to the form proposed by Rosensweig [6]:

$$|E_{v.d.W}| = \frac{A}{6}\left[\frac{2}{l^2+4l} + \frac{2}{(l+2)^2} + ln\left(\frac{l^2+4l}{(l+2)^2}\right)\right] \tag{2.13}$$

where $A$ is the Hamaker constant depending on the constitutive material of the particles (see [14]) and $l = 2\delta/d$ a normalized distance. When two particles adhere together, the normalized distance $l$ goes to zero ($l \to 0$), and then the expression in (2.13) diverges to infinity. In contrast with the magnetic dipole interaction energy, the van der Walls forces remain greater than the thermal force. Thus, thermal energy cannot prevent the suspended particles from being coagulated since they have contact and fails guaranteeing fluid stability. As mentioned in a previous part, a surfactant must be used to have a steric repulsion between particles, contributing to the suspension stability. As presented in figure (2.4), this steric repulsion occurs as soon as the distance between particle surfaces becomes smaller than $2s$ ($s$ is the thickness of the surfactant layer).

### Highlighting of colloidal stability

Let us now consider one of the numerical applications cited in [12], which validates previously detailed stability conditions. We consider a water-based ferrofluid, and the magnetic particles dispersed are made of soft ferrite $(M_n, Z_n)Fe_2O_4$ for instance. The physical particles of the suspension are known: $\rho_p = 4.9\ \mathrm{kg.m^{-3}}$, the polarization at the saturation of the particles is $J_s = 0.4\,\mathrm{T}$, the magnetic flux density is equal to $B = 100\,\mathrm{mT}$ and the reference temperature is $T = 25°\mathrm{C}$. The elevation of a soft ferrite particle is taken at $L = 0.1\ \mathrm{m}$, the free space magnetic permeability $\mu_0 = 4\pi \times 10^{-7}\ \mathrm{H.m^{-1}}$, the Boltzmann constant $k_b = 1.38 \times 10^{-23}\mathrm{J.K^{-1}}$ and the acceleration gravity $g = 9.81\ \mathrm{m.s^{-2}}$ . The maximum particle sizes according to equations (2.4), (2.6), and (2.12) are:

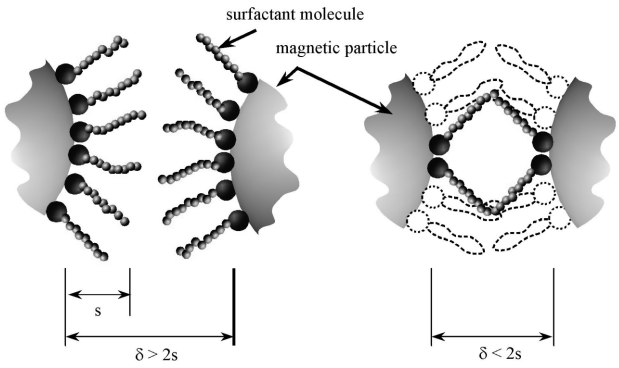


Figure 2.4: Sketch of the steric repulsion. As long as the surface distance between particles $\delta$ is greater than twice the surfactant layer thickness $s$, no steric repulsion exists. If the particles get close one to the other, the surfactant layer thickness $s$ will inhibit their agglomeration [10].

- $6.3$ nm regarding the presence in a magnetic field gradient;
- $12.7$ nm regarding the attraction by the gravitational field;
- $11.5$ nm regarding the dipole-dipole magnetic interaction.

Note that these values are consistent with the size of particles in standard ferrofluids.

### 2.1.4 Applications

Ferrofluids are involved in various applications, including mechanical and thermal engineering and biomedical purposes. One of the main applications of ferrofluid in mechanics is the sealing of rotating shafts [10] (see figure (2.5)). A permanent magnet surrounds a shaft made of a material with high magnetic permeability. If the gap between the shaft and the magnet is reduced, the magnetic flux density in the gap is increased (around $1\,\mathrm{T}$). When a ferrofluid is placed inside the gap, the magnetic force acting on the liquid can easily hold the volume in this area even if the pressure on the sealing side is high. The friction added by the magnetic fluid seal on the shaft is negligible compared to that of a mechanical seal. Magnetic plugs are another example of ferrofluid's benefit in replacing mechanical valves [12].

Ferrofluids are commonly used in heat transfer applications, typically in the cooling of loudspeakers. When a ferrofluid is injected in the speaker gap, as shown in figure (2.6), a strong magnetic field can hold the ferrofluid there and provide a high thermal conductivity (eight times larger than the one in the air). Thus, the heat exchange is enhanced between the voice coil and the speaker structure, increasing the speaker's acoustic power [10, 12].
Ferrofluids are also widely employed in biomedical applications. They can be used as a contrast agent for magnetic resonance imaging (MRI), in the magnetic separation for detecting a biologic object (DNA, proteins, bacteria, virus, etc.), and in cancer treatments by magnetic hyperthermia [8, 12, 15].

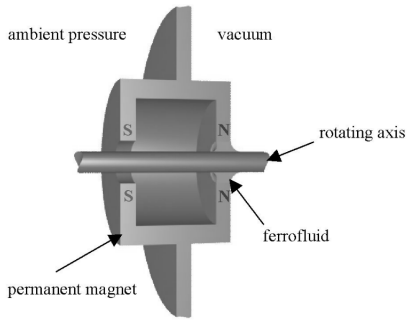


Figure 2.5: Sketch of the sealing of a rotating shaft with a ferrofluid [10].

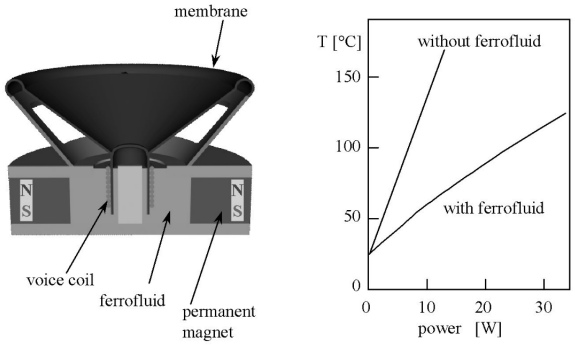


Figure 2.6: Sketch of the cooling of a loudspeaker with a ferrofluid. On the right panel, when a ferrofluid is used as a coolant, the temperature of the speaker decreases with the increase of the device power [10].

## 2.2 Ferrofluid modeling

In this section, we outline the main physical properties that have been considered for the ferrofluid modeling. Considering a continuous homogeneous medium, we present the superparamagnetism behavior of nanoparticles, their magnetization theory, and magnetic relaxation. Then the governing equations are described, and the thermophysical properties involved in this study are presented.

### 2.2.1 Equilibrium magnetization: superparamagnetism

As considered in the previous part, the suspended nanoparticles in a ferrofluid are monodomain ferromagnetic particles dispersed in a nonmagnetic carrier liquid. When no magnetic field is applied, the ferrofluid has no magnetization, and particles are randomly oriented, each with its magnetic moment $m$ [6]. Superparamagnetism is a magnetic state for magnetic monodomain particles which appears when the thermal agitation overcomes the anisotropy energy of the particle:

$$k_b T > K_1 V \tag{2.14}$$

where $K_1$ ($\mathrm{J.m^{-3}}$) is the anisotropy constant defined by the energy required to align the magnetization of a matter from its easy direction to its hard direction. This energy produces a force that maintains the magnetic moments $m$ of the particles in parallel directions [8, 9].
In contrast, if the ratio of the thermal energy to the anisotropy energy is lower than unity ($k_bT < K_1V$), the particles are distributed in ferromagnetic state or in ferrimagnetic state. The magnetization of the particle becomes blocked in the direction of the easy axis, and unable to rotate between two equilibrium positions. There is only one equilibrium position. This can be explained by a strong interaction between the particle magnetic moment and its crystal structure. If the particles need to change from ferromagnetic state to superparamagnetism state, a blockage temperature should be exceeded [9, 12].
According to (2.14), the anisotropy energy cannot permanently maintain the magnetic moments of the particles aligned together. The magnetization changes its direction to another one or rotates in a characteristic time called "Néel" relaxation time (see appendix A for more details on the magnetic relaxation). Two equilibrium positions for the magnetization are possible. As soon as the magnetic field strength increases, the tendency of particles to be aligned with the applied magnetic field becomes higher. The particles are entirely aligned with the magnetic field at a very high magnetic field strength, and the magnetization reaches its saturation value. In the following, we introduce Langevin's theory to outline the superparamagnetism principle, assuming that the particle-particle magnetic interaction is negligible.

### 2.2.2 Magnetization theory

As mentioned before, considering a system of magnetic dipoles thermally distributed and non interacting, Langevin's classical theory (Langevin 1905) describes the relationship between the applied magnetic field and the resultant ferrofluid magnetization. At first, it is convenient to define the energy ratio given by:

$$\alpha = \frac{\mu_0 m H}{k_b T} \tag{2.15}$$

where $m$ is the particle magnetic moment $\mathrm{A.m^2}$, $H$ the applied magnetic field $\mathrm{A.m^{-1}}$, $k_b$ the Boltzmann's constant $\mathrm{J.K^{-1}}$, and $T$ the absolute temperature in *K*. The ferrofluid magnetization is aligned with the applied magnetic field and has a magnitude equal to the total of the moments of magnetic particles suspended in the fluid volume. The saturation magnetization of a ferrofluid depends on the saturation moment of the bulk material and the volume fraction of nanoparticles:

$$M_s = \phi M_d \tag{2.16}$$

where $M_s$ is the magnetization of the ferrofluid at saturation (in $\mathrm{A.m^{-1}}$), $\phi$ the volume fraction of the nanoparticles, and $M_d$ the spontaneous domain magnetization at saturation of a nanoparticle (in $\mathrm{A.m^{-1}}$). The dependence of ferrofluid magnetization on the applied magnetic field yields to the superparamagnetism law (Langevin's theory) for monodisperse colloidal ferrofluid:

$$M = \phi M_d \left( \coth \alpha - \frac{1}{\alpha} \right) = M_s L(\alpha) \tag{2.17}$$

where $L(\alpha)$ is the Langevin function and $\alpha$ the energy ratio that can be rewritten as:

$$\alpha = \frac{\pi}{6}\frac{\mu_0 M_d H d^3}{k_b T} \tag{2.18}$$

where $m = M_d V = \frac{\pi}{6} M_d d^3$. From equation (2.17), the magnetization curves of a ferrofluid versus the magnetic flux density $B$ for various particle diameters are plotted in figure (2.7) (see [6, p. 59]).

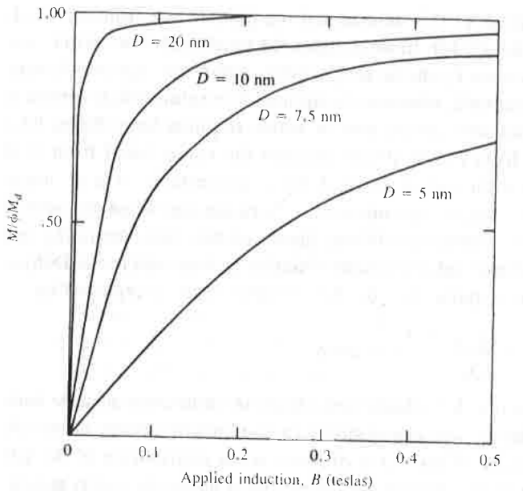


Figure 2.7: Magnetization curves computed for monodisperse spherical particles of magnetite ($M_d = 4.46 \times 10^5 \mathrm{A.m^{-1}}$) [6].

The saturation state is reached for all curves at a high magnetic flux density. Nevertheless, the initial susceptibility of the ferrofluid represented by the magnetization curve slope at a low magnetic field depends on the particle diameters. This susceptibility is small as long as the particle size is small. If the particle diameter increases, the initial susceptibility of the ferrofluid overgrows. In addition to the particle size, the magnetization of a ferrofluid also depends on the magnetic field strength $H$, the domain magnetization of a particle $M_d$, and the temperature $T$. Thus, when $H$ increases, $\alpha$ grows, and $M$ increases. As discussed before, the saturation state $M_s$ is reached at a high magnetic field, i.e., if $\alpha \to \infty$. The Langevin function $L(\alpha)$ satisfies:

$$\lim_{\alpha \to +\infty} L(\alpha) = \lim_{\alpha \to +\infty} \left(1 - \frac{1}{\alpha}\right) = 1 \tag{2.19}$$

On the other hand, the Langevin function can be written through a Taylor series expansion close to 0:

$$L(\alpha) \approx \frac{\alpha}{3} - \frac{\alpha^3}{45} + o(\alpha^3) \tag{2.20}$$

According to equation (2.20), for a weak magnetic field ($\alpha \to 0$), the Langevin function takes the form:

$$L(\alpha) \approx \frac{\alpha}{3} + o(\alpha) \tag{2.21}$$

In such a case, the magnetization $M$ of the ferrofluid becomes linear and proportional to the magnetic field $H$:

$$M = \chi_i H \tag{2.22}$$

where $\chi_i$ is the initial magnetic susceptibility of the ferrofluid, defined by its ability to be magnetically polarised when subjected to a magnetic field:

$$\chi_i = \frac{\pi}{18}\phi\mu_0\frac{{M_d}^2 d^3}{k_b T} \qquad (\alpha \ll 1) \tag{2.23}$$

At saturation, the energy ratio $\alpha$ grows to infinity, and then the magnetization of the ferrofluid given in (2.17) changes to:

$$M = \phi M_d \left(1 - \frac{6}{\pi}\frac{k_b T}{\mu_0 M_d H d^3}\right) \qquad (\alpha \gg 1) \tag{2.24}$$

According to the asymptotic form of the Langevin function given in (2.24), figure (2.8) illustrates the shape of $L(\alpha)$ for small and large values of $\alpha$:

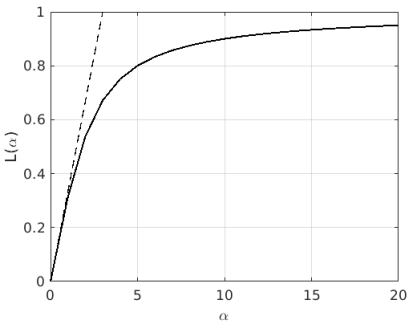


Figure 2.8: Langevin's function. The dashed line corresponds to the linearization of $L(\alpha)$ close to 0.

However, ferrofluids usually exhibit a normal distribution of particle sizes. In 1978, Chantrell et al. [16] presented a method that provides the log-normal distribution of particle sizes in a ferrofluid medium. They applied their method to several ferrofluids containing ferrite and cobalt particles. In this method, a distribution function $f(y)$ called distribution of volume fraction appears, where $y = d/d_v$ refers to the reduced diameter, $d_v$ being the median diameter, and $d$ the particle diameter. This distribution of particle sizes affects the magnetic properties of the ferrofluid, and thus its magnetization is given by:

$$M = M_s \int_o^\infty L(\alpha) f(y) dy \tag{2.25}$$

where $\alpha$ is defined in (2.18) and also depends on $y$. Injecting these expressions in (2.23) leads to a new formula for the initial magnetic susceptibility [16, 17]:

$$\chi_i = \frac{\pi}{18}\phi\mu_0\frac{{M_d}^2{d_v}^3}{k_bT}\int_o^\infty y^3 f(y)dy \qquad (\alpha \ll 1) \tag{2.26}$$

Figure (2.9) presents the log-normal distribution of particle sizes for a solution of ferrofluid composed of Midel vegetable oil ($Midel\ eN\ 1215$) containing Cobalt ferrite nanoparticles ($CoFe_2O_4$). This solution has been manufactured by Sophie Neveu at PHENIX laboratory (Sorbonne University) and will serve in the experiments presented in the next chapters. The log-normal distribution of $CoFe_2O_4$ nanoparticles has been used to determine their average diameter required in numerical modeling.

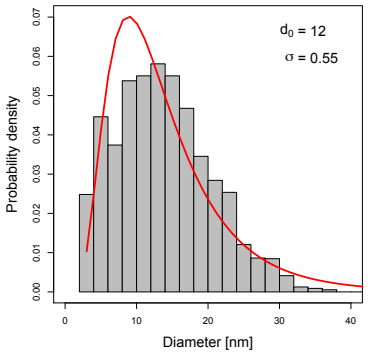


Figure 2.9: Log-normal distribution of particle sizes in $Midel\ eN\ 1215$ oil seeded with $CoFe_2O_4$.

As an illustration, we consider two magnetization curves: the first corresponds to a theoretical ferrofluid [18], the other corresponds to the ferrofluid used in the next chapter ($Midel\ eN\ 1215$ with $CoFe_2O_4$). As shown in figure (2.10), the intensity of the magnetization reaches its maximum $M_s$ at a high magnetic field. As expected, for weak magnetic fields, the magnetization of the ferrofluid is proportional to the magnetic field and satisfies the linear law $M = \chi H$ where $\chi$ denotes the initial susceptibility in figure (2.10).
To compare, figure (2.11) shows the experimental curve for the manufactured $CoFe_2O_4$ ferrofluid. The magnetization at saturation is measured to be $M_s = 16240\ \mathrm{A.m^{-1}}$, whereas the volume fraction of nanoparticles suspended in the solution is $\phi = 5.41\%$, assuming that particles have been coated with oleic acid as a surfactant (its thickness value is given by $s = 2\ \mathrm{nm}$).

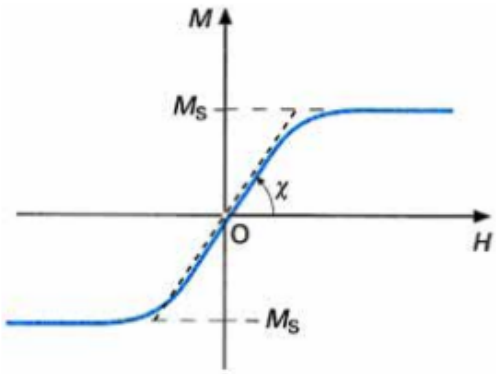


Figure 2.10: Theoretical magnetization curve [18].

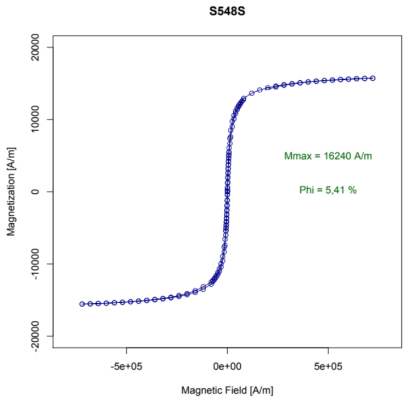


Figure 2.11: Experimental magnetization curve for $Midel\ eN\ 1215$ with $CoFe_2O_4$.

### 2.2.3 Governing equations

In this part, we report the classical governing laws for ferrohydrodynamics as presented in the study of Neuringer and Rosensweig [19]. We write by order: the magnetostatic equations, the fluid dynamic equations and the temperature equation for a full description of ferrohydrodynamic interactions.

#### Magnetostatic equations

The ferrofluid is considered as a magnetically polarizable and non-conductive fluid. The magnetization **M** and the magnetic field **H** are assumed to be collinear ($\|$) with the same direction. The eddy and displacement currents are neglected. The equation governing the magnetic field is given by Maxwell-Ampere's law:

$$\boldsymbol{\nabla} \times \mathbf{H} = \mathbf{J} \tag{2.27}$$

where **J** is the current density and $\mathbf{J} \neq \mathbf{0}$ only in the coil. The divergence free condition is:

$$\boldsymbol{\nabla} \cdot \mathbf{B} = 0 \tag{2.28}$$

where **B** is the magnetic flux density.
For the ferrofluid, the magnetic flux density and the magnetic field are related through the relation:

$$\mathbf{B} = \mu_0(\mathbf{H} + \mathbf{M}(T)) \tag{2.29}$$

where $\mu_0$ is the free space magnetic permeability and **M** the magnetization vector deduced by (2.23).

#### Fluid dynamic equations

Ferrofluids are usually considered incompressible Newtonian fluids. The well-known Navier-Stokes equations report the continuity equation (or mass conservation) and the momentum conservation for incompressible colloidal ferrofluid:

$$\boldsymbol{\nabla} \cdot \mathbf{u} = 0, \tag{2.30}$$

$$\rho \partial_t \mathbf{u} + \rho(\mathbf{u} \cdot \boldsymbol{\nabla})\mathbf{u} + \boldsymbol{\nabla} p - \eta \boldsymbol{\nabla}^2 \mathbf{u} = -\rho \mathbf{g} \beta (T - T_{ext}) + \mathbf{F}_m \tag{2.31}$$

where $\mathbf{u}$ is the velocity vector, $p$ the pressure, $\eta$ the dynamic viscosity of ferrofluid, $\rho$ the ferrofluid density at the reference temperature $T_{ext}$, $\mathbf{g}$ the gravity acceleration, and $\beta$ the thermal expansion coefficient. At the right-hand side of the Navier-Stokes equations, $\rho \mathbf{g} \beta (T - T_{ext})$ refers to the buoyancy force having thermal and gravitational origin and is deduced from the Boussinesq approximation. $\mathbf{F}_m$ denotes the magnetic body force, i.e., the magnetic force per unit volume exerted on a ferrofluid when subjected to a magnetic field.

### Magnetic body force

This part aims to resume the different formulations for the magnetic force used in the literature and provides some examples. S. Afkhami [20, p. 379] reports that the magnetic Kelvin force acting on a volume containing magnetic dipoles of magnetization $\mathbf{M}$ will be:

$$\mathbf{F}_K = \mu_0 (\mathbf{M} \cdot \boldsymbol{\nabla}) \mathbf{H} \tag{2.32}$$

This force has been usually used in numerical modeling and is reported for instance in [21–25] without any justification. As indicated in [26, p. 3.8], the Kelvin force density does not consider the magnetic dipole-dipole interaction. In parallel, A. Bossavit has explained that more formulas exist to describe the force density acting on a medium of ferrofluid subjected to a magnetic field [27]. Helmholtz force and Maxwell force are two examples:

$$\mathbf{F}_H = -\frac{1}{2} H^2 \boldsymbol{\nabla} \mu \tag{2.33}$$

$$\mathbf{F}_M = \mu_0 \boldsymbol{\nabla} \mathbf{H} \cdot \mathbf{M} \tag{2.34}$$

where $\mu$ is the magnetic permeability of the ferrofluid defined by $\mu = \mu_0(1 + \chi(T))$. Helmholtz force seems to be the least used magnetic body force to model the ferrofluid in heat transfer applications. Note that the force densities given in (2.32) and (2.34) are equivalent in a *non-conducting* ferrofluid [13, p. 22] as long as the following vector identity is true:

$$\boldsymbol{\nabla}(\mathbf{M} \cdot \mathbf{H}) - \mathbf{M} \cdot \boldsymbol{\nabla} \mathbf{H} = \mathbf{M} \times (\boldsymbol{\nabla} \times \mathbf{H}), \qquad \mathbf{M} \times \mathbf{J} = \mathbf{0}$$

While the two magnetic body forces (Kelvin and Helmholtz) are cited in the literature, nobody prevails using one of these force models on the other. In the next chapter, we will compare these two force models and conclude about the impact of each force on the ferrofluid modeling.

### Heat transfer equation

The magnetic body force developed in the previous section is both magnetic field and temperature-dependent. The thermodynamic analysis conducted on a magnetized matter in [19] yields the following equation for the temperature field T:

$$\rho c \partial_t T + \rho c(\mathbf{u}\cdot\boldsymbol{\nabla})T - \mu_0 K T(\partial_t H + (\mathbf{u}\cdot\boldsymbol{\nabla})H) - \boldsymbol{\nabla}\cdot(\lambda\boldsymbol{\nabla}T) = 2\eta\boldsymbol{\nabla}^s\mathbf{u} : \boldsymbol{\nabla}\mathbf{u} + Q \quad (2.35)$$

where $c$ is the specific heat at constant pressure, $\lambda$ is the thermal conductivity of the ferrofluid, Q is the heat source per unit volume, and $K$ is the pyromagnetic coefficient defined by:

$$K = -\left(\frac{\partial M}{\partial T}\right)_H, \qquad \left(\frac{\partial M}{\partial T}\right)_H < 0 \quad (2.36)$$

The first term at the right-hand side of (2.35) denotes the viscous dissipation power per unit volume, depending on $\boldsymbol{\nabla}^s\mathbf{u}$ the strain rate tensor given by:

$$\boldsymbol{\nabla}^s\mathbf{u} = \frac{1}{2}\left(\boldsymbol{\nabla}\mathbf{u} + (\boldsymbol{\nabla}\mathbf{u})^T\right) \quad (2.37)$$

The convective term $(\mu_0 K T(\mathbf{u}\cdot\boldsymbol{\nabla})H)$ involving the magnetic field $\mathbf{H}$ in (2.35) represents the heating due to adiabatic magnetization as mentioned in [19]. This term will not be considered in the present modeling of ferrofluid based on the comparison made in [13, p. 133] which neglects the pyromagnetic coefficient term compared to the convective $(\rho c(\mathbf{u}\cdot\boldsymbol{\nabla})T)$ and the diffusive $(\boldsymbol{\nabla}\cdot(\lambda\boldsymbol{\nabla}T))$ terms.

### 2.2.4 Thermophysical properties

For successful use in any heat transfer application, a ferrofluid requires special thermophysical properties such as high thermal conductivity, high heat capacity, high thermal expansion coefficient and low viscosity. According to these convenient properties, and with adding a magnetic force, ferrofluids can enhance the thermomagnetic convection through the ferrofluid medium to achieve a better cooling process. We present in this part the major models for the thermophysical properties that a ferrofluid may exhibit.

#### Density and heat capacity

The presence of magnetic nanoparticles in the base fluid modifies the transport properties in the fluid flow and the heat transfer characteristics. Many articles deal with determining the density and the heat capacity of ferrofluids [28–33]. In the following, we define the effective density and heat capacity of ferrofluid as in [34]. Let us consider a ferrofluid medium of volume $V_{ff}$ with a volume fraction of nanoparticles $\phi$. The volume of magnetic nanoparticles is called $V_p$, and the one for the base fluid is denoted $V_{bf}$. The relations connecting $V_p$ and $V_{bf}$ to $V_{ff}$ are given by:

$$V_p = \phi V_{ff}, \qquad V_{bf} = (1-\phi)V_{ff} \quad (2.38)$$

The density of ferrofluid is defined by:

$$\rho_{ff} = \frac{M_{ff}}{V_{ff}} = \frac{M_{bf}+M_p}{V_{ff}} = \frac{\rho_{bf}V_{bf}+\rho_p V_p}{V_{ff}} = \frac{V_{bf}}{V_{ff}}\rho_{bf} + \frac{V_p}{V_{ff}}\rho_p$$

where $\rho_{ff}$, $\rho_{bf}$ and $\rho_p$ are the density of ferrofluid, the base fluid, and the magnetic nanoparticles. $M_{ff}$, $M_{bf}$, and $M_p$ stand for the mass of ferrofluid, the base fluid, and the magnetic particles, respectively. Replacing the equations given in (2.38) in the ferrofluid density formula yields to:

$$\rho_{ff} = (1-\phi)\rho_{bf} + \phi\rho_p \tag{2.39}$$

Let us denote by $c_{ff}$, $c_{bf}$, and $c_p$ the specific heat capacity of the ferrofluid, the base fluid, and the magnetic nanoparticles. By using the following relation:

$$\rho_{ff}c_{ff}V_{ff} = \rho_{bf}c_{bf}V_{bf} + \rho_p c_p V_p$$

and after dividing by $V_{ff}$ owing to (2.38), we can write the law describing the specific heat of a ferrofluid:

$$\rho_{ff}c_{ff} = (1-\phi)\rho_{bf}c_{bf} + \phi\rho_p c_p \tag{2.40}$$

**Thermal expansion coefficient**

Let us represent $\beta_{ff}$, $\beta_{bf}$, and $\beta_p$ the thermal expansion coefficients for the ferrofluid, the base fluid, and the magnetic nanoparticles. The thermal expansion coefficient for a ferrofluid defined by the tendency of this ferrofluid to change its volume regarding a temperature change is given by [13, p. 24]:

$$\beta_{ff} = \frac{1}{\rho_{ff}}\left(\frac{\partial\rho_{ff}}{\partial T}\right) = -\frac{1}{V_{ff}}\left(\frac{\partial V_{ff}}{\partial T}\right) = -\frac{1}{V_{ff}}\frac{\partial(V_{bf}+V_p)}{\partial T} = -\frac{1}{V_{ff}}\frac{\partial V_{bf}}{\partial T} - \frac{1}{V_{ff}}\frac{\partial V_p}{\partial T}$$

Modifying equation (2.38) yields to:

$$\frac{1}{V_{ff}} = \frac{1-\phi}{V_{bf}} = \frac{\phi}{V_p}$$

Therefore, we can write the law describing the thermal expansion coefficient for a ferrofluid:

$$\beta_{ff} = (1-\phi)\beta_{bf} + \phi\beta_p \tag{2.41}$$

**Thermal conductivity**

In literature, many articles describe numerical calculations and experimental measurements of the thermal conductivity of ferrofluids [35–41]. Abareshi et al. [42] measured the effective thermal conductivity of a water-based magnetite ferrofluid with different volume fractions and at several temperatures. The measured thermal conductivity increases with an increase in volume fraction of nanoparticles and temperature. Hamilton-Crosser's model [34, p. 618] and Bruggeman's model [34,43] are two examples of predictions of the thermal conductivity of ferrofluids depending on the shape of magnetic nanoparticles. However, the most common model used in literature to predict the thermal conductivity of a ferrofluid remains the one established by Maxwell, cited in [44, p. 1] and in [34, p. 617] with different forms and defined by:

$$\lambda_{ff} = \left(1 + \frac{3\phi(\lambda_p - \lambda_{bf})}{3\lambda_{bf} + (1-\phi)(\lambda_p - \lambda_{bf})}\right)\lambda_{bf} \tag{2.42}$$

where $\lambda_{ff}$ is the thermal conductivity of the ferrofluid, $\lambda_{bf}$ the thermal conductivity of the base fluid, and $\lambda_p$ the thermal conductivity of the magnetic nanoparticles.
Other papers focus on the enhancement of the thermal conductivity of ferrofluids under various magnetic fields. The magnitude and the orientation of the applied magnetic field can affect the thermal conductivity of ferrofluids, as explained in [45]. The ratio of thermal conductivity of ferrofluid to that of base fluid ($\lambda_{ff}/\lambda_{bf}$) characterizes this enhancement. Li et al. [45, p. 115] proved that, when the direction of the applied magnetic field is parallel to the temperature gradient, the thermal conductivity of ferrofluid increases with the increase of the field strength (see figure (2.12)). This increase is explained by the formation of particle chains like aggregation structures in the ferrofluid which build more bridges for heat transport. Such effect will not be considered in the present study.

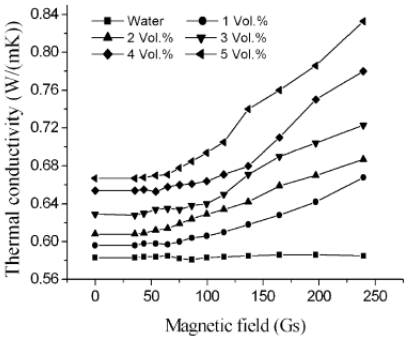


Figure 2.12: Evolution of the thermal conductivity of a water-based magnetite fluid with respect to the magnetic field [45]. Note that the applied magnetic field is parallel to the temperature gradient.

### Viscosity

The viscosity of a ferrofluid is the tendency of this fluid to resist flowing. It quantifies the friction forces existing between internal layers of fluid that are in movement. The dynamic viscosity $\eta$ is given by the ratio of the shear stress $\tau$ to the shear rate $\dot{\gamma}$ ($\eta = \frac{\tau}{\dot{\gamma}}$). A fluid is called Newtonian when its viscosity remains constant at various shear rates, while it is called non-Newtonian if the viscosity depends on the shear rate change. Many studies have reported models to predict the ferrofluid viscosity, starting with Brinkman [46] and Lundgren [47] (extended formulas of Einstein's law) and followed by Batchelor [48], who considered the effects of Brownian motion and spherical particles on the effective viscosity of a ferrofluid. The most popular law describing the ferrofluid viscosity is still the Einstein's formula [49] given by:

$$\eta_{ff} = \left(1 + \frac{5}{2}\phi\right)\eta_{bf} \tag{2.43}$$

where $\eta_{ff}$ is the dynamic viscosity of the ferrofluid, $\eta_{bf}$ the one of the base fluid, and $\phi$ denotes the volume fraction of spherical nanoparticles uncoated with surfactant. This model can only be

considered for low concentrations of nanoparticles [6, 40] when no magnetic field is applied.
The ferrofluid viscosity increases with the volume fraction of nanoparticles, as mentioned in [37, p. 567] and [40, p. 437]. Particularly, when particles are coated with a dispersing agent of thickness $s$, an increase in the viscosity of ferrofluid is readily obtained. The relation connecting the volume fraction of nanoparticles coated and uncoated with surfactant respectively is given by:

$$\widetilde{\phi} = \left(1 + 2\frac{s}{d}\right)^3 \phi \tag{2.44}$$

where $\widetilde{\phi}$ is the volume fraction of nanoparticles coated with a surfactant, $d$ the diameter of spherical particles, and $s$ the surfactant layer thickness.
However, Einstein's model given in (2.43) is theoretical and does not produce accurate values for the intrinsic viscosity of ferrofluids. Venerus et al. [50, p. 44582-3] found that the formula (2.43) underestimates the measured nanofluid viscosity. However, Einstein's model remains valid for $\widetilde{\phi} \leq 5\%$. On the other hand, Rosensweig [6] proposed another model to describe the viscosity of a ferrofluid for moderate concentrations of spherical nanoparticles and when no external field is applied:

$$\eta_{ff} = \left(1 - \frac{5}{2}\widetilde{\phi} + \left(\frac{\frac{5}{2}\widetilde{\phi_c} - 1}{\widetilde{\phi_c}^2}\right)\widetilde{\phi}^2\right)^{-1} \eta_{bf} \tag{2.45}$$

where $\widetilde{\phi}$ is the volume fraction of coated nanoparticles and $\widetilde{\phi_c} = 0.74$ corresponds to a close packing of spheres [6, p. 64]. Einstein and Rosensweig's models have been compared to each other in figure (2.13) where the two corresponding calculated curves are plotted together with experimental viscosity measurements of a ferrofluid (kerosene + magnetite) with $\widetilde{\phi} \leq 30\%$. This figure proves that Rosensweig's model excellently matches experimental data for the whole range of $\widetilde{\phi}$. Nonetheless, the two models remain valid for low concentrations of nanoparticles.

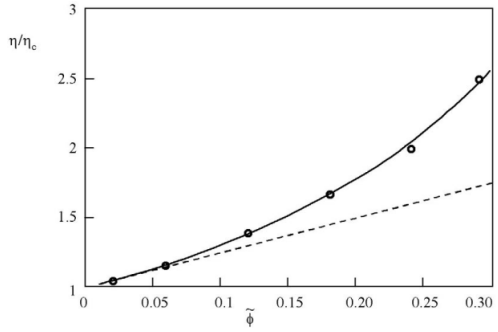


Figure 2.13: Einstein's (dashed line), Rosensweig's viscosity (solid line) models and experimental viscosity measurements (circles) of kerosene-based ferrofluid versus the volume fraction of coated particles. $\eta = \eta_{ff}$, $\eta_c = \eta_{bf}$ [10, p. 24].

Other studies report a prediction of the viscosity of ferrofluids under changing magnetic fields. McTague [51], Hall, and Busenburg [52] introduced the magnetoviscous effects in ferrofluids and proved a dependence of the viscosity of ferrofluids upon the strength of the applied magnetic field and its direction comparing to the flow. They explained that, if a magnetic field **H** is perpendicular

to the flow vorticity ($\boldsymbol{\nabla} \times \mathbf{u}$), an hindrance in the rotation of suspended particles occurs, which causes an increase in the ferrofluid viscosity. Shliomis [53] described the theoretical viscosity dependence on the magnetic field strength and direction by the following relation:

$$\frac{\eta_{ff}^{r} - \eta_{ff}^{0}}{\eta_{ff}^{r}} = \frac{3}{2}\widetilde{\phi}\frac{\zeta - \tanh(\zeta)}{\zeta + \tanh(\zeta)}\sin^2(\theta) \tag{2.46}$$

where $\eta_{ff}^{r}$ is called the dynamic rotational viscosity of ferrofluid when a magnetic field $\mathbf{H}$ is applied, $\eta_{ff}^{0}$ is the dynamic viscosity of ferrofluid in the absence of magnetic field ($\mathbf{H} = \mathbf{0}$), $\zeta$ is the energy ratio given in (2.15) and defined by $\zeta = \frac{\mu_0 m H}{k_b T}$ and $\theta$ is the angle between $\mathbf{H}$ and the vorticity ($\boldsymbol{\nabla} \times \mathbf{u}$). Equation (2.46) is valid only for highly diluted suspensions ($\widetilde{\phi} \ll 5\%$) [51] containing magnetically hard particles (the relaxation process occurs by rotation of the particle). Note that, if $\mathbf{H}$ is collinear to the vorticity ($\mathbf{H} \| (\boldsymbol{\nabla} \times \mathbf{u})$), the viscosity of ferrofluid is independent of the field. Odenbach [54] explained the magnetoviscous effect in ferrofluids by the formation of clusters enclosing large nanoparticles in the presence of a magnetic field. He confirmed experimentally that ferrofluids with a high concentration of large particles have a much stronger magnetoviscous effect than those with a small concentration of large particles.

**Summary of the dependences of the thermophysical properties**

As explained in the preceding section, the thermophysical properties of the considered ferrofluid are crucial in determining the transport properties of the fluid flow and their heat transfer characteristics. Table (2.1) presents a list of all parameters susceptible to influence the thermophysical properties of a ferrofluid:

| Property | Dependence |
|---|---|
| Density (kg/m$^3$) | $\rho_{ff} = \rho_{ff}(T, \phi, \rho_{bf}, \rho_p)$ |
| Heat capacity (J/K·kg) | $c_{ff} = c_{ff}(T, \phi, \rho_{bf}, c_{bf}, \rho_p, c_p, \rho_{ff})$ |
| Thermal expansion coefficient (/K) | $\beta_{ff} = \beta_{ff}(\widetilde{\phi}, \beta_{bf}, \beta_p)$ |
| Thermal conductivity (W/m·K) | $\lambda_{ff} = \lambda_{ff}(T, \phi, \lambda_{bf}, \lambda_p, H)$ |
| Dynamic viscosity (Pa.s) | $\eta_{ff} = \eta_{ff}(T, \widetilde{\phi}, s, d, \eta_{bf}, H)$ |
| Magnetic permeability (H/m) | $\mu_{ff} = \mu_{ff}(T, H, \widetilde{\phi})$ |

Table 2.1: Thermophysical properties dependences in a colloidal ferrofluid.

## 2.3 Thermomagnetic convection

Thermomagnetic convection is typically the phenomenon that arises in a heated ferrofluid where a temperature gradient is applied and causes a magnetization variation in the presence of a magnetic field gradient. The most important point in this convection is that the magnetization of the ferrofluid, being a function of the temperature, will induce a convective instability in the ferrofluid due to a temperature difference. In the following, we detail the origin of this thermoconvective instability and we report on numerical studies and experimental investigations from the literature.

### 2.3.1 Thermoconvective instability

Thermal convection refers to the transfer of temperature by velocity. It is called natural thermal convection in the case of a horizontal layer of fluid subjected to a vertical temperature gradient. Indeed, due to the temperature difference, a density variation is induced inside the volume. Thus a thermal Buoyancy force ($\mathbf{f}_b = -\rho\mathbf{g}\beta(T - T_{ext})$) depending on the gravity and the density variation of the fluid appears and may cause a hydrodynamic instability in the solution. The dimensionless Rayleigh number is given by (Chandrasekhar [55]):

$$Ra = \frac{\rho g \beta \Delta T L^3}{\kappa \eta} \tag{2.47}$$

where $\Delta T$ is the temperature difference, $L$ is the elevation of the fluid layer represented by $d$ in figure (2.14), $\kappa$ and $\eta$ denote respectively, the thermal diffusivity, and the fluid dynamic viscosity. The Rayleigh number gives an idea about the strength of the thermal driving force in natural convection and describes the balance of the thermal force to the viscous and the thermal dissipation [23, p. 121]. It also depends on the geometric conditions of the problem. If $Ra$ exceeds a critical Rayleigh number, the nature of the heat transfer in the medium varies from heat conduction to thermal convection.
Let us consider a ferrofluid. The magnetization of this latter depends on the strength of the applied magnetic field and the fluid temperature $M = M(H, T)$ which variations are given by:

$$\chi_T = \left(\frac{\partial M}{\partial H}\right)_T, \qquad K = -\left(\frac{\partial M}{\partial T}\right)_H \tag{2.48}$$

where $\chi_T$ is the magnetic susceptibility given by Finlayson [43] and $K$ is the pyromagnetic coefficient defined in (2.36). The magnetic Kelvin force given by (2.32) depends on the magnetization intensity and is oriented towards the source of the magnetic field. The magnetization intensity being inversely proportional to the temperature, see section (2.2.2), the magnetic Kelvin force is greater in a cold medium than in a hot one. Thus, a cold ferrofluid will be more strongly magnetized [56]. To clarify the principle of magnetic convection, we report here the explanation given by Engler and Odenbach in [57]. A horizontal layer of ferrofluid, heated at the top and cooled at the bottom, is taken as an example, see figure (2.14). Due to the temperature difference $\Delta T$ of the two plates, a temperature gradient $\boldsymbol{\nabla} T$ is induced vertically upward in the fluid layer. Thus a density gradient $\boldsymbol{\nabla}\rho$ is produced in the ferrofluid parallel to $\boldsymbol{\nabla} T$. In addition, a magnetic field $\mathbf{H}_0$ is applied parallel to the temperature gradient $\boldsymbol{\nabla} T$. Throughout the fluid layer, the inner magnetic field can be written as $\mathbf{H}_i = \mathbf{H}_0 - a\mathbf{M}$ where $a$ denotes the magnetization factor ($a > 0$). Thus an inner magnetic field gradient $\boldsymbol{\nabla}\mathbf{H}_i = -a\boldsymbol{\nabla}\mathbf{M}$ is induced inside the fluid layer antiparallel to the temperature gradient $\boldsymbol{\nabla} T$. Let us take a ferrofluid particle with volume $V$, temperature $T$, density $\rho$, magnetization intensity $M$, and located at height $z$. The ferrofluid is in equilibrium state. If this particle slightly moves up to a height $z + \Delta z$, and no conduction heat transfer occurs during this displacement, the particle conserves its temperature, magnetization intensity and density. Therefore, the total force acting on the particle after displacement, is composed of the the gravity, the magnetic Kelvin force and the pressure force:

$$\mathbf{F}_{tot} = \rho V \mathbf{g} + \mu_0 V M \frac{dH}{dz}\mathbf{e_z} + \mathbf{F}_{pressure} \tag{2.49}$$

with $\mathbf{e_z}$ the unit vertical vector oriented upwards.

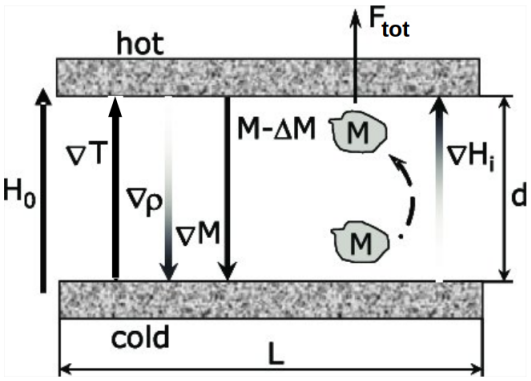


Figure 2.14: Schematic sketch of the thermomagnetic convection in ferrofluids [57].

The pressure force acting on the particle after displacement is the same as the one exerted on the replaced fluid volume. The surrounding ferrofluid is at temperature $T + \Delta T$, density $\rho - \Delta\rho$, and magnetization intensity $M - \Delta M$ ($\Delta\rho > 0$ and $\Delta M > 0$). Using the fundamental law of dynamics, The pressure force exerted on a volume of the replaced fluid is given by:

$$\mathbf{F}_{pressure} = -(\rho - \Delta\rho)V\mathbf{g} - \mu_0 V(M - \Delta M)\frac{dH}{dz}\mathbf{e_z} \tag{2.50}$$

Injecting (2.50) in (2.49) leads to:

$$\mathbf{F}_{tot} = (-\Delta\rho g + \mu_0 \Delta M \frac{dH}{dz})V\mathbf{e_z} \tag{2.51}$$

If the magnetization intensity difference $\Delta M$ and the magnetic field gradient $\frac{dH}{dz}$ are greater enough, we can write:

$$\mu_0 \Delta M \frac{dH}{dz} > \Delta\rho g \tag{2.52}$$

The resulting force given by (2.51) and shown in figure (2.14) is oriented towards the hot plate ($\mathbf{F_{tot}} \cdot \mathbf{e_z} > \mathbf{0}$) and moves upward the ferrofluid volume in its upward displacement. As a result, the situation is unstable and a convective flow appears between the plates, called thermomagnetic convection.
As in natural convection, the dimensionless magnetic Rayleigh number introduced by Finlayson [43] characterizes the state of the ferrofluid in a thermomagnetic convection:

$$Ra_m = \frac{\mu_0 K \|\nabla H\| \Delta T L^3}{\kappa\eta} \tag{2.53}$$

It describes the ratio of magnetic force to viscous dissipation and heat diffusion [23, p. 121]. If $\Delta T$ and $\|\nabla H\|$ highly increase compared to the stabilization factors (thermal diffusion $\kappa$ and viscous dissipation $\eta$), the magnetic Rayleigh number may exceed a critical value and therefore induces an instability in the fluid layer.

Furthermore, another dimensionless number can be used to evaluate the heat transfer enhancement in a heated ferrofluid medium, called the Nusselt Number $Nu$. This number represents the ratio of the total heat transfer rate to the conductive heat transfer [23, p. 122]:

$$Nu = \frac{QL}{\lambda \Delta T} \tag{2.54}$$

where $Q$ represents the total rate of heat transfer and $\lambda$ the thermal conductivity of the fluid. If $Nu = 1$, the heat transfer entirely occurs by conduction. As soon as the Nusselt number becomes greater than unity ($Nu > 1$), the convective heat transfer dominates.

### 2.3.2 Numerical studies

Thermomagnetic convection has been studied numerically and highlighted for its benefit in heat transfer applications [58–61]. Finlayson [43] is one of the first physicists to study theoretically the convective instability in a heated fluid layer under a uniform vertical magnetic field. He predicted that a critical temperature gradient is only possible when the magnetic force prevails over the buoyancy one.

Changing geometries of models with ferrofluid can alter the flow field in thermomagnetic convection and thus impact the heat transfer through the cooling setup. A 3D numerical study was carried out in [62] to compare the fluid flow in curved and straight tubes. In curved geometries, a centrifugal force is added to the thermal buoyancy force and the magnetic Kelvin force and intensifies the convective flow. Zablockis et al. [63] reported a numerical investigation of the thermomagnetic convection in a heated cylinder under a non-uniform constant magnetic field generated by a solenoid. They suggested that auxiliary magnets should be used to enhance the generated magnetic force in the ferrofluid medium.

Other articles present the effect of changing the magnetic field configuration on thermomagnetic convection. Krakov et al. [64] investigated numerically the contribution of a uniform external magnetic field in a square cavity filled with ferrofluid. They showed that changing the angle between the temperature gradient and the applied magnetic field can modify the convection flow pattern and thus the heat flux across the cavity.

In addition, Ashouri et al. [25] studied numerically with the finite volume method the thermomagnetic convection in a square cavity filled with ferrofluid and subjected to a permanent magnet fixed at the center of the cavity. They investigated the flow convection fields for various magnetic Rayleigh numbers, magnet sizes or temperature differences between the hot and cold walls of the cavity. They found that increasing the magnetic Rayleigh number increases the flow intensity in the cavity and improves the heat transfer process. It is also reported that an optimum size for the permanent magnet can be found for an enhanced heat transfer rate.

In parallel, the transition from natural convection to a thermomagnetic one has been studied numerically in a square cavity filled with ferrofluid and subjected to a permanent magnetic pole at the top of the enclosure, as explained in [24]. Results show that the transition occurs when two distinct convection cells appear in the fluid domain instead of one in natural convection, and that the buoyancy and Kelvin forces are equal in strength. As long as the magnetic Kelvin force overcomes the buoyancy one in the fluid domain, the magnetic mechanism dominates the global heat transfer of the cavity.

In a recent paper [65], Zanella et al. studied the thermal convection in a cylindrical container heated by a solenoid. The container is filled with an oil-based ferrofluid, as shown in figure (2.15).

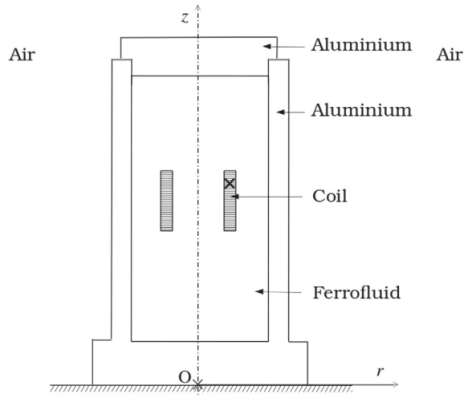


Figure 2.15: Geometry of a heated solenoid immersed in a cylindrical container [65]. The cross mark shows the position of the coil monitored temperature.

First, Zanella et al. verified numerically the improvement of the coolant thermophysical properties when a ferrofluid replaces a pure transformer oil. Then they demonstrated the impact of a constant magnetic field on the heat transfer process with ferrofluids. Figure (2.16) shows the temperature fields for the heated solenoid considering several configurations: (a) when a transformer oil is used for cooling, (b) with a ferrofluid and no applied field, and (c) with the same ferrofluid ($\phi = 7\%$) and an applied magnetic field. Results show a decrease in solenoid temperature of $2\,°\mathrm{C}$ when the physical properties of the solution are changed between (a) and (b). When a magnetic field is applied in (c), and with ferrofluid usage, the solenoid temperature shows a decrease of $4\,°\mathrm{C}$ roughly comparing to (a).

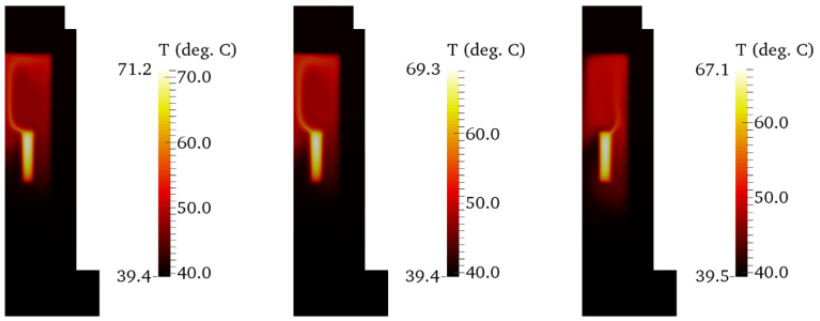


(a) Pure oil (b) Ferrofluid - $H = 0$ (c) Ferrofluid

Figure 2.16: Temperature fields (in °C) in the meridian plane at $t = 10000s$ for the model when the heated solenoid is immersed (a) in pure transformer oil, (b) in ferrofluid, (c) in ferrofluid with an applied magnetic field. The symmetry axis ($Oz$) is on the left and $\phi = 7\%$ in (b) and (c).

### 2.3.3 Experimental investigations

First, Schwab et al. [66] performed experiments to study the Rayleigh-Bénard convection in a ferrofluid layer ($M_s = 32\ \mathrm{kA.m^{-1}}$) subjected to a homogeneous vertical magnetic field. The

study aimed to determine the critical temperature difference associated to the onset of the thermomagnetic convection when both buoyancy and Kelvin force are present. Visualization of the flow pattern in such a setting was demonstrated in [67]. The ferrofluid being opaque, a direct visualisation of the convection pattern in the ferrofluid is not possible. Therefore the experiment was performed between a bottom aluminum plate and a top glass plate (see figure (2.17)). Owing to the heat conduction in the glass plate, the glass temperature reflects the flow patterns in the ferrofluid layer. Figure (2.18) visualizes the shadow of the vortices and allows to measure the wavelengths of the flow patterns. A temperature difference has been applied between the upper and the lower boundaries of the ferrofluid layer in the presence of a transverse vertical magnetic field $\mathbf{H}_t$ (see figure 2.18, (d) $\Delta T = +30K, |\mathbf{H}_t| = 13.3\ \mathrm{kA.m^{-1}}, |\mathbf{H}_l| = 0$). We observe irregularly misaligned and interpenetrated waves that reach the cylinder wall perpendicularly. In figure (2.18, a-b-c), a horizontal longitudinal magnetic field $\mathbf{H}_l$ has been applied to align the axis of the rolls. The conducted theoretical study agrees with these observations since the increase in magnetic Rayleigh number ($\Delta T$ increases, $H$ increases) induces an increase of the wavevectors in the convection patterns as observed in figure 2.18, (a) $\Delta T = -10K, |\mathbf{H}_t| = 0, |\mathbf{H}_l| = 3.3\ \mathrm{kA.m^{-1}}$ - (b) $\Delta T = -10K, |\mathbf{H}_t| = 13.3\ \mathrm{kA.m^{-1}}, |\mathbf{H}_l| = 3.3\ \mathrm{kA.m^{-1}}$ - (c) $\Delta T = +30K, |\mathbf{H}_t| = 13.3\ \mathrm{kA.m^{-1}}, |\mathbf{H}_l| = 3.3\ \mathrm{kA.m^{-1}}$.

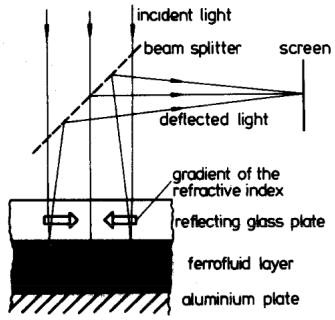

Fig. 2. Principle of flow visualization.

Figure 2.17: Technique of flow visualization [67]

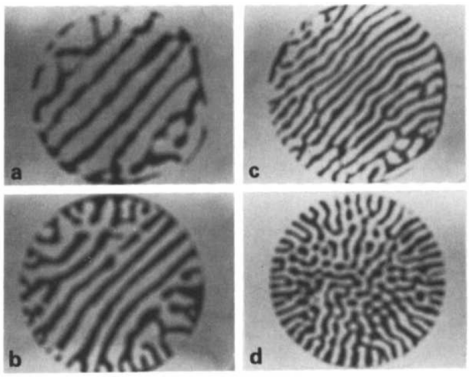


Figure 2.18: Shadow of convection flow patterns with a hydrocarbon-based ferrofluid [67]

Another article described a similar experimental setup where the focus was on the ferrofluid free surface deflection under both vertical magnetic field and temperature gradient due to magnetostatic and hydrodynamic stresses [68].
Recently, Vatani et al. [22] studied the onset of the thermomagnetic convection by measuring the temperature rise for a hot vertical wire enclosed in a channel of ferrofluid, see figure (2.19).

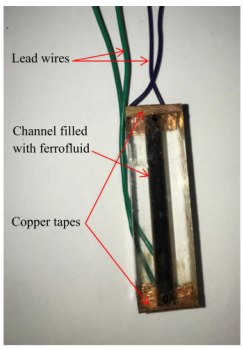


Figure 2.19: Measurement set up with a heated wire passing through a ferrofluid channel [22, p. 302]

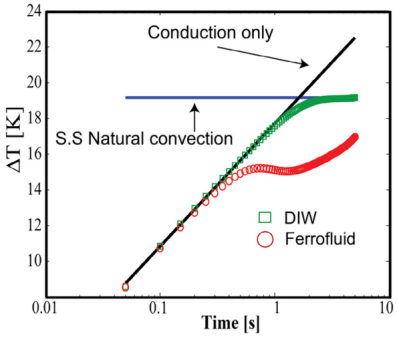


Figure 2.20: Temperature increase for the heated wire, bath temperature = 40°C, supplied current $I = 1.5\text{A}$ [22, p. 303]

The experimental measurements were compared to natural convection in a deionized water ($DIW$) for similar experimental conditions, as shown in figure (2.20). These temperature rise measurements prove that thermomagnetic convection occurs before the natural convection in a non-magnetic fluid sets in. While natural convection in a deionized water ($DIW$) starts at 1.4s, thermomagnetic convection in a ferrofluid occurs at 0.47s.

### 2.3.4 Experimental & numerical comparisons

Several articles investigate the thermomagnetic convection experimentally and propose validating it by a numerical approach. One of these papers [23] performed an experimental setup based on a perspex cavity filled with a ferrofluid and subjected to an external magnetic field generated by a permanent magnet. The upper and the lower surfaces of the cavity have been chosen to be respectively hot and cold. The magnet was placed either near the top surface or at the left side of the cavity to provide different magnetic field configurations (see figure (2.21)).

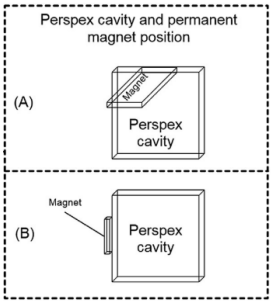


Figure 2.21: Experimental set up with different permanent magnet configurations [23, p. 120]

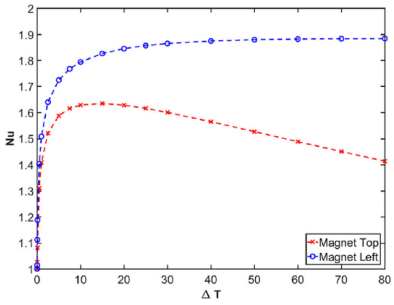


Figure 2.22: Evolution of Nusselt number regarding the temperature difference [23, p. 125]

To quantify the heat transfer occurring across the cavity, the dimensionless Nusselt number $Nu$ was evaluated against the temperature difference $\Delta T$ for different positions of the permanent magnet as shown in figure (2.22). According to this figure, we can observe an increase in heat transfer by thermomagnetic convection for both external magnetic field configurations since the Nusselt number is greater than unity ($Nu > 1$). However, the heat transfer does not occur in the

same manner for the two positions of the magnet: when it is placed near the top of the cavity, $Nu$ first increases reaching a maximum of 1.63 and then decreases progressively with $\Delta T$. On the other hand, when the magnet is at the left, $Nu$ increases monotonously with $\Delta T$ until reaching approximately $Nu = 1.9$.

Another recent study was conducted by Vatani et al. [21] to assess the fluid flow and temperature rise of a heated vertical wire passing through a ferrofluid channel (see figure (2.23)). The microwire is supplied by a constant current. The study demonstrates that 20 % of temperature decrease was registered when the heated wire is cooled with ferrofluid instead of deionized water ($DIW$). Figure (2.24) presents the velocity fields and streamlines after 10 s only for the thermomagnetic convection without considering the buoyancy force. As seen in this figure, when the supplied current increases, the vortices' large scale grows immediately, and as a result, their number decreases. As seen in figure (2.24), the vortices become more intense, and their velocity grows with the current. Therefore, the heat dissipated throughout the ferrofluid channel is enhanced because of the strongest circulation of the fluid flow.

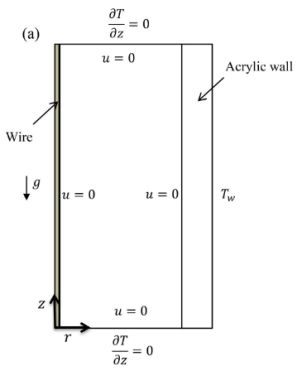


Figure 2.23: Schematic sketch of the set up model [21, p. 2]

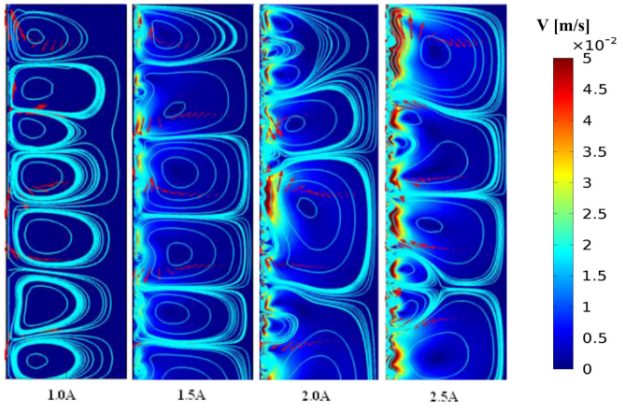


Figure 2.24: Velocity fields and streamlines for the induced thermomagnetic convection with various supplied currents after 10 s [21, p. 5]

## 2.4 Heat transfer under oscillating magnetic field

The heat transfer in ferrofluid under a time oscillating magnetic field has been studied experimentally and numerically in many articles [69–71]. Ghasemian et al. [70] reported a numerical study on the heat transfer via convection in a ferrofluid channel in the presence of constant or oscillating magnetic fields. A water-based ferrofluid ($\phi = 4\%$) flows in a 2D channel with isothermal bottom and top surfaces ($T = 290\,\mathrm{K}$), see figure (2.25). They have studied first the impact of a constant magnetic field generated by the current source of wire 1 located below the channel on the heat transfer. Then, the ferrofluid is subjected to an oscillating magnetic field produced by applying time varying functions to the current source of both wires shown in figure (2.25).

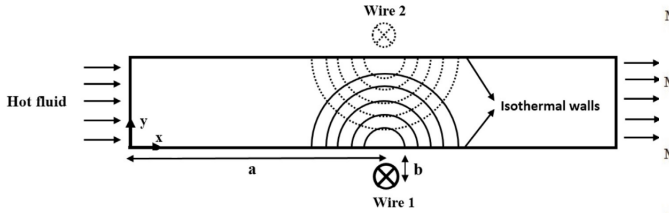


Figure 2.25: Schematic view of the 2D channel [70, p. 160].

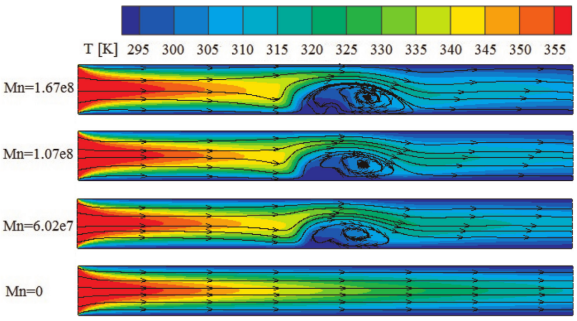


Figure 2.26: Temperature fields with streamlines for different magnetic field intensities at Reynolds number $Re = 25$ [70, p. 162].

They found that a new ferrofluid circulation appeared at the bottom of the channel with a constant magnetic field and grew with the field intensity, see figure (2.26). They have also reported that the convection vortices formed in the channel flow influence the thermal boundary layers near the channel walls. When the vortex flow direction opposes the fluid flow in the channel, the thickness of the thermal boundary layer decreases and produces an enhancement of the heat transfer. In contrast, if the vortex flow direction is the same as the fluid flow, the thermal boundary layer is unchanged, leading to a decrease in the heat transfer. Moreover, an oscillating magnetic field applied to the ferrofluid shakes the fluid particles periodically and creates an accelerated convection flow in the channel. Consequently, the heat transfer might be improved.

The influence of a constant or oscillating magnetic field has also been studied experimentally in [71], where a heated ferrofluid is pumped into a copper tube in the presence of a sequence of electromagnets, see figure (2.27). To produce the magnetic field, six U-shape zinc ferrite cores, made of low hysteresis materials, are used as electromagnets. The cores are placed in front of each other with opposite poles on both sides of the tube, as shown in figure (2.28).

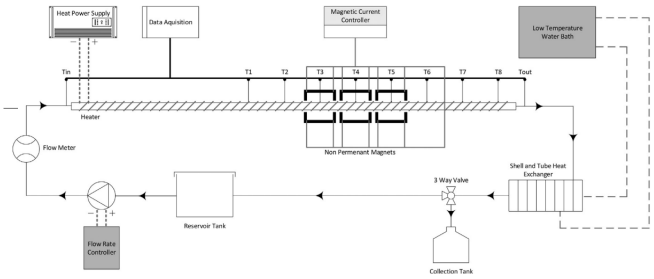


Figure 2.27: Schematic view of the experimental setup [71, p. 603].

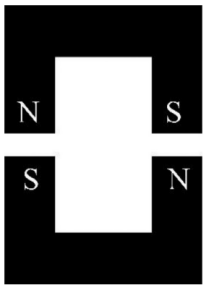


Figure 2.28: Arrangement of pair of electromagnets on the copper tube [71, p. 603].

The experiment showed that the heat transfer is strongly enhanced under oscillating magnetic fields, especially with a high volume fraction of nanoparticles and low Reynolds numbers, see figure (2.29). As seen in this figure, while using magnetic nanoparticles can enhance the local heat transfer in ferrofluids with no magnetic field applied, the convective heat transfer is reduced with a constant magnetic field. Furthermore, increasing the frequency of the oscillating magnetic field

results in an increase in the local heat transfer coefficient.
At lower Reynolds Numbers ($Re < 1000$), the motion of particles is slow so that the magnetic field has sufficient time to exert its magnetic force on the fluid particles. Hence, the thermal boundary layer is disrupted by the formed vortices, and as a result, the local heat transfer can be accelerated. It is also demonstrated that increasing the concentration of magnetic nanoparticles in the ferrofluid under an oscillating magnetic field can enhance the local heat transfer.

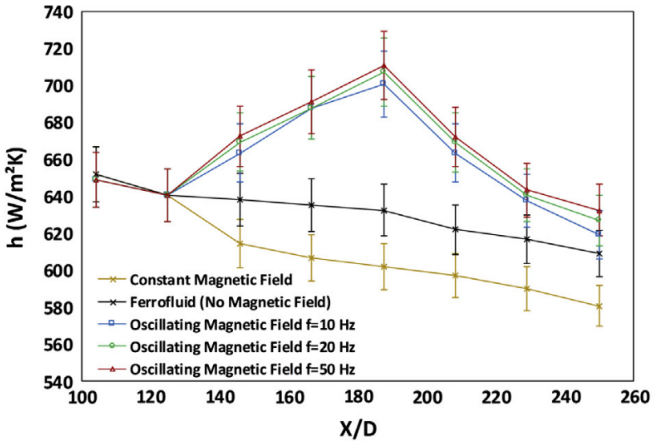


Figure 2.29: Evolution of the local convective heat transfer coefficient with respect to the dimensionless distance with constant or various oscillating magnetic fields ($\phi = 2.5\%$, Reynolds number $Re = 465$, $X/D$ is the dimensionless distance from the entrance of the tube) [71, p. 608].

## 2.5 Effect of magnets on cooling

Using permanent magnets to enhance the heat transfer was reported a few decades ago when Raj et al. [72] deposed their invention using magnets as auxiliary components to improve the cooling of an electromagnetic device. Power transformers, for example, exhibit a high operational temperature that results in a decrease in their performance. The idea of the patent was to set permanent magnets around the core of the power transformer to enhance the leakage flux in the ferrofluid. Therefore, the fluid is drawn toward the high-strength magnetic field regions, and as a result, the cooling performance is improved. In this patent, it is also recommended that the Curie temperature of the used ferrofluid remains close to the device operating temperature.
Other papers report several applications using permanent magnets to improve the cooling of devices with ferrofluid [73, 74]. In the same context, Chaudhary el al. [75] built a self-pumping cooling system based on a water-based ferrofluid flowing through a heated tube under the influence of an external magnetic field, see figure (2.30). Their study confirmed that increasing the concentration of nanoparticles, the applied magnetic field strength, or the initial temperature load result in a good performance of the cooling device. Figure (2.31) shows the influence of applying and removing the magnetic field on the temperature profile of the heat load. As seen in this figure, the temperature reaches a steady-state in the absence of a magnetic field. When the magnet is present ($B_R = 0.3\mathrm{T}$), the temperature drops quickly in less than 3 minutes with a temperature difference of $\Delta T = 28°\mathrm{C}$. The same tests have been repeated several times and led to periodic crenelations in the temperature curve with the same amplitude.

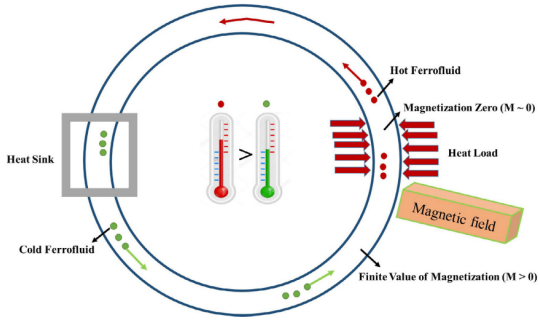


Figure 2.30: Schematic view of the self-pumping cooling system [75, p. 2]

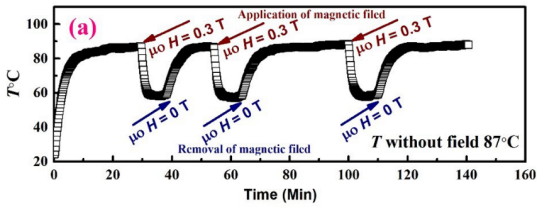


Figure 2.31: Influence of switching the applied magnetic field between two states $B = 0$ and $B = 0.3$ T on the heat load temperature for initial heat load temperature of 87°C [75, p. 7].

## 2.6 Power transformer

One of the applications of ferrofluids as a coolant medium is power transformers. These power devices undergo a hot spot temperature that can affect their life span and reduce their performances and efficiency along the time. This section presents the state of the art regarding the use of ferrofluids for transformer applications. We provide an overview of the dielectric properties of a ferrofluid-based power transformer and report on the relevant experiments and numerical modeling to describe the heat transfer that occurs inside these devices.

### 2.6.1 Dielectric properties

#### AC Breakdown strength regarding water content

As explained before, ferrofluids can be used as insulation liquids in power transformers to enhance heat transfer within these devices. However, adding magnetic nanoparticles to a transformer oil still has adverse effects on its dielectric strength. The breakdown voltage determines the threshold from which a dielectric fluid subjected to an electric field does not fulfill its insulating function. Segal et al. [76] reported first measurements on the AC breakdown strength and the impulse breakdown voltage in a colloidal ferrofluid based on magnetite nanoparticles dispersed in a mineral transformer oil. Results presented in table (2.32) show that both oil and colloid ferrofluid exhibit a decrease in their AC breakdown voltage when the proportion of moisture in the considered solution increases. Note that a reduction of the AC breakdown voltage of the dielectric fluid reduces the device's life span since the degradation of cellulose papers is accelerated. The insulation period in a power transformer is programmed for 40 years or more [77, 78]. Nonetheless, the AC breakdown voltage of a ferrofluid remains less dependent on the moisture content than that of mineral oil.

| Fluid | Moisture content, ppm, in the oil carrier | | | | | | | |
|---|---|---|---|---|---|---|---|---|
| | < 5 | | 10 to 20 | | 20 to 30 | | >30 | |
| | kV | STD | kV | STD | kV | STD | kV | STD |
| Oil | 50 | 3.5 | 43 | 4.2 | 37 | 4.5 | 28 | 5.7 |
| Colloid | 50 | 2.9 | 47 | 2.8 | 44 | 3.9 | 40 | 3.5 |

Figure 2.32: Dependence of the AC Breakdown voltage on the moisture content in ferrofluid and transformer oil [76].

### AC Breakdown strength regarding thermal aging

Segal et al. [76] proved experimentally that several properties of the ferrofluid (electrical resistivity, viscosity, and magnetic particle density) remain unchanged after thermal aging for 34 weeks at 185°C. According to the preceding section, the stability of a colloidal ferrofluid depends particularly on the stability of its carrier liquid. Recent measurements were carried out by Kurimsky et al. [78] to investigate the AC breakdown strength after thermal aging of a ferrofluid filled with iron oxide nanoparticles. As cited in [78], a ferrofluid exhibits normally an AC breakdown strength similar to or higher than that of transformer oil. The presence of magnetic nanoparticles inhibits the charge displacement in the fluid so that the electrical breakdown strength of a colloidal ferrofluid becomes higher. Measurements taken for three ferrofluid volumes with different particles concentration show that the real part of the AC magnetic susceptibility decreases its amplitude after accelerated thermal aging. In all ferrofluid samples, separation of components and sedimentation of particles are observed after 600 hours of aging tests (see figure 2.33). The ferrofluid is no longer homogeneous. As a result, the dielectric performances of the ferrofluid after accelerated thermal aging decrease. During thermal aging, the trapping of electric charges by magnetic nanoparticles is reduced due to their sedimentation. Consequently, the ferrofluid conduction grows, and its AC breakdown strength decreases. Note that an increase of the volume fraction of nanoparticles results in a decrease in the resistivity of a ferrofluid.

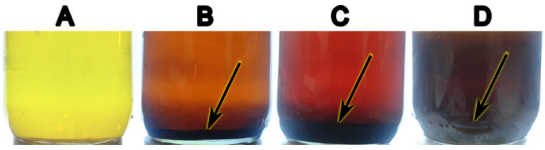


Figure 2.33: Destabilization of a colloidal ferrofluid after accelerated thermal aging tests. (A) transformer oil, (B) ferrofluid with $\phi = 0.05\%$, (C) ferrofluid with $\phi = 0.15\%$, (D) ferrofluid with $\phi = 0.35\%$ [78, p. 139]

### Dielectric permittivity

Recent measurements of dielectric permittivity and dissipation factor were carried out by Rajnak et al. [79] for both transformer oil and iron oxide nanoparticles ($\phi = 0.93\%$)-based ferrofluid. They reported that the superparamagnetic behavior of magnetic nanoparticles in ferrofluids is followed because their magnetization curve shows no hysteresis effect. The hysteresis losses in ferrofluids are negligible. Figure (2.34) shows the dielectric permittivity dependence on temperature for transformer oil and ferrofluid.

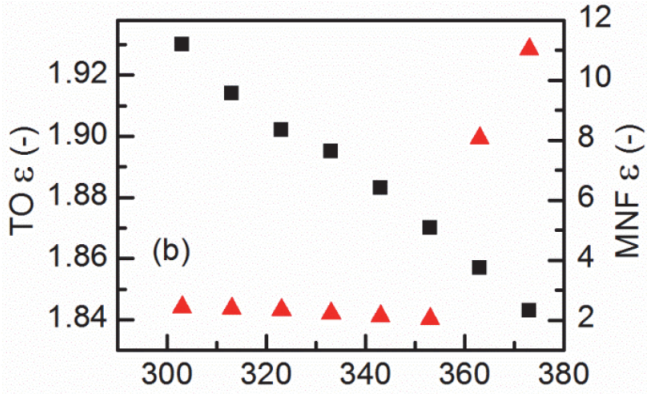


Figure 2.34: Dielectric permittivity of transformer oil (TO - black squares) and ferrofluid (MNF - red triangles) respectively versus temperature (in $K$) [79, p. 1347].

As presented in figure (2.34), both transformer oil and ferrofluid show that the permittivity decreases with the temperature in the range [300-353]$K$. While the permittivity decrease stays limited with transformer oil, a reduction from 2.45 to 2.1 is registered with ferrofluid. It is also shown that the dielectric permittivity of the ferrofluid sharply increases when the temperature grows from 360 to 373 $K$ and reaches a value 9.2 times greater than that obtained with pure transformer oil at 373$K$. This increase in dielectric losses of ferrofluids compared to transformer oil can be related to several factors like the AC conductivity of ferrofluids and the interfacial polarization mechanism detailed in [79, p. 1346,1347].

### 2.6.2 Cooling performances

#### Experimental measurements

According to the work presented in [79], using a ferrofluid with high dielectric losses in transformer cooling applications may lead to excessive heating. In contrast, a slight decrease of $1K$ of the average temperature (see table (2.2)) is obtained in [79] when a commercial ferrofluid (with magnetite particles, $\phi = 0.93\%$) has replaced the pure transformer oil in a single-phase power transformer model shown in figure (2.35). In table (2.2), $\Delta T$ is the temperature difference after 11 hours between the transformer part and the ambient temperature (in $\mathrm{K}$). This slight decrease of the device temperature has been related to the thermomagnetic convection in ferrofluids and the Brownian motion of magnetic nanoparticles. The authors considered that the thermal conductivity of the used ferrofluid does not significantly contribute to the improvement of the device cooling. Note that a Curie temperature ($T_c = 858K$) much higher than the device operating temperature is considered in their experiment. As mentioned before [72], using magnetic nanoparticles with high Curie temperature in the ferrofluid could not be adapted with the improvement of heat transfer. Finally, the authors assumed that a better performance for transformer cooling could be reached with bigger devices in which the applied magnetic field is much stronger.

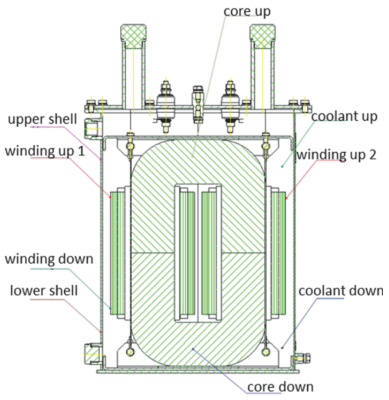


Figure 2.35: Cross section of the power transformer model [79, p. 1345].

| | Core down | Core up | Wind. down | Wind. up |
|---|---|---|---|---|
| Pure oil, $\Delta T$ | 52.59 | 67.54 | 55.83 | 71.19 |
| Nanofluid, $\Delta T$ | 52.18 | 67.22 | 55.51 | 70.63 |
| Difference in $\Delta T$ | 0.41 | 0.32 | 0.32 | 0.56 |

Table 2.2: Comparison of the cooling effect in the power transformer model (T1N-5-400/230, underloading 4.3 $\mathrm{kVA}$) [79, p. 1348].

Several years ago, Patel et al. [80] investigated the efficiency of a synthesized ferrofluid ($\phi = 1.27\%$) as a coolant in a 3 $\mathrm{kVA}$ power transformer (230 $\mathrm{V}$, 13 $\mathrm{A}$) with overloading conditions. The ferrofluid used is the TCF-56 based on Mn-Zn nanoparticles with a Curie temperature $T_c = 380K$, a pyromagnetic coefficient $K = 177\mathrm{A.m^{-1}K^{-1}}$ and a breakdown voltage $BDV = 69.5$ $\mathrm{kV}$ (an improvement of $BDV$ by 115% comparing to measured transformer oil, TASHOIL-50, which has $BDV = 32.3$ $\mathrm{kV}$). They recommended, as explained before, that the Curie temperature of the ferrofluid has to be close to the operating temperature of the transformer (70-300°C) to make sure that strong thermomagnetic convection occurs [72]. For a high voltage power transformer, the maximum operating temperature is estimated to 110°C. Experimental measurements for the coil and the temperature of the windings show an interesting decrease of their maximum temperature with TCF-56 compared to transformer oil, see figure (2.36).

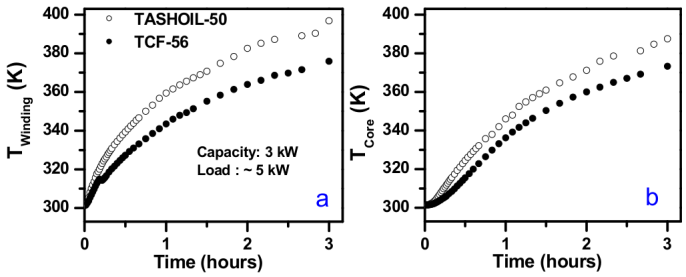


Figure 2.36: Temperature measurements of the windings and the core of a power transformer versus time. (TCF-56: ferrofluid, TASHOIL-50: transformer oil [80, p. 38]).

As shown in figure (2.36), a sharp decrease in core and windings temperature of 14 and 21 *K* is respectively observed with TCF-56. The authors claimed that they had repeated three times the measurements of the transformer part temperature to make sure of the comparison. However, the work was not confirmed by a numerical model. They related this noticeable enhancement to the thermomagnetic convection. They estimated that a decrease by 21 *K* of the maximum temperature of the windings results in rising nine times the life span of the power transformer [80].

### Numerical modeling

Some authors proposed various models to study the heat transfer in ferrofluid-based power transformers using either the finite element method FEM [81–86] or the finite volume method FVM [87,88]. The first proposed reference does not consider the ferrohydrodynamics problem, but it is described here as it compares 2D and 3D approaches. A triple-phase power transformer, 31.5 $\mathrm{MVA}$, 132/33 $\mathrm{kV}$, 50$\mathrm{Hz}$, with concentrical windings, has been modeled by Jimenez-Mondragon et al. [82] to evaluate the electric current and the magnetic flux density in normal load and short-circuit condition (see figure (2.37)). They investigated a 3D model but also a simplified 2D axisymmetric model. For this purpose, the complex 3D structure of the power transformer is simplified into three sub-domains with axisymmetric geometries based on the circular shape of the windings, see figure (2.38). They compared the results from these 2 computations and found a good agreement, then validating the 2D axisymmetric model. Owing to this simplified approach, one can assume that using 2D axisymmetric finite element analysis instead of the 3D finite element one remains simple, consistent, and with low computational cost. However, the authors did not report on the cooling effect nor provide the characteristics of the solution used to cool this power transformer model, whether it was a ferrofluid or transformer oil.

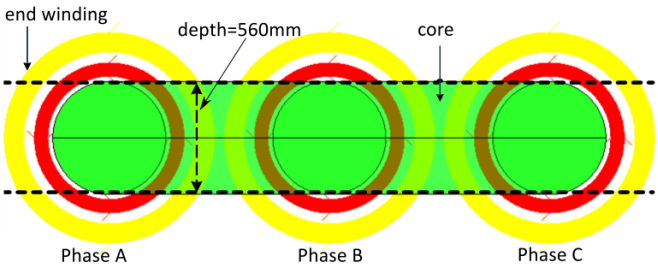


Figure 2.37: Top view of the 3D power transformer model [82, p. 2].

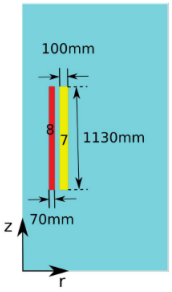


Figure 2.38: Axisymmetric model for each core leg in the transformer [82, p. 3].

Morega et al. [86] designed a single phase-power transformer, low frequency, 2-36$\mathrm{kV}$, 40$\mathrm{kVA}$, immersed in a transformer oil containing magnetite particles. The idea was to evaluate the electromagnetic field in the transformer and the heat transfer process throughout the cooling ferrofluid using the finite element method (COMSOL Multiphysics). In their study, the authors considered only the stationary momentum and temperature equations, i.e., no unsteady phenomenon is taken into account. In addition, the ferrofluid magnetization has been approximated by an analytic formula that is not temperature-dependent (the ferrofluid magnetization $M$ depends only on the magnetic field $H$ in this study). Figures (2.39, 2.40) respectively show a partial vertical view of the power transformer model and a 3D color map of the streamlines. In figure (2.39), we distinguish by colors: the core and the external winding (green), the internal winding (cyan), the gap between windings (red), the ferrofluid domain (purple), the base (pink).

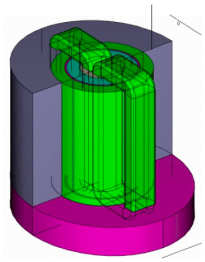

Figure 2.39: Partial view of a prototype power transformer cooled with ferrofluid [86, p. 145].

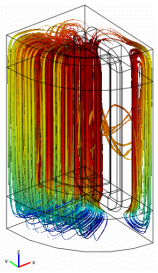

Figure 2.40: Streamlines of the velocity field in the vertical configuration [86, p. 146].

Owing to their study, vertical positioning of the 3D model provides more heat dissipation through the device and induces a steep temperature decrease ranging between 20 °C and 30 °C. The hot spot temperature is found to be in the core and not in the windings. They also found that the magnetic force (Kelvin expression) acts mainly on the top of the windings.

Three years later, Pislaru-Danescu et al. [85] prepared a magnetite-based ferrofluid ($\phi = 1.1\%$) for cooling a single-phase power transformer prototype, see figure (2.41). In parallel, they tried to model the experimental setup using the finite element method (COMSOL Multiphysics). They also found that building a power transformer prototype in a vertical layout remains better for cooling with a sharp decrease in the hot spot temperature by $20\,°\mathrm{C}$ when the ferrofluid is used, see figure (2.42). However, their study did not consider the magnetization dependence on the temperature, while the thermomagnetic convection requires a temperature-dependent magnetization to occur. The authors claimed that the convective term $((\mathbf{u}\cdot\boldsymbol{\nabla})T)$ in the temperature equation is responsible for the cooling enhancement obtained with ferrofluids.

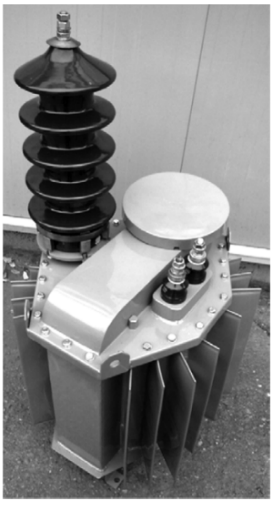

Figure 2.41: Power transformer prototype [85, p. 5491].

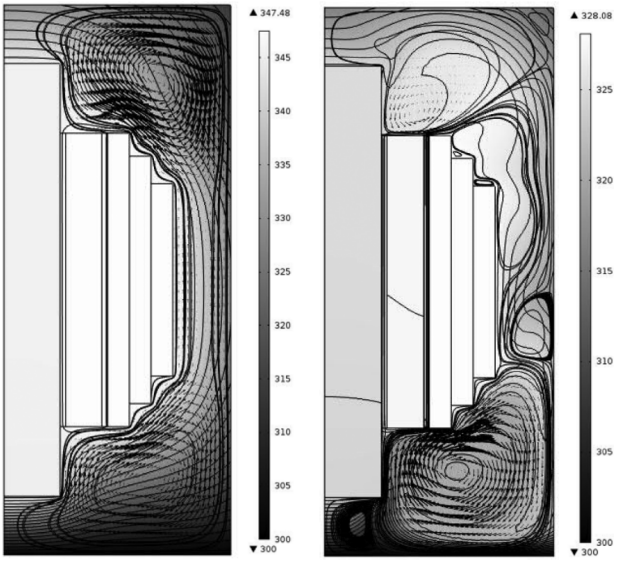


Figure 2.42: Temperature fields in (K), with transformer oil on the left and ferrofluid on the right [85, p. 5492].

In the same context, a study was recently reported by Pislaru-Danescu et al. [81] to model a miniature planar spiral transformer with ferrofluid cooling. They focused on the role of the coolant in removing air cavities and minimizing leakage of magnetic flux to improve magnetic coupling.

Other studies focused on improving the cooling performance of power transformers by creating barriers and radiators in their design and thus rising cooling zones [83]. Recent research in [87] aimed to evaluate the cooling of disc-type transformer windings with ferrofluid. The authors found that increasing the concentration of nanoparticles in ferrofluid decreases the maximum temperature rise in the transformer.

The thermomagnetic convection effect in the presence of oscillating electric and magnetic fields has been recently evaluated in [89]. The numerical model consists of a circular coil placed in a cylindrical container and supplied by a time-dependent current, see figure (2.43). The container is filled with a conductive water-based ferrofluid with a low concentration of ferrite nanoparticles ($\phi = 0.3\%$). The electromagnetic field generated in the ferrofluid depends on the current variation in the coil. The originality of this study is that the authors have modeled the impact of the electromagnetic field using an electromagnetic force with the consideration of eddy currents in the ferrofluid. This force, having both electric and magnetic origins, is written as the sum of Lorentz and Kelvin forces:

$$\mathbf{F} = \mathbf{J} \times \mathbf{B} + \mu_0(\mathbf{M} \cdot \boldsymbol{\nabla})\mathbf{H} \tag{2.55}$$

It seems that Boussinesq term is missing in the Navier-Stokes equation, which means that this study did not consider the density variation of the ferrofluid with temperature. The study focuses on the importance of improving the magnetic flux density in a conductive ferrofluid medium that can enhance the eddy current in the suspension and therefore maximize the electromagnetic force. The authors did not report on the coil maximum temperature reduction.

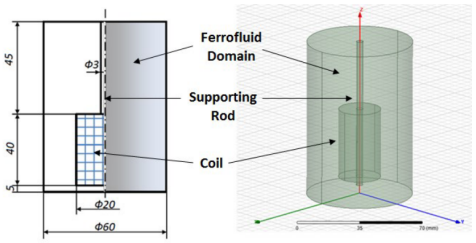


Figure 2.43: Cross section view (a) and 3D geometrical model (b) [89].

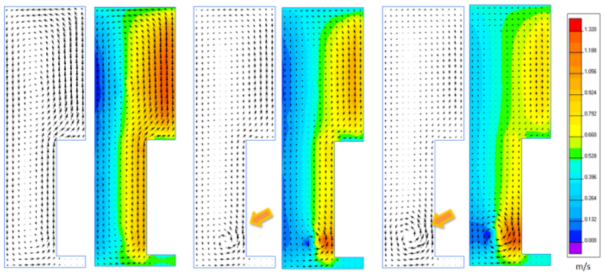


Figure 2.44: Color maps of the velocity fields with vectors in three configurations of the modeling [89].

Figure (2.44) shows the velocity distributions with velocity vectors in the ferrofluid medium at a steady-state for three cases: the suspension is non-magnetic and non-conductive (a), the suspension is non-magnetic but conductive (b), and the suspension is both magnetic and conductive (c). According to their study, one convection cell is observed when a conductive ferrofluid (c) replaces a nonmagnetic and a non-conductive fluid (a). They found that the ferrofluid velocity is increased by

$40\%$ compared to the non-magnetic convection. The thermophysical properties of the suspension are mentioned, while the major laws for calculating these properties are not detailed. The ferrofluid magnetization dependence is not reported.

To conclude, several articles have already discussed the possibility of lowering the maximum temperature rise in a power transformer by replacing the transformer oil with ferrofluids. However, the presented models often suffer from a lack of details, and it is still challenging to conclude whether the numerical approaches consider all the phenomena with adequate assumptions. Consequently, adding magnetic nanoparticles to the cooling oil remains a current problem worth studying in view of improving the heat transfer.

## 2.7 Conclusions

A ferrofluid is defined as a suspension of magnetic nanoparticles in a non-magnetic carrier fluid. Since the magnetic particles have nanometric sizes, they are fully dispersed in the solution and form a homogeneous, stable suspension. The presence of magnetic particles in the carrier liquid confers to the ferrofluid both rheological and magnetic properties. A ferrofluid is magnetized when subjected to a magnetic field but remains flowable even when its magnetization reaches saturation state. Adding a dispersal agent or surfactant to a ferrofluid avoids the internal aggregation of particles, as the Brownian movement inhibits the precipitation of these particles.

Particles in ferrofluid generally exhibit a superparamagnetic state. They are randomly oriented in the ferrofluid when no magnetic field is applied and at an ordinary magnetic field intensity. Particles tend to be aligned with the field lines when subjected to a high magnetic field, and the ferrofluid reaches its saturation state. Langevin's theory gives a description of the superparamagnetic behavior of a ferrofluid. The heat transfer process in a ferrofluid under the influence of both magnetic field and temperature gradient is described by the set of magnetostatic, Navier-Stokes, and heat transfer equations. Thermophysical properties of ferrofluids can be deduced by mixture laws from literature.

Thermomagnetic convection is the phenomenon that arises when a ferrofluid medium is simultaneously subjected to an external magnetic field and a temperature gradient. Due to the dependence of the ferrofluid magnetization on temperature, a thermoconvective instability can occur in the liquid. Magnetic Rayleigh numbers and other dimensionless numbers may be used to describe the state of ferrofluid in thermomagnetic convection.

The effect of oscillating magnetic fields on heat transfer applications is studied in some papers. Reported studies mentioned that changing magnetic field creates an accelerated convection flow that can allow more heat dissipation through the studied system. Articles have shown that increasing the frequency of an oscillating magnetic field can increase the heat transfer coefficient. In these studies, strong assumptions have been made when considering the magnetostatic equations. In addition, some of these papers describe an experimental approach with ferrofluids without performing a numerical validation. The impact of magnets on the cooling is reported, but rare have applied auxiliary magnets in their numerical model to validate the improvement of the cooling performance.

The maximum temperature rise in the windings has to be controlled for power transformer devices to maintain sustainability and good performances over time. Indeed, a hot temperature can affect the dielectric properties of the coolant or deteriorates the device. The AC breakdown voltage and the dielectric permittivity are examined as critical dielectric properties in ferrofluids in some works. Numerical and experimental studies on the cooling of transformers with ferrofluid show the benefit of using such a solution as a coolant to lower maximum temperature rise in the windings and retain better performances for these devices with a long life span. In the discussed papers, the magnetization of ferrofluid is sometimes questionable since it does not show a temperature dependence. Furthermore, the magnetic body force used to model the ferrofluid is usually based on the Kelvin model, while few papers have mentioned the Helmholtz model. Nevertheless, these studies remain rare and their outcomes need to be clarified.

# Chapter 3

# Heat transfer: Solenoid study

This chapter introduces our two complementary approaches, experimental and numerical, on the problem of enhancing the cooling of a heated solenoid immersed in a ferrofluid using the thermomagnetic convection effect. At first, we present the experimental prototype developed at GeePs laboratory with the different types of equipment. In a second section, we describe the ferrofluid used in the experiment. Then, in a third section, we explain the 2D axisymmetric numerical model built in COMSOL Multiphysics to assess the solenoid cooling and detail the coupling method. In the fourth section, we compare several formulations for the magnetic force responsible of the thermomagnetic convection. The results validating the impact of the thermomagnetic convection are also discussed. We show a cross-validation of the experimental and numerical results performed with the 2D-axisymmetric model of the solenoid. Finally, we present two different tests for improving the thermomagnetic convection in the solenoid system. The first one studies the impact of Curie temperature of magnetic nanoparticles on the thermomagnetic convection. The second one evaluates the effect of adding external magnets on the heat transfer. The numerical results are compared against experimental ones and are therefore interpreted. We also study the effect of adding a ferromagnetic core to optimize the cooling process in the coil.

## 3.1 Experimental bench

### 3.1.1 General description

One first objective of this thesis is to study the thermo-magnetic behavior of a simple setup, mainly a heated solenoid immersed in a ferrofluid medium. This study is a starting point for the more complex configuration of a power transformer cooled by a ferrofluid that will be the subject of the next chapter.
This experiment requires a test cell, a supply source, and a computer system driving the experiment protocol, with a connector system to have a closed circuit, as shown in figure (3.1). Thermocouples connected to a dSPACE card are used to measure the setup temperatures at different points and their interpretation is simplified with the plot of the time evolution curves on the fly. The study is performed in the "Nano" room in GeePs laboratory equipped with air extractions to avoid the dispersion of magnetic nanoparticles to the environment and well-respecting all the security conditions. Ferrofluid handling requires the operator to wear protective clothing: a white blouse,

protective gloves, goggles and a breathing mask. In the following, we detail the various components of the setup.

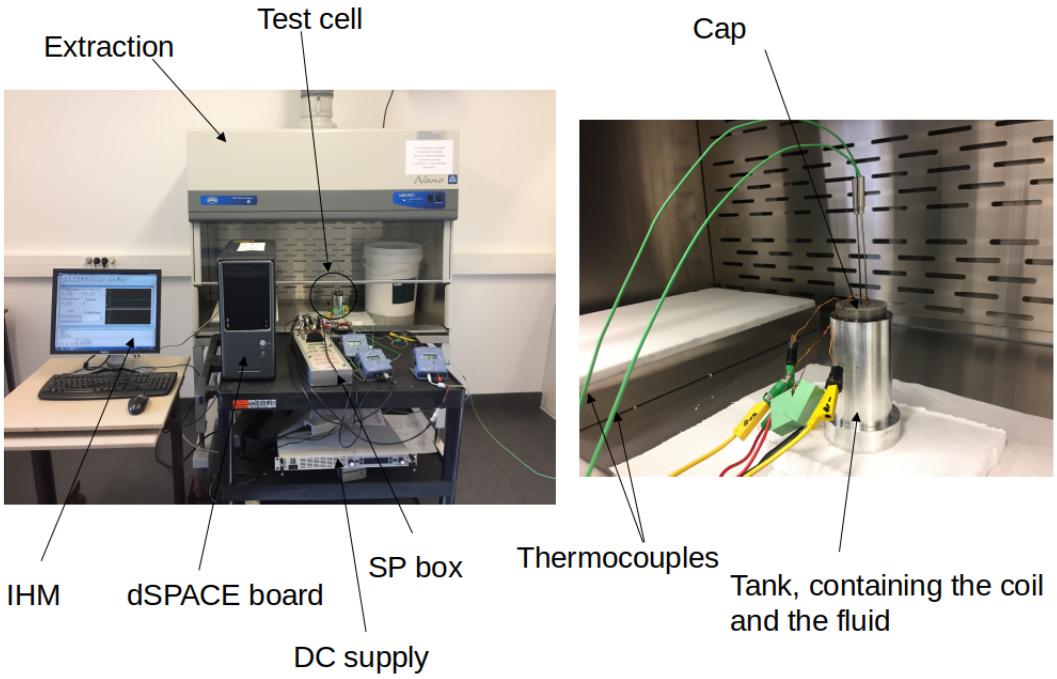


Figure 3.1: Experimental setup for a heated solenoid immersed in a ferrofluid.

### 3.1.2 Supply source and power control

A DC source with reference EA-PS 9200-50 2U (see figure (3.2)) supplies the coil. A control box monitors the DC source and allows the measurements of voltage and power. The electrical power dissipated by Joule effect inside the solenoid is controlled with a closed loop system, as shown in figure (3.3), to maintain constant losses when the copper resistivity increases due to the temperature rise. A computer connected to the dSPACE board allows the control of the power injected into the coil.

Figure 3.2: DC current source.

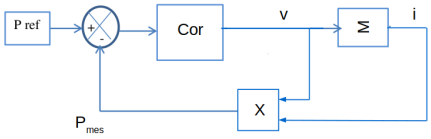


Figure 3.3: Scheme of the power control.

### 3.1.3 dSPACE board and SP box

When connected to a computer, the dSPACE DS1104 R&D Controller Board (see figure (3.4)) allows the execution of the continuous models in real-time. It is programmed using a SIMULINK modeling tool by building a control system in a "block diagram" or interconnected blocks. Such a

solution minimizes the time taken for prototyping the system.
The connection between the command input of the supply source and the dSPACE controller board is made using the $SP\_1104$ box shown in figure (3.5), having 8 ADC (Analog to Digital Converter) inputs and 8 DAC (Digital to Analog Converter) outputs.

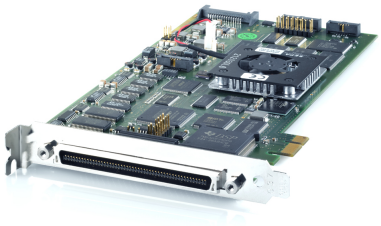

Figure 3.4: dSPACE DS1104 R&D Controller Board.

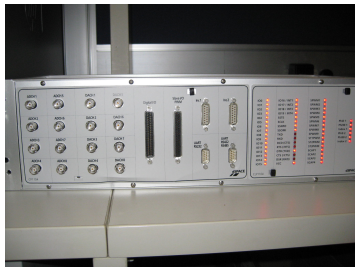

Figure 3.5: $DSM04$ connector.

### 3.1.4 Test cell and thermocouples

The test cell consists of a copper coil, wound in the form of a two-wire conductor, chosen to obtain two identical coaxial resistors, as shown in figure (3.6). This form of the coil was designed in order to be able to cancel the magnetic field in the setup. When the directions of the currents flowing in the two resistors of the coil are opposite, the generated magnetic fields are compensated in the device, and the thermomagnetic convection effect is deactivated (see figure ((3.6)a)). On the other hand, if the current directions are the same, a magnetic field is applied in the test cell, and the thermomagnetic convection effect is activated (see figure ((3.6)b)). In both configurations, the same amount of heat is dissipated by Joule effect in the solenoid. The main interest of this approach is to evaluate separately the impacts of material properties and thermomagnetic convection.

The copper coil is made of 33 turns wound in 3 layers with a double wire of $0.75\ \mathrm{mm}$ diameter each. The coil entirely immersed in ferrofluid is set into an Aluminium tank closed at the top by a polyvinyl chloride (PVC) cap to insulate the metal wires of temperature probes (avoiding short-circuit). Aluminum is chosen to maximize the heat exchange between the tank and the surroundings. The thermal insulation on the bottom of the tank is ensured by a polystyrene support. A schematic view of the test cell is given in figure (3.7). The setup dimensions shown in figure (3.7) are reported in table (3.1).

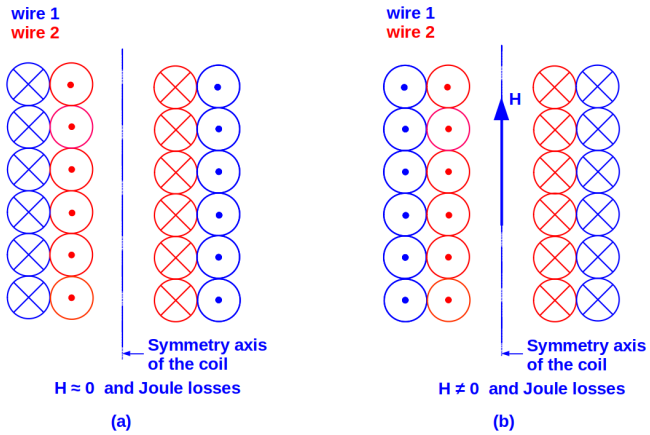


Figure 3.6: Inversion method of the magnetic field in the coils.

Three thermocouples are used to instantly measure the temperatures at a defined point of the coil, at a hot spot in the ferrofluid, and at the exterior (ambient temperature), as shown in figure (3.8). The dSPACE board records the temperature and its time evolution is plotted using MATLAB. The total variation of temperature is much greater than the precision of the thermocouples, which guarantees the reliability of the measurements.

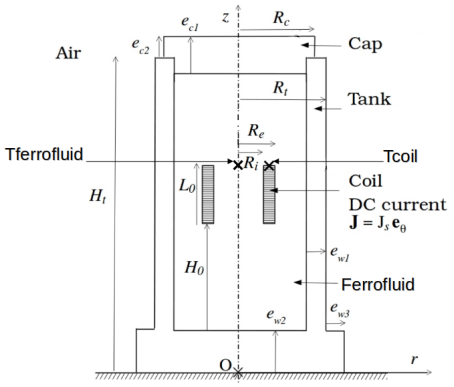


Figure 3.7: Schematic view for the test cell.

Figure 3.8: Thermocouples.

## 3.2 Ferrofluid properties

### 3.2.1 Ferrofluid solution

The ferrofluid used to cool the solenoid is synthesized in the Phenix lab at Sorbonne University. The solution consists of a Midel vegetable oil $Midel\ eN\ 1215$ seeded with cobalt ferrite nanoparticles $CoFe_2O_4$ (coated nanoparticle volume fraction $\widetilde{\phi} = 5.41\%$) of an average diameter of 16 nm. The magnetization at saturation of the ferrofluid measured at 20 °C is $M_s = 16240\ \mathrm{A.m^{-1}}$. An oleic acid is added to homogenize the mixture and to avoid the aggregation of nanoparticles. The

| Parameter | $H_t$ | $R_t$ | $e_{w1}$ | $e_{w2}$ | $e_{w3}$ | $H_0$ |
|---|---|---|---|---|---|---|
| Value (cm) | 12.5 | 3.1 | 1 | 2 | 1 | 3.9 |
| Parameter | $L_0$ | $R_i$ | $R_e$ | $R_c$ | $e_{c1}$ | $e_{c2}$ |
| Value (cm) | 2.1 | 0.8 | 1.175 | 2.6 | 2 | 1 |

Table 3.1: Experimental setup dimensions

log-normal distribution of particles sizes for the mixture ($Midel\ eN$ 1215+ $CoFe_2O_4$) and the magnetization curve are given respectively in figures (3.9) and (3.10).

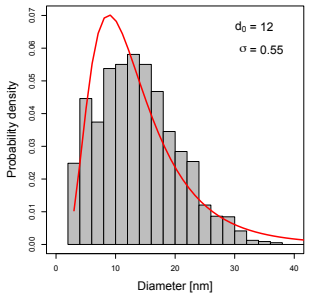


Figure 3.9: Log-normal distribution of particles sizes.

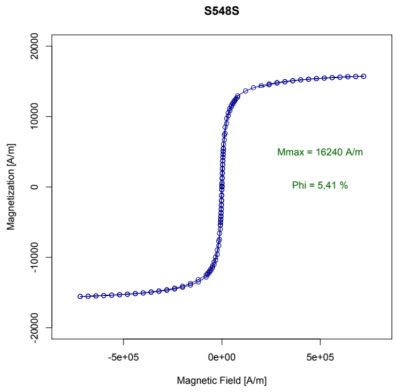


Figure 3.10: Magnetization curve.

### 3.2.2 Thermophysical properties

As explained in the preceding section, the ferromagnetic particles used to create the ferrofluid suspension are cobalt ferrite nanoparticles $CoFe_2O_4$. These particles are dispersed in a given volume of $Midel\ eN$ 1215 whose thermophysical properties are known from the manufacturer ($\rho_{bf} = 922$ kg.m$^{-3}$, $c_{bf} = 1970$ J.kg$^{-1}$K$^{-1}$, $\beta_{bf} = 7.4 \times 10^{-4}$ K$^{-1}$, $\lambda_{bf} = 0.166$ W.m$^{-1}$K$^{-1}$, $\eta_{bf} = 2.9 \times 10^{-2}$ Pa.s). The dynamic viscosity of the Midel oil depends on the temperature and is given by:

$$\eta(T) = E \exp\left(\frac{F}{T}\right) \tag{3.1}$$

where $E \simeq 1.3 \times 10^{-6}$ Pa.s, $F \simeq 3.1 \times 10^3$ $K$, and $T$ the temperature in $K$. The viscosity law given in (3.1) has been compared to the experimental values provided by the manufacturer for $Midel\ eN$ 1215 dynamic viscosity, as shown in figure (3.11). The variation of the other properties of the base fluid regarding the temperature is considered negligible over the range of solenoid temperature rise in our experiment [13, p. 106]. Therefore we assume that these prop-

erties (density, heat capacity, thermal conductivity, thermal expansion, and dynamic viscosity) for $Midel\ eN\ 1215$ remain constant and retain their values at 20 °C.

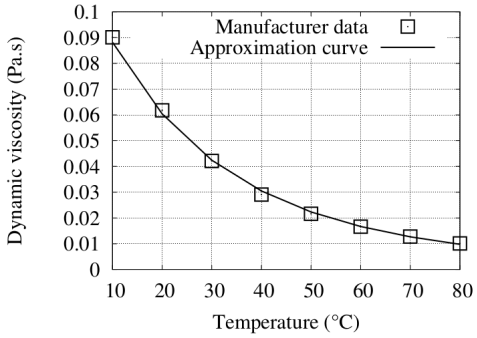


Figure 3.11: Comparison between manufacturer's data and analytic law (3.1) for the dynamic viscosity of $Midel\ eN\ 1215$ regarding temperature [13, p. 106].

We have conducted a bibliographic investigation to find the thermophysical properties of cobalt ferrite nanoparticles. These properties are found to be the density $\rho_p = 5390\ \mathrm{kg.m^{-3}}$, the thermal conductivity $\lambda_p = 4.1\ \mathrm{W.m^{-1}K^{-1}}$ and the specific heat at constant pressure $c_p = 604\ \mathrm{J.kg^{-1}K^{-1}}$. The volume fraction of ferrite cobalt nanoparticles calculated using equation (2.44) is $\phi = 2.76\%$. The experimental value of the volume fraction of coated ferrite cobalt nanoparticles given by the manufacturer is $\widetilde{\phi} = 5.4\%$. The diameter of these particles is optimized to be $d = 16\ \mathrm{nm}$, the Curie temperature is $T_c = 793\ K$, and the experimental value of the particle magnetization at saturation and ambient temperature is $M_d(20°\mathrm{C}) = 300\ \mathrm{kA.m^{-1}}$.

**Ferrofluid properties**

Owing to the physical properties of the carrier fluid $Midel\ eN\ 1215$ and the magnetic nanoparticles $CoFe_2O_4$, the properties of the experimental ferrofluid can be deduced using the mixed law detailed in section 2 of chapter 1. By using equations (2.39) and (2.40), the density and heat capacity of the ferrofluid are calculated ($\rho_{ff} = 1045.5\ \mathrm{kg.m^{-3}}$, $c_{ff} = 1775.3\ \mathrm{J.kg^{-1}K^{-1}}$). The thermal expansion coefficient of this ferrofluid computed using (2.41) is $\beta_{ff} = 7.0004 \times 10^{-4}\ \mathrm{K^{-1}}$. Owing to Maxwell's law for thermal conductivity given in (2.42), we find the thermal conductivity of our ferrofluid to be $\lambda_{ff} = 0.1785\ \mathrm{W.m^{-1}K^{-1}}$. The dynamic viscosity of the ferrofluid is calculated using a combination law of the Rosensweig model given in (2.45) and the exponential form of the dynamic viscosity of the base fluid given in (3.1). Thus, the dynamic viscosity of the ferrofluid is calculated using the following expression:

$$\eta_{ff}(T) = \left(1 - \frac{5}{2}\widetilde{\phi} + \left(\frac{\frac{5}{2}\widetilde{\phi_c} - 1}{\widetilde{\phi_c}^{\,2}}\right)\widetilde{\phi}^{2}\right)^{-1} \times E \exp\left(\frac{F}{T}\right) \tag{3.2}$$

According to this equation, the value found for the dynamic viscosity at the reference temperature $T_{ext} = 22\ °\mathrm{C}$, is $\eta_{ff}(22\ °\mathrm{C}) = 0.0545\ \mathrm{Pa.s}$.

**Solenoid properties**

Practically, the coil has turns that are not perfectly contiguous, which then makes possible the penetration of the ferrofluid. Thus, the solenoid is approximated by an homogenized coil with a filling rate estimated to $\tau_{cu} = 37\%$. This rate represents the volume of copper present in the coil body by taking into account the coil body dimensions, the wire dimensions, and the number of turns. Owing to this approximation, the solenoid properties that will be used in the numerical modeling can be calculated using homogenized laws for the density and the specific heat capacity, respectively:

$$\rho_{solenoid} = \tau_{cu}\rho_{cu} + (1 - \tau_{cu})\rho_{uu} \tag{3.3}$$

$$\rho_{solenoid}c_{solenoid} = \tau_{cu}\rho_{cu}c_{cu} + (1 - \tau_{cu})\rho_{uu}c_{uu} \tag{3.4}$$

The index "uu" refers either to the base fluid or to the ferrofluid regarding the solution considered in simulations. The homogenized law used to evaluate the thermal conductivity of the solenoid is given in [90]:

$$\frac{\lambda_{solenoid}}{\lambda_{uu}} = 1 - 2\tau_{cu}\left(\zeta + \tau_{cu} - \frac{0.075422{\tau_{cu}}^6\zeta}{\zeta^2 - 1.060283{\tau_{cu}}^{12}} - \frac{0.000076{\tau_{cu}}^{12}}{\zeta}\right)^{-1}, \tag{3.5}$$

$$\text{with} \quad \zeta = \left(1 + \frac{\lambda_{cu}}{\lambda_{uu}}\right)\left(1 - \frac{\lambda_{cu}}{\lambda_{uu}}\right)^{-1} \tag{3.6}$$

The thermophysical properties for Copper, Aluminium and PVC are found in [13, p. 106]. To summarize, table (3.2) lists all the thermophysical properties of solid materials and solutions calculated at $T_{ext} = 22\ ^\circ\mathrm{C}$ and used in the numerical simulations for the study of the solenoid cooling.

| Properties | Copper | Aluminum | PVC | Cobalt Ferrite | Hom.Coil | Oil | Ferrofluid |
|---|---|---|---|---|---|---|---|
| Density (Kg/m$^3$) | 8933 | 2.70e3 | 1.4e3 | 5.39e3 | 3.9639e3 | 922 | 1.0455e3 |
| Thermal expansion (K$^{-1}$) | - | - | - | | - | 7.4e-4 | 7.0004e-4 |
| Heat capacity (J/Kg.K) | 385 | 945 | 1e3 | 604 | 616.0276 | 1970 | 1.7753e3 |
| Therm. cond. (W/m.K) | 401 | 201 | 0.16 | 4.1 | 0.3880 | 0.166 | 0.1785 |
| Dynamic viscosity (Pa.s) | - | - | - | - | - | 2.9e-2 | 0.0545 |

Table 3.2: Ferrofluid and materials properties used in solenoid simulation

### 3.2.3 Magnetic properties

As the solenoid is being supplied by a current, its temperature increases, and the surrounding ferrofluid is effectively warmed by the temperature elevation. With a constant magnetic field, the magnetic permeability of a hot ferrofluid is smaller than that of a cold one (see chapter 1). The relation between the ferrofluid magnetization and magnetic field is taken into account by using the assumption of a linear magnetic material for ferrofluids cited in (2.22) and given by:

$$\mathbf{M} = \chi(T)\mathbf{H} \tag{3.7}$$

where **M** is the ferrofluid magnetization, $T$ is the temperature, and **H** is the magnetic field. Here, $\chi$ is the magnetic susceptibility of the ferrofluid defined by:

$$\chi(T) = \frac{\phi \mu_0 \pi d^3 M_d(T)^2}{18 k_b T}, \quad \frac{M_d(T)}{M_0} = 1 - \left(\frac{T}{T_c}\right)^{\frac{3}{2}} \tag{3.8}$$

where $\phi$ is the volume fraction of magnetic particles, $\mu_0$ the vacuum magnetic permeability, $d$ the average particle diameter, $M_d(T)$ the temperature-dependent particle magnetization, $k_b$ the Boltzmann's constant, $M_0$ the particle magnetization at saturation and 0 K ($M_0 = 387$ kA.m$^{-1}$), and $T_c$ the Curie temperature of the cobalt ferrite nanoparticles.
In the following, we summarize the thermophysical properties dependences for the modeled ferrofluid, see table (3.3). In this table, we denote in bold the parameters that affect the properties of the ferrofluid suspension in our model.

| Property | Dependence |
|---|---|
| Density (kg/m$^3$) | $\rho_{ff} = \rho(T, \boldsymbol{\phi}, \boldsymbol{\rho_{bf}}, \boldsymbol{\rho_p})$ |
| Heat capacity (J/K·kg) | $c_{ff} = c(T, \boldsymbol{\phi}, \boldsymbol{\rho_{bf}}, \boldsymbol{c_{bf}}, \boldsymbol{\rho_p}, \boldsymbol{c_p}, \boldsymbol{\rho_{ff}})$ |
| Thermal expansion coefficient (/K) | $\beta_{ff} = \beta(T, \widetilde{\boldsymbol{\phi}}, \boldsymbol{\beta_{bf}}, \beta_p)$ |
| Thermal conductivity (W/m·K) | $\lambda_{ff} = \lambda(T, \boldsymbol{\phi}, \boldsymbol{\lambda_{bf}}, \boldsymbol{\lambda_p}, H)$ |
| Dynamic viscosity (Pa.s) | $\eta_{ff} = \eta(T, \widetilde{\boldsymbol{\phi}}, \boldsymbol{s}, \boldsymbol{d}, \boldsymbol{\eta_{bf}}, H)$ |
| Magnetic permeability (H/m) | $\mu_{ff} = \mu(T, \boldsymbol{H}, \widetilde{\boldsymbol{\phi}})$ |

Table 3.3: Thermophysical properties dependences in the considered ferrofluid.

## 3.3 2D axisymmetric modeling

As explained before, we aim to study the heat transfer properties when a ferrofluid is used to cool a heated solenoid. At first, we describe the finite-element code solving the coupled thermo-magnetohydrodynamics system. Then we present our model which is a follow up of the one studied by R. Zanella during his PhD thesis [13].

During his PhD thesis, Zanella implemented the ferrohydrodynamic equations in a finite element code called "SFEMaNS" [91, 92]. He found that using ferrofluids for heat transfer applications, for example in an electromagnetic device, could reduce the maximum temperature rise of heated windings. However, SFEMaNS is based on a meridian plane discretization of continuous finite elements coupled to a Fourrier decomposition in the azimutal direction, making it difficult to model complex geometries in a 3D approach. Hence the idea was to move to a reliable commercial solution, "COMSOL Multiphysics", where we focus on simulations of complex 3D power transformer setups. In the following, a description of the two computational codes, SFEMaNS and COMSOL, is given, and numerical results issued from the two codes are compared.

### 3.3.1 Finite element codes

#### SFEMaNS code

We use the code SFEMaNS (the acronym stands for Spectral/Finite Elements for the Maxwell and Navier-Stokes equations) for solving the coupled system of ferrohydrodynamic equations. We use a Fourier decomposition in the azimuthal $\theta$-direction and continuous finite elements in the meridian section (piecewise linear Lagrange elements for the pressure and piecewise quadratic Lagrange elements for the velocity, the magnetic field, and the temperature). For instance the approximate temperature field has the following representation:

$$T = \sum_{m=0}^{m_{\max}-1} T_m^c(r,z,t)\cos(m\theta) + \sum_{m=1}^{m_{\max}-1} T_m^s(r,z,t)\sin(m\theta), \tag{3.9}$$

where $T_m^c(r,z,t)$ and $T_m^s(r,z,t)$ are scalar-valued finite elements functions and $m_{\max}$ is the number of (complex) Fourier mode used in the discretization. All the fields, either vector-valued or scalar-valued, are represented as above. Modulo the computation of nonlinear terms using FFTW, the handling of the Fourier modes in the meridian plane, $(r,z)$, can be done in parallel. The divergence of $\mu\mathbf{H}$ is controlled by a technique using a negative Sobolev norm that guarantees convergence under minimal regularity. SFEMaNS has been thoroughly validated on numerous analytical solutions and against other magnetohydrodynamics codes [91, 92]. All the computations reported in this chapter are done assuming axisymmetry, i.e. $m_{\max} = 1$.

#### COMSOL code

The COMSOL Multiphysics software is a code that allows the numerical resolution of multiphysics problems (coupling fluid mechanics, electromagnetism, solid mechanics, heat transfers ...) using the finite element method. COMSOL contains most of the equations describing the coupling phenomena, with a graphical interface allowing the visualization of results for unsteady or stationary studies and a possibility to interface with the MATLAB software. The advantage in COMSOL multiphysics is the possibility to consider more complex structures for the coupling problem in a 3D configuration in addition to the 2D possible studies.

### 3.3.2 Numerical approach

#### Axisymmetric model

In this part, we first consider a 2D axisymmetric model using cylindrical coordinates $(r,z)$ for the representation of our experimental setup. The coil is assimilated to a copper rectangle surrounded by the magnetic liquid, as shown in figure (3.12).

#### Governing equations

The magnetic fluid is considered as a homogeneous continuous medium with incompressible Newtonian fluid behavior. The study of the thermal exchanges through the cooling device requires the knowledge of the velocity field, which we assume to be described by the incompressible Navier–Stokes equations:

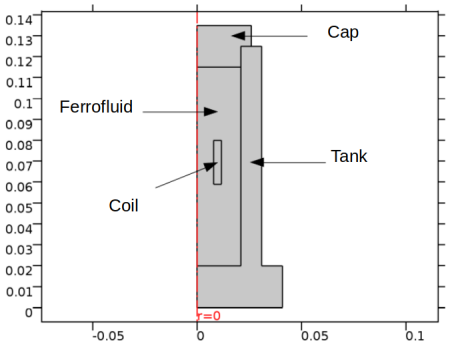


Figure 3.12: 2D axisymmetric model for the heated solenoid from COMSOL Multiphysics. In red color, the symmetry axis at $r = 0$ is indicated with z in the upward direction.

$$\begin{cases} \boldsymbol{\nabla} \cdot \mathbf{u} = 0, \\ \rho \partial_t \mathbf{u} + \rho(\mathbf{u} \cdot \boldsymbol{\nabla})\mathbf{u} + \boldsymbol{\nabla} p - \eta(T_{ext})\boldsymbol{\nabla}^2 \mathbf{u} = -\rho \mathbf{g} \beta (T - T_{ext}) + \mathbf{F}_m, \end{cases} \tag{3.10}$$

with $\mathbf{u}$ the velocity vector, $\eta(T_{ext})$ the dynamic viscosity of the ferrofluid given by (3.2), $p$ the pressure, $\rho$ the reference density at $T = T_{ext}$, $\beta$ the thermal expansion coefficient, $g$ the gravity, $T$ the temperature, and $T_{\text{ext}}$ the reference temperature. The last two terms on the right hand side of the momentum equation are respectively the buoyancy force considering the Boussinesq approximation and the magnetic body force (in N/m$^3$) that connects the variations in the magnetization with the thermal gradient.

The heat equation describes the heat transfer process that occurs in the ferrofluid:

$$\rho c \partial_t T + \rho c(\mathbf{u} \cdot \boldsymbol{\nabla})T - \mu_0 K T(\partial_t H + (\mathbf{u} \cdot \boldsymbol{\nabla})H) - \boldsymbol{\nabla} \cdot (\lambda \boldsymbol{\nabla} T) = 2\eta \boldsymbol{\nabla}^s \mathbf{u} : \boldsymbol{\nabla} \mathbf{u} + Q, \tag{3.11}$$

where $c$ is the specific heat capacity at constant pressure, $\lambda$ the thermal conductivity and $Q$ the volumic heat source dissipated by Joule effect in the coil ($Q = 6.14 \times 10^5\,\mathrm{W/m^3}$ ) and given by $\frac{1}{\sigma} J_s^2$ where $\sigma$ is the copper electrical conductivity ($\sigma = 5.998 \times 10^7\,\mathrm{Sm^{-1}}$), and $J_s$ the current density in the coil ($J_s = 3.35 \times 10^6\,\mathrm{Am^{-2}}$). The electrical current in the coil is $I = 4\,\mathrm{A}$, the number of turns is $N = 33$, and the total coil resistance at the reference temperature is $R_t = 188\,\mathrm{m\Omega}$. The Joule losses are calculated to be $P_J = 3\,\mathrm{W}$. The ambient air is characterized by the exterior temperature $T_{\text{ext}} = 295.15\,\mathrm{K}$ and the heat transfer coefficient $h = 6.5\,\mathrm{W/m^2K}$ (an optimized value). The other parameters are $\phi = 5.4\%$, $d = 16\,\mathrm{nm}$, $M_0 = 3.87 \times 10^5\,\mathrm{Am^{-1}}$, $T_c = 793\,\mathrm{K}$.
The computed electromagnetic field is assumed to be steady, and the ferrofluid magnetization is considered instantaneously aligned with the magnetic field [13, p. 22-23]. The pyromagnetic coefficient is neglected. We assume that the effect of the temperature on the magnetic permeability of the ferrofluid is negligible. The magnetostatic equations are given by:

$$\begin{cases} \boldsymbol{\nabla} \times \mathbf{H} = \mathbf{J}, \\ \boldsymbol{\nabla} \cdot (\mu \mathbf{H}) = 0, \end{cases} \tag{3.12}$$

with $\mathbf{J} = J_s \mathbf{e}_\theta$ and $\mu$ the magnetic permeability of the ferrofluid $\mu = \mu_0(1 + \chi(T))$. Recall that $\chi$ is given by equation (3.8) and $\mu_0$ is the magnetic permeability of vacuum.

### Boundary conditions

At the boundaries of the cylinder indicated in red and green in figure (3.13), the boundary condition for the magnetic problem $\mathbf{A} \times \mathbf{n} = \mathbf{0}$ is enforced, where $\mathbf{A}$ is the magnetic vector potential. The non-slip boundary condition $\mathbf{u} = \mathbf{0}$ is applied at the border of the fluid domain (see blue lines on figure (3.13)). The air convection at the top and on the lateral wall of the PVC-Aluminium tank is modeled by using a Robin boundary condition on the temperature:

$$-\lambda \nabla T \cdot \mathbf{n} = h(T - T_{ext}), \tag{3.13}$$

where $h$ is the convection coefficient, and $\mathbf{n}$ is the outer unit normal vector (see red lines on figure (3.13)). The homogeneous Neumann boundary condition $\partial_z T = 0$ is enforced at the bottom of the tank (see green line on figure (3.13)). The initial conditions are $\mathbf{u} = \mathbf{0}$, $T = T_{\text{ext}}$, and $\mathbf{A} = \mathbf{0}$.

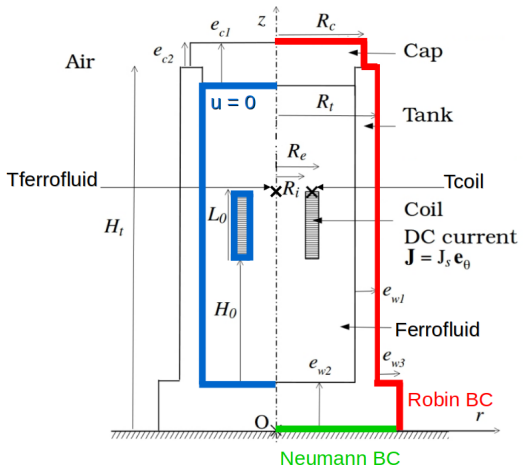


Figure 3.13: 2D axisymmetric model, geometric notations and boundary conditions.

### Coupling theory in COMSOL code

Four fields must be evaluated in a ferrohydrodynamic application: the magnetic field $\mathbf{H}$, the velocity and pressure fields ($\mathbf{u}$, $p$), and the temperature field $T$. In the following studies, we use a weak coupling method of variables since the magnetic field is not directly coupled with the velocity field and the temperature. Figure (3.14) shows the flowchart diagram in a schematic view. The flowchart has two steps: in the first step, the static magnetic field is computed once for all; The dependence of the relative magnetic permeability in the ferrofluid on temperature has no significant impact on the magnetic field. Therefore, the magnetic susceptibility of the ferrofluid ($\mu_r = 1.5$) is not considered temperature-dependent. This magnetic field is then used in the time marching step for the evaluation of ($\mathbf{u}$, $p$, $T$).

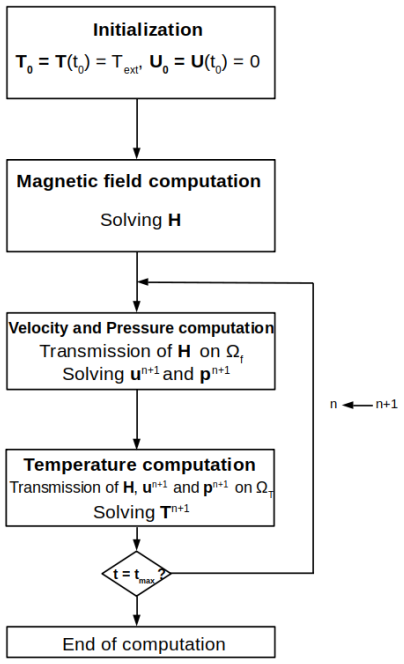


Figure 3.14: Time-marching algorithm corresponding to the coupling method.

## 3.4 Magnetic force formulas

This part outlines the different models of the magnetic body force $\mathbf{F}_m$ (see equation (3.10)) and its developments regarding the assumptions considered by different authors. We proceed in the following to the comparison of these models in order to choose the suitable expressions to be implemented in the fluid domain. James R. Melcher (1981) described in his book "Continuum Electromechanics" [26] how it is possible to deduce the magnetic force density acting on a ferrofluid. He proposed an analogy between the ferrofluid containing magnetic dipoles and a medium of electric dipoles where a macroscopic electric force occurs. Two systems of the same surface $S$ are considered, the first one enclosing electric dipoles (free electric charges), the second one regrouping magnetic dipoles (free magnetic current), as seen in figure (3.15).

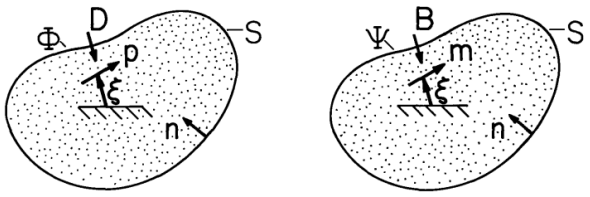


Figure 3.15: Electrostatic-Magnetostatic analogy. On the left side, the volume corresponds to free electric charges inducing polarization **P**. On the right side, the volume corresponds to free magnetic charges inducing magnetization **M** [26].

**D** represents the electric current density in the electrostatic case, **P** denotes the electric polarization vector ($\mathbf{P} = n\mathbf{p}$, **p** is the polarization of each dipole), and $n$ the number of dipoles per unit

volume. By analogy, **B** represents the magnetic flux density in the magnetostatic case, **M** denotes the magnetization vector ($\mathbf{M} = n\mathbf{m}$). Assuming that the Kelvin polarization force density having electric origin is given by:

$$\mathbf{F}_K^e = (\mathbf{P} \cdot \boldsymbol{\nabla})\mathbf{E} \tag{3.14}$$

S. Afkhami [20, p. 379] reports that the magnetic force acting on a particle of magnetic moment **m** is $\mu_0(\mathbf{m} \cdot \boldsymbol{\nabla})\mathbf{H}$. Referring to the analysis of Neuringer and Rosensweig [19], the expression of the magnetic Kelvin force can be simplified if the direction of the ferrofluid magnetization remains parallel to the direction of the applied magnetic field. Thus equation (2.32) takes the form:

$$\mu_0(\mathbf{M} \cdot \boldsymbol{\nabla})\mathbf{H} = (\mu_0 \frac{M}{H})(\mathbf{H} \cdot \boldsymbol{\nabla})\mathbf{H}$$

Owing to the vector identity:

$$(\mathbf{H} \cdot \boldsymbol{\nabla})\mathbf{H} = \frac{1}{2}\boldsymbol{\nabla}(\mathbf{H} \cdot \mathbf{H}) - \mathbf{H} \times (\boldsymbol{\nabla} \times \mathbf{H})$$

and assuming that the oil-based ferrofluid considered in this work is electrically non-conductive, it follows that $\boldsymbol{\nabla} \times \mathbf{H} = \mathbf{0}$. Then the reduced form of the Kelvin body force will be:

$$\mathbf{F}_K^{\parallel} = \mu_0(\mathbf{M} \cdot \boldsymbol{\nabla}\mathbf{H}) = (\mu_0 \frac{M}{H})\frac{1}{2}\boldsymbol{\nabla}(\mathbf{H} \cdot \mathbf{H}) = \mu_0 M \boldsymbol{\nabla} H \qquad (\text{with } \mathbf{M} \| \mathbf{H}) \tag{3.15}$$

If we combine equation (3.15) with (2.22) connecting the magnetization of ferrofluid to the local magnetic field for linear magnetic material, the Kelvin force can finally be written as:

$$\mathbf{F}_K^{\parallel,l} = \mu_0 \chi \boldsymbol{\nabla}\left(\frac{H^2}{2}\right) \tag{3.16}$$

Let us go back now to the Helmholtz force given in (2.33). This latter is obtained using the virtual power principle VPP as mentioned in [93]. The form of the magnetic force (2.33) remains important since the Helmholtz expression shows a temperature gradient. Owing on the relation connecting $\mu$ and $\mu_0$ ($\mu = \mu_0(1 + \chi)$), the Helmholtz force expression changes to:

$$\mathbf{F}_H = -\frac{1}{2}\mu_0 H^2 \boldsymbol{\nabla}\chi \tag{3.17}$$

If we rewrite the form (3.16) of the Kelvin force, we find the following relation:

$$\mu_0 \chi \boldsymbol{\nabla}\left(\frac{H^2}{2}\right) = -\frac{1}{2}\mu_0 H^2 \boldsymbol{\nabla}\chi + \boldsymbol{\nabla}\left(\mu_0 \chi \frac{H^2}{2}\right) \tag{3.18}$$

Thus the Kelvin body force in (3.16) and the Helmholtz force in (3.17) are equal to each other up to a gradient:

$$\mathbf{F}_K^{\parallel,l} = \mathbf{F}_H + \boldsymbol{\nabla}\Phi, \qquad \Phi = \mu_0 \chi \frac{H^2}{2} \tag{3.19}$$

Another method is often used to compute the magnetic body force by using the Maxwell stress tensor. A. Bossavit [94] presents a particular form of the Maxwell tensor $\sigma_{0m}$ where the linear law ($\mathbf{B} = \mu\mathbf{H}$) is applied, and the magnetic permeability of the material $\mu$ is a scalar $\mu = \mu_0$:

$$[\sigma_{0m}] = \mathbf{H} \otimes \mathbf{B} - \frac{1}{2}(\mathbf{H} \cdot \mathbf{B})[\delta] = \mathbf{H} \otimes \mathbf{B} - \frac{1}{2}\mu_0 \mathbf{H}^2[\delta] \tag{3.20}$$

where $[\delta]$ is the identity tensor and $\otimes$ the dyadic product of $\mathbf{H}$ and $\mathbf{B}$. Then the magnetic Kelvin force is the divergence of this version of the Maxwell tensor:

$$\boldsymbol{\nabla} \cdot [\sigma_{0m}] = \boldsymbol{\nabla} \cdot (\mathbf{H} \otimes \mathbf{B}) - \frac{1}{2}\mu_0 \boldsymbol{\nabla}(\mathbf{H}^2) = \mathbf{F}_K \tag{3.21}$$

In parallel, S. Afkhami [20] presents another formulation to compute the magnetic force density using the Maxwell tensor. This formulation makes worthwhile the divergence method even in ferromagnetic material domains or magnets where the constitutive law ($\mathbf{B} = \mu(\mathbf{H} + \mathbf{M})$) is applied. Another method is possible to compute the magnetic body force using the classical Maxwell tensor defined by:

$$[\sigma_m] = \mathbf{H} \otimes \mathbf{B} - \frac{1}{2}(\mathbf{H} \cdot \mathbf{B})[\delta] = \mathbf{H} \otimes \mathbf{B} - \frac{1}{2}\mu \mathbf{H}^2[\delta] \tag{3.22}$$

The divergence of $[\sigma_m]$ is equal to the Helmholtz body force when a non-conducting medium is modeled ($\boldsymbol{\nabla} \times \mathbf{H} = \mathbf{0}$), as mentioned in [94]. Thus, the Helmholtz force takes the form:

$$\mathbf{F}_H = \boldsymbol{\nabla} \cdot [\sigma_m] = \boldsymbol{\nabla} \cdot (\mathbf{H} \otimes \mathbf{B}) - \frac{1}{2}\boldsymbol{\nabla}(\mu \mathbf{H}^2) \tag{3.23}$$

Again, note that in the form provided in (3.21), the second term $-(1/2)\mu_0 \boldsymbol{\nabla}(\mathbf{H}^2)$ is absorbed into the pressure field for the whole domain as explained in [20] and can be integrated in the pressure term of the momentum equation. The conclusion of this part is that all these force expressions will lead to the same fluid flow, and therefore it is possible to choose the one that suits the situation.

## 3.5 Results and comparisons

### 3.5.1 Magnetic force modeling: a comparison

This part of the study is devoted to evaluating the impact of the different models of the magnetic force on the cooling process of the immersed solenoid. Among these models, we mention the Helmholtz force given in (3.17) and the Kelvin force given in (3.16). According to equation (3.19), the Kelvin body force in (3.16) and the Helmholtz force in (3.17) are equal to each other up to a gradient.

Although the Helmholtz and Kelvin expressions are different, these two force densities produce the same velocity field and hence the same temperature field. Moreover, the Kelvin force in its original form (3.16) often causes numerical instabilities. Thus, we recommend changing it to have the following form [13, p. 80]:

$$\mathbf{F_{Km}} = \mu_0 \Delta\chi(T) \nabla \left( \frac{H^2}{2} \right) \tag{3.24}$$

with $\Delta\chi(T) = \chi(T) - \chi(T_{ext})$ the difference in magnetic susceptibility of the ferrofluid between the local temperature $T(\mathbf{x}, t)$ and the external temperature $T_{ext}$. Because of using the Navier-Stokes equations in their incompressible form with Boussineq approximation, the gradient term in the magnetic force $\mu_0\chi(T_{ext})\nabla(\frac{H^2}{2})$ has no thermodynamic signification. It can be integrated in the pressure gradient term of the momentum equation by changing the variable $p \longleftarrow p - \mu_0\chi(T_{ext})\nabla(\frac{H^2}{2})$.

### Mesh choice

An extra fine triangular mesh is chosen for the ferrofluid and solenoid domains, ranging from $6.15 \times 10^{-3}\,\mathrm{mm}$ to $5.33 \times 10^{-1}\,\mathrm{mm}$. The size selected in the tank and the cap is $1.5\,\mathrm{mm}$. The meridian mesh shown in figure ((3.16)a) contains $34618$ elements. The four corners of the section of the coil are smoothed to let the ferrofluid flows smoothly around the solenoid. The time step is automatically adapted and varies upon the range $[0.01\,\mathrm{s}$ - $0.5\,\mathrm{s}]$.

Let us discuss the stability of the numerical scheme using the CFL condition (Courant–Friedrichs–Lewy) given by $u\frac{\Delta t}{\Delta x} < \frac{1}{2}$. We wonder whether the time step in the numerical scheme respects the time condition resulting from the CFL condition. We use the maximum velocity $u = 2.4 \times 10^{-3}\,\mathrm{m\,s^{-1}}$ on the $Oz$-axis obtained from the ferrohydrodynamic case where the mesh is $\Delta x = 5.33 \times 10^{-4}\,\mathrm{m}$. We find that $\Delta t < 0.5(\frac{\Delta x}{u}) \simeq 0.1\,\mathrm{s}$ which is compatible with the time range used by the code.

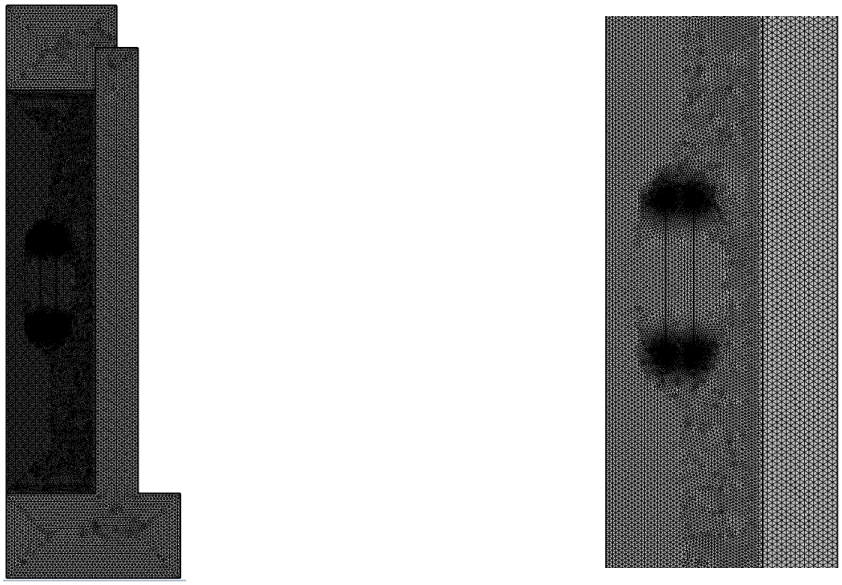

(a) Total mesh for the 2D axisymmetric model

(b) Finite mesh in the solenoid (zoom)

Figure 3.16: Meridian mesh in the $(r, z)$ plane for the comparison of magnetic force models.

### Numerical results

In order to compare the magnetic force and its contribution to the heat transfer process, we consider the ferrohydrodynamic case of the study. This means that the velocity and the temperature are coupled to the coil magnetic field. Figure (3.17) gives an idea about the magnetic field generated by the coil. We present the $z$ component of the magnetic field intensity $H_z$ and its variation along a horizontal line crossing the center of the coil.

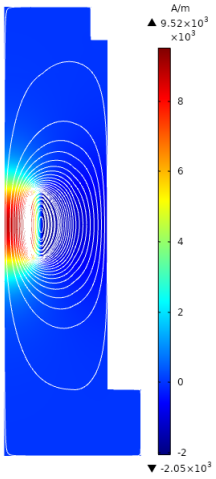


(a) Intensity of the $z$ component of the magnetic field $H_z$.

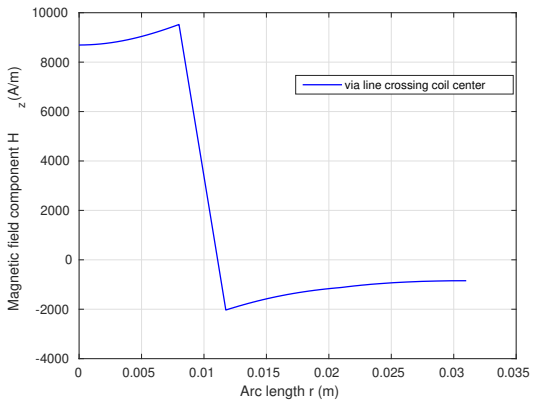


(b) Magnetic field $H_z$ versus the arc length $r$.

Figure 3.17: Distribution of the coil magnetic field (in $\mathrm{A.m^{-1}}$) inside the tank in $(r, z)$ plane .

The intensity distributions (in $\mathrm{N/m^3}$) of each model of the magnetic forces are investigated in figure (3.18). As seen in this figure, the distribution of the magnitude is not identical for the three cases. While the Helmholtz force is localized at the interior boundary of the coil, both Kelvin and Kelvin modified forces are concentrated on the upper and the lower boundaries of the coil. This means that we should refine the mesh of the model where the magnetic body force is concentrated.

According to the spatial distribution of the magnetic forces presented in figure (3.19), the Helmholtz force attracts the fluid towards the coil. In contrast, the modified Kelvin force pushes the fluid away from the coil. The Kelvin force has the same impact as the Helmholtz one on the fluid behavior. However, the different models do not have the same magnitude. The Helmholtz force has a smooth variation while both Kelvin and modified Kelvin models show sharp variations due to the large gradients of $H$ at the inner corners of the coil. Therefore, the actual values of their maximum intensity depend on the spatial resolution. However, the three different forces lead to the same effect on the fluid as expected.

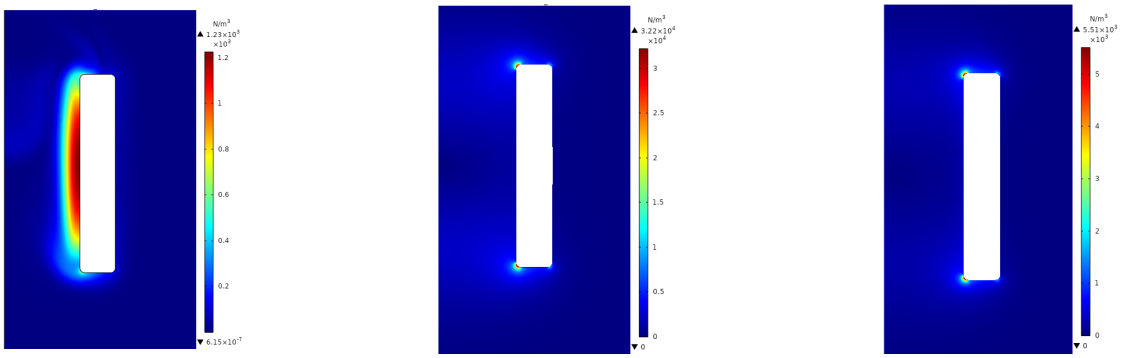

(a) Helmholtz model (b) Kelvin model (c) Modified Kelvin model

Figure 3.18: Intensity distribution of the magnetic body force (in $\mathrm{N/m^3}$) for different models at $t = 24\,000\,\mathrm{s}$.

Figure (3.19) shows the different magnetic force distributions for the Helmholtz, Kelvin, and modified Kelvin models obtained in the steady state regime.

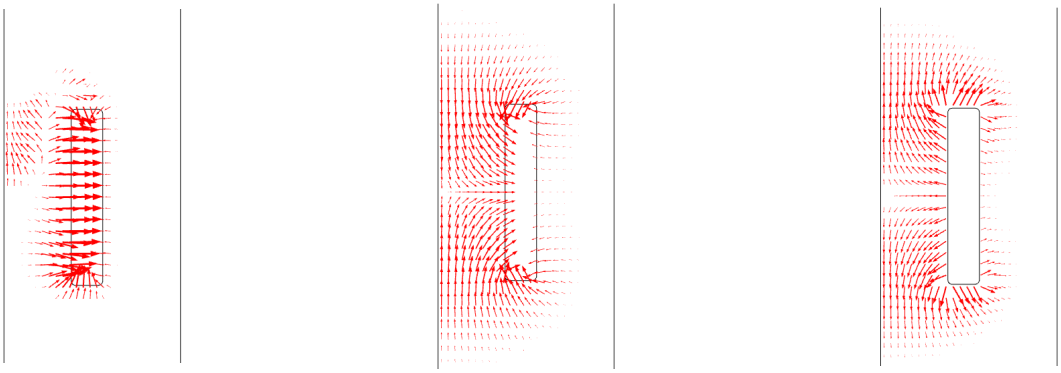

(a) Helmholtz model (b) Kelvin model (c) Modified Kelvin model

Figure 3.19: Spatial distribution of magnetic force fields for different models at $t = 24\,000\,\mathrm{s}$.

Figure (3.19) shows that the spatial distribution of the magnetic force differs with models. However, as expected, the observed temperature [see figure (3.20)] and velocity fields [see figure (3.21)] are qualitatively and quantitatively the same especially when comparing both the Helmholtz and modified Kelvin forces. A more detailed comparison should help us to select the most appropriate model for the magnetic body force. First, note that a difference in the maximum velocity magnitude by an order of $14\%$ is recorded with the Kelvin expression.
Second, the time evolution of the temperature on the top of the solenoid at point (0.01, 0.08) and in the fluid at point (0, 0.08) according to the different expressions of the magnetic force density is shown in figure (3.22). Both the Helmholtz and modified Kelvin forces superimpose perfectly in the transient regime and then reach the same temperature in the steady state. In this state, the solenoid temperatures obtained are $T = 49.9\,^{\circ}\mathrm{C}$ (with Helmholtz), $T = 49.7\,^{\circ}\mathrm{C}$ (with Kelvin), and $T = 49.9\,^{\circ}\mathrm{C}$ (with modified Kelvin).

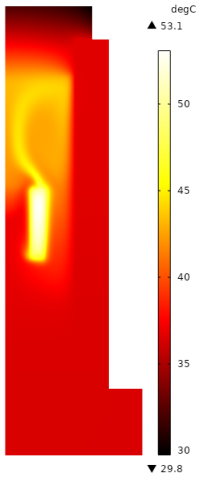


(a) Helmholtz force at $t = 24000\ s$

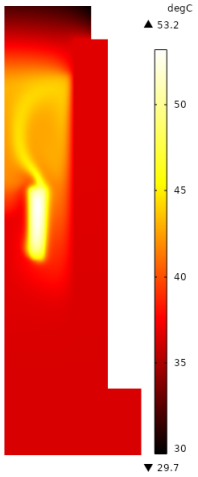


(b) Kelvin force at $t = 24000\ s$

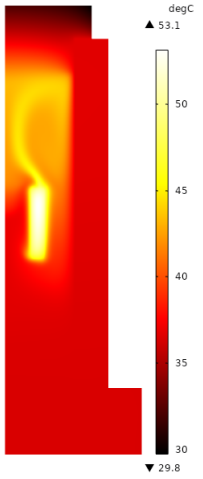


(c) Modified Kelvin force at $t = 24000\ s$

Figure 3.20: Temperature field (in °C) regarding the expression of the magnetic force. The symmetry axis ($Oz$) is on the left.

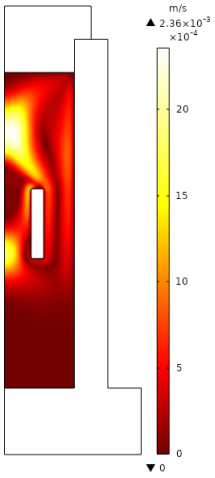


(a) Helmholtz force at $t = 24000\ s$

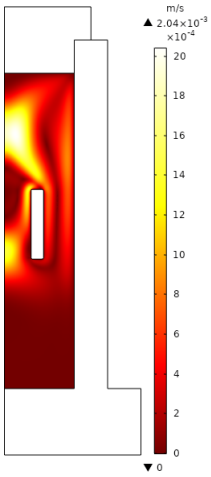


(b) Kelvin force at $t = 24000\ s$

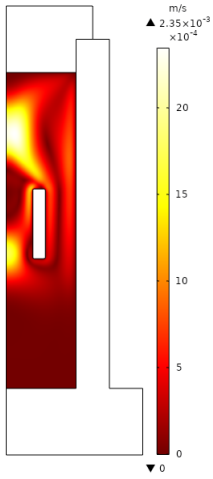


(c) Modified Kelvin force at $t = 24000\ s$

Figure 3.21: Color maps of the velocity magnitude (in $\mathrm{m.s^{-1}}$) regarding the expression of the magnetic force. The symmetry axis ($Oz$) is on the left.

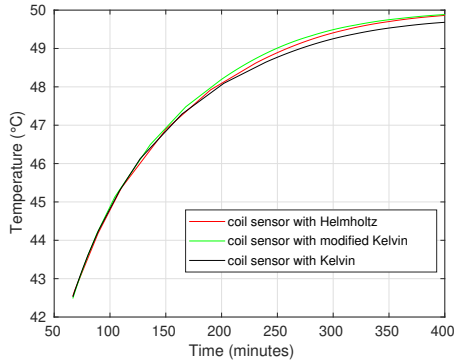


(a) Coil temperature

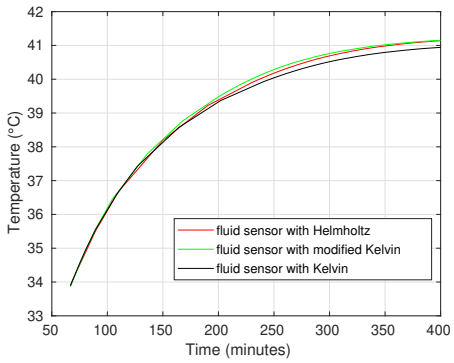


(b) Fluid temperature

Figure 3.22: Time evolution at the sensors temperature in the solenoid and in the fluid regarding the magnetic force expression.

Consequently, all the magnetic forces used previously can model the impact of the magnetic field on the ferrofluid motion because they lead to the same velocity and temperature fields. Therefore, we consider the Helmholtz magnetic force in the following modeling.
About the stability and the computation time when using these forces, we prefer using the Helmholtz or the modified Kelvin expressions rather than the Kelvin expression. From a numerical point of view, the classical Kelvin expression may lead to numerical instability that is overcome by using very small time steps. Therefore, the computation time is in some cases very large ($3\,\mathrm{h}\ 56\,\mathrm{min}\ 43\,\mathrm{s}$) rather than ($21\,\mathrm{min}\ 55\,\mathrm{s}$) with the Helmholtz force.

### 3.5.2 Thermomagnetic convection impact

In this part, the impact of magnetic nanoparticles on the cooling of the heated solenoid is validated when two simulations are run over a period of $24\,000\,\mathrm{s}$, the first with the magnetic force, the second with no magnetic force applied. Snapshots of temperature and velocity fields at $t = 24\,000\,\mathrm{s}$ for both configurations of the magnetic force are shown in figures (3.23) and (3.24) using Paraview software.

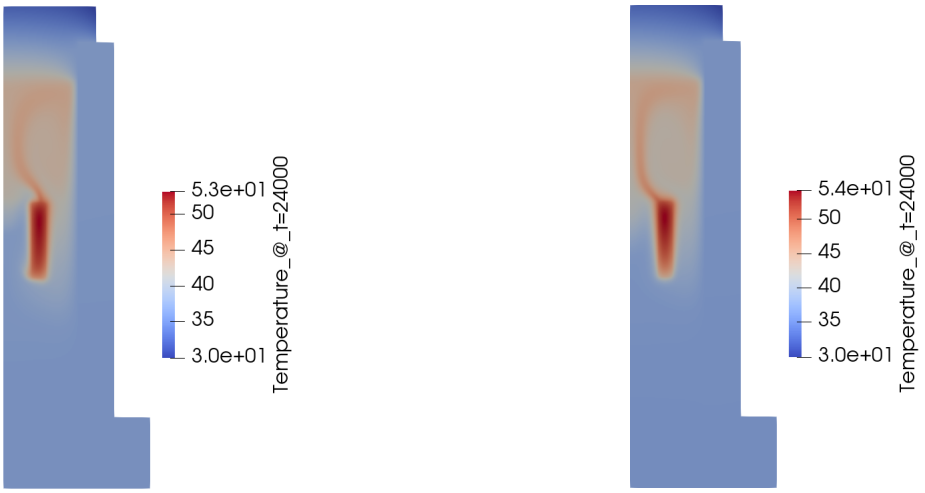


(a) Helmholtz force at $t = 24000\ s$

(b) No Helmholtz force at $t = 24000\ s$

Figure 3.23: Temperature field (in °C) with and without the magnetic force. The symmetry axis ($Oz$) is on the left.

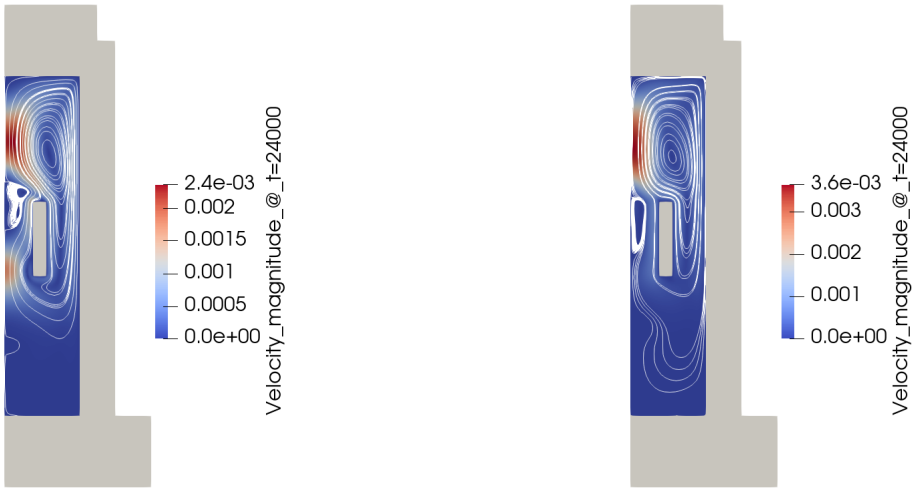


(a) Helmholtz force at $t = 24000\ s$

(b) No Helmholtz force at $t = 24000\ s$

Figure 3.24: Color maps of the velocity magnitude (in $\mathrm{m.s^{-1}}$) with and without the magnetic force. The symmetry axis ($Oz$) is on the left.

According to these figures, the magnetic force has an impact on the thermal plume when it is applied: a velocity recirculation appears near the bottom of the coil and enhances the heat transfer from the inside of the tank. The maximum value of the solenoid temperature is lowered by $1\,\mathrm{K}$ when the magnetic force is activated. While the resulting reduction of temperature is not really significant, this decrease of maximum temperature in the solenoid remains highly desirable. It is instructive to say that decreasing by $6\,\mathrm{K}$ the maximum temperature rise of the windings in a power transformer could extend their lifespan by an order of 2.

### 3.5.3 Experiment vs. numerics for the coil experiment

In this part, we aim to validate the impact of the thermomagnetic convection when the magnetic field generated by the coil is activated and deactivated periodically. The copper coil that we use is doubly winded to form two coaxial resistors. When the direction of the current $I$ is the same in the two windings (the magnetic field produced by the coil is non-zero), both the Joule effect and the Helmholtz force are operative. When the direction of the current is opposite in the windings, only the Joule effect is operative (see figure (3.6)(a,b)). We can therefore highlight the action of the Helmholtz force in the same experimental configuration.

#### Meridian mesh

In this part, the mesh is modified compared to the one in the previous section. The reason is that we aim to compare the numerical results obtained from two numerical codes (COMSOL and SFEMaNS). We need thus to adapt the mesh in both codes to be close to each other. Therefore, a fine triangular mesh is provided for the ferrofluid domain ranging from $4.1 \times 10^{-5}\,\mathrm{m}$ to $1.44 \times 10^{-3}\,\mathrm{m}$. The solenoid boundaries are extremely fine, going from $8.2 \times 10^{-7}\,\mathrm{m}$ to $2.75 \times 10^{-4}\,\mathrm{m}$. The solenoid, tank, and cap domains have a spatial mesh size ranging from $2.7 \times 10^{-6}\,\mathrm{m}$ to $1.35 \times 10^{-3}\,\mathrm{m}$. The simulation runs for $24\,000\,\mathrm{s}$, and the numerical results are saved every $5\,\mathrm{s}$. The meridian mesh shown in figure (3.25) contains $20957$ elements. The time step is automatically adapted and varies upon the range $[0.01\,\mathrm{s}\ -\ 0.3\,\mathrm{s}]$.

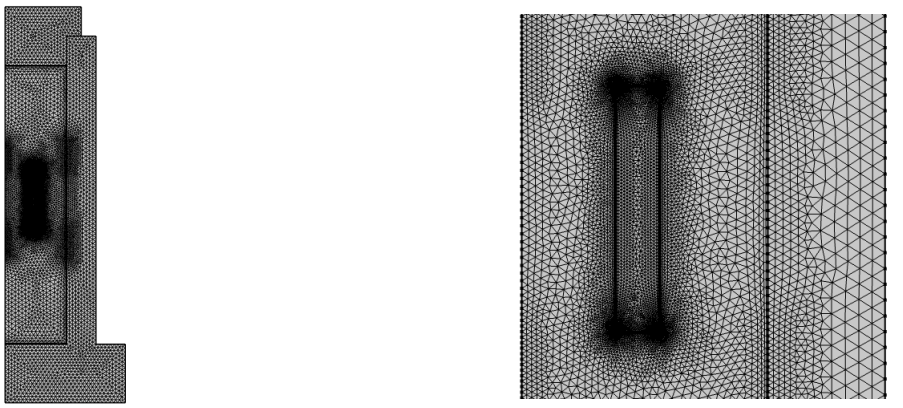

(a) Total mesh

(b) Extremely fine mesh in the coil

Figure 3.25: Meridian mesh in $(r, z)$ plane for the 2D axisymmetric model.

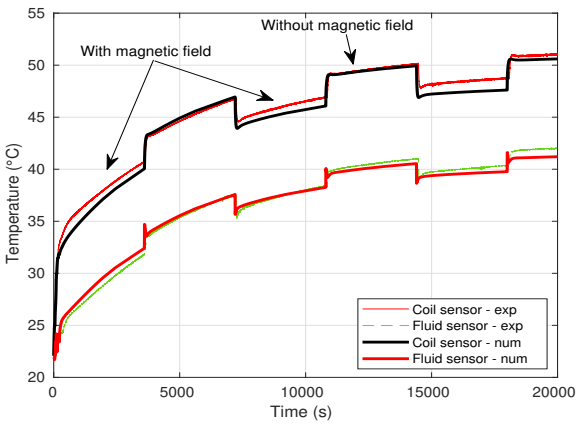


(a) Results computed in COMSOL code

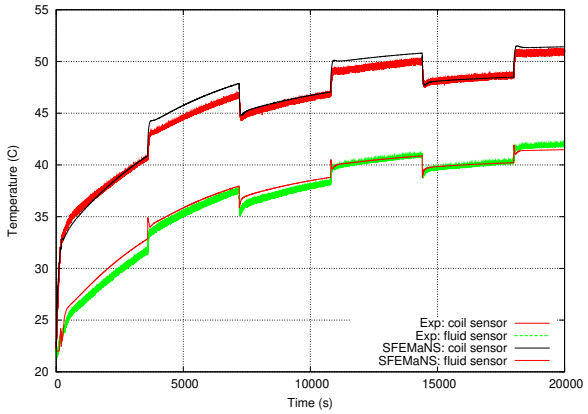


(b) Results computed in SFEMaNS code

Figure 3.26: Experimental and numerical temperature measurements with alternating magnetic force: the Helmholtz force is operative for $0 \leq t < 3600\ s$ and switched off for $3600\ s \leq t < 7200\ s$ with a total period of $7200\ s$.

Temperatures are continuously measured at two locations: on the coil and in the fluid on the symmetry axis (see the symbols "Tcoil" and "Tferrofluid" in figure (3.13)). The Helmholtz force is periodically switched on and off with a total period of $7200\,\mathrm{s}$, starting with an active force at $t = 0\,\mathrm{s}$. The time evolution on the two sensors computed in both COMSOL and SFEMaNS codes is shown respectively on figure (3.26(a)) and (3.26(b)). The agreement between the experimental measurements of the temperatures on the two sensors and the numerical computations resulting from both codes is excellent and validates our ferrofluid modeling.
Snapshots of temperature and velocity fields when the Helmholtz force is active or inactive are shown in figures (3.27) and (3.28) for COMSOL and SFEMaNS codes.
Figure (3.27) shows that the Helmholtz force has an impact on the thermal plume. When the Helmholtz force is active, the plume is deviated in the bulk above the coil, whereas it is centered on the symmetry axis when the Helmholtz force is switched off. This deviation is due to a re-circulation localized near the bottom of the coil, which pushes the hot fluid away from the axis [see figure (3.28(a,b))]. This lower recirculation does not exist when the Helmholtz force is inactive: the buoyancy force alone generates a single recirculation in the top part of the tank [see figure (3.28(c,d))]. Notice that the maximum value of the temperature is lowered by $2\,\mathrm{K}$ when the Helmholtz force is activated. This proves that the thermomagnetic convection mechanism is beneficial in this configuration.

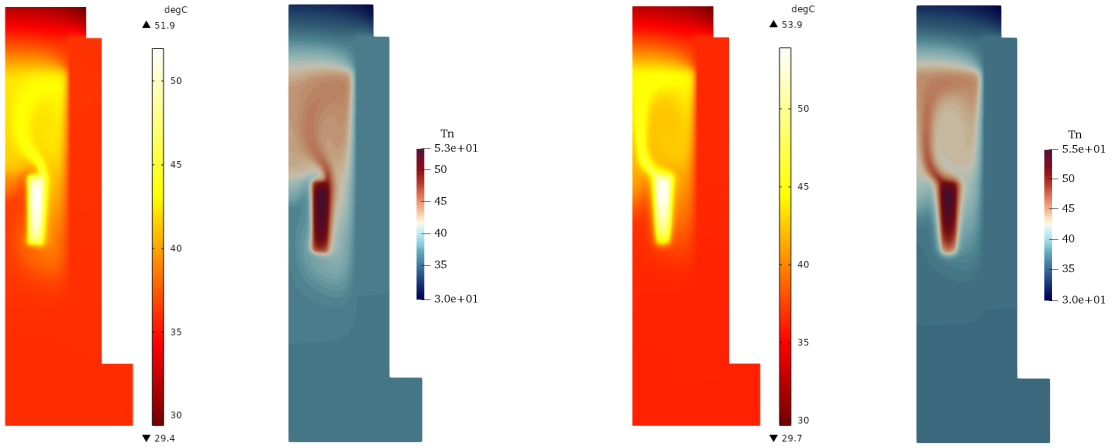


(a) Helmholtz force at $t = 16000\ s$, COMSOL code

(b) Helmholtz force at $t = 16000\ s$, SFEMaNS code

(c) No Helmholtz force at $t = 20000\ s$, COMSOL code

(d) No Helmholtz force at $t = 20000\ s$, SFEMaNS code

Figure 3.27: Temperature field (in °C) with alternating magnetic force. The symmetry axis ($Oz$) is on the left.

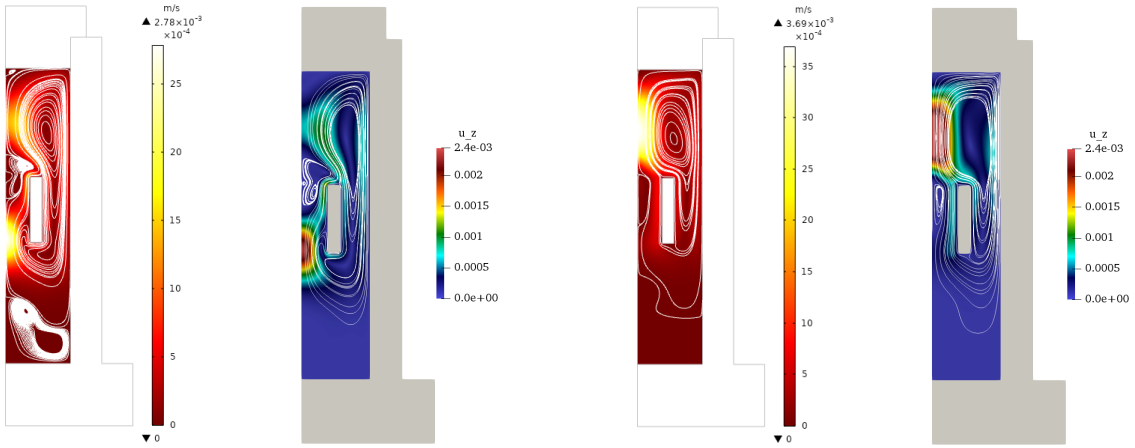


(a) Helmholtz force at $t = 16000\ s$, COMSOL code

(b) Helmholtz force at $t = 16000\ s$, SFEMaNS code

(c) No Helmholtz force at $t = 20000\ s$, COMSOL code

(d) No Helmholtz force at $t = 20000\ s$, SFEMaNS code

Figure 3.28: Color maps of the velocity magnitude (in $\mathrm{m.s^{-1}}$) and velocity streamlines with alternating magnetic force. The symmetry axis ($Oz$) is on the left.

Note that the maximum velocities obtained with both COMSOL and SFEMaNS codes are not the same, see figure (3.28(a,b,c,d)). The calculated velocity error is $14\%$ when the Helmholtz force is applied and $35\%$ when it is absent.
Consequently, both COMSOL and SFEMaNS confirm their ability to model the thermomagnetic convection in the solenoid system, and the compared results are in agreement. In the following, we use only COMSOL for the modeling because we seek to model more complex geometries, and it is still challenging to model 3D structures with SFEMaNS code due to its modal approach.

## 3.6 Improvement of the thermomagnetic convection

This section performs numerical and experimental studies in the context of improving thermomagnetic convection. We have shown that using ferrofluid in the solenoid setup presents a benefit in terms of cooling. The maximum temperature of the coil is lowered via thermomagnetic convection. In the following, we search for possible methods to enhance the heat transfer process in the solenoid setup. We consider first the Curie temperature of the magnetic nanoparticles in the ferrofluid suspension and determine the impact of increasing this temperature on the thermomagnetic convection. In a second test, we use an auxiliary magnet to modify the magnetic field distribution in the ferrofluid domain and evaluate the effect on the heat transfer by adding this magnet.

### 3.6.1 Influence of the Curie temperature on heat transfer

Previous studies have recommended that the Curie temperature of ferromagnetic particles should be comparable to the device's operating temperature [72,80,95]. To verify the interest of ferromagnetic materials with low Curie temperature, the time evolution of the temperature at the top of the solenoid is recorded using ferrofluids with various Curie temperatures. The saturation magnetization of the magnetic nanoparticles is given by the Bloch's law:

$$M_s(T) = \begin{cases} M_s(0)\left(1 - \left(\dfrac{T}{T_c}\right)^{\frac{3}{2}}\right) & \text{if } T \leq T_c, \\ 0 \quad \text{if } T \geq T_c \end{cases} \tag{3.25}$$

where $T_c$ is the Curie temperature. According to this law, the lower $T_c$ is, the lower the intensity of the saturation magnetization of the ferrofluid.
The mesh considered in this study is the same as the one used to compare the expressions of the magnetic force density in section (2.4.1).
The numerical results show that the temperature at the top of the solenoid (0.01, 0.08) at steady state is lower when the Curie temperature decreases, see figure (3.29). This is in agreement with the tests carried out in [13, p. 132].

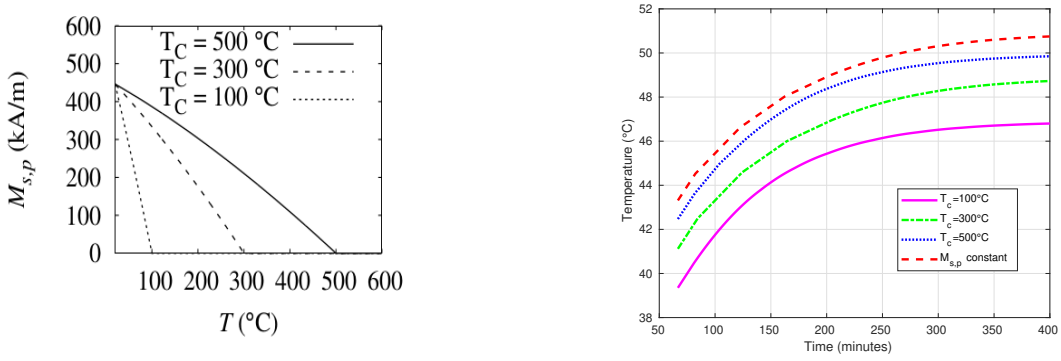


(a) Bloch's law for saturation magnetization at various Curie temperature.

(b) Temperature on the top of the solenoid versus time using fluids with various Curie temperatures.

Figure 3.29: Curie temperature impact on the solenoid temperature rise.

### 3.6.2 Adding auxiliary magnets

This part explains the idea of adding auxiliary magnets on the solenoid cooling system presented in chapter 1 in order to enhance the heat transfer process. The main objective is to analyze in which configuration the addition of the static magnetic field of the magnet allows the improvement of the heat transfer. At first, we present the experimental prototype, the simple system based on the solenoid immersed in a ferrofluid, to which a ring magnet surrounding the device is added. In a second section, we describe the 2D axisymmetric numerical model used to study the effect of the added magnet on cooling. We conclude numerically on the magnetic configuration and the positioning of the auxiliary magnet suitable to enhance the heat evacuation from the setup. In the third section, we compare the numerical and experimental results from adding a real ring magnet to the setup, and we discuss the velocity and temperature fields. At the end of this part, we describe a 2D axisymmetric model considering a cylindrical core added to the geometry of the typical solenoid setup.

#### Experimental setup

The setup is based on the copper solenoid immersed in a cobalt ferrite ferrofluid ($\widetilde{\phi} = 5.4\%$), the suspension presented in chapter 2. It is placed in an aluminum tank, closed at the top by a PVC plug as shown in figure (3.30). An annular magnet of square section is placed against the tank, to study the impact of the external field provided by the magnet. The dimensions of the experimental setup are given in table (3.1).

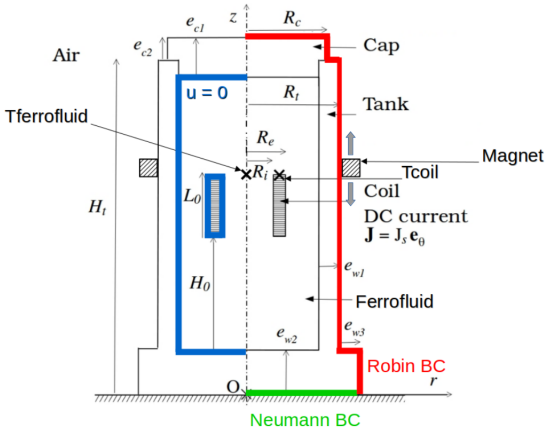


(a) Geometric notations and boundary conditions (see text).

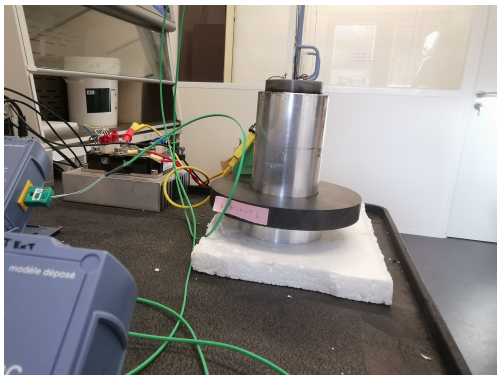

(b) Experimental setup.

Figure 3.30: 2D axisymmetric model of the solenoid with magnet.

#### Numerical modeling

In the following, we present the 2D axisymmetric model in cylindrical coordinates $(r, z)$ used to describe the magnet surrounding the solenoid setup, as shown in figure (3.31). Comparing to the previous study, an air surface is added around the test cell to ensure the closure of the magnetic field lines for the magnetic numerical calculation.

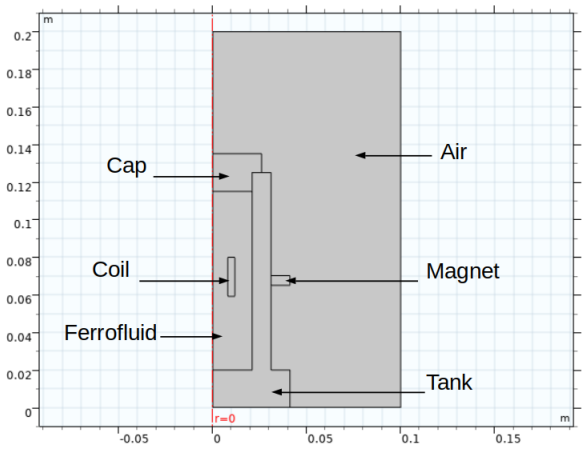


Figure 3.31: 2D axisymmetric model in (r,z) coordinates.

The ferrofluid used is again considered to be an incompressible Newtonian fluid, homogeneous and continuous. The main difference with the previous part is the consideration of the magnet behavior law:

$$\mathbf{B} = \mu_0 \mathbf{H} + \boldsymbol{B_r}, \tag{3.26}$$

where $\boldsymbol{B_r}$ is the remanent magnetization. The magnetic force is here modeled by the modified Kelvin expression (in $\mathrm{N/m^3}$):

$$F = \mu_0(\chi(T) - \chi(T_{ext}))\nabla\frac{H^2}{2}, \tag{3.27}$$

where $H = \|\mathbf{H}\|$.

### Boundary conditions

As mentioned before, an air volume is added around the test cell to ensure the closure of the magnetic field lines for the magnetic numerical calculation. The boundary condition for the magnetic problem $\mathbf{A} \times \mathbf{n} = \mathbf{0}$ is now enforced on the air boundaries, where $\mathbf{A}$ is the magnetic vector potential. The non-slip boundary condition $\mathbf{u} = \mathbf{0}$ is applied at the border of the fluid domain (see blue lines on figure (3.30)). The air convection at the top and on the lateral wall of the PVC-Aluminium tank is still modeled by using a Robin boundary condition for the temperature:

$$-\lambda\nabla T \cdot \mathbf{n} = h(T - T_{ext}), \tag{3.28}$$

where $h$ is the convection coefficient, and $\mathbf{n}$ is the outer unit normal vector (see red lines on figure (3.30)). The homogeneous Neumann boundary condition $\partial_z T = 0$ is enforced at the bottom of the tank (see green line on figure (3.30)). The initial conditions are $\mathbf{u} = \mathbf{0}$, $\mathbf{A} = \mathbf{0}$ and $T = T_{ext}$.

### Meridian mesh

We choose an extremely fine triangular mesh in the ferrofluid domain ranging from $2 \times 10^{-6}\,\mathrm{m}$ to $6.7 \times 10^{-4}\,\mathrm{m}$. A fine triangular mesh is chosen for the solenoid domain, ranging from $3 \times 10^{-4}\,\mathrm{m}$ to $7 \times 10^{-4}\,\mathrm{m}$. The mesh selected in the tank, the cap, the air layer and the magnet domain ranges

from $8 \times 10^{-4}\,\mathrm{m}$ to $1.5 \times 10^{-3}\,\mathrm{m}$. The meridian mesh shown in figure ((3.32)a) contains $47679$ elements. The four corners of the coil are smoothed to let the ferrofluid flows smoothly around the solenoid. The time step is automatically adapted and varies upon the range [$0.01\,\mathrm{s}$ - $0.1\,\mathrm{s}$].

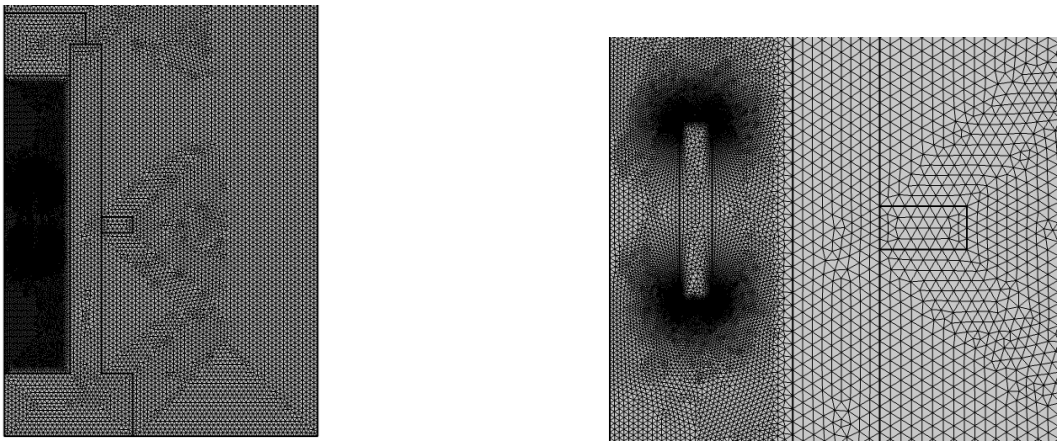

(a) Total mesh for the 2D axisymmetric model with the added magnet.

(b) Finite mesh in the solenoid (zoom).

Figure 3.32: Meridian mesh in the $(r, z)$ plane.

### Numerical results

We now study numerically the impact of an annular magnet with a remanent induction amplitude of $0.3\,\mathrm{T}$. The magnet is localized alongside the PVC-Aluminium tank. The objective is to use the magnet to improve the cooling by changing the distribution of the magnetic field induced by the coil. Optimization of the location, strength, and orientation of the magnet are presented in the next section using COMSOL Multiphysics. After this part, the numerical results obtained with the magnet improvement tests are compared to experimental ones.

**Results conducted on COMSOL Multiphysics** The tested magnet is assimilated to a rectangle in the numerical model, as shown in figure ((3.32)b). The characteristics of this magnet are $r_i = 3.1\,\mathrm{cm}$ (inner radius), $r_e = 3.6\,\mathrm{cm}$ (outer radius), $H = 1\,\mathrm{cm}$ (height). The air layer of height $20\,\mathrm{cm}$ and thickness $10\,\mathrm{cm}$ is added around the cylindrical cavity to ensure the closure of the magnetic field lines across the interface of the tank. The numerical results are saved every $5\,\mathrm{s}$.

**Magnet with a vertical remanent induction field** We call optimal positioning of the magnet the vertical location which realizes the maximum reduction in the coil temperature. First, we determine the optimal position of the magnet with a vertical remanent induction field $B_z = -0.3\,\mathrm{T}$. Figure ((3.33)a) shows the magnetic field distribution $H_z$ in the model geometry. The evolution of the $z$ component of the magnetic field with the radius $r$ is presented in figure ((3.33)b). According to this distribution of $H_z$, the magnetic field generated by the magnet dominates the magnetic field due to the coil.

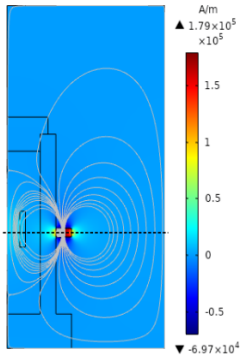


(a) Color map of the distribution of the $z$ component of the magnetic field in $(\mathrm{A.m^{-1}})$ in the 2D axisymmetric model.

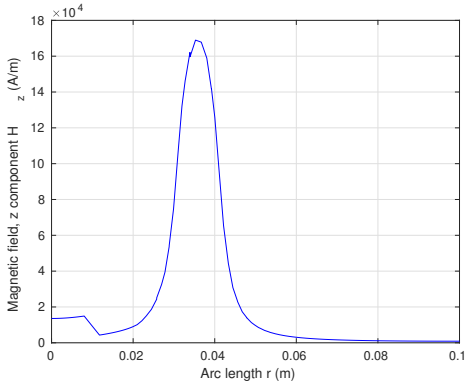


(b) $H_z$ versus the radius $r$. The $z$ component of the magnetic field is computed through a horizontal line defined at $Z = 0.0675$ m and crossing the magnet center.

Figure 3.33: Magnetic field distribution in the numerical model.

By varying the vertical position of the magnet, a $1\,^{\circ}\mathrm{C}$ decrease in the maximum temperature of the solenoid is detected at $Z = 0.065\ m$ (base corner of the magnet), as shown in figure (3.34). However, the thermal plumes are the same in the two configurations.

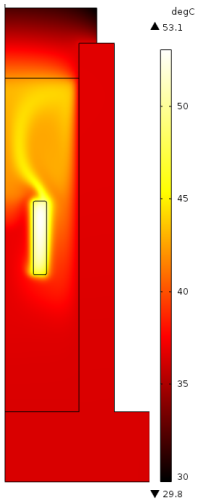


(a) Only coil.

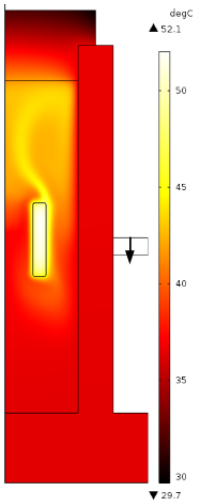


(b) $B_z = -0.3$ T and coil.

Figure 3.34: Temperature field (in $^{\circ}\mathrm{C}$) at $t = 25\,000\,\mathrm{s}$ with the coil and annular magnet $B_z = -0.3\,\mathrm{T}$.

Figure (3.35) shows the velocity distributions with streamlines in two cases: when only the coil magnetic field is present ((3.35)a), and when the remanent induction field is added ((3.35)b). If the annular magnet is added ($B_z = -0.3\,\mathrm{T}$), the number of fluid recirculations at the bottom of the coil increases. The maximum velocity magnitude in the fluid domain is enhanced by an order of $36\%$. This enhancement can explain the decrease in the maximum temperature of the solenoid.

(a) Only coil. (b) $B_z = -0.3$ T and coil.

Figure 3.35: Color maps of the velocity magnitude (in $\mathrm{m.s^{-1}}$) and velocity streamlines at $t = 25\,000\,\mathrm{s}$ with the coil and annular magnet $B_z = -0.3\,\mathrm{T}$. The symmetry axis $(Oz)$ is on the left.

The maximum temperature evolution in the solenoid as a function of the vertical position of the magnet is plotted in figure (3.36). The temperature records (at $t = 25\,000\,\mathrm{s}$) of the fluid (at point $(0, 0.08\ m)$), in the solenoid (at the top $(0.01\ m, 0.08\ m)$ and in the middle $(0.01\ m, 0.0695\ m)$) are also shown in this figure.

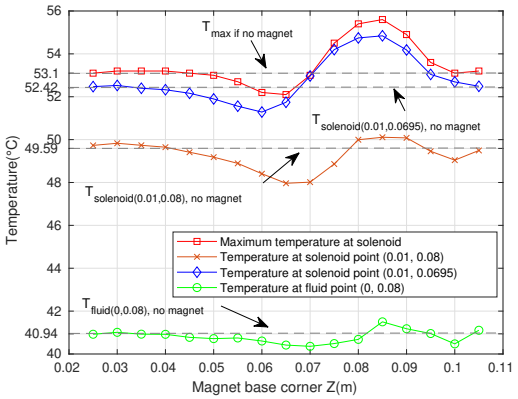


Figure 3.36: Temperature evolution with respect of the magnet positioning, $B_z = -0.3$ T and coil.

As shown in this figure, the maximum temperature in the coil reaches its minimum (52 °C) at $Z = 0.065\ m$. Note that the temperature at the middle of the coil (see blue line) in this magnet position ($Z = 0.065\ m$) is roughly the same as the one measured at the maximum (see red line).

**Magnet with other configurations of the remanent induction field** In this part, other configurations of the remanent induction field are tested. We start by a vertical remanent induction field $B_z = 0.3$ T [see figure ((3.37)a)] opposite to the one described in the previous part. Then, we study the effect of a radial remanent field induction with opposite signs $B_r = \pm 0.3$ T, [see figure ((3.37)b,c)]. Figure (3.37) shows the temperature fields for each magnetization direction.

The magnets shown in this figure are placed at the optimal locations found for each magnetization direction, namely at $Z = 0.105\ m$ for ((3.37)a), at $Z = 0.045\ m$ for ((3.37)b) and at $Z = 0.08\ m$ for ((3.37)c).

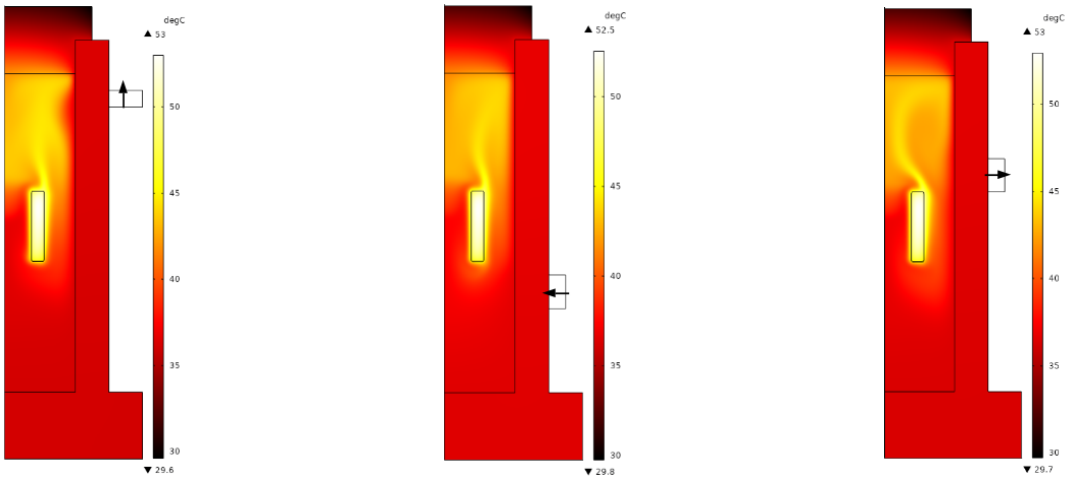

(a) $B_z = 0.3$ T and coil. (b) $B_r = -0.3$ T and coil. (c) $B_r = 0.3$ T and coil.

Figure 3.37: Color maps of the temperature fields (in °C) at $t = 25\,000$ s for various configurations of the remanent induction field. The symmetry axis $(Oz)$ is on the left.

In parallel, we present the velocity distributions at $t = 25\,000$ s for the three cases of the remanent induction field, as shown in figure (3.38).

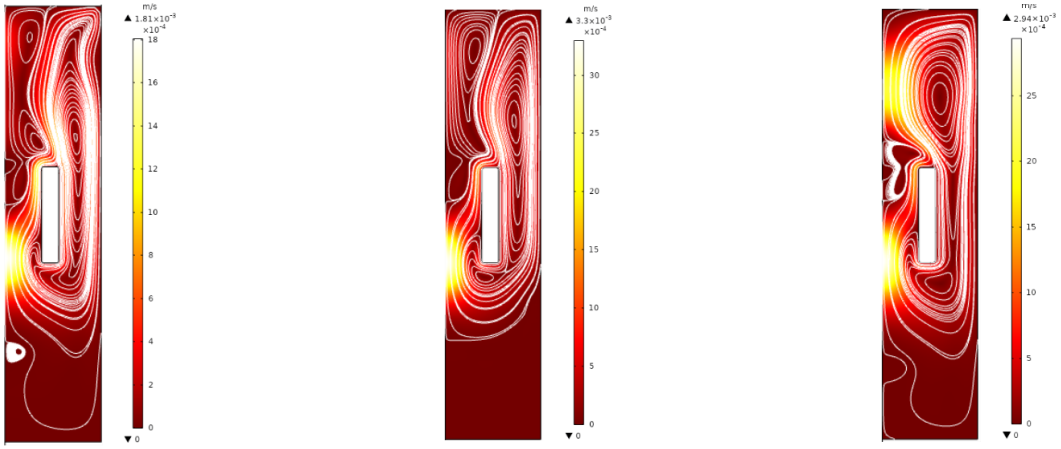

(a) $B_z = 0.3$ T and coil. (b) $B_r = -0.3$ T and coil. (c) $B_r = 0.3$ T and coil.

Figure 3.38: Color maps of the velocity magnitude (in $\mathrm{m\,s^{-1}}$) and streamlines at $t = 25\,000$ s with various configurations of the remanent induction field. The symmetry axis $(Oz)$ is on the left.

According to figure ((3.37)a), the decrease in the maximum temperature of the coil is negligible ($0.1$ °C). The thermal plume is deviated from the symmetry axis at the left due to strong fluid recirculations active at the upper side of the tank, as shown in figure ((3.38)a). The maximum

velocity magnitude is reduced by $19\%$ comparing to the case where no magnet is added [see figure ((3.35)a)]. It seems that the positively magnetized axial magnet has only a slight effect on the solenoid cooling at this positioning of the magnet $Z = 0.105\ m$.
Let us describe the impact of changing the direction of the remanent induction field from a vertical to a radial magnetization. Results observed in ((3.37)b,c) show a slight decrease of the maximum temperature in the coil from $0.6\,°\mathrm{C}$ when $B_r = -0.3\ \mathrm{T}$ to $0.1\,°\mathrm{C}$ when $B_r = 0.3\ \mathrm{T}$. Figure ((3.38)b) presents an increase in the number of vortices in the fluid domain that enclose the entire body of the coil comparing to the case where no external field is applied. Despite the enhancement in the maximum velocity magnitude ($32\%$), the reduction in the maximum temperature of the coil remains not significant for this location of the magnet $Z = 0.045\ m$. Figure ((3.38)c) also shows an enhancement in the maximum velocity magnitude of the fluid ($24\%$), but the decrease in the maximum temperature of the coil is still negligible with the magnet located at $Z = 0.08\ m$.

The impact of increasing the vertical remanent induction field in the magnet is also studied when the location of the magnet is fixed at $Z = 0.065\ m$. Note that if the magnitude ($|B_z|$) of the remanent induction field increases, the maximum temperature in the coil does not monotonously decrease but reaches $49.3\,°\mathrm{C}$ when $B_z = -0.9\mathrm{T}$, as shown in figure (3.39).

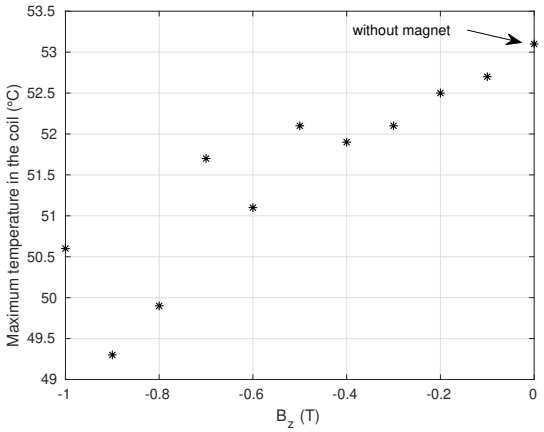


Figure 3.39: Decrease of the maximum temperature in the coil when the magnitude of the remanent induction field increases.

**Conclusive remarks** The impact of adding auxiliary magnets to the solenoid setup in order to enhance the heat transfer process has been numerically studied. It is shown that we can modify the ferrofluid behavior inside the tank by adding an external magnetic field. This decrease in the maximum temperature of the coil can only happen with some particular locations of the magnet and with the convenient direction of its magnetization. Optimization of the magnet location, strength, and orientation can enhance the heat transfer in the solenoid system.

### Experiment with coil and annular magnet

We perform an experiment using a ring magnet ($\Phi\ 140 \times 63 \times 17\ \mathrm{mm}$) with a vertical remanent induction field $B_z = 0.2\,\mathrm{T}$. The magnet is placed at the optimal location numerically found $Z =$

$0.065\ m$. Two thermocouples are used to measure the temperature at the surface of the solenoid and in the fluid (see figure (3.30)), the ambient temperature for this experiment being $T_{ext} = 288\,\mathrm{K}$. The only parameter that is changed in the modeling is the dynamic viscosity of the ferrofluid due to the reference temperature changing ($\eta(T = 288.15\ K) = 0.07\,\mathrm{Pa.s}$). We choose the same triangular finite element mesh adopted in section (1.2.2) (see figure (3.32)). The meridian mesh contains $47665$ elements. The four corners of the coil are smoothed to let the ferrofluid flows smoothly around the solenoid. A numerical calculation is launched to record the temperature evolutions at the same measurement points as the experimental setup. The results of the numerical and experimental realizations are presented in figure (3.40).

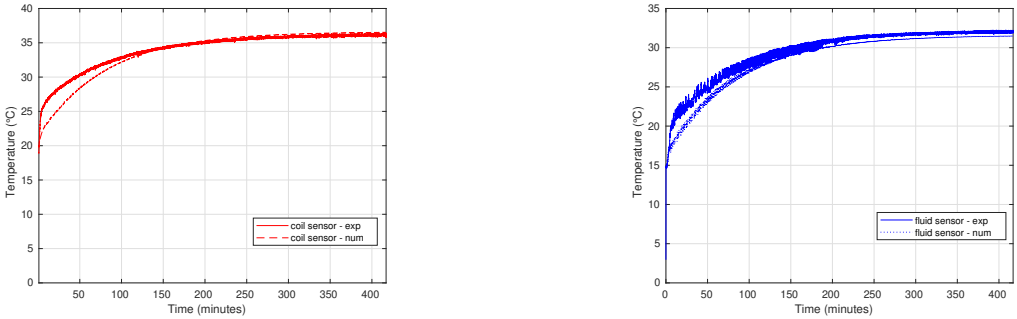


(a) Temperatures at coil sensor, $B_z = -0.2\,\mathrm{T}$. (b) Temperatures at fluid sensor, $B_z = -0.2\,\mathrm{T}$.

Figure 3.40: Experimental-numerical cross-validation for the temperature records.

A difference of time constant in the transient regime is observed, with a faster thermal diffusion time in the experimental than in the numerical recordings, perhaps related to the homogenized thermal model of the coil. The steady-state temperatures are, however, very close for both measurement points. Evaluation of the impact of the auxiliary magnets on the cooling process is studied in two experimental tests: the first one corresponds to the presence of the axial magnet and the other one without a magnet. The temperature curves are shown in figure (3.41).

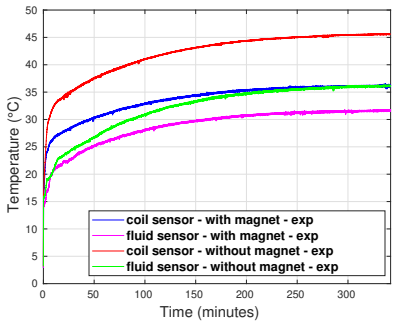


Figure 3.41: Temperature measurements for the comparison with/without axial magnet.

It is shown that in the case where the axial magnet is present, the surface temperature of the solenoid is decreased by about $9\,^{\circ}\mathrm{C}$. This is due to the intensification of the magnetic fluxes in the ferrofluid, which amplifies the magnitude of the magnetic force, and therefore maximizes the flow of the fluid around the coil. The heat exchange with the outside is thus directly favored.

**Velocity and temperature distributions** The magnetic field, velocity and temperature distributions at $t = 25\,000\,\mathrm{s}$ are presented in figures (3.42), (3.43) and (3.44), respectively, for the cases with or without an axial magnet.

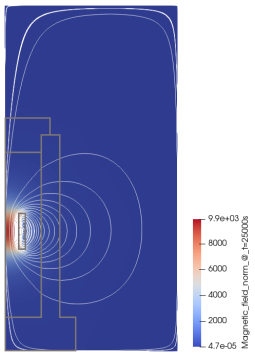


(a) Magnetic field intensity ($\mathrm{A.m^{-1}}$), coil only.

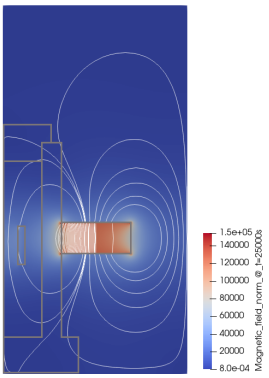


(b) Magnetic field intensity ($\mathrm{A.m^{-1}}$), $B_z = -0.2\,\mathrm{T}$ and coil.

Figure 3.42: Magnetic field distribution in the numerical model.

Comparison of the velocity and temperature fields at $t = 25\,000\,\mathrm{s}$ confirms the change in fluid flow around the solenoid, and therefore the effect caused by the external magnet on the cooling. When the magnet is not added, the fluid circulations (in figure (3.43)a) are due to the presence of the magnetic force acting on the ferrofluid in addition to the thermally induced buoyancy force. Figure ((3.44)a) shows that the temperature plume emerges from the top of the solenoid approaches the axis of symmetry (left edge of the figure), and then bends outward.

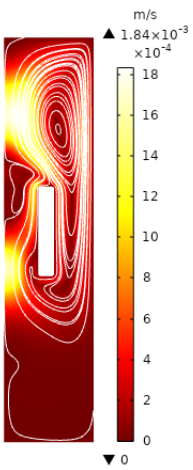


(a) Velocity magnitude and streamlines, coil only.

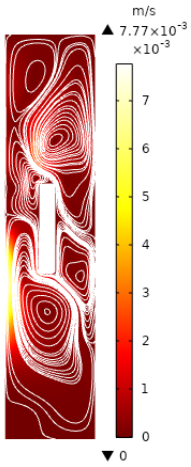


(b) Velocity magnitude and streamlines, $B_z = -0.2\,\mathrm{T}$ and coil.

Figure 3.43: Velocity fields distributions with streamlines in the numerical model at $t = 25\,000\,\mathrm{s}$.

When the "axial" magnet with $B_z = -0.2\ T$ is present (see figure ((3.42)b)), changes in the fluid circulation appear in the part located under the solenoid (see figure ((3.43)b)), which amplify

the heat removal. The velocity magnitude is increased (the maximum velocity magnitude is enhanced by 76%). This is caused by the modification of the field lines and the intensification of the magnetic flux in the fluid. A new thermal plume appears moving downwards and outwards as shown in figure ((3.44)b): it is driven by the two lower fluid circulation cells. Another ascending and less active plume is present in the upper part of the tank. It follows the contours of the upper convection cells. As a consequence of these new fluid cells, the maximum temperature of the solenoid is lowered by $5.5\,°\mathrm{C}$. The impact of adding an auxiliary magnet on the solenoid cooling is verified.

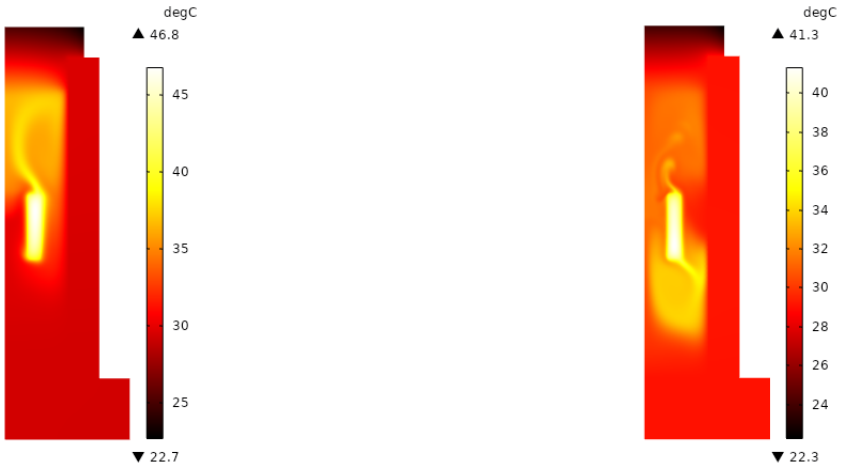


(a) Temperature, coil only.

(b) Temperature, $B_z = -0.2\,\mathrm{T}$ and coil.

Figure 3.44: Thermal plumes in the numerical model at $t = 25\,000\,\mathrm{s}$.

Concerning the time trends, figure (3.45) shows the temperature in two points defined respectively at the surface of the solenoid and in the fluid for the two configurations: the first one when the magnetic field of the solenoid is only present, the second one concerns the case when the external magnet ($B_z = -0.2\,\mathrm{T}$) is added.

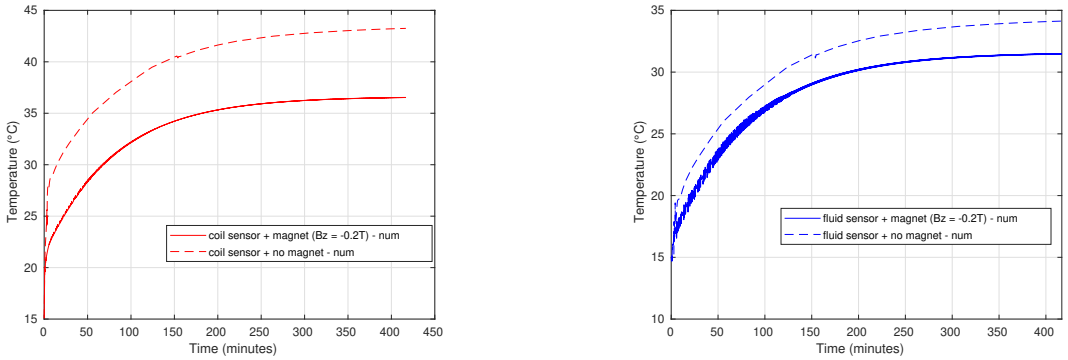


(a) Temperatures at coil sensor.

(b) Temperatures at fluid sensor.

Figure 3.45: Numerical temperature curves for two configurations of the magnet (On, Off).

The temperature curves reach a steady state after about $25\,000\,\mathrm{s}$ for both the fluid and the winding. For the winding, a decrease of $7\,\mathrm{K}$ is to be noted in the presence of the magnet. For the fluid,

a less significant decrease of the temperature of about $3\,\mathrm{K}$ is recorded. Oscillations on the temperature curve of the fluid are present during the transient regime for a duration of about $7500\,\mathrm{s}$ when the magnet is added.

### Model with ferromagnetic core

In this part, the idea is to insert a ferromagnetic core placed on the axis of symmetry to get closer to the real structure of a power transformer. An axial magnet $B_z = 0.3\,\mathrm{T}$ is still fixed on the upper part of the core to increase and modify the magnetic fluxes in the vicinity of the solenoid. In connection with these two configurations, two numerical calculations have been launched: the first one concerns the model of the solenoid to which the ferromagnetic core is added (see figure (3.46)a), and the second one corresponds to the case where an auxiliary magnet is placed above the ferromagnetic core (see figure (3.46)b). The initial temperature for this simulation is $T_{ext} = 295.15\,\mathrm{K}$.

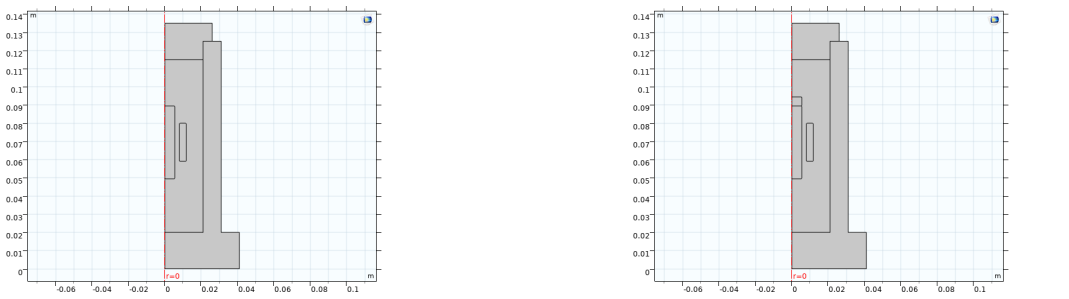

(a) Coil and core only.

(b) Coil and core with magnet $B_z = 0.3\,\mathrm{T}$.

Figure 3.46: 2D axisymmetric models in (r,z) coordinates.

**Finite element mesh** We should refine the mesh near the boundaries of the ferromagnetic core, the magnet, and the coil where the magnetic body force is concentrated. Refining the mesh in these places may help increase the resolution of the fluid flows in the vicinity of these components.
We choose an extra fine triangular mesh in the ferrofluid, coil, core and magnet domains ranging from $6.15 \times 10^{-6}\,\mathrm{m}$ to $5.33 \times 10^{-4}\,\mathrm{m}$. The mesh selected in the tank and the cap has a size of $1.5 \times 10^{-3}\,\mathrm{m}$. The meridian mesh shown in figure ((3.47)a) contains $40870$ elements. The four corners of the coil and the ferromagnetic core are smoothed to let the ferrofluid flows smoothly around the solenoid and the core. The time step is automatically adapted and varies upon the range $[0.01\,\mathrm{s}$ - $0.1\,\mathrm{s}]$.

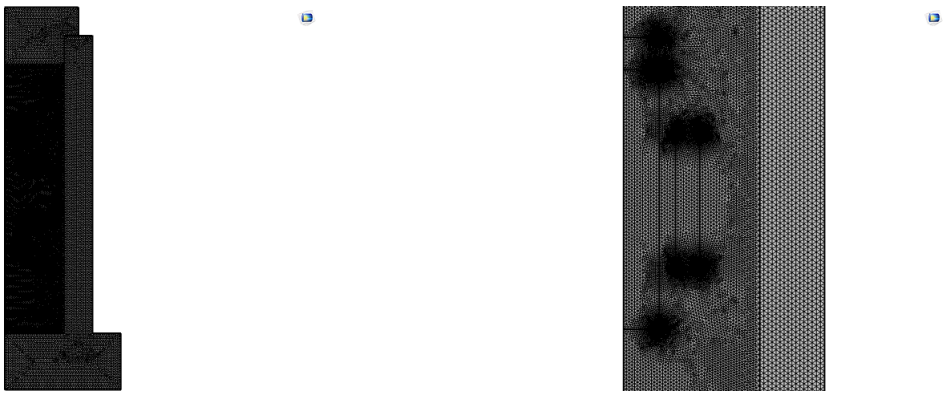

(a) Total mesh. (b) Extra fine mesh in the ferrofluid domain (zoom).

Figure 3.47: Meridian mesh in (r,z) coordinates.

In this section, the ferrofluid is modeled using the Helmholtz magnetic force:

$$\mathbf{F} = -\mu_0 \frac{H^2}{2} \boldsymbol{\nabla} \chi(T), \tag{3.29}$$

where $H = \|\mathbf{H}\|$. As explained before, only three proposed models of the magnetic force lead to the same ferrofluid motion.

**Numerical results** Figure (3.48) shows the magnetic field distributions at $t = 10\,000\,\mathrm{s}$ for each of both cases presented below.


(a) Magnetic field intensity ($\mathrm{A.m^{-1}}$), no magnet. (b) Magnetic field intensity ($\mathrm{A.m^{-1}}$), $B_z = 0.3\,\mathrm{T}$.

Figure 3.48: Magnetic field distributions when a ferromagnetic core is added.

In figure ((3.48)a), the added ferromagnetic core increases the focalization of the magnetic flux by concentrating its lines on the axis of symmetry inside the coil. When an axial magnet is added on top of the core (see figure ((3.48)b)), the distribution of the magnetic flux lines is modified as expected. Indeed, an intensification of these lines appears near the magnet, and the magnetic field intensity is amplified. This results leads to an increase of the magnetic force towards the upper part of the system (see figures ((3.49)a,b)).

(a) No magnet. (b) $B_z = 0.3\,\mathrm{T}$.

Figure 3.49: Helmholtz force distributions in the two presented cases.

Figures (3.50) and (3.51) show the velocity and temperature profiles at $t = 10\,000\,\mathrm{s}$ corresponding to the different distributions of the magnetic field.


(a) Velocity magnitude ($\mathrm{m\,s^{-1}}$), no magnet. (b) Velocity magnitude ($\mathrm{m\,s^{-1}}$), $B_z = 0.3\,\mathrm{T}$.

Figure 3.50: Velocity distributions with streamlines at $10\,000\,\mathrm{s}$.

The ferrofluid flow around the solenoid and into the tank is strongly modified after adding the magnet. In figure ((3.50)b), a new convection cell appears above the ferromagnetic core resulting in a change in fluid flow compared to its behavior in figure ((3.50)a) when the magnet is removed. The ferrofluid then acquires a higher velocity (enhancement by $32\%$ in the maximum velocity) and improves the heat dissipation through the tank by its modified flow.

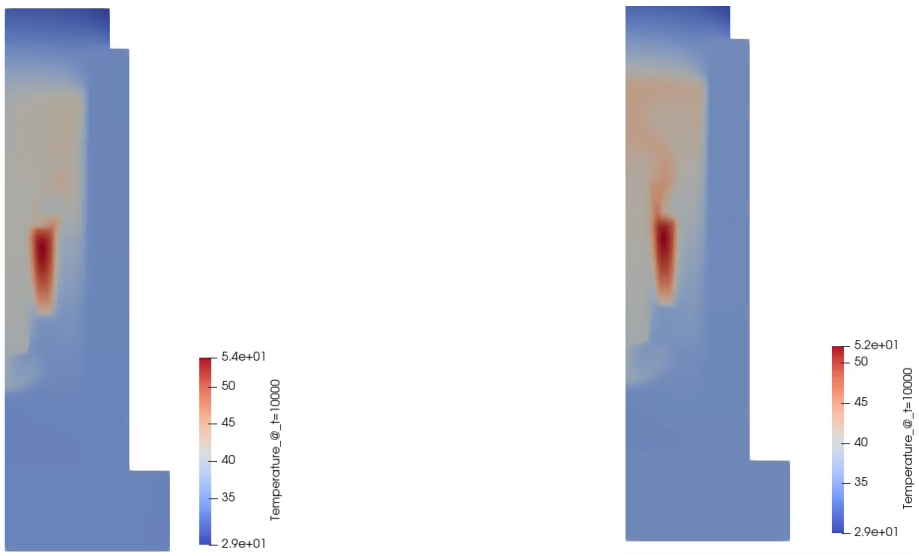


(a) Temperature (°C), No magnet.

(b) Temperature (°C), $B_z = 0.3\,\mathrm{T}$.

Figure 3.51: Temperature profiles at $10\,000\,\mathrm{s}$.

The analysis of the thermal plumes of the two cases shows the effect induced by the axial magnet on the cooling. A decrease of the maximum temperature of $2\,\mathrm{K}$ is recorded. The volutes of the plumes at $t = 10\,000\,\mathrm{s}$ for the case with the magnet (figure ((3.51)b)) show an enhanced heat removal above the winding. In this configuration, the beneficial effect of the magnet on the heat exchange process is again confirmed.

## 3.7 Conclusions

An experimental setup has been developed in GeePs laboratory to evaluate the heat transfer in a heated solenoid immersed in a ferrofluid medium. It consists of a copper coil immersed in a cylindrical container filled with ferrofluid. The experimental ferrofluid is based on cobalt ferrite nanoparticles ($CoFe_2O_4$) dispersed in $Midel\ eN\ 1215$ vegetable oil. The ferrofluid thermophysical properties are calculated using the mixed laws introduced in chapter 1. The solenoid physical properties are evaluated using the homogenized laws reported in section (2.2.2). This setup is thought as the first step towards the study of a power transformer with a more complex geometry.

A 2D axisymmetric modeling is first performed to validate the impact of the thermomagnetic convection on the solenoid cooling. When the magnetic force is activated, a new recirculation appears at the bottom of the coil and changes the flow pattern in the container. Hence, the cooling process is enhanced. A decrease in the maximum temperature of the coil of about $2\,^{\circ}\mathrm{C}$ is obtained when the magnetic force is active. While this reduction in the solenoid temperature seems to be not significant, experts claim that a reduction by $6\,^{\circ}\mathrm{C}$ in the maximum temperature of the windings in power transformers could extend by 2 their lifespan.

Simulations are performed with two different finite element codes, SFEMaNS and COMSOL Multiphysics, the latter being the solution retained to develop the 3D models. Numerical results are in

very good agreement. The velocity distributions obtained are qualitatively the same and lead consequently to the same thermal plumes. In parallel, the experimental and numerical results cross-validate, and the 2D axisymmetric approach is therefore verified and confirms our choice of the boundary conditions.

The impact of the different models of the magnetic force on the cooling process is then studied. In literature, different forms of the magnetic force are proposed to model the ferrofluid. In our setup, we compare the Kelvin model to the Helmholtz one. They give the same velocity and temperature distributions in a ferrofluid. This result is expected since the two forces are equal up to a gradient that can be associated to a new pressure field. According to the numerical simulations, the Helmholtz and modified Kelvin forces give consistent results during a short calculation time. We did not encounter numerical instabilities with these expressions. In contrast, the Kelvin expression may yield numerical instabilities that are overcome using smaller time steps, hence longer computational times.

Tests are proposed in order to enhance the heat transfer process in the solenoid system. First, the effect of the Curie temperature of magnetic nanoparticles on the heat transfer is assessed. It is shown that using ferrofluid made of nanoparticles with low Curie temperature can limit the temperature rise in the solenoid and then improve the cooling process.

The second improvement test considers the addition of an external magnetic field to the solenoid setup to improve the heat transfer process. The magnetic field distribution into the tank being modified, the ferrofluid circulation is usually intensified. The number of vortices around the solenoid increases, and the maximum temperature in the coil can be reduced. This improvement in the system heat transfer depends on the magnetic configuration of the magnet: magnetization, orientation, and its location. Optimization tests have served to choose the best configuration of the magnet.

Numerical and experimental results have shown that adding a magnet at an optimized location can modify the ferrofluid flow around the electromagnetic system and enhance its cooling at a low cost. The modified velocity and temperature maps of the studied system validate the impact induced by an auxiliary magnetic field. The fluid circulations in the tank and around the winding are reinforced, and the thermal plumes show that the heat exchange via thermomagnetic convection is favored. In our case, the most interested configuration of the magnet was the vertical remanent induction field $B_z = -0.3\,\mathrm{T}$ at $Z = 0.065\,\mathrm{m}$ numerically. The experimental validation was performed with a magnet of $B_z = -0.2\,\mathrm{T}$ placed at the same optimal location. Optimization tests with the insertion of a ferromagnetic core have also shown a significant reduction in the solenoid maximum temperature, depending on the magnet configuration.

The next chapter will first present a simulation test dealing with a 3D model of the solenoid that serves as a transition to the 3D modeling. Then, we will perform a 3D non-axisymmetric modeling for a $3\,\mathrm{kVA}$ power transformer model using the finite element method.

# Chapter 4

# Thermomagnetic Convection in Power Transformers

This chapter introduces a finite element analysis for the heat transfer process in a power transformer system. The study evaluates the cooling performance in such devices by using a ferrofluid solution instead of mineral oil. At first, we perform a 3D validation of the 2D-axisymmetric model of the solenoid system as a transition to the 3D modeling. We investigate the velocity and temperature fields for both 2D-axisymmetric and 3D approaches and compare the results. Next, we present a 2D axisymmetric modeling for a $40\ \mathrm{kVA}$ single-phase power transformer model along with the relevant results. We verify the impact of the ferrofluid on the cooling process. In a third section, we perform a 3D study for the same geometry of the $40\ \mathrm{kVA}$ simplified power transformer and make some comparisons. In a fourth section, a $3\ \mathrm{kVA}$ power transformer model is studied using a 3D non-axisymmetric finite element analysis. We outline the magnetic field calculation using both transient and static approaches. Then we describe our coupling strategy to study the heat transfer problem in the power transformer. The numerical results referring to both hydrodynamic and ferrohydrodynamic cases are compared with a first manageable spatial/temporal resolution. At the end of this chapter, we perform a convergence study on a hydrodynamical configuration using our available computational resources.

## 4.1 Three-dimensional study and comparisons

In this part, we aim to verify whether the 3D modeling of the solenoid matches with the 2D axisymmetric model described before. We also investigate the impact of considering the complex structure in the modeling on the computational time. We begin with the comparison between 3D and 2D axisymmetric results using COMSOL Multiphysics. We aim to evaluate two cases: the hydrodynamic case where the magnetic force does not exist and the ferrohydrodynamic case where the magnetic force influences the ferrofluid. We start by using the Kelvin force in its modified form (3.24) to model the magnetic body force.

#### 3D tetrahedral mesh

We choose a fine tetrahedral mesh for the ferrofluid domain ranging from $1.23 \times 10^{-1}\ \mathrm{mm}$ to $1.89\ \mathrm{mm}$. The solenoid boundaries have a thickness size of $1\ \mathrm{mm}$. An extremely fine mesh is used

inside the coil ranging from $1.64 \times 10^{-2}\,\mathrm{mm}$ to $1.07\,\mathrm{mm}$. The tank and cap domains have a coarser mesh with a spatial mesh size ranging from $3.78\,\mathrm{mm}$ to $20.3\,\mathrm{mm}$. The simulation runs for $24\,000\,\mathrm{s}$, and the numerical results are saved every $50\,\mathrm{s}$. The three-dimensional mesh shown in figure (4.1) contains $656397$ elements. The time step is automatically adapted and varies upon the range [$0.01\,\mathrm{s}$ - $0.5\,\mathrm{s}$].

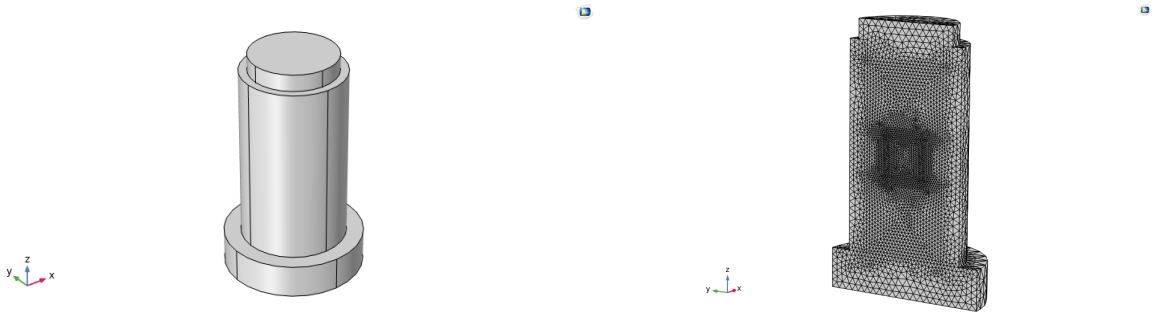

(a) 3D model of the solenoid

(b) Cross section view of the 3D mesh

Figure 4.1: Free tetrahedral mesh in 3D view for the solenoid model.

The meridian mesh used for the 2D-axisymmetric model is previously presented in chapter 3, section 3.5.1. In the following, snapshots of the numerical velocity and temperature fields when the Kelvin force is deactivated are shown in figures (4.2) and (4.3). Comparing these 3D and 2D axisymmetric results proves the qualitative and quantitative agreement of the velocity and temperature fields in both cases and confirms the choice of the simplified 2D axisymmetric model.

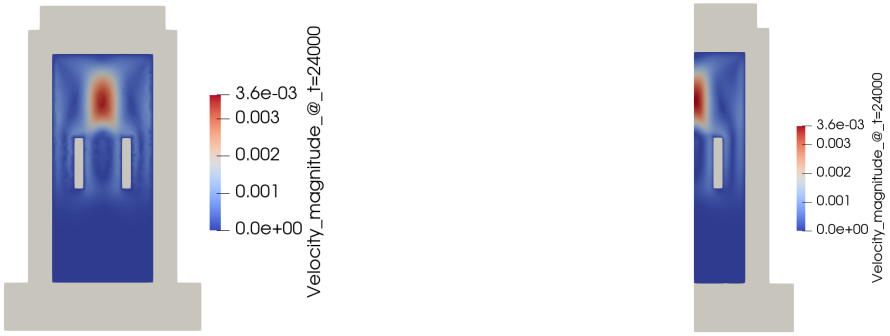


(a) 3D case at $t = 24000\ s$

(b) Axisymmetric case at $t = 24000\ s$

Figure 4.2: Color maps of the velocity magnitude (in $\mathrm{m.s^{-1}}$) when the magnetic force is inactive. The symmetry axis ($Oz$) is on the left for the axisymmetric model (panel b).

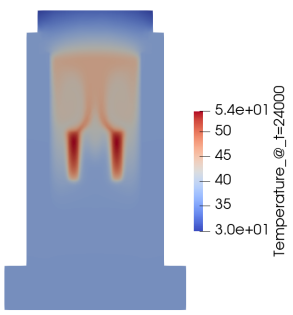


(a) 3D case at $t = 24000\ s$

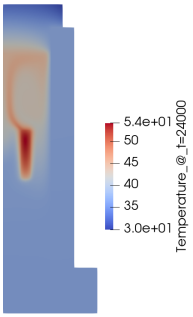


(b) Axisymmetric case at $t = 24000\ s$

Figure 4.3: Temperature field (in °C) when the magnetic force is inactive. The symmetry axis ($Oz$) is on the left for the axisymmetric model (panel b).

Temperatures are continuously measured at two locations: on the top of the coil and in the fluid on the symmetry axis (see the symbols "Tcoil" and "Tferrofluid" in figure (3.13)). The time evolution on the two sensors is shown respectively in figure (4.4(a)) and (4.4(b)).

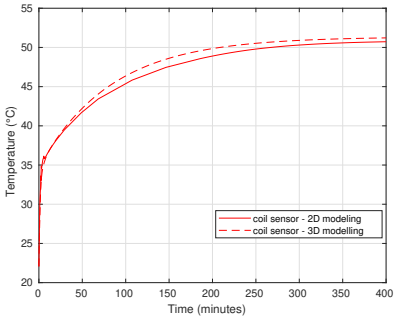


(a) Coil temperature

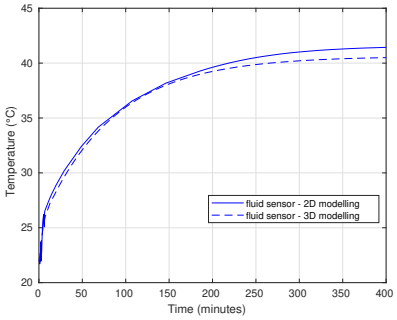


(b) Fluid temperature

Figure 4.4: Time evolution of the temperature at the coil top and in the fluid in a 3D setting compared to a 2D axisymmetric configuration.

These temperature curves appear to be better superimposed in transient than in the steady-state regime. The relative difference between 2D and 3D curves at the steady-state is $1\%$ and $2.2\%$ for the coil and the fluid sensors. We ascribe these small discrepancies to the mesh size which is larger in the 3D setting than in the 2D one. In summary, the agreement between the two sets of results is very good and validates a posteriori our 3D model for the solenoid system.

Let us now describe the results in the ferrohydrodynamic case when the magnetic force is active. Snapshots of the magnetic, velocity and temperature fields when the Kelvin force is activated are shown in figures (4.5) and (4.6). The steady-state is reached at $t = 24000\ s$. The 3D magnetic, velocity, and temperature fields show a qualitative agreement with the 2D fields. However, the quantitative error on the maximum temperature of the coil is about 4%, and the maximum velocity error is 33%. Refining the mesh for the 3D computations does not improve the comparison and leads to the same velocity and temperature distributions presented in (4.5). The agreement is rather

poor: the problem appears to be due to the use of the PDE tool of COMSOL Multiphysics (see next part).

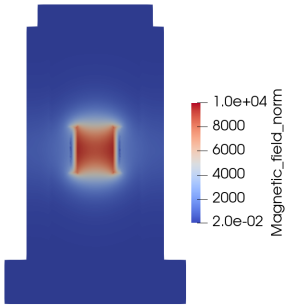


(a) Magnetic field intensity at $t = 24000\ s$

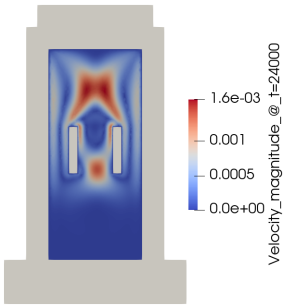


(b) Velocity magnitude at $t = 24000\ s$

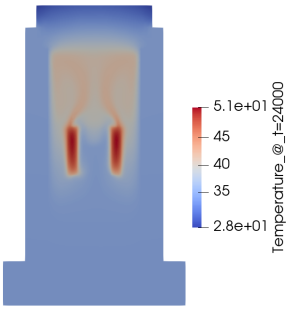


(c) Temperature at $t = 24000\ s$

Figure 4.5: Color maps of the magnetic field (in $\mathrm{A.m^{-1}}$), velocity magnitude (in $\mathrm{m.s^{-1}}$), and temperature (in $^\circ\mathrm{C}$) when the magnetic force is active in the 3D configuration.

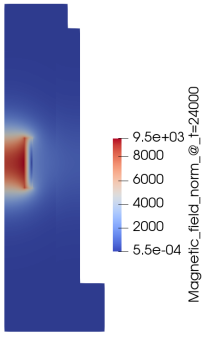


(a) Magnetic field intensity at $t = 24000\ s$

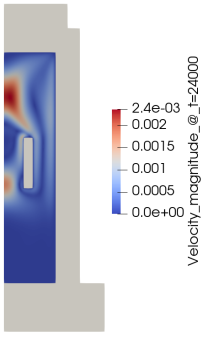


(b) Velocity magnitude at $t = 24000\ s$

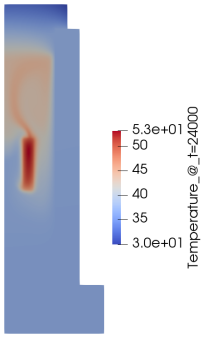


(c) Temperature at $t = 24000\ s$

Figure 4.6: Color maps of the magnetic field (in $\mathrm{A.m^{-1}}$), velocity magnitude (in $\mathrm{m.s^{-1}}$), and temperature (in $^\circ\mathrm{C}$) when the magnetic force is active in the 2D axisymmetric setting. The symmetry axis ($Oz$) is on the left.

### PDE mathematical tool

The elements used for the calculation of the magnetic field in 3D configuration are vector elements called edge elements. The order of the shape function for an edge element varies according to the different directions. For instance, the tangential component of the shape function $S_{jk}$ along edge $jk$ and any direction parallel to edge $jk$ is constant (order 0), while its perpendicular components are described by a linear function (order 1). With Comsol, these elements do not give access to the second derivatives of the calculated variables. Thus in 3D modeling, the second derivative of the magnetic field components that is necessary for the force calculation is equal to zero. To overcome this problem, a PDE tool (see COMSOL Reference Manual) is created to translate the magnetic field components into Lagrangian elements, thus allowing access to the second deriva-

tives of the **H** field.
Note that the magnetic flux density is connected to the magnetic vector potential **A** through:

$$\mathbf{B} = \boldsymbol{\nabla} \times \mathbf{A}, \qquad \mathbf{B} = \mu \mathbf{H} \tag{4.1}$$

According to (4.1), the computation of the first derivative of the magnetic field ($\partial \mathbf{H}$) present in (3.24) needs an evaluation of the second derivative of the magnetic vector potential ($\partial^2 \mathbf{A}$). It seems that the evaluation of $\partial^2 \mathbf{A}$ with the PDE leads to errors in **H** that have a great impact on the velocity and temperature fields. Therefore, the computation of the associated magnetic force may lead to inconsistent distributions of velocity and temperature. Thus, we propose another modeling in the following.

**Solution for the ferrohydrodynamic case**

As explained in the previous part, we encounter a problem with the computation of the magnetic body force in the 3D modeling when considering the Kelvin body force. An alternative solution to this problem is to consider another expression of the magnetic force that does not undergo the second derivative of the magnetic vector potential. Therefore, we take advantage of the alternative expression of the so-called Helmholtz magnetic force in which the square of the magnetic field is outside of the gradient term as shown in equation (3.29). Consequently, we do not employ the PDE tool to calculate the derivative of the magnetic field.

We adapt the mesh in the 3D model with extra-fine meshes in the fluid, extremely fine in the solenoid, and refined fluid-solenoid contacts [see figure ((4.1)b)]. The time step is automatically adapted and varies upon the range [$0.02\,\mathrm{s}$ - $0.5\,\mathrm{s}$]. The computation time is $27\,\mathrm{h}\,6\,\mathrm{min}\,55\,\mathrm{s}$ compared to $21\,\mathrm{min}\,55\,\mathrm{s}$ in the 2D computation. The calculation is run on a PC Intel(R) Xeon(R) W-2125 CPU @ 4.00GHZ using 4 cores over 10 from its overall capacity.
Snapshots of the magnetic, velocity, and temperature fields when the Helmholtz force is activated are shown in figures (4.7) and (4.8). The steady-state is reached at $t = 24000\ s$. The distributions of the magnetic field, velocity, and temperature are now in good qualitative and quantitative agreement for both 3D and 2D axisymmetric settings. The maximum velocity error is estimated to be $8\%$. A finer mesh in the 3D model could decrease this maximum velocity error.

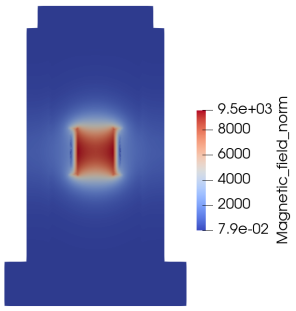


(a) Magnetic field intensity at $t = 24000\ s$

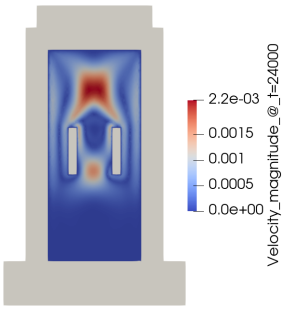


(b) Velocity magnitude at $t = 24000\ s$

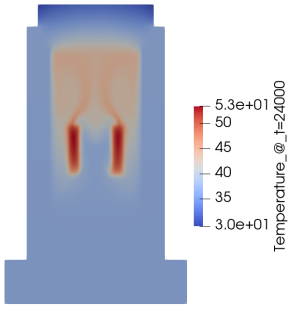


(c) Temperature at $t = 24000\ s$

Figure 4.7: Color maps of the magnetic field (in $\mathrm{A.m^{-1}}$), velocity magnitude (in $\mathrm{m.s^{-1}}$), and temperature (in $^\circ\mathrm{C}$) when the magnetic force is active in the 3D configuration.

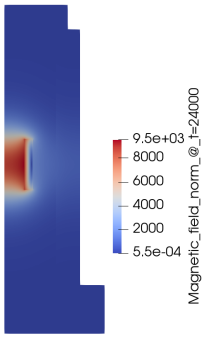


(a) Magnetic field intensity at $t = 24000\ s$

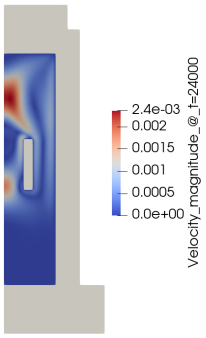


(b) Velocity magnitude at $t = 24000\ s$

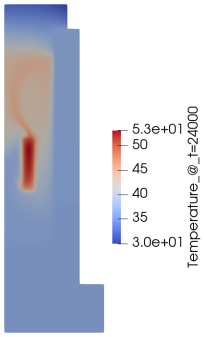


(c) Temperature at $t = 24000\ s$

Figure 4.8: Color maps of the magnetic field (in $\mathrm{A.m^{-1}}$), velocity magnitude (in $\mathrm{m.s^{-1}}$), and temperature (in $^{\circ}\mathrm{C}$) when the magnetic force is active in the 2D axisymmetric approach. The symmetry axis ($Oz$) is on the left.

**Conclusive remarks**

A first 3D study is performed with the solenoid model by testing both hydrodynamic and ferrohydrodynamic cases. A good agreement is found for the hydrodynamic case when comparing the velocity and temperature fields with those of the 2D axisymmetric setting. However, the calculation ran in the ferrohydrodynamic case with the magnetic Kelvin force leads to errors on the magnetic field that can affect the velocity and temperature fields. The computation of the magnetic Kelvin force in COMSOL Multiphysics needs to evaluate the second derivative of the magnetic vector potential ($\partial^2\mathbf{A}$) by the PDE tool. This evaluation yields errors in the magnetic field $\mathbf{H}$ and the discrepancies appear in the compared results. Using the Helmholtz model for the magnetic force rather than the Kelvin model avoids the evaluation of the first derivative of $\mathbf{H}$ and makes unnecessary the use of PDE tool.

## 4.2 2D axisymmetric modeling of a "transformer"

One of the most important industrial applications that could incorporate ferrofluids as a coolant to reduce excessive heating of electric components is the power transformer. Initially, the latter is often cooled by mineral oil, whose main drawbacks are its harmful biological effects and its progressive disappearance. Tests with vegetable oil associated with ferromagnetic nanoparticles allow us to consider temperature decreases of the windings when this kind of suspension is submitted to a magnetic field. In this context, we model a simplified version of a $40\ \mathrm{kVA}$ single-phase power transformer, of $0.46\,\mathrm{m}$ height, and in a 2D axisymmetric configuration. The objective is to verify the role of magnetic liquids in the cooling process of power transformers and to study some thermophysical properties of these magnetic suspensions to understand their behavior in the presence of the Helmholtz magnetic force.
Table (4.1) shows the electrical characteristics of the power transformer modeled in this study.

| | Voltage (V) | Current (A) | coil number |
|---|---|---|---|
| Primary winding | 20000 | 2 | 10000 |
| Secondary winding | 400 | 100 | 200 |

Table 4.1: $40\ \mathrm{kVA}$ power transformer model characteristics.

We consider the simplified structure of the power transformer model presented in figure ((4.9)a) in order to focus first on a 2D-axisymmetric geometry. In such a case, the numerical model proposed in the previous chapter can still be used.

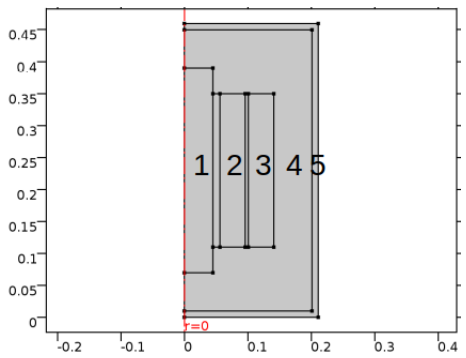


(a) 2D axisymmetric model in $(r, z)$ coordinates.

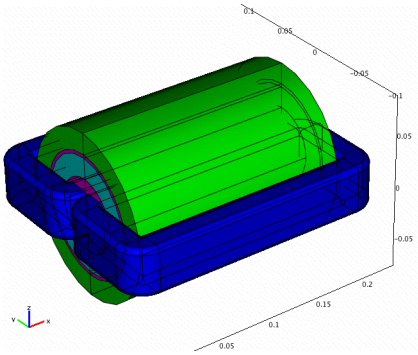

(b) Actual structure for a 3D power transformer: windings and core [86].

Figure 4.9: $40\ \mathrm{kVA}$ power transformer model.

The numbers assigned to the geometry elements in the representative scheme of figure ((4.9)a) refer to the constitutive elements in the transformer structure:

1. The ferromagnetic core made of iron with relative magnetic permeability $\mu_r = 4000$ ;
2. The secondary winding made of copper with nominal current density $j_0 = -2\,\mathrm{A.mm^{-2}}$;
3. The primary winding made of copper with nominal current density $j_0 = 2\,\mathrm{A.mm^{-2}}$;
4. The ferrofluid (Midel vegetable oil $Midel\ eN\ 1215$ + magnetite nanoparticles $Fe_2O_3$), $\phi = 1\%$;
5. The tank made of steel ($\mu_r = 100$).

A small gap of $5\,\mathrm{mm}$ is considered to allow the circulation of ferrofluid between the secondary winding and the ferromagnetic core. As explained before, we aim first to have a 2D-axisymmetric approach for the $40\ \mathrm{kVA}$ model. In the next step, we compare the 2D-axisymmetric model to a 3D approach. Thus, we do not directly consider the transformer model in its 3D structure of the figure ((4.9)b). We simulate only the inner part of the ferromagnetic core as seen in figure ((4.9)b), without considering the non-axisymmetric parts of the core. The thermophysical properties for the material domains are presented in table (4.2). The dynamic viscosity of the regular oil is calculated using equation (3.1).

| | Copper | Steel | Iron | Regular oil | Ferrofluid |
|---|---|---|---|---|---|
| Density ($\mathrm{kg.m^{-3}}$) | 8933 | 7850 | 7870 | 922 | 965 |
| Heat capacity ($\mathrm{J.kg^{-1}K^{-1}}$) | 385 | 475 | 447 | 1970 | 1898 |
| Therm. cond. ($\mathrm{W.m^{-1}K^{-1}}$) | 401 | 44.5 | 80 | 0.166 | 0.171 |
| Dynamic viscosity (Pa.s) | - | - | - | $E\exp(\frac{F}{T})$ | 0.065 |

Table 4.2: Thermophysical properties for the $40$ kVA transformer model materials.

### 4.2.1 Boundary conditions

At the boundaries of the model (see black lines on figure ((4.10)a)), the boundary condition for the magnetic problem $\mathbf{A} \times \mathbf{n} = \mathbf{0}$ is enforced, where $\mathbf{A}$ is the magnetic vector potential.

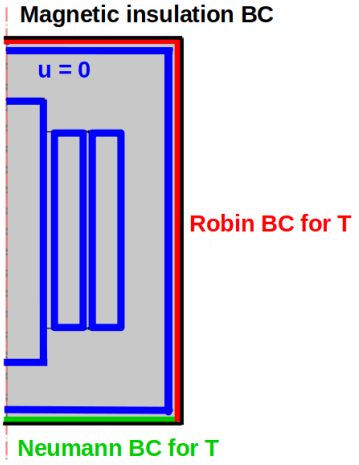


(a) Geometric notations and boundary conditions for fluid, temperature and magnetic field.

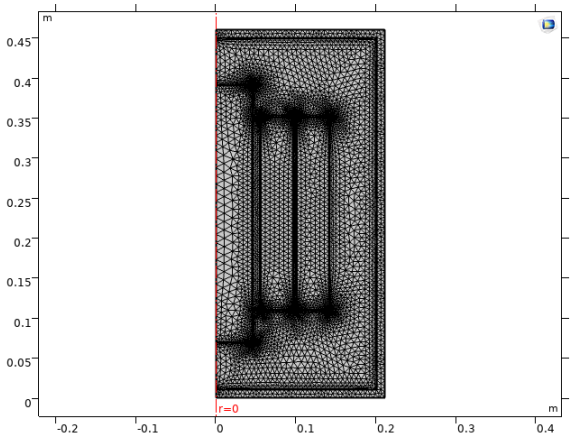


(b) Meridian mesh in the (r,z) plane.

Figure 4.10: Schematic sketch for the 2D axisymmetric model in COMSOL Multiphysics.

The non-slip boundary condition $\mathbf{u} = \mathbf{0}$ is applied at the border of the fluid domain (see blue lines on figure ((4.10)a)). The air convection at the top and on the lateral wall of the steel tank is modeled by using a Robin boundary condition for the temperature:

$$-\lambda \nabla T \cdot \mathbf{n} = h(T - T_{ext}), \tag{4.2}$$

where $h$ is the convection coefficient, and $\mathbf{n}$ is the outer unit normal vector (see red lines on figure ((4.10)a)). The homogeneous Neumann boundary condition $\partial_z T = 0$ is enforced at the bottom of the tank (see green line on figure ((4.10)a)). The initial conditions are $\mathbf{u} = \mathbf{0}$, $\mathbf{A} = \mathbf{0}$ and $T = T_{\text{ext}}$.

### 4.2.2 Finite element mesh

We choose a simple, unstructured triangular mesh for the model. The mesh is automatically created and adapted for the model's physics settings. The mesh in the ferrofluid domain is ranging

from $2.11 \times 10^{-4}\,\mathrm{m}$ to $7.39 \times 10^{-3}\,\mathrm{m}$. A triangular mesh is chosen for the windings and the core domains, ranging from $1.38 \times 10^{-4}\,\mathrm{m}$ to $2.44 \times 10^{-2}\,\mathrm{m}$. The ferrofluid contacts with the solid domains are fine, going from $1.38 \times 10^{-4}\,\mathrm{m}$ to $7.39 \times 10^{-3}\,\mathrm{m}$. The meridian mesh shown in figure ((4.10)b) contains $10740$ elements. The time step is automatically adapted and varies upon the range $[0.01\,\mathrm{s}\ -\ 0.5\,\mathrm{s}]$.
Let us discuss again the stability of the numerical scheme using the CFL condition ($u\frac{\Delta t}{\Delta x} < \frac{1}{2}$). To verify whether the time step taken by the solver respects the time condition resulting from the CFL condition, we use the maximum velocity $u = 2.8 \times 10^{-2}\,\mathrm{m\,s^{-1}}$ on the $Oz$-axis where the mesh is $\Delta x = 2.44 \times 10^{-2}\,\mathrm{m}$. We find that $\Delta t < 0.5(\frac{\Delta x}{u}) \simeq 0.5\,\mathrm{s}$ which is compatible with the time range used by the code. In such coupling problems, if we fix the time step to a lower value ($\Delta t < 0.05\,\mathrm{s}$), the simulation will take a longer time to be completed.

### 4.2.3 Selection of the heat transfer coefficient

The transformer is usually placed in the ambient air. Natural convection is established due to the temperature difference between the tank and the environment. As a result, the heat exchange coefficient $h$ ranges between 5 and 25 $\mathrm{W.m^{-2}K^{-1}}$.
In order to optimize the heat removal process from the system, the transformers are often equipped with fins (see figure ((4.11)a)), which give the air a larger convective exchange surface between the tank to be cooled and the environment. The use of these fins multiplies the heat exchange coefficient $h$ by a factor of 20 (from 25 $\mathrm{W.m^{-2}K^{-1}}$ to 500 $\mathrm{W.m^{-2}K^{-1}}$), see figure ((4.11)b).
For our model, we choose a coefficient $h = 150$ $\mathrm{W.m^{-2}K^{-1}}$ simulating the presence of cooling fins and promoting the free convective exchange of the tank-air heat.

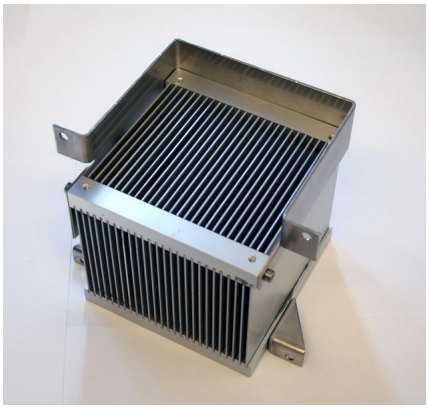

(a) Example of cooling fins.

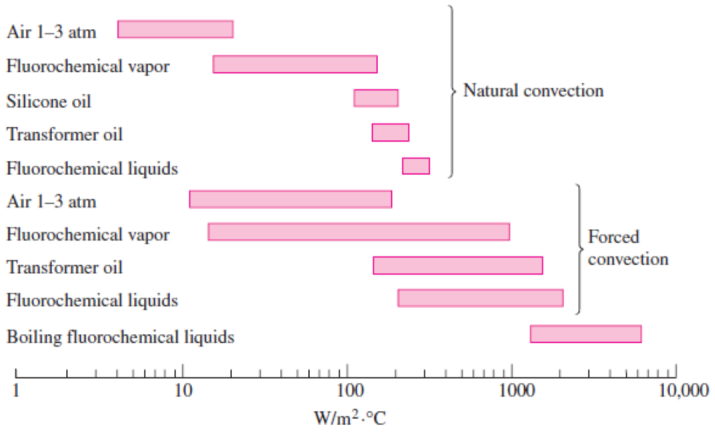


(b) Variation of the heat transfer coefficient with respect to the application [96].

Figure 4.11: Heat transfer coefficient selection.

### 4.2.4 Numerical results

Numerical simulations have been in the first case performed when the cooling liquid is the regular transformer oil, then in the second case with ferrofluid, in order to determine the changes

induced by this choice and to evaluate the temperature gain related to the phenomenon of thermomagnetic convection. We compare the temperature curves obtained at the middle of both inner and outer windings as a function of time (see figure (4.12)). We choose to evaluate the temperature at the middle points of the conductors because we think that the hot spot temperature is located near the center of the windings. The thermal steady-state is reached after about 3 hours ($10\,000\,\mathrm{s}$).
We notice a faster evolution in the temperature of the primary external conductor with ferrofluid rather than with regular oil, during $6000\,\mathrm{s}$ ($1\,\mathrm{h}\ 40\,\mathrm{min}$) (see figure ((4.12)a)). At $t = 10\,000\,\mathrm{s}$, the temperature curve of the conventional oil rises above the one obtained with ferrofluid, with a temperature difference of $1.8\,^{\circ}\mathrm{C}$. The temperature of the primary winding when using ferrofluid ($57.5\,^{\circ}\mathrm{C}$) is lower than the one obtained with regular oil ($59.3\,^{\circ}\mathrm{C}$).
The coolant material properties are changed since the conventional oil is replaced with the ferrofluid. The magnetic field is simultaneously applied. Thus we expect that a thermomagnetic convection occurs inside the tank. It appears that the cumulated effect of these two factors in the study has an influence on the maximum temperature of the primary winding.

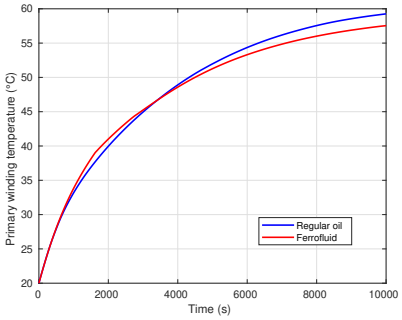


(a) Primary winding.

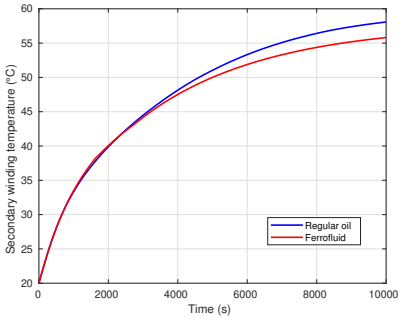


(b) Secondary winding.

Figure 4.12: Temperature evolution ($^{\circ}\mathrm{C}$) versus time ($\mathrm{s}$).

Let us now observe the temperature evolution at the middle of the secondary internal conductor ((4.12)b). We see an almost identical evolution of the temperature curves obtained with regular oil or ferrofluid at the transient regime. At large times, the temperature with the ferrofluid ($55.8\,^{\circ}\mathrm{C}$) is much lower than the one obtained with the regular oil ($58.1\,^{\circ}\mathrm{C}$). This temperature difference of $2.3\,^{\circ}\mathrm{C}$ shows that the secondary winding is well cooled compared to the primary winding, revealing a more interesting temperature decrease. It seems that changing material properties of the coolant and the created thermomagnetic convection play here a significant role in cooling of the secondary winding.

### Velocity and temperature distributions

The analysis of the temperature distributions corresponding to the presence of each type of fluid is important. It allows the detection of the hottest areas around the windings. Similarly, the study of velocity fields is essential to understand the motion of the magnetic fluid during its heating. We can then quantify the influence of the thermomagnetic convection on the velocity field in the presence of a ferrofluid.
Figures (4.13) and (4.14) show the distributions of the velocity and temperature fields at $t = 10\,000\,\mathrm{s}$ for both oil and ferrofluid cases.


(a) Regular oil. (b) Ferrofluid ($\phi = 1\%$).

Figure 4.13: Distribution of the velocity magnitude (in $\mathrm{m\,s^{-1}}$) at $t = 10\,000\,\mathrm{s}$.

New convection cells are observed in the case with ferrofluid, above and below the windings (see figure ((4.13)b)). In this figure, the maximum velocity magnitude reached at the steady-state is nevertheless lower (decrease by $32\%$ comparing to the oil case) when the thermomagnetic convection occurs. This decrease in the maximum velocity can be explained by the difference in the maximum temperature: with magnetic oil, the temperature reached is $58\,^{\circ}\mathrm{C}$ at $t = 10\,000\,\mathrm{s}$, whereas $60\,^{\circ}\mathrm{C}$ is obtained with regular oil (see figures ((4.14)a,b)). Thus, a more intense temperature gradient is present in the conventional oil and may accelerate its motion on the axis of the cavity in the upper part.


(a) Regular oil. (b) Ferrofluid ($\phi = 1\%$).

Figure 4.14: Temperature distributions (in $^{\circ}\mathrm{C}$) at $t = 10\,000\,\mathrm{s}$.

A decrease by $2\,^{\circ}\mathrm{C}$ in the maximum temperature is recorded when the magnetic fluid replaces the conventional oil. Fluid circulations appear at the bottom of the windings in the presence of the magnetic fluid (figure ((4.13)b)), and modify the heat diffusion inside the tank. Consequently, the cooling process is improved. The effect resulted from changing the material properties of the solution and considering the thermomagnetic convection is beneficial in the cooling process.

### Influence of the tank magnetic permeability

In this section, we consider the impact of the magnetic permeability of the tank, made of steel, on the cooling performance. Such parameter directly influences the magnetic field distribution (magnetic flux leakage in the transformer application) and may modify the thermomagnetic convection. Several simulations are performed with different values of the relative permeability of the steel $\mu_r$ considering the latter as a ferromagnetic material. Figure (4.15) shows the temporal evolution of the temperature of the primary winding according to the values of $\mu_r$.

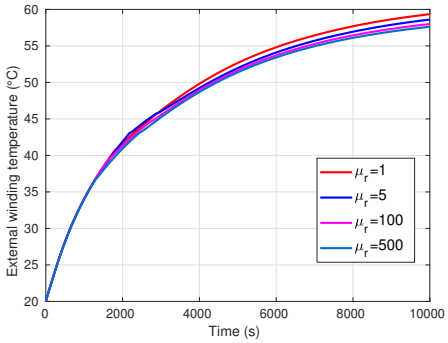


Figure 4.15: Time evolution of the external conductor temperature for several magnetic permeabilities of steel.

As observed in figure (4.15), by using ferromagnetic materials such as steel, the thermomagnetic convection is more intense within the liquid as $\mu_r$ increases. Thus, a decrease in the temperature of the hottest point of the primary winding can be obtained with increased permeability of the steel tank in the range from $\mu_r = 1$ to $\mu_r = 500$.

Figures (4.16) and (4.17) show the magnetic flux density, magnetic field, velocity and temperature distributions when the steel magnetic permeability changes from $\mu_r = 1$ to $\mu_r = 100$. The analysis of the velocity field profiles and the magnetic flux density confirms our results. With a non-magnetic tank ($\mu_r = 1$), the induction field lines flow through the iron core at the interior part of the tank. We see fewer magnetic flux lines channeling the exterior part of the tank (see figure ((4.16)a)). We also observe a small velocity in the ferrofluid domain (see figure ((4.16)b)), and the effect of thermomagnetic convection remains modest (see the decrease of the maximum temperature in figure ((4.16)d)).

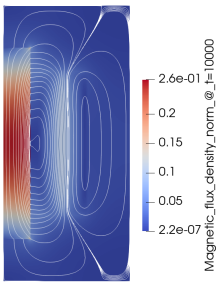


(a) Magnetic flux density (in T).

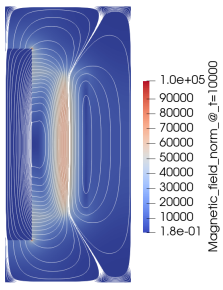


(b) Magnetic field magnitude (in $\mathrm{A.m^{-1}}$).

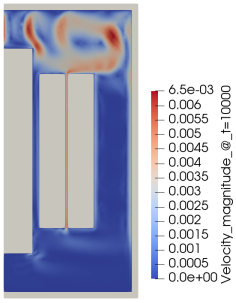


(c) Velocity magnitude (in $\mathrm{m.s^{-1}}$).

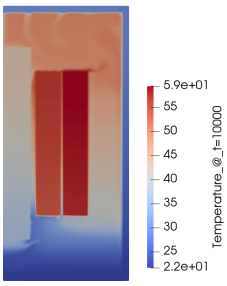


(d) Temperature (in °C).

Figure 4.16: Magnetic flux density, magnetic field and velocity magnitudes, and temperature distributions for a magnetic permeability $\mu_r = 1$ at $t = 10\,000\,\mathrm{s}$.

Once the ferromagnetic steel is used ($\mu_r = 100$), the magnetic fluxes created by the two coils are canalized either by the iron core or by the steel tank (see figure ((4.17)a)). We see more magnetic flux lines channeling the tank thickness.

Concerning the magnetic field distribution, we are more interested in the magnetic field that is exerted in the fluid domain, because the magnetic body force is influenced by the intensity of this magnetic field. Figure ((4.17)b) shows a concentrated magnetic field in the gap between the windings and a negligible magnetic field in the tank thickness. In contrast, figure ((4.16)b) presents a weaker magnetic field in the gap compared to ((4.17)b). Consequently, the magnetic force (the Helmholtz one is computed here) is maximized in the gap of the figure ((4.17)b) since it is proportional to the square of the magnetic field magnitude. An intense thermomagnetic convection is produced (see figure ((4.17)c)), and the velocity of the ferrofluid above the core is roughly three times higher compared to the case when $\mu_r = 1$ (enhancement by $66\%$ in figure ((4.17)b)), which improves the cooling process.

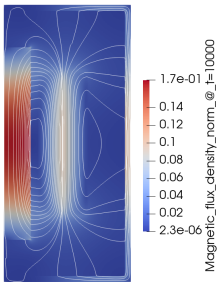


(a) Magnetic flux density (in T).

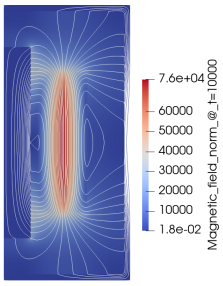


(b) Magnetic field magnitude (in $\mathrm{A.m^{-1}}$).

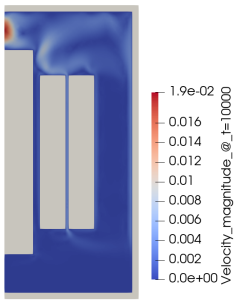


(c) Velocity magnitude (in $\mathrm{m.s^{-1}}$).

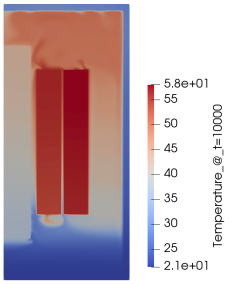


(d) Temperature (in °C).

Figure 4.17: Magnetic flux density, magnetic field and velocity magnitudes, and temperature distributions for a "steel" magnetic permeability $\mu_r = 100$ at $t = 10\,000\,\mathrm{s}$.

The evolution of the external winding temperature as a function of the relative magnetic permeability of steel $\mu_r$ is shown in figure (4.18). The temperature variation in the windings follows a decreasing curve from $59.4\,°\mathrm{C}$ for $\mu_r = 1$ to $57.6\,°\mathrm{C}$ for $\mu_r = 500$.

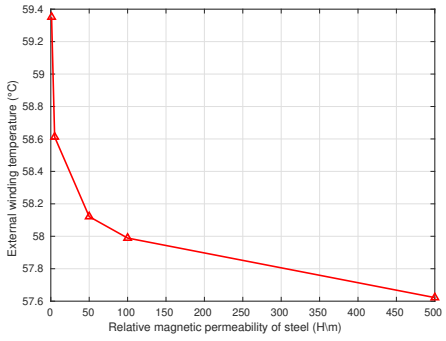


Figure 4.18: Variation of the external conductor temperature versus the relative magnetic permeability of steel.

Subsequently, we assess the evolution of the magnetic field $H$ in the ferrofluid domain with the variation of the permeability of the steel tank. Ampere's theorem states that the circulation of the magnetic field generated by a current distribution along a closed circuit (see red spire in figure

((4.19)b)) is equal to the algebraic sum of the currents flowing through the surface defined by the oriented circuit:

$$\oint \overrightarrow{H}.\overrightarrow{dl} = NI \tag{4.3}$$

where $\overrightarrow{dl}$ is the infinitesimal element of displacement along the closed circuit, $N$ the number of turns, and $I$ the current (in A) flowing through them.
In our model, the magnetic field lines circulate between the coils in the magnetic liquid and through the steel tank, and therefore Ampere's law will be of the following form:

$$\oint \overrightarrow{H}.\overrightarrow{dl} = \int_{ff} \overrightarrow{H}.\overrightarrow{dl} + \int_{st} \overrightarrow{H}.\overrightarrow{dl} = NI \tag{4.4}$$

Increasing the relative permeability $\mu_r$ of the tank steel leads to a decrease of the field $H_{st}$ in the steel and thus to an increase of the value of the field $H_{ff}$ in the ferrofluid so that the relation (4.4) remains verified. Figure ((4.19)a) illustrates this variation of the magnetic field as a function of altitude $Z$, along a vertical line bounded by the upper and lower ends of the tank (see figure ((4.19)b)).

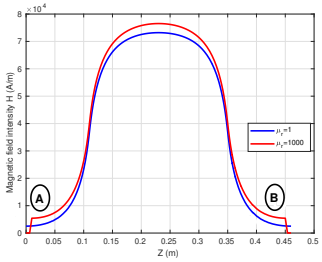


(a) Magnetic field intensity versus altitude $Z$.

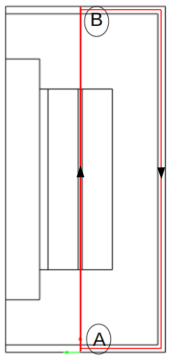


(b) Vertical section line.

Figure 4.19: Evolution of the magnetic field intensity for different steel magnetic permeabilities.

We notice that the magnetic field $H$ reaches a maximum value of $7.65 \times 10^4\,\mathrm{A\,m^{-1}}$ for $\mu_r = 1000$, on the point located in the middle of the gap. Similarly, high values of the magnetic field are observed on the points located at the fluid-tank boundaries. Then, we can say that the field $H_{ff}$ increases with the steel relative permeability $\mu_r$ of the tank. As a result, intensified magnetic forces may appear and contribute to the enhancement of the heat exchange.

**Influence of the gap thickness**

Another essential factor to be studied in the transformer model is the gap thickness separating the two inner and outer windings. As the fluid that flows between the two coils can easily transport heat, we need to know if increasing this thickness plays a positive role in the cooling process for each type of fluid, conventional and magnetic. The simulations performed lead to the time evolution curves of the temperature at the hottest point of the primary winding cooled with ferrofluid shown in figure (4.20).

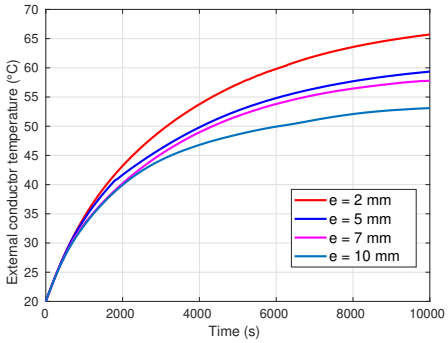


Figure 4.20: Time evolution of the external conductor temperature for various gap thicknesses with ferrofluid.

A monotonous decrease in the temperature is observed, going from $65.7\,°\mathrm{C}$ for a thickness $e = 2mm$ to $53.1\,°\mathrm{C}$ for $e = 10mm$, as shown in figure (4.21). This can be directly interpreted by an increase of the ferrofluid flow circulating between the windings and promoting heat removal. We also show on figure (4.21) that for a vegetable oil, the temperature of the external conductor decreases from $70.9\,°\mathrm{C}$ for $e = 2mm$ to $64.8\,°\mathrm{C}$ for $e = 5mm$ then remains constant at $64\,°\mathrm{C}$ for larger gaps. This saturation differs from the decreasing behavior observed with ferrofluid.

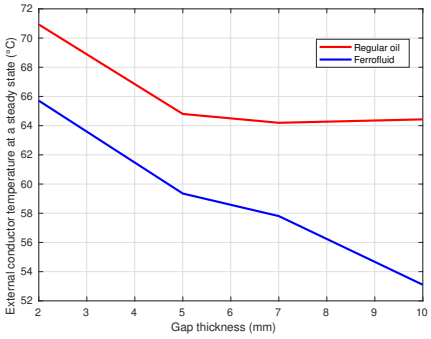


Figure 4.21: Variation of the external conductor temperature versus the gap thickness with respect to the fluid type.

Therefore, we can expect a more efficient cooling of the winding with the magnetic liquid when this gap thickness admits a significant value. Nevertheless, we have to keep in mind that this gap thickness also plays a major role in the flux leakage of a power transformer.

## 4.3 3D validation of the 40 kVA transformer model

We have performed a 2D-axisymmetric modeling for the solenoid setup to study the impact of the thermomagnetic convection on the heat transfer process. The 2D-axisymmetric model was validated against experimental measurements (see chapter 3, section 3.5.3). Our final objective is to consider more complex geometries of immersed power transformers in 3D configuration with this modeling method. We should verify first that the 3D modeling of the $40\ \mathrm{kVA}$ single-phase

power transformer yields the same results as those obtained with the 2D-axisymmetric model already analyzed.
In this part, we model the same $40\ \mathrm{kVA}$ power transformer simplified model but in a 3D configuration. This transformer has an axisymmetric structure with a ferromagnetic core simplified to a cylindrical rod of diameter $90\,\mathrm{mm}$ and height $320\,\mathrm{mm}$ placed in the center of the windings. A cylindrical steel tank surrounds the windings and the ferromagnetic core and serves as a container for the cooling liquid (vegetable oil or ferrofluid). Figure (4.22) shows the mesh of the 3D model.

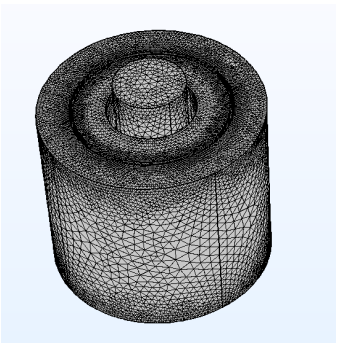

(a) Windings and cylindrical core mesh.

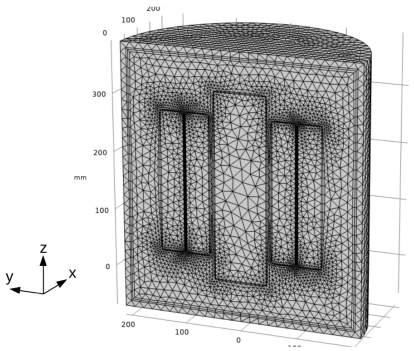


(b) Cross section of the total mesh.

Figure 4.22: 3D model mesh.

We choose a simple, unstructured tetrahedral mesh for the model. The mesh is automatically created and adapted for the model's physics settings. The number of elements associated with this mesh is $1103530$ elements. The time step is automatically adapted and varies upon the range $[0.01\,\mathrm{s}\ -\ 0.5\,\mathrm{s}]$. The recorded computation time is very long and equal to $9\,\mathrm{d}\ 5\,\mathrm{h}\ 25\,\mathrm{min}\ 5\,\mathrm{s}$. The thermophysical properties of the material domains are the same as the ones considered in the 2D axisymmetric modeling. The heat exchange coefficient is chosen as $h = 150\ \mathrm{W.m^{-2}K^{-1}}$, and the relative magnetic permeability of the steel tank is set to $\mu_r = 100$.

Our transformer model is first placed in a vegetable oil ($Midel\ eN\ 1215$) solution which thermophysical properties (dynamic viscosity, thermal conductivity, density, and heat capacity) are known. The nanoparticles being absent in the solution, the magnetic force is not modeled in the fluid domain. Therefore we compute an hydrodynamic case. Figure (4.23) shows the longitudinal ($y$) and the axial ($z$) components of the velocity field at $20\,000\,\mathrm{s}$.

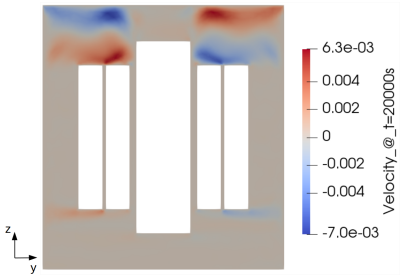


(a) $y$ component of the velocity field $v$ (in $\mathrm{m.s^{-1}}$).

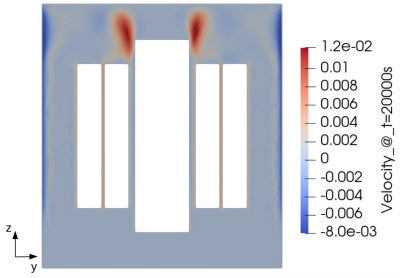


(b) $z$ component of the velocity field $w$ (in $\mathrm{m.s^{-1}}$).

Figure 4.23: Velocity field components at $20\,000\,\mathrm{s}$.

Let us compare these components of the velocity field with those obtained in the 2D-axisymmet -ric model, see figure ((4.24)(a,b)). We observe similar convection cells at the upper part of the tank with both radial and axial components of the velocity field. However, a recirculation above the core observed in the 2D-axisymmetric configuration is absent in the 3D configuration. We attribute this discrepancy to the mesh.

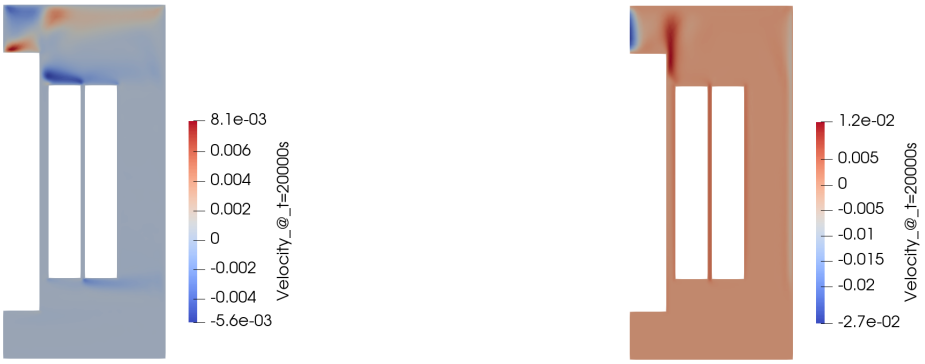


(a) Radial component of the velocity field $u_r$, symme-try axis at the left.

(b) Axial component of the velocity field $u_z$, symmetry axis at the left.

Figure 4.24: Velocity field components at $20\,000\,\mathrm{s}$.

Figure (4.25) presents the velocity magnitude and temperature distributions at $20\,000\,\mathrm{s}$ for the hydrodynamic case.

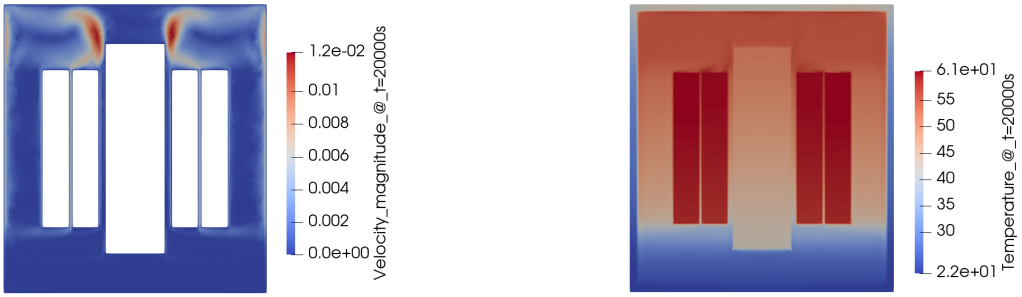


(a) Velocity magnitude (in $\mathrm{m.s^{-1}}$).

(b) Temperature (in °C).

Figure 4.25: Velocity magnitude and temperature fields at $20\,000\,\mathrm{s}$.

Let us compare these 3D results with those produced by the 2D-axisymmetric modeling. If we take the case of the transformer immersed in regular oil, the associated velocity field (see figure ((4.26)a)) is similar to the one obtained in figure ((4.25)a) except near the axis above the core. The same convection cell appears at the upper corner of the simplified ferromagnetic core with a velocity intensity of $12 \times 10^{-3}\,\mathrm{m\,s^{-1}}$. Simultaneously, the oil flow channeling the gap between the conductors has the same order of magnitude ($4 \times 10^{-3}\,\mathrm{m\,s^{-1}}$).

The temperature distribution obtained in figure ((4.25)b) is the same as the one reached with the 2D-axisymmetric model (see figure ((4.26)b)). The thermal plumes (see figure ((4.25)b)) at the top

of the secondary winding deviate near the ferromagnetic core. This deviation is due to the convection cells appearing at the corners of the core, which push the warmer fluid towards the top lid (see figure ((4.25)a)). The maximum temperature obtained in the primary winding is the same for both cases ($T = 61\,°\mathrm{C}$ with the 3D and 2D-axisymmetric modeling). Moreover, the temperature plume obtained shows qualitative and quantitative agreement (the maximum temperature difference is $2.3\%$) again with the calculation performed in [13, p. 146], see figure ((4.27)a) using $T_{ext} = 20\,°\mathrm{C}$ instead of $T_{ext} = 22\,°\mathrm{C}$.

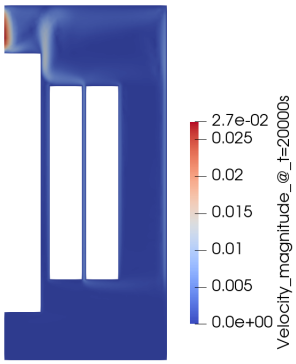


(a) Velocity magnitude (in $\mathrm{m.s^{-1}}$), symmetry axis at the left.

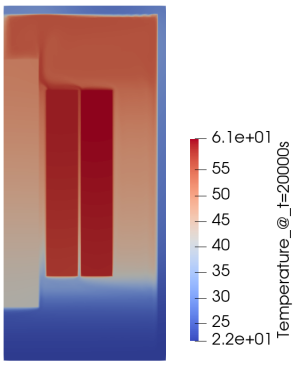


(b) Temperature (in °C), symmetry axis at the left.

Figure 4.26: Velocity magnitude and temperature fields at $20\,000\,\mathrm{s}$, 2D-axisymmetric model.

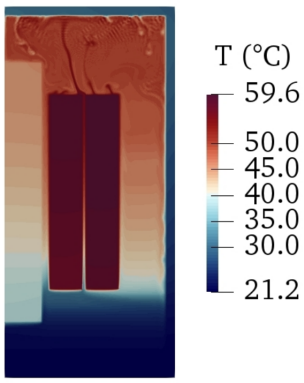


(a) Temperature (in °C) at $t = 20\,000\,\mathrm{s}$.

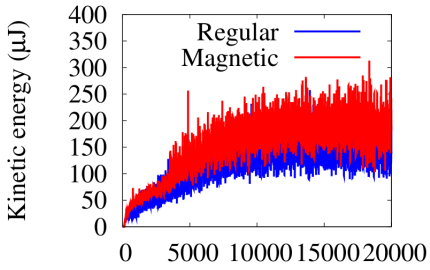


(b) Kinetic energy (in µJ).

Figure 4.27: Temperature field and kinetic energy of the oil in the hydrodynamic case [13].

The time evolution of the temperature for the points located at the middle of the ferromagnetic core, the primary and secondary windings, and on the surface of each of these components are shown in figure (4.28). These temperature curves show the agreement of the 2D axisymmetric and 3D modeling results again. If we compare the temperature curves obtained at the middle points of the conductors, the primary and the secondary windings reach approximately the same temperature (around $60\,°\mathrm{C}$) at the thermal steady-state in the hydrodynamic case (see figures ((4.28)a) and (4.12)). The transient regime of these curves is similar in both 2D-axisymmetric and 3D modeling.

These curves reveal that the primary conductor is slightly warmer compared to the secondary conductor. At steady-state, the temperature of the secondary coil reaches $60.3\,°\mathrm{C}$, while the primary reaches $60.5\,°\mathrm{C}$.

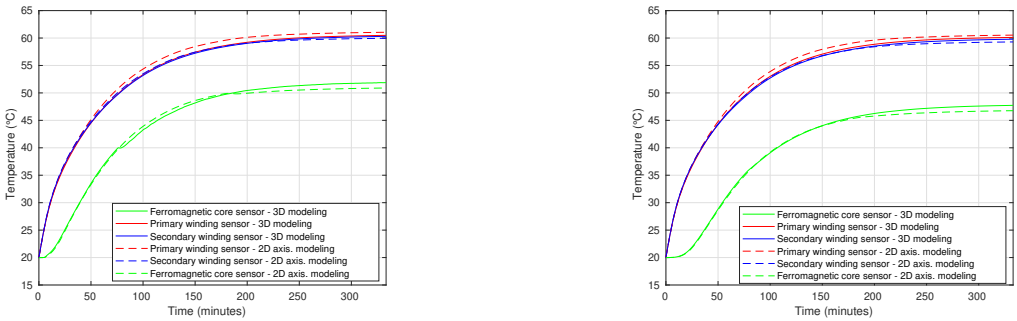


(a) Temperature (in °C) at the surface points.

(b) Temperature (in °C) at the middle points.

Figure 4.28: Time evolution for temperature of conductors and core over $20\,000\,\mathrm{s}$.

The temperature curves show the same evolution trend whether the recording point is located at the surface (see figure ((4.28)a)) or at the middle point (see figure ((4.28)b)). The temperature reached in the windings at the steady-state (after $20\,000\,\mathrm{s}$) is roughly the same (around $60.5\,°\mathrm{C}$). According to these temperature curves and the temperature distribution presented in figure ((4.25)b), the temperature is almost uniformly distributed in both conductors. In contrast, while the temperature is $51.9\,°\mathrm{C}$ at the surface of the ferromagnetic core, it reaches $47.7\,°\mathrm{C}$ at the middle of the core. However, the temperature in the ferromagnetic core $[47-52]°\mathrm{C}$ is lower than the temperature of the windings $[59.5-60.5]°\mathrm{C}$, as expected.

To compare our results with the ones previously obtained with the SFEMaNS code, figure (4.29) shows the time evolution for the vegetable oil kinetic energy and the average temperature of the system defined by:

$$E_{kinetic} = \int_{\Omega_{bf}} \frac{1}{2}\rho_{bf} u^2 dV, \qquad T_{av} = \left(\frac{1}{V}\int_{\Omega} T^2 dV\right)^{1/2} \tag{4.5}$$

where $\Omega_{bf}$ is the base fluid domain, $\rho_{bf}$ the base fluid density, $\Omega$ the system domain, and $V$ the total volume. The values of the kinetic energy reached at the steady-state for both 2D-axisymmetric and 3D cases are the same ($98\,\mu\mathrm{J}$) and similar to the ones presented in [13, p. 145], see figure ((4.27)b). However, in the transient regime, oscillations appear in the 2D axisymmetric setting from the beginning of this regime. These perturbations start a little later in the 3D case. These oscillations are probably due to the small scales produced by the thermal plumes. The average temperature of the system seems to grow smoothly due to a large time constant for both 2D-axisymmetric and 3D models, as seen in figure ((4.29)b). At the transient regime, the two curves are superimposed. At the thermal steady-state, the average temperature in the 3D model $45.7\,°\mathrm{C}$ is greater than the one obtained in the 2D-axisymmetric model $44.3\,°\mathrm{C}$. This is qualitatively similar.

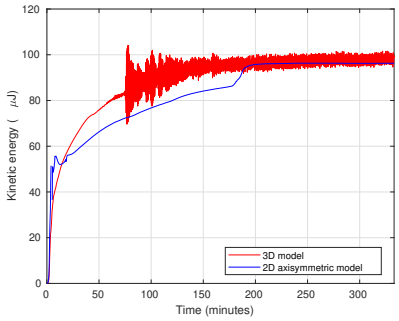


(a) Kinetic energy (in µJ), 3D computation.

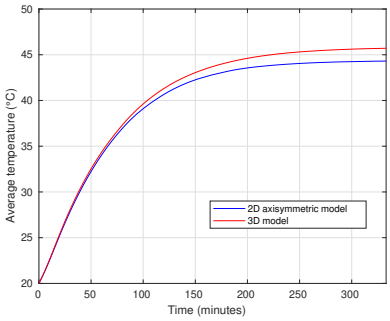


(b) Average temperature (in °C).

Figure 4.29: Comparison of the kinetic energy and the average temperature over $20\,000\,\mathrm{s}$.

To conclude this part, the numerical results obtained from the 3D modeling are globally validated against the 2D-axisymmetric results. The $40\,\mathrm{kVA}$ single-phase simplified power transformer model is confirmed with a small relative error on the maximum temperature of the windings $(0.8\%)$. In the following, we propose to model a more realistic power transformer that makes it mandatory to use 3D computations.

## 4.4 3 kVA Power transformer

This section aims to model a 3D structure of a power transformer $(3\,\mathrm{kVA})$ by considering the non-axisymmetric geometry of the ferromagnetic core. We realize a dimensioning for the 3D model and study the cooling performance using the finite element approach. A fluid-thermal-magnetic analysis is followed to quantify the heat transfer inside this device and study the thermomagnetic convection. Few studies on this subject have modeled a 3D power transformer to study the cooling performance associated with the use of a ferrofluid solution.

### 4.4.1 Transformer design

A $3\,\mathrm{kVA}$, 400/230 V non-axisymmetric core power transformer is designed. The characteristic length of the ferromagnetic core is defined by $L = 8.7\,\mathrm{cm}$ (see appendix B.1 for the calculation of $L$). The different dimensions of the core are shown in the annotated schematic sketch presented in figure (4.30). The filling coefficient of copper considered in this modeling is $k_b = 0.5$. The number of turns in the primary and secondary windings are respectively $N_p = 336$ and $N_s = 193$ (see appendix B.2). The nominal current density is first considered with $J_0 = 2\,\mathrm{A.mm^{-2}}$. The resistances of the two primary and secondary windings have the values $R_p = 1.04\,\Omega$ and $R_s = 0.25\,\Omega$ (see appendix B.3). In figure ((4.30)a), the red numbers denote respectively by 1 the primary winding of the transformer model and by 2 its secondary winding.

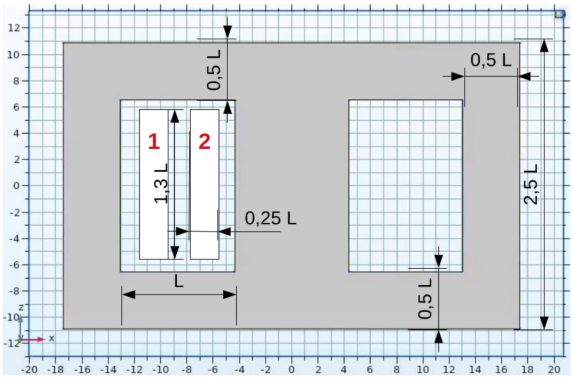


(a) Ferromagnetic core in $(x, z)$ plane.

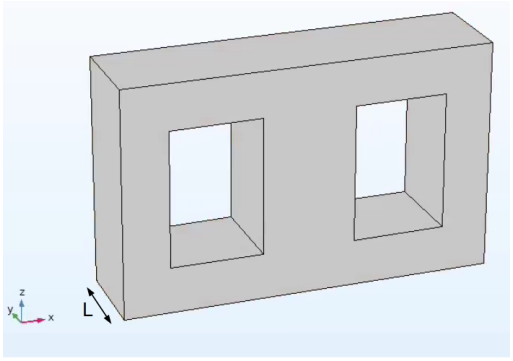


(b) Thickness of the ferromagnetic core in a 3D configuration.

Figure 4.30: Schematic sketch of a 3D non-axisymmetric core.

The inner winding is considered as the secondary coil in the model with a current density $J_2$. The outer winding is considered as the primary coil with $J_1$ the injected current density. This configuration is chosen for reasons of the positioning of the HV/LV conductors. The LV (low voltage) winding is, with few exceptions, always placed near the core and the HV (high voltage) outside. For reasons of dielectric insulation, the core being grounded, it is easier to control the insulation of the HV when it is outside. Indeed, the LV can then be close to the core.

### 4.4.2 Magnetic calculation

In order to perform a coupling calculation for our multiphysics problem, a magnetostatic calculation is needed in addition to the thermal and fluid calculation. Of course, actual power transformers do not work in DC, but with an alternative excitation. The objective of the next part is then first to obtain the actual magnetic field distribution in the ferrofluid with a transient study, and next to choose a DC current excitation that leads to "equivalent magnetic forces".

#### Time-dependent calculation with electrical circuit

The 3D single-phase power transformer model $(400/230)\ \mathrm{V}$ considered in the following works in alternative mode with frequency $f = 50\,\mathrm{Hz}$. We propose, therefore, to make first a time-dependent calculation for the evaluation of the magnetic current densities. A coupling calculation with an external electrical circuit is performed to achieve this objective. The primary winding is connected to the AC voltage source $V_{ac}$, while the secondary winding is connected to the load resistor $R_{load}$ as shown in figure ((4.31)b).

As explained before, we need to perform a time-dependent calculation of the magnetic field to evaluate the magnetic current densities in the conductors. These current densities $J_{s1}, J_{s2}$ require evaluating the primary and secondary RMS (Root Mean Square) currents (see appendix B.5). We consider the case of the $3\,\mathrm{kVA}$ transformer under nominal load with $R_{load} = 17.75\,\Omega$. The nominal RMS currents to be found in the windings are respectively $I_1 = 7.5\,\mathrm{A}$ and $I_2 = 13\,\mathrm{A}$ (see appendix B.4). The ferromagnetic core material is considered saturated (soft Iron without losses). The B(H)

curve of the ferromagnetic core material is given in figure ((4.31)a). The electrical circuit coupled to the magnetic time-dependent calculation is given in figure ((4.31)b).

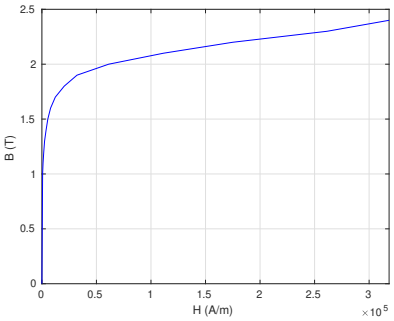


(a) B(H) curve for the soft Iron without losses.

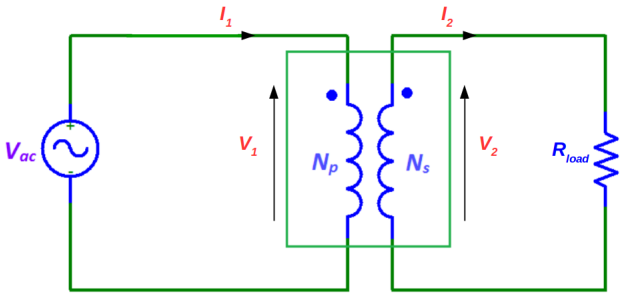


(b) Electrical circuit coupled to the time-dependent calculation, the coil resistances are included in the coil symbols.

Figure 4.31: B(H) curve of the material of the core (at left panel) and electrical circuit (at right panel).

The different parameters of the time calculation are shown in table (4.3). The calculation time is $34\,\mathrm{h}\ 36\,\mathrm{min}\ 10\,\mathrm{s}$. As explained before, we proceed to find the magnetic field in the air domain. When the transformer model is immersed in the fluid, the air domain will of course change to be the ferrofluid domain. In the following, the magnetic flux density $B$ in the middle of the central leg of the core and the magnetic field $H$ in the air will then be evaluated.

| Name | Expression | Description |
|---|---|---|
| $L$ | $8.7\,\mathrm{cm}$ | Characteristic dimension of the transformer |
| $f$ | $50\,\mathrm{Hz}$ | Frequency of supply voltage |
| $N_p$ | 336 | Number of turns in primary winding |
| $N_s$ | 193 | Number of turns in secondary winding |
| $R_{load}$ | $17.75\,\Omega$ | Load resistance |
| $V_{ac}$ | $565.69\,\mathrm{V}$ | Supply voltage |

Table 4.3: Input parameters of the time-dependent calculation.

**Results of the magnetic time-dependent calculation**

In a power transformer, a supply source ($V_{ac}$) feeds the primary winding bounds with a voltage denoted $V_1$. The current circulating in the primary winding ($I_1$) is time-dependent, and therefore a magnetic flux associated with the primary winding is created in the ferromagnetic core. This magnetic flux induces a secondary current in the secondary conductor ($I_2$) which is also time-dependent. Thus, we suggest investigating first the time evolution of the magnetic flux density $B_z$ then its distribution in the ferromagnetic core.

Figure ((4.32)(a,b)) shows respectively the time evolution of the magnetic flux density $B_z$ at the

transient and the steady-state regimes. The value of $B_z$ is calculated at the middle of the central leg in the ferromagnetic core. In the transient regime, the $B_z$ curve is a superposition of a sinusoidal function and a decreasing time function due to the "inrush" phenomena. $B_z$ keeps oscillating in time while decreasing to be finally averaged around zero at the steady-state.
The magnetic flux density $B$ is evaluated at time $t = 4.9905\,\mathrm{s}$ (steady-state) of the simulation when the $B_z$ curve reaches a maximum value (see figure ((4.32)b)). The section of $B$ in the $(x, z)$ plane is given in figure ((4.32)c).

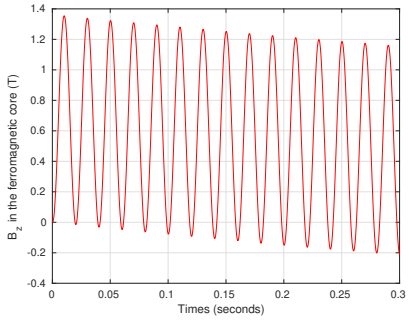


(a) $B_z$ (in T) versus time, transient regime.

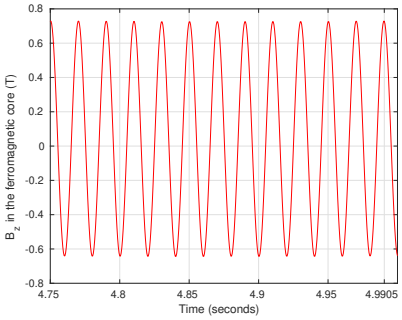


(b) $B_z$ (in T) versus time, steady-state regime.

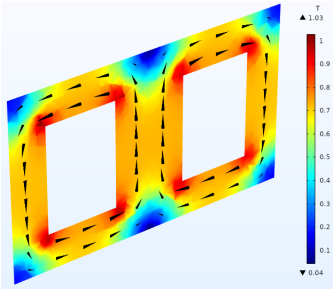

(c) Magnetic flux density and arrows in the ferromagnetic core, $t = 4.9905\,\mathrm{s}$..

Figure 4.32: Magnetic flux density distribution, time-dependent calculation.

We now verify that the magnetic flux density distribution is as expected. A normal distribution of the magnetic flux density is obtained when the value of this density in the central leg (denoted by $B_{leg}$) of the core is equal to its value in the external legs of the core (denoted by $B_{sides}$). We investigate thus the norm of these magnetic flux densities. The analysis of the distribution of the magnetic flux density $B$ in the section presented in figure ((4.32)c) shows that $B_{leg} = 0.684\,\mathrm{T}$ and $B_{sides} = 0.684\,\mathrm{T}$. The RMS value of the maximum of the magnetic flux density shown in this figure is $B_{eff} = 0.484\,\mathrm{T}$.

The norm of the magnetic flux density $B$ has been respectively evaluated on two horizontal and vertical lines $B_1$ and $B_2$, intersecting the ferromagnetic core, according to the scheme presented in figure ((4.33)a). The magnetic field component $H_z$ in the air parts is also computed along two lines $H_1$ and $H_2$, the first horizontal line crossing the core above the windings, and the second vertical line crossing the core at the level of the gap between the conductors (see figure ((4.33)b)). The curves of $B_{norm}$ along these two lines at $t = 4.9905\,\mathrm{s}$ are presented in figure (4.34(a,b)). We also present the magnetic field curves at $t = 4.9855\,\mathrm{s}$ in figure (4.34(c,d)), where the magnetic field in the air domain reaches a maximum.

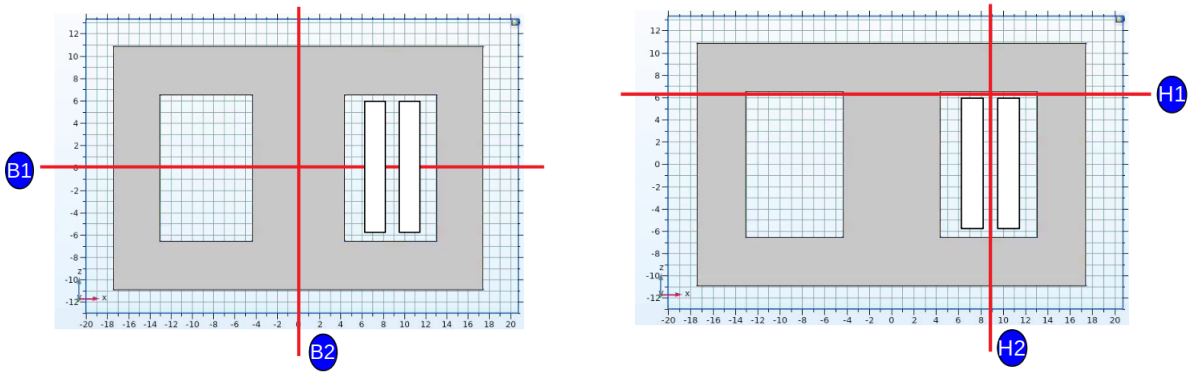


(a) Measurement lines of the magnetic flux density $B_1$ and $B_2$.

(b) Measurement lines of the magnetic field intensity $H_1$ and $H_2$.

Figure 4.33: Measurement lines.

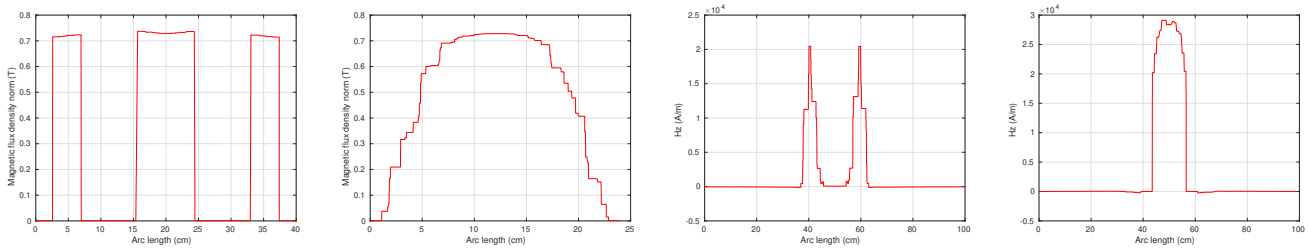


(a) Magnetic flux density (in T) along $B_1$.

(b) Magnetic flux density (in T) along $B_2$.

(c) Magnetic field magnitude (in $\mathrm{A.m^{-1}}$) along $H_1$.

(d) Magnetic field magnitude (in $\mathrm{A.m^{-1}}$) along $H_2$.

Figure 4.34: Magnetic flux density and magnetic field intensity curves.

The shape of $B_{norm}$ along the two lines is as expected and confirms the good distribution of the magnetic flux density in the time-dependent calculation. The maximum values obtained for $B$ seem to be coherent and confirm the distribution obtained previously ($B_{eff} = 0.484\,\mathrm{T}$).

The effective electrical quantities also seem to be coherent. The time evolutions of the induced voltages and currents in both windings are presented in figures (4.35) and (4.36). In these figures, $V_1$ and $V_2$ denote the voltages respectively at the bounds of the primary and the secondary windings, $I_1$ and $I_2$ the currents in the primary and the secondary windings. $V_{1max}$ and $V_{2max}$ are respectively the maximum values of the primary and the secondary windings evaluated from figure (4.35). We observe a phase shift between the currents of both primary and secondary windings, see figure ((4.36)c). We obtain in the primary circuit: $V_{1max} = 567.5\,\mathrm{V}$, $I_1 = 10.2\,\mathrm{A}$, $I_{1eff} = 7.2\,\mathrm{A}$ and $N_1 I_{1eff} = 2419.2\,\mathrm{A.t}$, and in the secondary circuit: $V_{2max} = 312\,\mathrm{V}$, $I_2 = 17.6\,\mathrm{A}$, $I_{2eff} = 12.4\,\mathrm{A}$ and $N_2 I_{2eff} = 2393.2\,\mathrm{A.t}$. Table (4.4) lists the RMS values for the electrical outputs of the time-dependent calculation.

| Output | RMS value |
|---|---|
| $I_{1eff}$ | 7.2 A |
| $N_1 I_{1eff}$ | 2419.2 A.t |
| $I_{2eff}$ | 12.4 A |
| $N_2 I_{2eff}$ | 2393.2 A.t |

Table 4.4: RMS values for the electrical outputs respectively in the primary (denoted by 1) and secondary windings (denoted by 2).

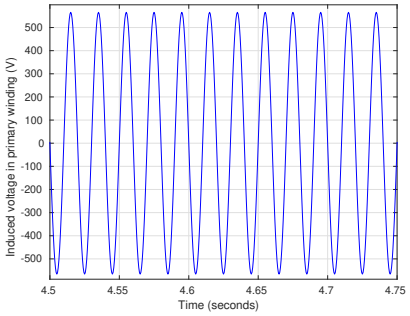


(a) Voltage $V_1$ versus time.

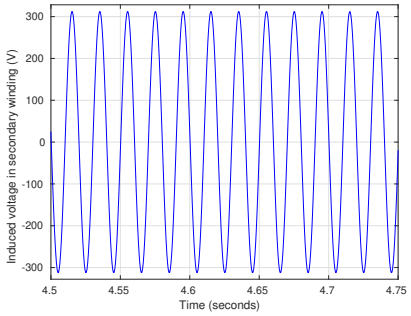


(b) Voltage $V_2$ versus time.

Figure 4.35: Voltages at both windings.

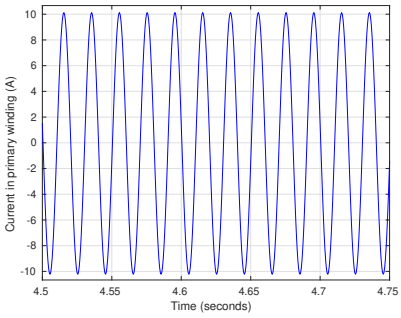


(a) Current $I_1$ versus time.

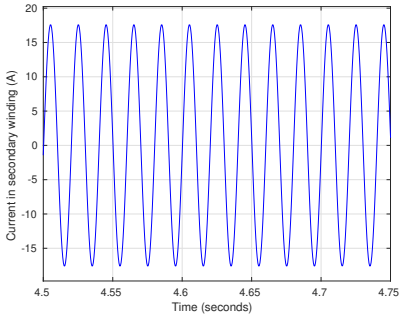


(b) Current $I_2$ versus time.

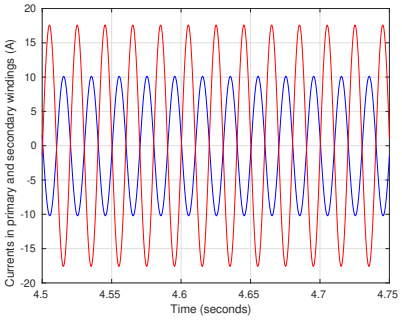


(c) Currents $I_1$ and $I_2$ versus time.

Figure 4.36: Currents in both windings.

As a conclusion for this part, we have performed a time-dependent calculation to evaluate the magnetic current densities in the coils of the power transformer model and the magnetic distribution in the core and the air. Such magnetic distribution will lead to the presence of magnetic forces. The next part aims to adapt the current excitations to obtain equivalent magnetic forces with the magnetostatic model. The magnetic flux density computed in the magnetostatic study and the associated magnetic field in the air will be compared to those obtained in the time-dependent calculation.

### Magnetostatic calculation

The objective in this part is to determine the current densities that should be injected into the inner and the outer coils of the transformer. These current densities are essential in the magnetostatic calculation. In the following, we propose four different methods to compute the current densities in the transformer's coils. We will investigate the magnetic flux density distribution in the ferromagnetic core and the magnetic field in the air domain. These distributions resulting from the magnetostatic calculation will be compared to the time-dependent calculation results for each of these methods. The idea is to obtain the same mean value of the magnetic force in the two simulations. We see from Helmholtz force expression that it comes to get the same RMS value for $H$ in the fluid.

The four methods proposed to achieve the magnetostatic calculation are:

1. **First approach**: The magnetic current densities to be injected in each conductor are calculated according to the $NI_{eff}$ values deduced from the time-dependent calculation. The cross-section of the primary and secondary windings being identical and equal to $S_b = 0.25L \times 1.3L = 2.46 \times 10^{-3}\,\mathrm{m}^2$, the current densities to be injected in magnetostatics will be: $J_1 = N_1 I_{1eff}/S_b = 0.983 \times 10^6\,\mathrm{A/m}^2$ and $J_2 = N_2 I_{2eff}/S_b = 0.973 \times 10^6\,\mathrm{A/m}^2$.

2. **Second approach**: This method consists in calculating the magnetizing current of the transformer and then injecting it into the external primary coil. The value of the magnetizing current is calculated by the formula $i_m = (n_1 i_1 - n_2 i_2)/n_1$ with $n_1$ and $n_2$ the number of turns in the primary and secondary windings respectively and $J = n_1 i_m/S_b$ the density of the magnetizing current to be injected into the primary winding ($J = 10\,569\,\mathrm{A/m}^2$).

3. **Third approach**: This third method consists in estimating the magnetizing current by Ampere's law through the formula:

$$\Delta J \times S_b = \sum NI = \oint_{core} Hdl = H \times 7L \tag{4.6}$$

   The current difference is then estimated at $\Delta J = 24\,634\,\mathrm{A/m}^2$ which is much higher than the magnetizing current calculated by the second approach (with the analytical formula and the data of the time-dependent calculation). This current is finally injected into the external primary coil.

4. **Fourth approach**: The fourth method consists to impose identical current densities with opposite signs in the conductors and which value equals the one calculated in the temporal study. We consider for example $JS = Ni$ with $J_1 = J_2 = \pm 0.983 \times 10^6\,\mathrm{A/m}^2$.

### Results of the magnetostatic calculation

In this part, we compare at a first step the magnetic flux density distribution in the ferromagnetic core of the model for each of the previous approaches. Then, we proceed to compute the magnetic flux density component $B_z$ along the two horizontal and vertical lines cutting the ferromagnetic core, as shown in figure ((4.33)a) and the magnetic field intensity $H_z$ along the two lines $H_1$ and $H_2$ as shown in figure ((4.33)b).

Figure (4.37) shows the distribution of the magnetic flux density norm in $(x, z)$ plane obtained with the four considered approaches.

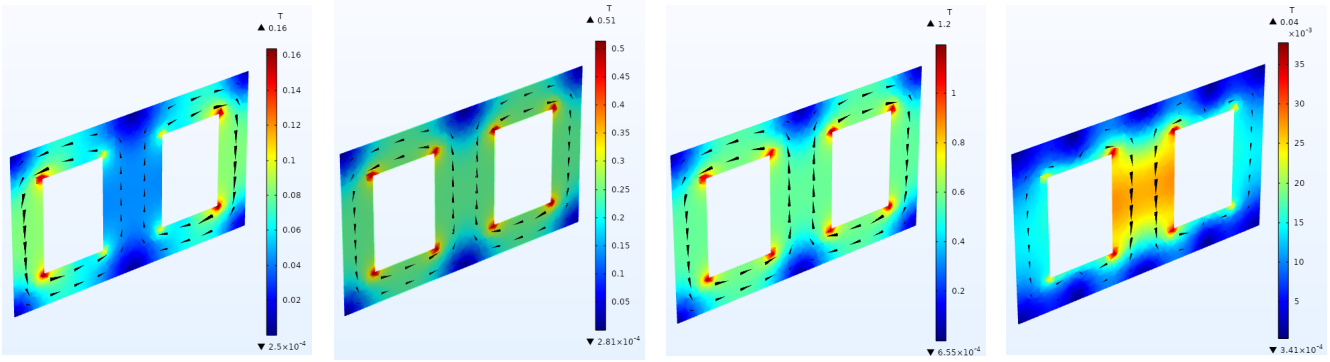

(a) Approach 1. (b) Approach 2. (c) Approach 3. (d) Approach 4.

Figure 4.37: Magnetic flux density (in T) for each of the four approaches considered in the magnetostatic calculation in the $(x, z)$ plane ($y = 0$).

For the first approach, the cross-section of $B_{norm}$ shows an anomaly in the magnitude distribution of the magnetic flux density when the two current densities $J_1$ and $J_2$ deduced from the time-dependent calculation are injected in the coils. Indeed, larger values of $B$ appear in the lateral legs of the ferromagnetic core. On the other hand, the value of $B$ is almost negligible in the central leg of the core (see figure ((4.37)a)).
In the second approach, the distribution of $B$ appears normal with the same values of $B_{norm}$ in the lateral legs and in the central leg of the ferromagnetic core (see figure ((4.37)b)).
According to the third approach, the distribution of the magnetic flux density $B$ seems as expected. The values of $B_{norm}$ in the lateral legs and in the central leg of the ferromagnetic core are equal as shown in figure ((4.37)c).
In the fourth approach, the distribution of $B_{norm}$ obtained is as expected: the value of $B_{norm}$ in the central leg ($28 \times 10^{-3}\,\mathrm{T}$) is roughly two times greater than the one observed in the sides ($15 \times 10^{-3}\,\mathrm{T}$). Nevertheless, this value of $B_{norm}$ in the central leg remains negligible compared to the value of $0.7\,\mathrm{T}$ obtained in the time-dependent magnetic case and shown in figure ((4.34)b). This is because the magnetic flux lines compensate each other in the core. The application of two identical currents but of opposite signs in the two coils leads to this distribution of the magnetic flux density in the core.

In parallel, the magnetic flux density $B_z$ is computed along the measurement lines presented in figure ((4.33)a). Figures (4.38), (4.39), (4.40) and (4.41) show the distribution of $B_z$ with respect to the arc length for each of the considered approach.

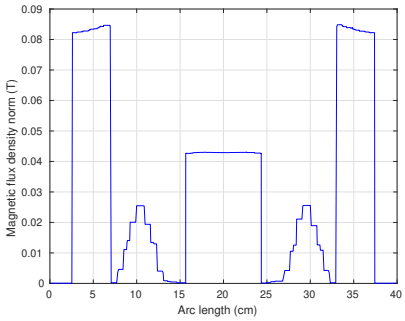


(a) Magnetic flux density (in T) along $B_1$.

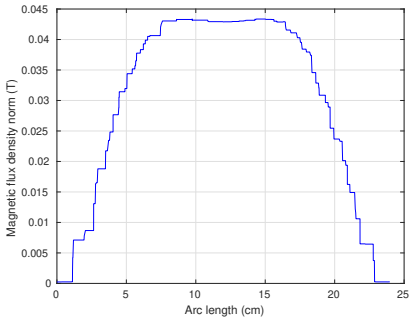


(b) Magnetic flux density (in T) along $B_2$.

Figure 4.38: Magnetic flux density $B_z$ in T for approach 1.

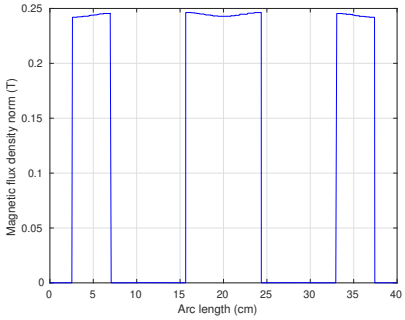


(a) Magnetic flux density (in T) along $B_1$.

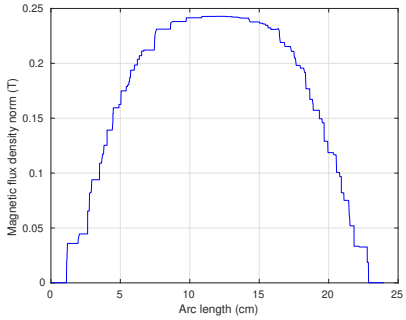


(b) Magnetic flux density (in T) along $B_2$.

Figure 4.39: Magnetic flux density $B_z$ in T for approach 2.

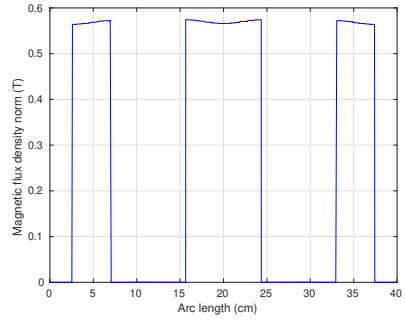


(a) Magnetic flux density (in T) along $B_1$.

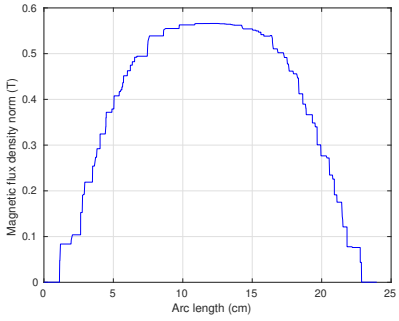


(b) Magnetic flux density (in T) along $B_2$.

Figure 4.40: Magnetic flux density $B_z$ in T for approach 3.

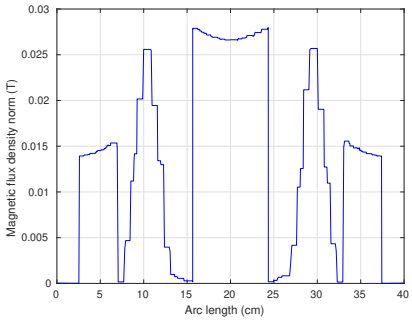


(a) Magnetic flux density (in T) along $B_1$.

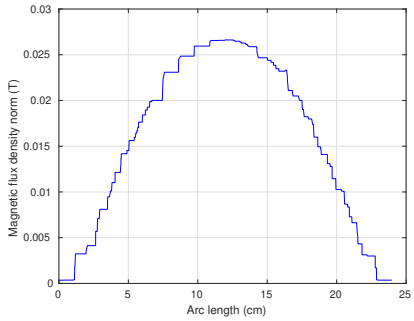


(b) Magnetic flux density (in T) along $B_2$.

Figure 4.41: Magnetic flux density $B_z$ in T for approach 4.

For the first and the fourth approaches, the curves of $B_z$ confirm the abnormal distributions of the induction field $B$ in the ferromagnetic core. In parallel, large values of $B$ ($B = 0.026\,\mathrm{T}$) appear in the air between the legs of the core, revealing a critical magnetic leakage in this model of the transformer. This contradicts the $B$ distribution obtained in the time-dependent calculation. This may be related to the electric currents considered in the study as we consider here the RMS values of the currents to evaluate the current densities in the coils and not the actual currents with their phase shift in this approach (see figure ((4.36)c)).

In the second approach, the analysis of the curves of $B_z$ along the two lines $B_1$ and $B_2$ confirms the distribution obtained in the $B_{norm}$ section. However, the magnetic flux density obtained in this study $B = 0.24\,\mathrm{T}$ is lower than the one obtained in the time-dependent calculation $B_{eff} = 0.5\,\mathrm{T}$. This lower value obtained of the magnetic flux density may depend on the calculated magnetizing current injected in the primary coil. It seems that this current is underestimated with this second approach that will not be used.

In the third approach, the values of $B_z$ in the lateral legs and in the central leg of the ferromagnetic core are equal as confirmed by the $B_{norm}$ distribution. The leakage fluxes are negligible, and the RMS value of the magnetic flux density is identical to that obtained in the time-dependent calculation $B_{eff} = 0.5\,\mathrm{T}$.

At a final step, we evaluate the magnetic field intensity $H_z$ along the measurement line presented in figure ((4.33)b). We mention again that the magnetic force exerted to the ferrofluid in the 3D computation is proportional to the square of the magnetic field. It is then sufficient to compare the $H_z$ curves in the air to determine the magnetic leakage flux in the ferrofluid. Figures (4.42), (4.43), (4.44) and (4.45) show the distribution of $H_z$ with respect to the arc length for each of the considered approaches compared to the time-dependent magnetic calculation.

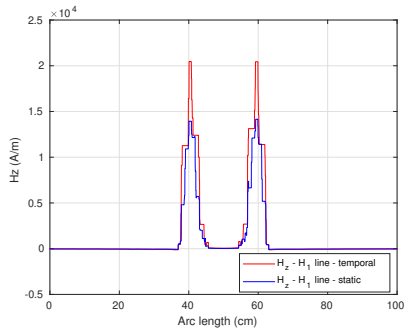


(a) Magnetic field intensity (in $\mathrm{A.m^{-1}}$) along $H_1$.

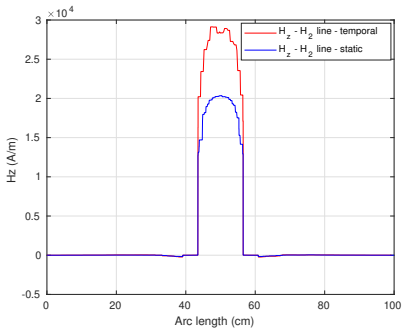


(b) Magnetic field intensity (in $\mathrm{A.m^{-1}}$) along $H_2$.

Figure 4.42: Magnetic field intensity (in $\mathrm{A.m^{-1}}$) for approach 1.

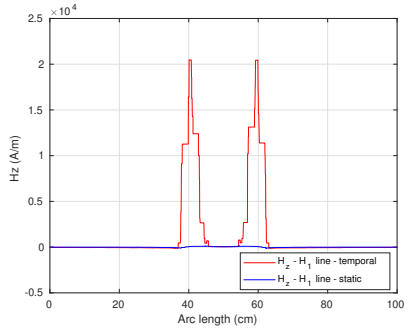


(a) Magnetic field intensity (in $\mathrm{A.m^{-1}}$) along $H_1$.

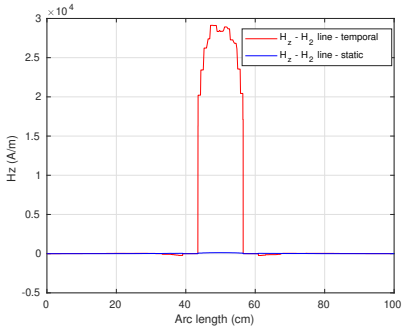


(b) Magnetic field intensity (in $\mathrm{A.m^{-1}}$) along $H_2$.

Figure 4.43: Magnetic field intensity (in $\mathrm{A.m^{-1}}$) for approach 2.

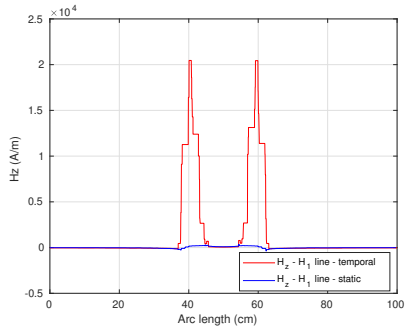


(a) Magnetic field intensity (in $\mathrm{A.m^{-1}}$) along $H_1$.

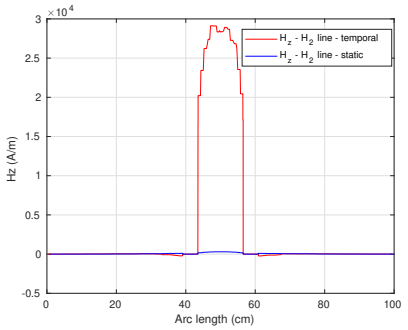


(b) Magnetic field intensity (in $\mathrm{A.m^{-1}}$) along $H_2$.

Figure 4.44: Magnetic field intensity (in $\mathrm{A.m^{-1}}$) for approach 3.

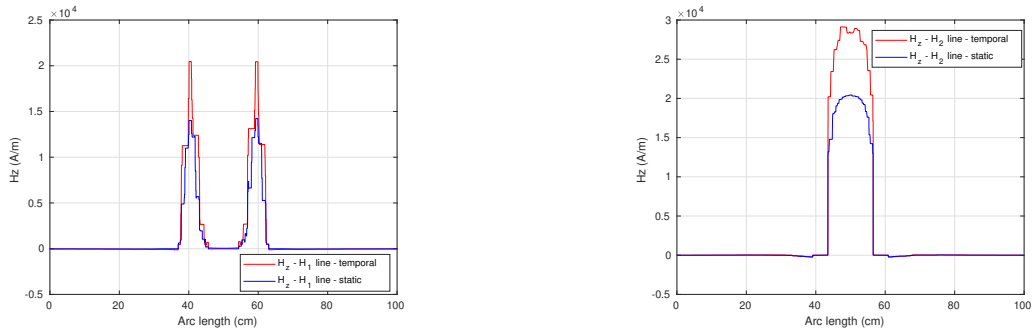


(a) Magnetic field intensity (in $\mathrm{A.m^{-1}}$) along $H_1$. (b) Magnetic field intensity (in $\mathrm{A.m^{-1}}$) along $H_2$.

Figure 4.45: Magnetic field intensity (in $\mathrm{A.m^{-1}}$) for approach 4.

For the first and the fourth approaches, the compared curves of $H_z$ along both measurement lines follow the same trend with a difference on the maximum value reached. The calculated RMS value of the maximum intensity $H_z$ in the temporal study is equal to the one obtained in the magnetostatic study ($H_{zeff} = 1.4 \times 10^4$ $\mathrm{A.m^{-1}}$ along $H_1$ and $H_{zeff} = 2.1 \times 10^4$ $\mathrm{A.m^{-1}}$ along $H_2$). Despite the abnormal magnetic flux density distribution in the core, these two approaches give a magnetic field distribution in agreement with the one obtained in the magnetic time-dependent study. Therefore, we will use this approximation of the magnetic field distribution **H** to study the ferrohydrodynamic coupling.

In the second and the third approaches, the $H_z$ variation curves are compared to those obtained with the time-dependent study. The comparison shows that $H_z$ is smaller in the magnetostatic case along the two cut lines. This means that the second and the third approaches underestimate the magnetic field.

### Conclusions for the magnetic calculation

The time-dependent magnetic calculation gives usual distributions for the magnetic flux density norm and the magnetic field intensity. The deduction of the current densities to be injected in a magnetostatic calculation is possible. In order to find the magnetic field intensity distributions consistent with those obtained in the temporal case, one must:

- evaluate the current densities for the primary and secondary coils obtained in the temporal case,
- use the first or the fourth approaches to compute the magnetic field,
- check that the correct distribution of the magnetic field intensity $H$ is obtained along the measurement lines in the air,
- proceed to a fluid-thermal-magnetic coupling with this approximation of the magnetic field **H** in magnetostatics.

### 4.4.3 Fluid-thermal-magnetic coupling

#### 3D Model

This section presents our methodology to achieve the fluid-thermal-magnetic coupling when modeling a $3\mathrm{kVA}$ power transformer. We investigate the cooling efficiency inside the power transformer model using the finite element method. The thermophysical properties of the based oil and the ferrofluid are given in table (3.2) in chapter 2.

First, we consider the actual geometry of the 3D model presented in figure ((4.46)a). We then divide the structure of the transformer into four parts. The magnetic field, velocity, and temperature are numerically computed using COMSOL Multiphysics in a quarter of the model in order to save computational resources, see figure ((4.46)b). In this figure, the shown numbers denote from right to left respectively: (1) the ferromagnetic core, (2) the secondary winding, (3) the primary winding, (4) the ferrofluid domain, and (5) the steel tank with a magnetic permeability $\mu_r = 100$. Note that our geometry imposes a $\frac{\pi}{2}$ rotation symmetry (meaning that only azimuthal modes $m = 4, 8, 12, ...$ are computed). This choice forbids the appearance of large scales in azimuth but not small scales in azimuth, and neither small scales in the horizontal and vertical directions.

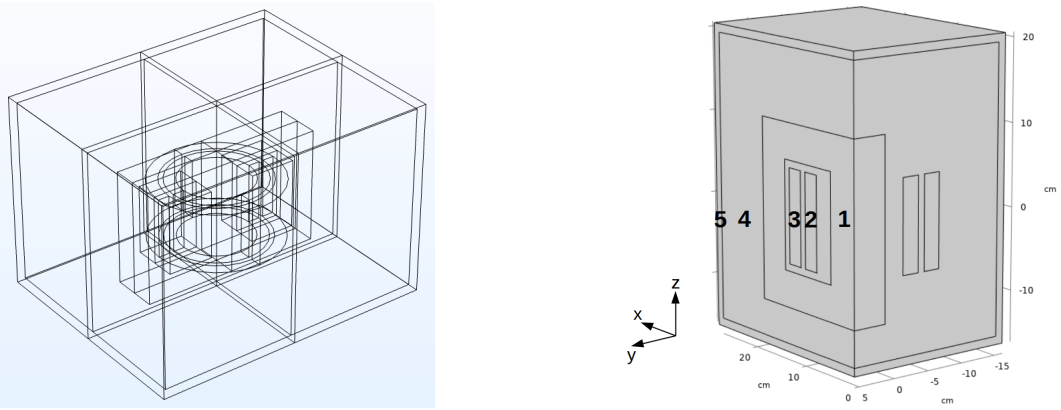


(a) Total 3D structure of the $3\mathrm{kVA}$ power transformer. (b) Quarter of the $3\mathrm{kVA}$ power transformer model.

Figure 4.46: 3D structures of the $3\mathrm{kVA}$ power transformer.

The heat transfer coefficient is fixed to $h = 150\ \mathrm{W.m^{-2}K^{-1}}$ in the heat transfer problem. The nominal current densities injected in both primary and secondary windings are here increased from $j_0 = 2\,\mathrm{A.mm^{-2}}$ to $j_0 = 5\,\mathrm{A.mm^{-2}}$ to maximize the heating of the copper inside the power transformer. According to this increase, the values of the RMS current densities injected in each conductor and the associated volume Joule losses are given in table (4.5).

| Input | value |
|---|---|
| $J_{1eff}$ | $2.46 \times 10^6\,\mathrm{A/m^2}$ |
| $Q_1$ | $196\,593\,\mathrm{W/m^3}$ |
| $J_{2eff}$ | $-2.46 \times 10^6\,\mathrm{A/m^2}$ |
| $Q_2$ | $193\,127\,\mathrm{W/m^3}$ |

Table 4.5: Input parameters for the ferrohydrodynamic coupling respectively in the primary (denoted by $1$) and secondary windings (denoted by $2$).

**Finite element mesh**

We choose a 3D tetrahedral mesh for the quarter model of the $3\ \mathrm{kVA}$ power transformer. A "fine" mesh is chosen for the ferrofluid domain, ranging from $0.97 \times 10^{-3}\,\mathrm{m}$ to $9.01 \times 10^{-3}\,\mathrm{m}$. We choose a "normal" mesh in the ferromagnetic core and the windings with a size of $10 \times 10^{-3}\,\mathrm{m}$. The size selected in the steel tank is ranging between $6.62 \times 10^{-3}\,\mathrm{m}$ and $36.8 \times 10^{-3}\,\mathrm{m}$. The 3D tetrahedral mesh shown in figure ((4.47)a) contains $1049891$ elements.
The magnetic body force is concentrated at the interior boundaries of the windings. Thus, we must refine the mesh in these zones to see the effect of the magnetic force on the ferrofluid behavior. In addition, at the solid-fluid contact, a thermal boundary layer exists that has an impact on the heat transfer, as explained in chapter 1. Therefore, we adapt the mapping in the 3D model with refined fluid-windings contacts (size = $3 \times 10^{-3}\,\mathrm{m}$). The time step is automatically adapted and varies upon the range $[0.01\,\mathrm{s}\ -\ 0.25\,\mathrm{s}]$. The computation time is $471\,\mathrm{h}\ 40\,\mathrm{min}\ 30\,\mathrm{s}$ in the ferrohydrodynamic case and to $37\,\mathrm{h}\ 29\,\mathrm{min}\ 25\,\mathrm{s}$ in the hydrodynamic case. The calculation is run on Intel(R) Xeon(R) W-2125 CPU @ 4.00GHZ using 4 cores for the ferrohydrodynamic case and using 8 cores for the hydrodynamic case.

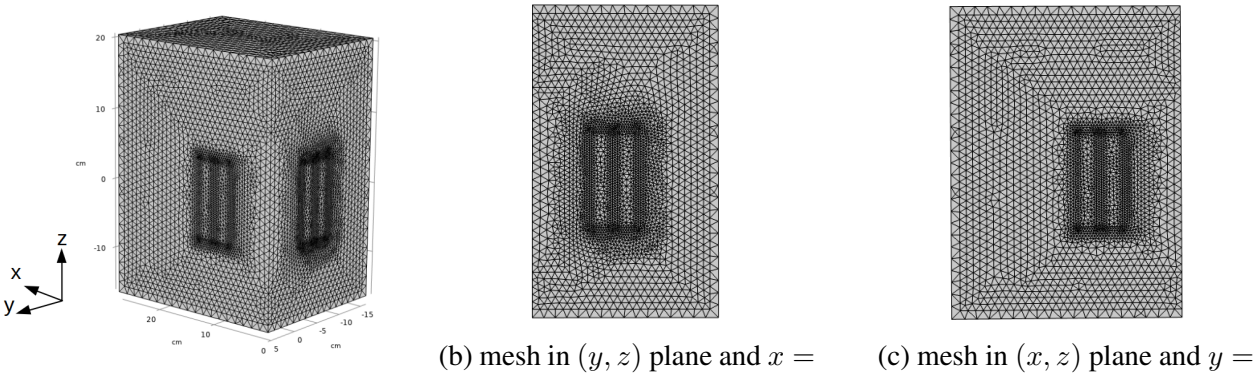


(a) 3D tetrahedral mesh.

(b) mesh in $(y, z)$ plane and $x = 0$.

(c) mesh in $(x, z)$ plane and $y = 0$.

Figure 4.47: Mapping of the quarter of the $3\ \mathrm{kVA}$ transformer model.

Let us evaluate now the time step condition. Using the CFL condition, we consider the maximum velocity in the hydrodynamic case $u = 2 \times 10^{-2}\,\mathrm{m\,s^{-1}}$ near the upper corner of the ferromagnetic core where the mesh is $\Delta x = 1 \times 10^{-2}\,\mathrm{m}$. We find that $\Delta t < 0.5(\frac{\Delta x}{u}) \simeq 0.25\,\mathrm{s}$ which is compatible with the time range used by the code.

**Boundary conditions**

The same boundary conditions applied in the case of the solenoid model in chapter 2 are used here for the quarter of the transformer model. At the borders of the steel tank, the boundary condition for the magnetic problem $\mathbf{A} \times \mathbf{n} = \mathbf{0}$ is enforced. The non-slip boundary condition $\mathbf{u} = \mathbf{0}$ is applied at the border of the fluid domain. The air convection at the top and on the lateral wall of the steel tank is modeled by using a Robin boundary condition on the temperature:

$$-\lambda \nabla T \cdot \mathbf{n} = h(T - T_{\text{ext}}), \tag{4.7}$$

where $h$ is the convection coefficient, and $\mathbf{n}$ is the outer unit normal vector. The homogeneous Neumann boundary condition $\partial_z T = 0$ is enforced at the bottom of the tank. The initial conditions are $\mathbf{u} = \mathbf{0}$, $\mathbf{A} = \mathbf{0}$ and $T = T_{\text{ext}} = 22\,^{\circ}\text{C}$. The impact of the magnetic field on the ferrofluid is modeled by the Helmholtz force given in (3.29).

### 4.4.4 Numerical results

The time evolution of the temperature is recorded whether the Helmholtz magnetic force is activated or not. For these two cases, the temperature curves computed at two sensors localized at the top of each winding are shown in figure (4.48). Comparing both time series, one can note a decrease of the local temperature of the two sensors by $10\,^{\circ}\text{C}$ approximately when the magnetic force is activated.

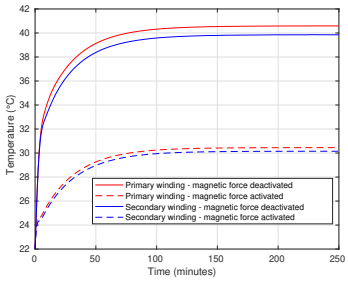


Figure 4.48: Time evolution of windings temperature in both hydrodynamic and ferrohydrodynamic cases.

Snapshots of the velocity field magnitude at $t = 15\,000\,\text{s}$ are shown in figure (4.49) for two cases: the hydrodynamic case where no magnetic force is applied, and the ferrohydrodynamic case where the magnetic force influences the ferrofluid. With no magnetic force (see figure ((4.49)a)), a large recirculation cell appears at the top of the fluid volume. If the magnetic force is applied (see figure ((4.49)b)), the maximum velocity amplitude is localized in the gap between the two windings, as well as at the top of their surface. A new convection cell, which is not present in the hydrodynamic case, appears between the core and the windings bottom. Therefore, the fluid circulation is modified between the core and the internal winding and amplifies the heat removal from the inside of the tank. As a result, the temperature of the windings is lowered. This proves again the beneficial effect of the thermomagnetic convection phenomenon.

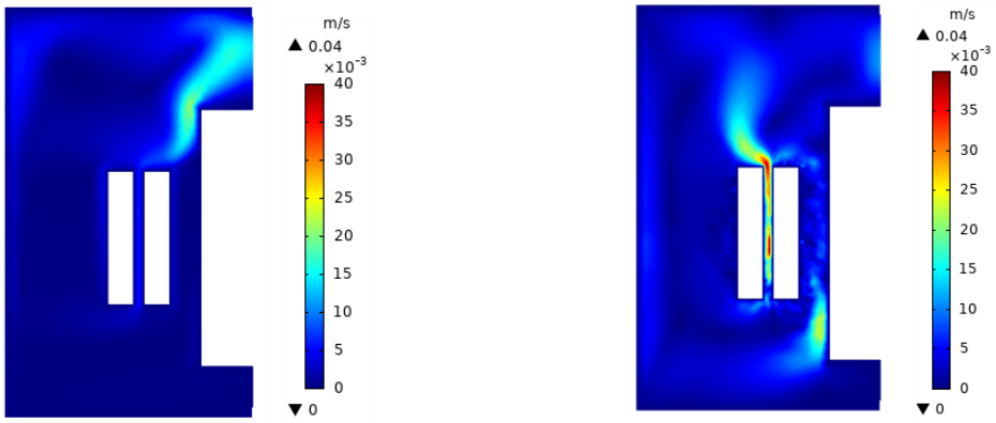


(a) Hydrodynamic case. (b) Ferrohydrodynamic case.

Figure 4.49: Velocity magnitude (in $\mathrm{m.s^{-1}}$) distributions in $(y, z)$ plane and $x = 0$ at a steady state $t = 15\,000\,\mathrm{s}$.

### Kinetic energy

In this part, we aim to quantify some physical quantities that seem important in our modeling. We first focus on the ferrofluid behavior inside the tank and its variation along the height of the tank. It appears in the ferrohydrodynamic case (see figure ((4.49)b)) that the ferrofluid flow is favored in the gap between the coils.
Let us start by comparing the velocity components in both hydrodynamic and ferrohydrodynamic cases. Figures (4.50) and (4.51) show respectively the distributions of the $y$ and $z$ components of the velocity field at steady-state ($t = 15\,000\,\mathrm{s}$).

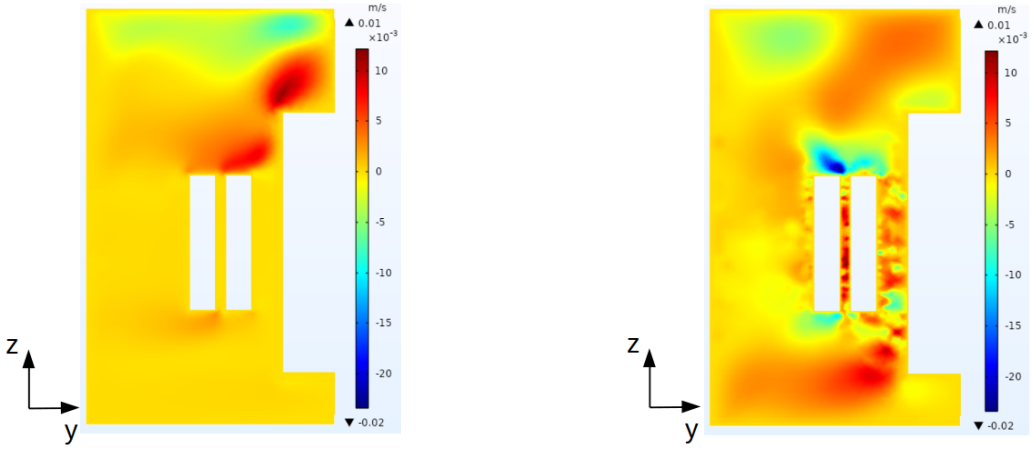


(a) Hydrodynamic case. (b) Ferrohydrodynamic case.

Figure 4.50: Distributions of the $y$ component of the velocity field $v_y$ (in $\mathrm{m.s^{-1}}$) in $(y, z)$ plane and $x = 0$ at a steady state $t = 15\,000\,\mathrm{s}$.

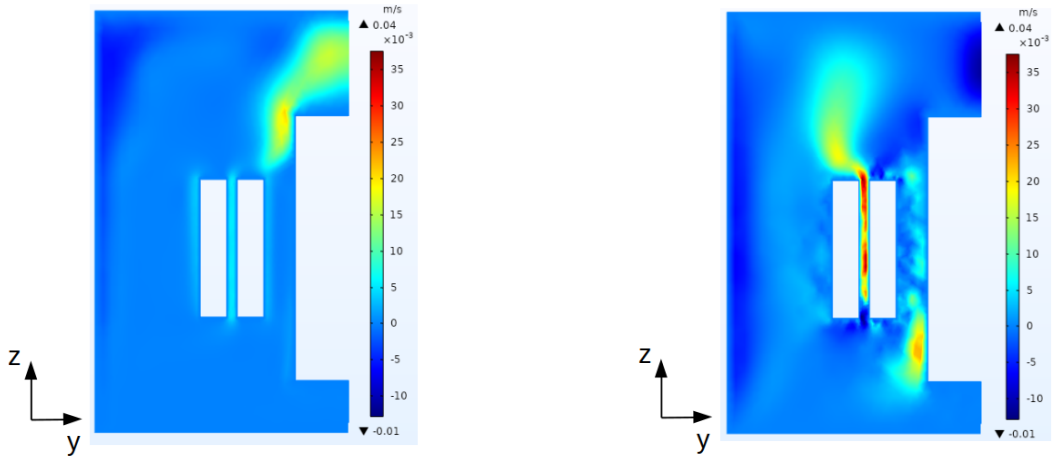


(a) Hydrodynamic case.

(b) Ferrohydrodynamic case.

Figure 4.51: Distributions of the $z$ component of the velocity field $v_z$ (in $\mathrm{m.s^{-1}}$) in $(y, z)$ plane and $x = 0$ at a steady state $t = 15\,000\,\mathrm{s}$.

Quantifying the velocity flow channeling the gap between the windings indicates how much the ferrofluid flow is reinforced to allow a better cooling performance inside the transformer. Thus, the velocity field components are evaluated along a vertical line in $(y, z)$ plane crossing the gap between the windings and reaching bottom and top lids of the tank. Figure (4.52) shows the profiles of the velocity field components $v_y$ and $v_z$ along this line.

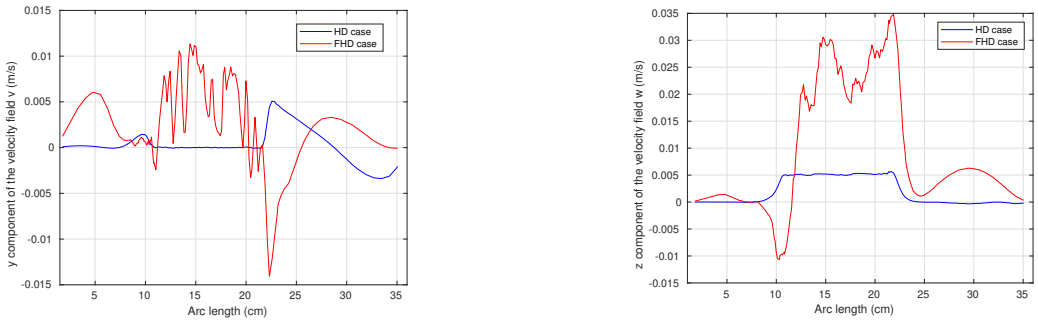


(a) $y$ component of the velocity field $v_y$.

(b) $z$ component of the velocity field $v_z$.

Figure 4.52: Distributions of the velocity field components (in $\mathrm{m.s^{-1}}$) at a steady state $t = 15\,000\,\mathrm{s}$.

Both components of the velocity fields are much greater in the ferrohydrodynamic case. If we compare figure ((4.52)a) to figure ((4.52)b), the velocity field component $v_z$ is 2.5 times greater than the velocity field component $v_y$. This means that the velocity flow moves upward in the gap between the windings. Therefore, the cooling performance is improved in the ferrohydrodynamic case where the velocity field component $v_z$ is enhanced by $86\%$ comparing to the one in the hydrodynamic case. This vertical velocity is generated by the Helmholtz force. We observe oscillations for both components $v_y$ and $v_z$ in the ferrohydrodynamic case. These oscillations are due to small scales motion in the gap, they are convected upward by the flow.

Let us now study the kinetic energy in both hydrodynamic and ferrohydrodynamic cases. Figure (4.53) shows the time evolution of the kinetic energy according to equation (4.5).

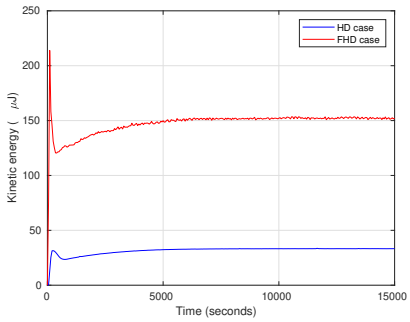


Figure 4.53: Kinetic energy (in μJ) over $15\,000\,\mathrm{s}$.

According to figure (4.53), the kinetic energy in the ferrohydrodynamic case is $4.6$ times greater than the one obtained in the hydrodynamic case. This increase in the kinetic energy is expected. When the magnetic force is applied, the ferrofluid circulation is modified inside the tank and the velocity field intensity is enhanced. Due to the presence of the magnetic force, the ferrofluid behavior is modified around the conductors. Oscillations missing in the hydrodynamic case appear in the short-time and long-time regimes in the ferrohydrodynamic case. They may be related to the small scales appearing in the gap between windings and between the conductors and the core central leg. We note that the simulation may be under-resolved. We also observe perturbations during the first seconds at the transient regime for both cases.

### Temperature distributions

Let us now compare the temperature in both conductors. Figure (4.54) shows the temperature distributions at a quasi-steady state ($t = 15\,000\,\mathrm{s}$) whether the magnetic force (see figure ((4.54)b)) is present or not (see figure ((4.54)a)).

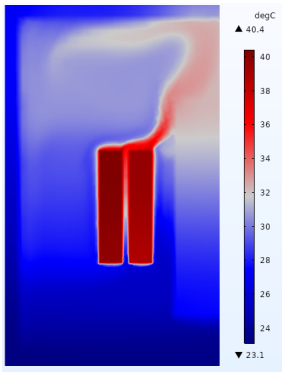


(a) Hydrodynamic case.

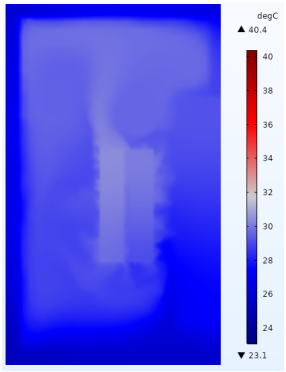


(b) Ferrohydrodynamic case, $T$ field in modified scale.

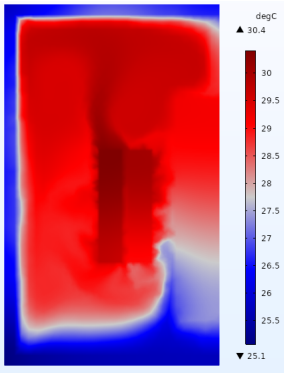


(c) Ferrohydrodynamic case, $T$ field in real scale.

Figure 4.54: Temperature (in °C) distributions in $(y, z)$ plane and $x = 0$ at a quasi-steady state $t = 15\,000\,\mathrm{s}$.

When no magnetic force is applied, only the buoyancy force can impact the ferrofluid motion. The thermal plume (see figure ((4.54)a)) born at the top of both windings follows the convection cell trajectory shown in figure ((4.49)a). It reaches the corner of the core then deviates at the left near the upper border of the tank. The primary winding reaches $40.4\,°\mathrm{C}$ at $t = 15\,000\,\mathrm{s}$. In contrast, when the magnetic force is present (see figure ((4.54)b)), the thermal plume, being deviated by the convection cell emerging between the conductors (see figure ((4.49)b)), rises vertically from the top of the primary winding and then spreads in the upper part of the ferrofluid domain. Another thermal plume rises at the bottom of both windings, being affected by the new convection cell that appears in the lower part of the tank between the core and the bottom of the windings. The ferrofluid flow is reinforced between the conductors, which allows effective cooling of the windings. The primary winding reaches $30.4\,°\mathrm{C}$ at $t = 15\,000\,\mathrm{s}$. Consequently, the maximum temperature in the conductors is decreased by $10\,°\mathrm{C}$ thanks to the impact of the thermomagnetic convection (see figure (4.55)).

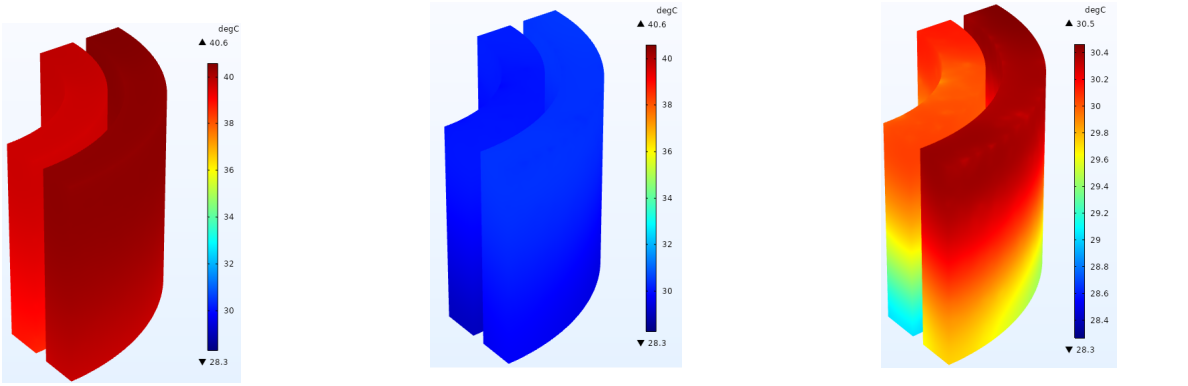


(a) Hydrodynamic case.

(b) Ferrohydrodynamic case, modified scale.

(c) Ferrohydrodynamic case, real scale.

Figure 4.55: Temperature distributions (in °C) for both windings in a 3D view at a steady state $t = 15\,000\,\mathrm{s}$.

As seen in figure (4.55), it is expected that the maximum temperature in the secondary winding for both cases is lower than the one in the primary winding. The secondary winding, cooled by the ferrofluid flow channeling the gap between the conductors, exchanges more heat than the primary one. The maximum temperature decrease for both conductors remains significant in reducing excessive heating in the power transformer.

Temperature distributions in the ferromagnetic core are also compared for both cases at a quasi-steady-state ($t = 15\,000\,\mathrm{s}$) in figure (4.56). In the panels of this figure, the central leg of the core is on the left.

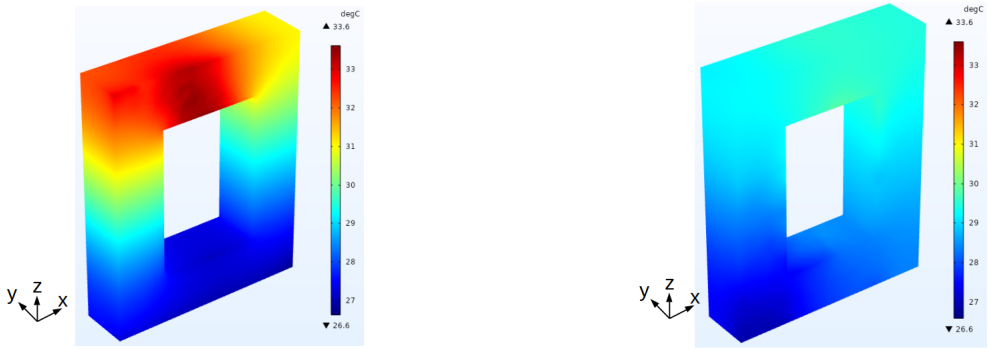


(a) Hydrodynamic case.

(b) Ferrohydrodynamic case.

Figure 4.56: Temperature distributions (in °C) for the ferromagnetic core in a 3D view at a steady state $t = 15\,000\,\mathrm{s}$.

The hot spot temperature is localized at the upper part of the core in both hydrodynamic and ferrohydrodynamic cases. The thermal plumes usually rise from the top of windings towards the upper part of the core and therefore increase the temperature of this core part. Consequently, the maximum temperature in the core is reduced by roughly $4\,^{\circ}\mathrm{C}$ when applying a magnetic force.
The hot spot temperature in the power transformer appears in the ferromagnetic core in some articles [81, 85, 86]. In contrast, the hot spot temperature in our configuration is localized, as expected, in the primary winding for the hydrodynamic ($40.4\,^{\circ}\mathrm{C}$) and the ferrohydrodynamic cases ($30.4\,^{\circ}\mathrm{C}$). These temperatures remain greater than the ones registered in the ferromagnetic core for both hydrodynamic and ferrohydrodynamic cases, respectively [33.6, 29.8]°C.

Let us compare the temperature profiles for the steel tank. Figure (4.57) shows the temperature distributions in the steel tank for both hydrodynamic and ferrohydrodynamic cases.

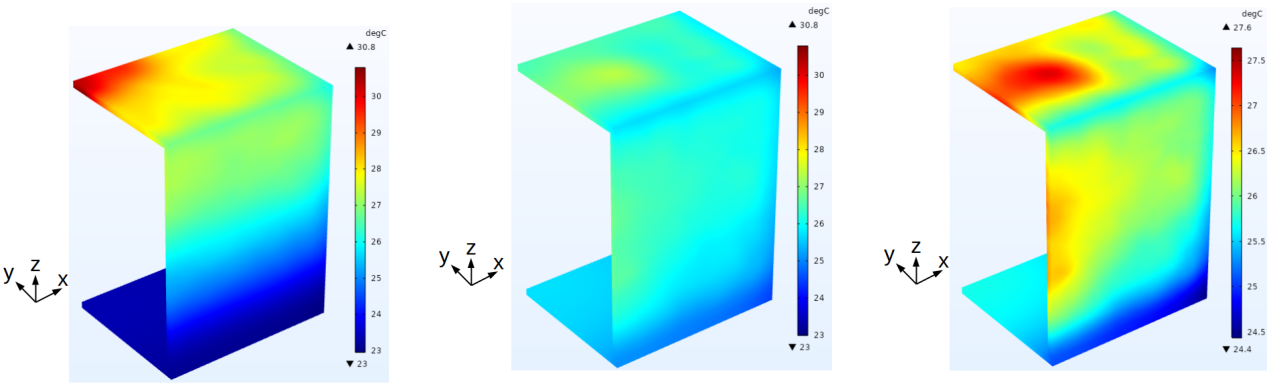


(a) Hydrodynamic case.

(b) Ferrohydrodynamic case, modified scale.

(c) Ferrohydrodynamic case, real scale.

Figure 4.57: Temperature distributions (in °C) for the tank in a 3D view at a steady state $t = 15\,000\,\mathrm{s}$.

If we compare the two cases, one can predict the hot spot temperature of the steel tank localized approximately at the center of the top surface in the hydrodynamic case (see figure ((4.57)a)), while

it is off centered for the ferrohydrodynamic case. Note that a Robin boundary condition is applied on the lateral and top walls of the tank to allow heat transfer with the exterior. This means that when the magnetic force is absent, the heat has a low tendency to leave the tank, and its temperature remains high ($30.8\,°\mathrm{C}$). In contrast, in the ferrohydrodynamic case (see figure ((4.57)b)), the zone of high temperature at the top surface of the tank is not localized at the top surface center. The maximum temperature in the tank is reduced to $27.6\,°\mathrm{C}$ comparing to the hydrodynamic case. This reveals an enhancement in the cooling process due to the thermomagnetic convection effect.

**Average temperature**

Let us study the average temperature of the structure in both hydrodynamic and ferrohydrodynamic cases. Figure (4.58) shows the time evolution of the average temperature of the system according to equation (4.5).

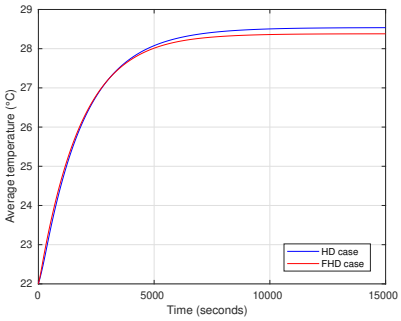


Figure 4.58: Average temperature (in °C) over $15\,000\,\mathrm{s}$.

The average temperature in both cases is similar as seen in figure (4.58). The average temperature reached when applying the magnetic force is $28.4\,°\mathrm{C}$ against $28.5\,°\mathrm{C}$ for the one obtained in the hydrodynamic case. The difference on the average temperature is $0.3\%$. This is expected since both configurations have to dissipate the same amount of injected Joule power considering the same conditions at the outer borders.

### 4.4.5 Mesh convergence study in the hydrodynamic case

We have performed a fully coupled method to study the cooling performance in a ferrofluid-immersed power transformer. We have considered a reasonable finite element mesh that we denote by mesh $0$ with $1049891$ elements. The results obtained in both hydrodynamic and ferrohydrodynamic cases have been compared and have shown the impact of the thermomagnetic convection on cooling the power transformer. The computing time is an essential parameter to minimize if we want to perform an optimization study by varying some physical properties. Nevertheless, we can ask whether the velocity and temperature distributions obtained with mesh $0$ are meaningful. Therefore, we refine the 3D mesh of the transformer model to respond to this question. The simulations presented thereafter concern only the hydrodynamic case. We did not perform the same simulations in the ferrohydrodynamic case because of the large time that simulations undergo (calculation over months).

In the following, we compare three cases of the hydrodynamic calculation with three different meshes: the mesh $0$ with $1049891$ elements presented in figure (4.47) that was used previously, the mesh $1$ with $2691084$ elements, and the mesh $2$ with $4353335$ elements. The computation time for the mesh $0$ is $37\,\mathrm{h}\ 29\,\mathrm{min}$, for the mesh $1$ is $116\,\mathrm{h}\ 53\,\mathrm{min}$, and for mesh $2$ is $199\,\mathrm{h}\ 3\,\mathrm{min}$. The calculation is run on Intel(R) Xeon(R) W-2125 CPU @ 4.00GHZ using 8 cores for each case of the considered meshes.

The time step is automatically adapted and varies upon the range $[0.01\,\mathrm{s}\ -\ 0.5\,\mathrm{s}]$. Figures (4.59) and (4.60) present respectively the meridian views in $(y, z)$ plane and $(x, z)$ plane for each of the three meshes considered.

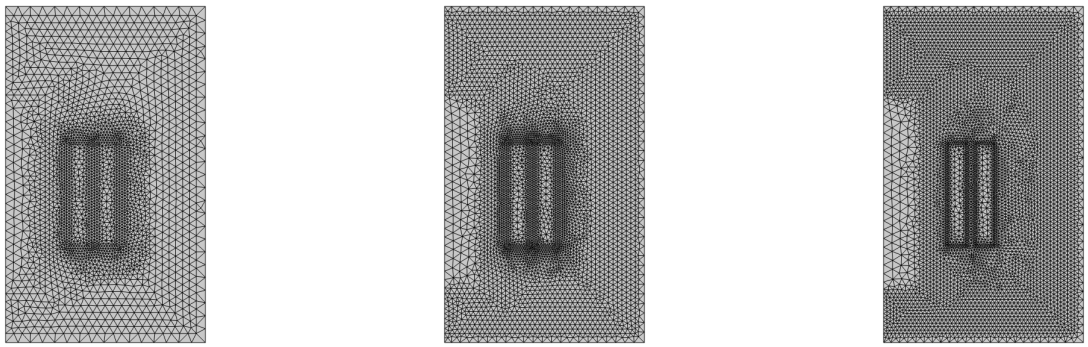

(a) Mesh $0$. (b) Mesh $1$. (c) Mesh $2$.

Figure 4.59: Mapping in $(y, z)$ plane and $x = 0$.

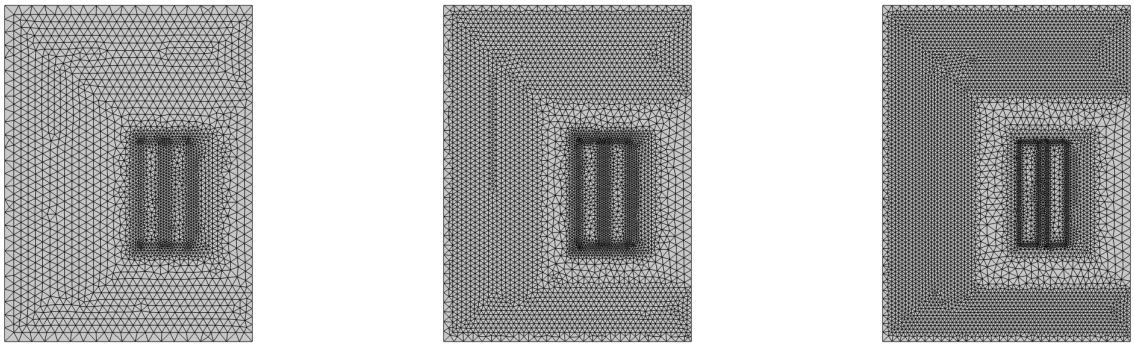

(a) Mesh $0$. (b) Mesh $1$. (c) Mesh $2$.

Figure 4.60: Mapping in $(x, z)$ plane and $y = 5$.

Temperatures on the top of both windings are registered for each case of the considered meshes, and the time evolutions of the windings temperatures are compared in figure (4.61).

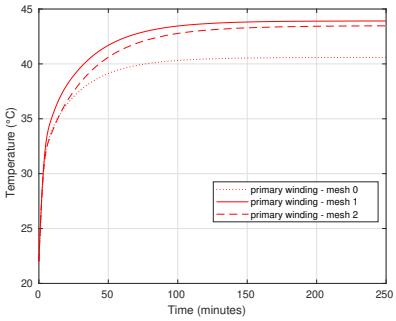


(a) Primary winding.

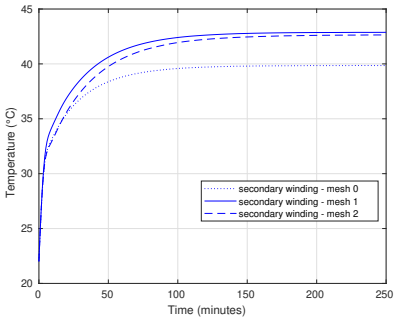


(b) Secondary winding.

Figure 4.61: Temperature evolution (°C) versus time (min).

The steady-state is reached after 15 000 s for both windings. We observe that the curves resulting from meshes 1 and 2 are almost similar for both windings, while curves of mesh 0 are quite far. Note that in the first part of the transient regime, the curves resulting from the three meshes are close. According to these curves, one deduces that the mesh 0 underestimates the temperature of the windings and that one of the meshes 1 or 2 could be chosen for the coupling calculation.
A calculation of the error resulting from the three meshes is given in the following to select one of the three meshes considered before for the coupling. Temperatures are registered on the top of both windings, and the relative error at time $t$ of the simulation is calculated for each case of the considered meshes using this formula:

$$\epsilon(t) = \frac{\Delta T^{(j)}(t) - \Delta T^{(2)}(t)}{\Delta T^{(2)}(t)}, \quad j = 0, 1 \tag{4.8}$$

where the subscripts refer to the meshes, $\Delta T^{(j)}(t) = T^{(j)}(t) - T_{ref}$, $\Delta T^{(2)}(t) = T^{(2)}(t) - T_{ref}$ and $T_{ref} = T_{ext} = 22\,°\mathrm{C}$. Figure (4.62) shows the relative error computed for both windings.

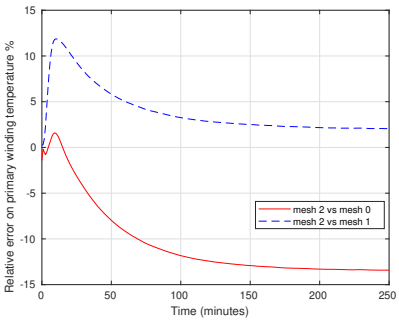


(a) Primary winding.

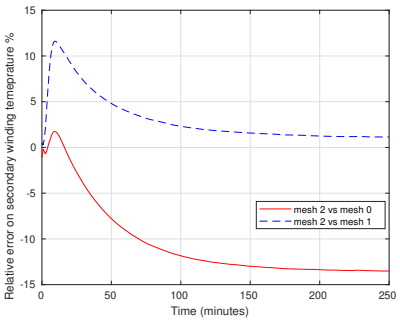


(b) Secondary winding.

Figure 4.62: Relative error on windings temperature (%) versus time (min).

Comparing the relative error in the primary winding case, we note that the relative error based on the comparison (mesh 2 vs mesh 1) is much lower (decrease by 6.4 times) at steady-state than the one based on the comparison (mesh 2 vs mesh 0). In the same way, a decrease by 12 times of the relative error is registered in the secondary winding case at steady-state. Therefore, we can say

that the mesh 1 is more adapted for the coupling calculation than the mesh 0 that underestimates the temperature of the components. In the following, we compare the velocity and the temperature distributions in different parts of the transformer to investigate whether the heat transfer occurs identically. Figures (4.63) and (4.64) show the velocity and temperature slices respectively at a steady-state $t = 15\,000\,\mathrm{s}$ in different $(y, z)$ planes for the hydrodynamic case and for the three meshes.

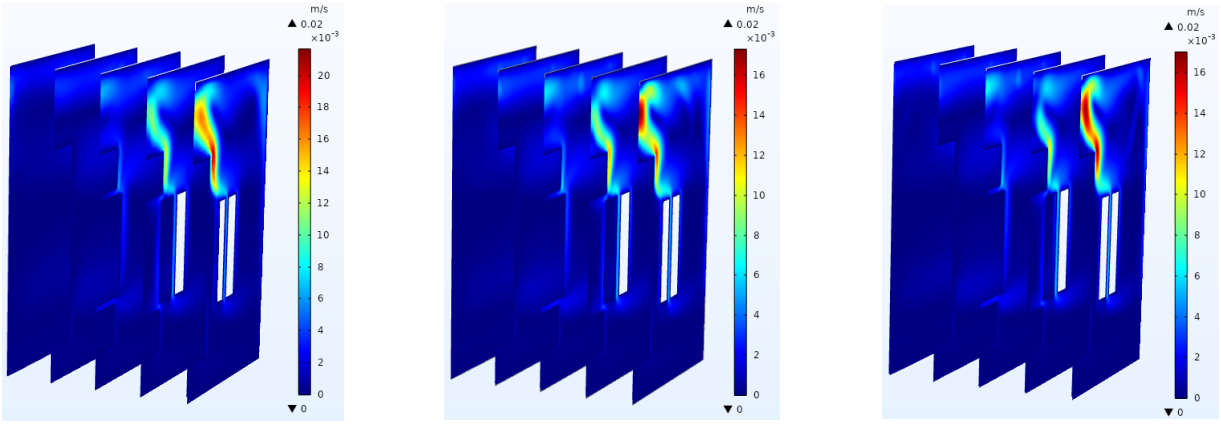


(a) Mesh 0. (b) Mesh 1. (c) Mesh 2.

Figure 4.63: Velocity magnitude (in $\mathrm{m.s^{-1}}$) distributions in $(y, z)$ plane at a steady state $t = 15\,000\,\mathrm{s}$.

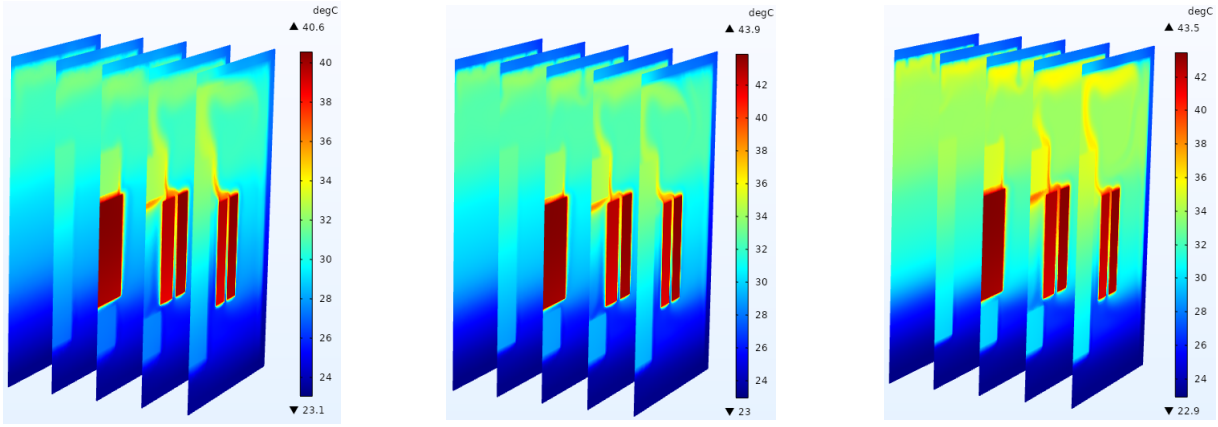


(a) Mesh 0. (b) Mesh 1. (c) Mesh 2.

Figure 4.64: Temperature (in °C) distributions in $(y, z)$ plane at a steady state $t = 15\,000\,\mathrm{s}$.

As seen in these figures, the shape of temperature plumes matches with the direction of the ferrofluid flow. The different slices show that the plumes emerge from the windings as expected. Comparing the three meshes, we confirm again that using mesh 1 is suitable for the coupling problem since the temperature and velocity profiles seem to reach a steady-state with very similar spatial distributions. The maximum temperature is slightly varying from $43.9\,°\mathrm{C}$ with mesh 1 to $43.5\,°\mathrm{C}$ with mesh 2.

Let us compare now the velocity and temperature distributions in $(y, z)$ and $x = 10$. The presented profiles of the velocity and temperature in figures (4.65) and (4.66) show the transformer windings taken in their front view.

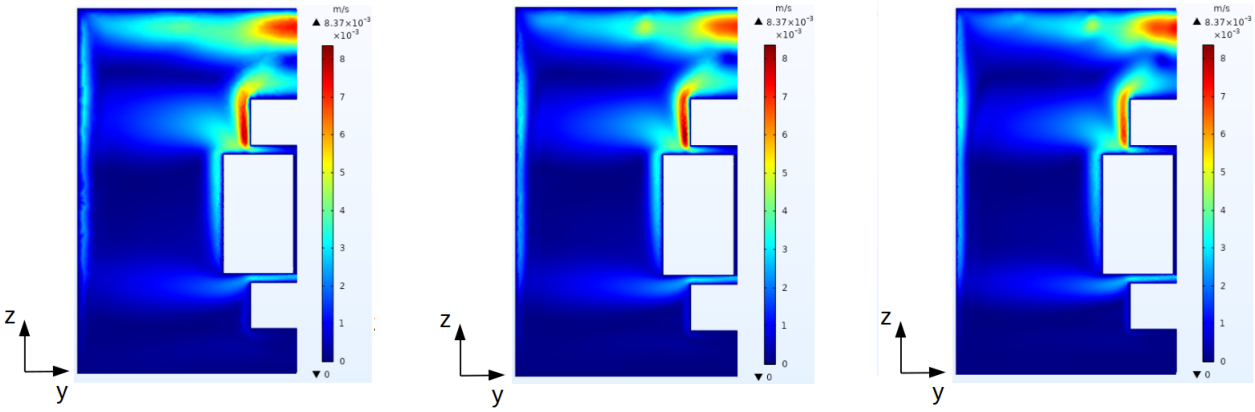


(a) Mesh 0. (b) Mesh 1. (c) Mesh 2.

Figure 4.65: Velocity magnitude (in $\mathrm{m.s^{-1}}$) distributions in $(y, z)$ plane and $x = 10$ at a steady state $t = 15\,000\,\mathrm{s}$.

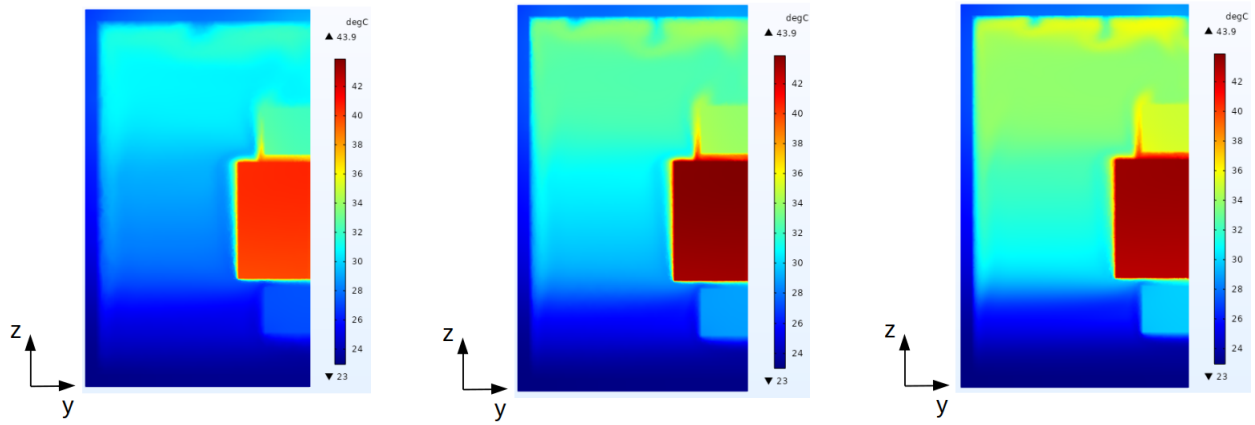


(a) Mesh 0. (b) Mesh 1. (c) Mesh 2.

Figure 4.66: Temperature (in °C) distributions in $(y, z)$ plane and $x = 10$ at a steady state $t = 15\,000\,\mathrm{s}$.

Comparing the temperature distributions (see figure (4.66)), we observe a uniformly distributed temperature inside both windings for the three meshes. While the temperature is underestimated in mesh 0, the meshes 1 and 2 give similar results for the temperature profiles. This confirms again that the temperature at the steady-state is well estimated using mesh 1. In addition, the thermal plumes in meshes 1 and 2 are similar and well contrasted, while it is not the case with mesh 0. For the velocity distributions (see figure (4.65)), the single convection cell seen at the upper border of the fluid domain in mesh 0 is split into two cells in meshes 1 and 2.

Further distributions of the velocity and temperature fields in different regions of the transformer structure, whether in $(x, z)$ or $(x, y)$ plane, are presented in the appendixes C.2 and C.3. We can verify again that the ferrofluid behavior changes when considering different slices of the fluid domain and that the temperature is not uniformly distributed through the transformer volume at the steady-state.

In this final part, after the mesh 1 is being confirmed, we are interested to evaluate the temperature and the velocity field where characteristic patterns emerge. For example, it is meaningful to assess the temperature along a line crossing the thermal plume of the temperature profile. In the same way, it is important to evaluate the components of the velocity fields through a line crossing the convection cell that arises in the ferrofluid.

The temperature and the velocity field magnitude are thus plotted along different lines in the $(y, z)$ plane and $x = 0$ for mesh 1 and for the hydrodynamic calculation. Figure (4.67) shows the temperature curves with respect to the measurement lines seen in figure ((4.67)a).

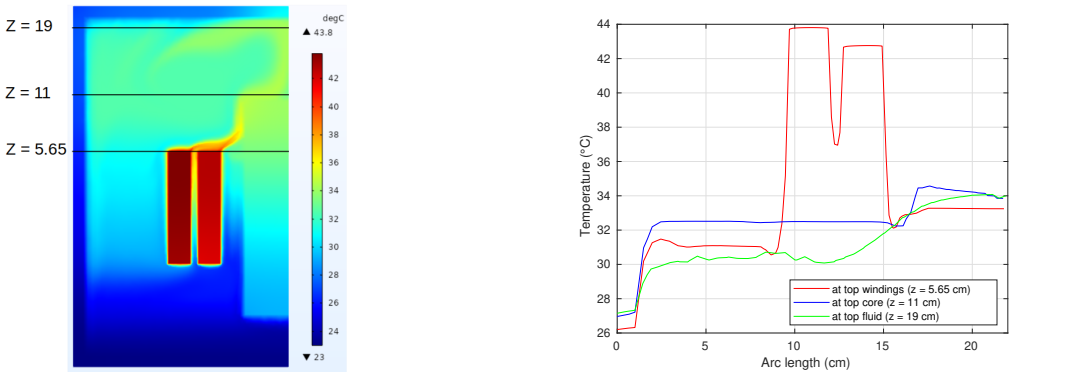


(a) Measurement lines (in solid line).

(b) Temperature curves versus the arc length.

Figure 4.67: Temperature evolution (in °C) in $(y, z)$ plane and $x = 0$ at a steady state $t = 15\,000\,\mathrm{s}$ using mesh 1.

As seen in this figure, the maximum temperature of the curves ($43.8\,^{\circ}\mathrm{C}$) is reached at the top of the external primary winding as expected (see red line). The primary winding temperature ($43.8\,^{\circ}\mathrm{C}$) is greater than the secondary winding temperature ($42.8\,^{\circ}\mathrm{C}$). The temperature at the top of the core remains constant ($32.5\,^{\circ}\mathrm{C}$) when the arc length $y$ varies upon the range [2-15]$\mathrm{cm}$ (see blue line). The temperature at the upper border of the fluid domain fluctuates between $30\,^{\circ}\mathrm{C}$ and $34\,^{\circ}\mathrm{C}$ in the fluid (see green line).
Let us evaluate now the velocity field components in the $(y, z)$ plane and $x = 0$. Figure (4.68) shows the evolution of the $z$ component of the velocity field $w$ along three measurement lines taken at different altitudes.

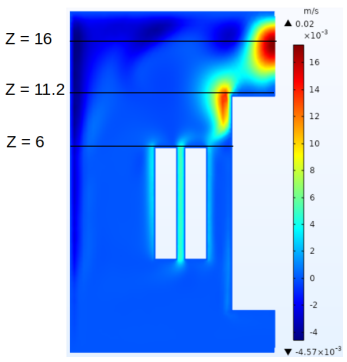


(a) Measurement lines (in solid line).

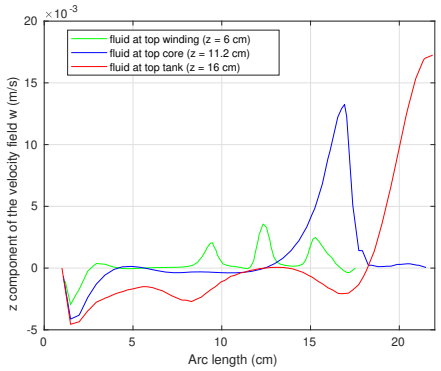


(b) Velocity $v_z$ versus the arc length $z$.

Figure 4.68: Evolution of the $z$ component of the velocity field (in $\mathrm{m.s^{-1}}$) in $(y, z)$ plane and $x = 0$ at a steady state $t = 15\,000\,\mathrm{s}$ using mesh 1.

As shown in these curves, the maximum velocity $v_z = 17.2\ \mathrm{mm.s^{-1}}$ is reached at the center of the convection cell located in the fluid domain at the top of the ferromagnetic core (see red line). The maximum velocity of the fluid at the upper corner of the core is $13.3\ \mathrm{mm.s^{-1}}$ (see blue line). The velocity profile at the top level of the windings shows a maximum velocity $w = 3.5\ \mathrm{mm.s^{-1}}$ of the fluid flow channeling the gap between the windings (see green line).
At a final step, we evaluate the $y$ component of the velocity field $v_y$ in the $(y, z)$ plane and $x = 0$. Figure (4.69) shows the evolution of the velocity $v_y$ along three measurement lines taken at different altitudes.

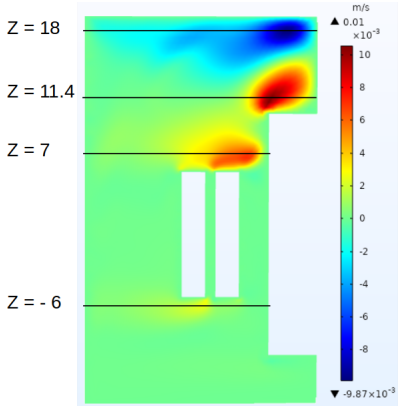


(a) Measurement lines (in solid line).

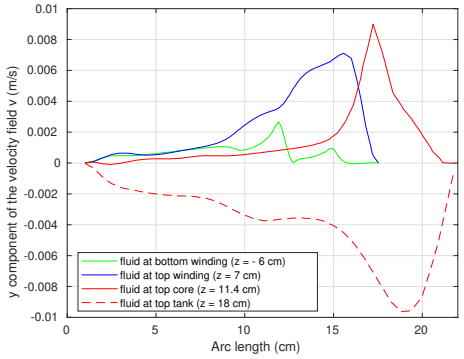


(b) Velocity $v$ versus the arc length $y$.

Figure 4.69: Evolution of the $y$ component of the velocity field (in $\mathrm{m.s^{-1}}$) in $(y, z)$ plane and $x = 0$ at a steady state $t = 15\,000\,\mathrm{s}$ using mesh 1.

Due to the convection cell shown in figure ((4.49)a), two-color spots, the first one in red color corresponding to a positive velocity $9\ \mathrm{mm.s^{-1}}$ and the second one in blue color corresponding to a negative velocity $-9.6\ \mathrm{mm.s^{-1}}$ appear (see dashed and solid red lines). While the maximum velocity $v$ is lower at the bottom level of the windings $2.6\ \mathrm{mm.s^{-1}}$ (see green line), it has a greater value $7.1\ \mathrm{mm.s^{-1}}$ that is reached at the center of the red spot located up to the secondary winding (see blue line).

At the end of this study, an experimental validation should be performed for cross-validation of the experimental and numerical results. This could validate the proposed 3D model of the power transformer. Due to the pandemic, it was difficult to develop the transformer bench to make temperature measurements. Another delay was caused by the ferrofluid solution that should be imported from the exterior of France.
For the modeling, the ferrohydrodynamic calculation with the magnetic force was not launched using mesh $1$ because of the large time that would be necessary for the simulation (months of calculation). The machine used for our mesh $0$ computations has low capacity comparing to the calculations needed. The coupling computations with mesh $1$ should be run on a cluster with a parallelized version of COMSOL Multiphysics.

## 4.5 Conclusions

A 3D study of the solenoid system is first performed to follow the path towards a 3D modeling. The numerical results are compared to those obtained with the 2D axisymmetric approach and show a good agreement in both hydrodynamic and ferrohydrodynamic cases.

Next, we have proposed a model for a power transformer and studied its cooling efficiency when ferrofluid solution is used. The 3D computation seemed challenging to be performed as a first step. Rather we have first considered a transformer's simplified structure to ensure the reliability of the multiphysics coupling theory with this kind of system. Therefore, a 2D axisymmetric model was performed to study the cooling performance in a $40\ \mathrm{kVA}$ simplified power transformer model. The numerical results were compared when the transformer is immersed in both regular oil and ferrofluid. The maximum temperature of the primary winding is reduced by $2\ ^{\circ}\mathrm{C}$ when the magnetic fluid replaces the regular oil. A new convection cell appears at the bottom of the windings and modifies the ferrofluid circulation inside the tank. It was then demonstrated that increasing the magnetic permeability of the steel in the tank may impact the cooling process. Consequently, the temperature of the primary winding decreases with the increase of the leakage flux in the ferrofluid domain. In parallel, it was shown that the temperature of the external conductor decreases when the gap thickness between the two conductors increases.

We have then performed a 3D study of this axisymmetric $40\ \mathrm{kVA}$ device when it is immersed in the regular oil. Numerical results showed good agreement between the 2D-axisymmetric and 3D approaches. Similar temperature and velocity fields were obtained showing that non-axisymmetric variation was not important for the chosen configuration.

Next, a 3D non-axisymmetric model for a $3\ \mathrm{kVA}$ power transformer was studied. We have considered the quarter of the 3D structure to reduce the computational resources needed. We have tested four approaches for the magnetostatic computation of the magnetic field in order to determine the magnetic leakage flux in the ferrofluid domain where the magnetic force influences. Comparing these approaches to the time-dependent magnetic calculation led to the best estimation of the magnetic field in the ferrofluid that was next used for the fluid-thermal-magnetic coupling.

We have first used a moderate 3D mesh (denoted by mesh $0$) to study a $3\ \mathrm{kVA}$ power transformer model. We have shown that the ferrofluid flow inside the tank is modified when the magnetic force is applied. A new convection cell appears again at the bottom of the conductors. The ferrofluid flow channeling the gap between the conductors is favored, and the windings cooling is thus improved. Consequently, the maximum temperature in the primary winding is reduced by $10\,^{\circ}\mathrm{C}$. Thus, the impact of the thermomagnetic convection is again validated on a 3D real structure of the power transformer. However, small scales in the temperature and velocity fields appear and question the spatial/temporal convergence of the computations performed with mesh $0$.

We have therefore conducted hydrodynamical runs using two other refined meshes denoted by mesh $1$ and mesh $2$. Comparing the results obtained with the three meshes determined that the mesh $1$ should be more efficient to study the ferrohydrodynamic problem and to confirm the preliminary very encouraging results that we obtained with mesh $0$, i.e., a decrease of $10\,^{\circ}\mathrm{C}$ in the maximum temperature reached in the quasi-steady regime. However, due to the lack of time and no access to a cluster, these computations are left for future investigation.

# Chapter 5

# Conclusion

## 5.1 Outcomes

This thesis has studied the thermomagnetic convection problem associated with ferrofluids for heat transfer application. We are interested in reducing the heating rise in electromagnetic devices, particularly in power transformers. This work has used both numerical and experimental approaches to understand the impact induced by the magnetic body force in these devices. We have first verified the impact of the thermomagnetic convection in a 2D-axisymmetric model of a heated solenoid, then validated the numerical results against the experimental setup. Next, it was proposed to model a structure of the power transformer by considering first a simplified 2D-axisymmetric model of a $40\ \mathrm{kVA}$ power transformer. In the last part, a 3D non-axisymmetric structure of an actual $3\ \mathrm{kVA}$ power transformer has been modeled to assess the cooling performance related to this innovative process.

### 5.1.1 Numerical modeling

We have considered a fully coupled fluid-thermal-magnetic approach to study the heat transfer problem associated with the ferrofluid motion using the finite element method. Therefore, we have worked with magnetostatic equations for studying the magnetic distribution, Navier-Stokes equations with magnetic force under Boussinesq approximation for the fluid dynamics, and the energy equation for the heat transfer problem. The ferrofluid has been considered as a continuum incompressible medium with homogeneous properties and Newtonian behavior. We have supposed that the magnetic field is proportional and collinear to the magnetization. We have used Langevin's theory in its linear form to describe the relationship between the ferrofluid magnetization and the magnetic field. The magnetic susceptibility of the ferrofluid has not been considered temperature-dependent because of the low impact induced by this dependence on the magnetic field. The impact of the magnetic field on the ferrofluid motion can be modeled using several models of the magnetic forces: Helmholtz, Kelvin, or Kelvin modified. The Kelvin force has been often used without any justification in the literature, while the Helmholtz one has been rarely modeled. The static magnetic field has been computed once for all (weak coupling of $\mathbf{H}$). Then the other variables ($\mathbf{u}$, $p$, $T$) have been evaluated using a strong coupling method.

**2D-axisymmetric model**

We have first considered the heat transfer problem in a simple electromagnetic system. It consists of a copper coil immersed in a ferrofluid. We have used two codes, COMSOL Multiphysics and SFEMaNS, to model the thermomagnetic convection in this system. The numerical results have shown a very good agreement after comparison and have validated the benefit of ferrofluid in enhancing the heat transfer. The maximum temperature in the coil was reduced by $2\,^{\circ}\mathrm{C}$ due to the effect of the thermomagnetic convection. Three models of the magnetic force have been modeled and led to the same velocity and temperature profiles. Our simulations confirm the possibility of using any of these forces to model the impact of the magnetic field on the ferrofluid. Nevertheless, some numerical instabilities could appear with the Kelvin expression of the magnetic force.

We have also performed two tests in order to improve the thermomagnetic convection in the solenoid system. The first test has concerned ferrofluid with nanoparticles of low Curie temperature. Numerical results have shown that using magnetic nanoparticles with low Curie temperature reduces the temperature of the coil. The second test has concerned the addition of a magnet to modify the magnetic field distribution generated by the coil in the ferrofluid and to study its effect on the cooling process. The associated results have confirmed the benefit of using a magnet to lower the maximum temperature in the coil, depending on the configuration of the magnet: direction, strength, location. We have also inserted a ferromagnetic core inside the solenoid model as a first approach for the transformer model. The relevant results have proved again the enhancement induced by the magnet on the heat transfer.

Next, a 2D-axisymmetric model for a simplified $40\ \mathrm{kVA}$ immersed power transfer has been studied. The objective was to verify the impact of the thermomagnetic convection on this system before working with more complex transformer structures. The results have shown that the maximum temperature in the windings is lowered by $2\,^{\circ}\mathrm{C}$ when the ferrofluid replaces the conventional transformer oil. The effect of the induced thermomagnetic convection added to the changes in the material properties of the fluid has been verified. Some optimizations have been then performed with the model. We have first increased the magnetic permeability of the "steel" tank to maximize the magnetic leakage flux in the ferrofluid and decrease the maximum temperature in the windings. We have also worked on the gap thickness between the coils, and a decrease in the maximum temperature of the windings has been also shown when increasing the gap thickness.
We have also performed a 3D computation to validate the $40\ \mathrm{kVA}$ simplified power transformer model when it is immersed in regular oil. Numerical results have shown a relatively good agreement between the 2D-axisymmetric and 3D approaches.

**3D non-axisymmetric model**

We have proposed to study a more realistic structure by considering a 3D-non axisymmetric model of a $3\ \mathrm{kVA}$ power transformer immersed in ferrofluid. We have performed first a time-dependent magnetic calculation to evaluate the magnetic field in the fluid. Then, we have considered several approaches to find an equivalent distribution of this magnetic field with a magnetostatic approach. The fluid-thermal-magnetic multiphysics numerical coupling has been realized. We have studied the cooling performance in this transformer, and have found an important decrease in the maximum temperature of the windings ($10\,^{\circ}\mathrm{C}$). At the end of this part, we have performed a numer-

ical study to optimize the mesh of this model regarding the computation capacities of the available machine. The comparison of the results obtained from this study has shown that a refined mesh should be more adapted to study the ferrohydrodynamic problem and to confirm the encouraging results obtained with the moderate mesh.

### 5.1.2 Experiments

An experimental setup has been developed at GeePs laboratory to study the heat transfer of a ferrofluid-immersed solenoid and to validate the numerical approach. The temperature measurements have first validated the impact of the magnetic field on the coil temperature. Then the experimental measurements have been compared against numerical ones, and they have presented a very good agreement (the relative error has been about $0.7\%$). An experimental test has been performed with an annular magnet to verify its impact on the heat transfer. The temperature of the coil has shown a decrease due to the addition of the magnet. The numerical/experimental cross-validation has also confirmed the impact induced by the magnet. The experiment has finally confirmed our choice of the model and of the boundary conditions applied in the modeling.

## 5.2 Perspectives

This work has answered many questions that arose at the beginning of the study, but some points are still to be worked on.

Concerning the modeling, we have verified the impact of the thermomagnetic convection on the heat transfer, and have assessed a large decrease in the maximum temperature of the coils of amount $10\,^{\circ}\mathrm{C}$ when the magnetic force is active. However, a ferrohydrodynamic calculation should be run with a more refined mesh of the 3D transformer model to confirm these encouraging results.

From an experimental point of view, temperature measurements on an actual $3\ \mathrm{kVA}$ power transformer prototype must be performed for cross-validation of the numerical and experimental results. While the modeling confirms the benefit of the thermomagnetic convection in the transformer, we have to verify this result with an experiment on an actual transformer and whether the proposed solution is viable for industrial deployment.

It also seems interesting to study the multiphysics problem by considering Langevin's theory in its classical form. This means that we shall consider the saturation of the magnetic field to study its influence on heat transfer. It is still challenging to know which expression of the magnetic force should be used when considering the non-linearity of the magnetic field.

A final point shall be clarified. We have proved the impact of magnets on the cooling process of the coil. The added magnet increases the magnetic leakage flux in the ferrofluid and thus improves the cooling in the solenoid system. However, in a power transformer, we tend to control the value of the leakage flux and concentrate the magnetic flux in the core to perform a better conversion between the windings. While the thermomagnetic convection requires an increase of the leakage flux in the power transformer, the power efficiency of this device could be reduced due to magnetic

flux leakage. We should find a compromise between the cooling performance of the transformer in terms of reducing its maximum temperature and its power efficiency from an electric point of view.

# Chapter 6

# Résumé en français

## 6.1 Introduction

La thèse porte sur une modélisation numérique et une étude expérimentale du transfert de chaleur au sein d'un système électromagnétique immergé dans un ferrofluide. Les ferrofluides sont constitués de nanoparticules ferromagnétiques dispersées dans un liquide porteur non magnétique, par exemple de l'huile végétale. L'ajout d'un surfactant et l'agitation thermique font de ce mélange une solution stable, et une bonne alternative aux huiles minérales dont les réserves s'amenuisent. Cette suspension magnétique et homogène réagit sous l'action d'un champ magnétique extérieur. Ainsi, en présence d'un gradient thermique, comme dans le cas d'un transformateur, le ferrofluide froid est attiré vers les bobinages, source simultanée de champ magnétique et de chaleur. Le fluide devenu chaud perd alors en partie son magnétisme et sera poussé par le fluide magnétique froid des alentours. La chaleur est ainsi transmise via le ferrofluide aux parois du système, puis à l'air ambiant. Ce phénomène de convection liée au champ magnétique est appelé convection thermo-magnétique. Cette dernière peut laisser envisager l'utilisation de systèmes électromagnétiques compacts, moins coûteux et moins polluants, et pouvant fonctionner sans avoir besoin d'une pompe mécanique.

Dans un premier temps, une étude expérimentale a été faite sur un dispositif simple représentatif du transformateur. Il s'agit d'un solénoïde immergé dans un bain de ferrofluide.
Une étude bibliographique a été menée pour déterminer les propriétés thermophysiques des nanoparticules ferromagnétiques, qui vont nous permettre ensuite de calculer les paramètres physiques du ferrofluide et du solénoïde immergé. Les premiers essais expérimentaux ont permis de valider l'effet de la convection thermo-magnétique sur le processus de refroidissement.

Des essais d'optimisation ont été menés pour améliorer le transfert de chaleur régissant ce type de systèmes électromagnétiques. Un aimant annulaire est ajouté à l'extérieur de la cuve du système élémentaire, et des simulations ont été lancées pour évaluer l'impact de cet aimant sur le refroidissement. Un champ magnétique supplémentaire est ainsi appliqué dans le processus et modifie la distribution des lignes de champ. Les simulations montrent que les champs de température et de vitesse sont impactés par la direction de l'aimantation de l'aimant et par son emplacement. D'autre part, une approche expérimentale a montré un accord qualitatif des résultats numériques et expérimentaux.

Nous nous sommes intéressés également à l'utilisation de suspensions à base de particules magnétiques à faible température de Curie. Les simulations menées ont vérifié la diminution de la température d'un point défini du solénoïde pour des ferrofluides de faibles températures de Curie.

Nous avons proposé un modèle numérique multi-physique pour un transformateur de puissance et étudié son efficacité de refroidissement lorsque la solution ferrofluide est utilisée. Dans un premier temps, nous avons considéré la structure simplifiée d'un transformateur pour assurer la fiabilité de la théorie de couplage multiphysique avec ce type de système. Ainsi, un modèle axisymétrique 2D a été réalisé pour étudier les performances de refroidissement dans un modèle simplifié de transformateur de puissance de $40\ \mathrm{kVA}$. Dans la dernière partie des travaux, une structure 3D non-axisymétrique d'un transformateur de puissance réel de $3\ \mathrm{kVA}$ a été modélisée pour évaluer les performances de refroidissement liées à ce procédé innovant.

## 6.2 Propriétés thermophysiques

Le ferrofluide est une suspension colloidale de nanoparticules ferromagnétiques dans un liquide porteur. Ces nanoparticules sont souvent des particules métalliques comme du fer, nickel, cobalt ou leurs oxydes magnétiques (ferrite, magnétite). Dans notre cas, les ferrites de cobalt sont les particules ensemencées dans notre fluide de base, l'huile Midel eN 1215.

Les propriétés utilisées dans la simulation du solénoïde sont données dans la table (6.1).

| Propriétés | Cuivre | Aluminium | PVC | Ferrite de Cobalt | Solénoïde | Huile | Ferrofluide |
|---|---|---|---|---|---|---|---|
| Densité (kg/m$^3$) | 8933 | 2.70e3 | 1.4e3 | 5.39e3 | 3.9639e3 | 922 | 1.0455e3 |
| Expansion thermique (k$^{-1}$) | - | - | - | | - | 7.4e-4 | 7.0004e-4 |
| Capacité calorifique (J/kg.k) | 385 | 945 | 1e3 | 604 | 616.0276 | 1970 | 1.7753e3 |
| Cond. therm. (W/m.k) | 401 | 201 | 0.16 | 4.1 | 0.3880 | 0.166 | 0.1785 |
| Viscosité dynamique (Pa.s) | - | - | - | - | - | 2.9e-2 | 0.0545 |

Table 6.1: Propriétés matériaux utilisées dans la simulation numérique.

Pour le calcul thermique, le coefficient d'échange choisi est $h = 6.5\ W/m^2.K$ (valeur optimisée) avec une température de référence $T_0 = 22C$.

## 6.3 Effet de la convection thermomagnétique

L'objectif de cette partie est d'étudier l'effet de la convection thermomagnétique sur le transfert de chaleur en utilisant les deux approches numérique et expérimentale. Le dispositif expérimental est constitué d'un solénoïde immergé dans un cylindre, rempli avec du ferrofluide à base de ferrite

de Cobalt. La solution contient un surfactant, qui est souvent de l'acide oléique (épaisseur $s = 2\ nm$). Le liquide porteur est l'huile végétale Midel eN 1215.

### 6.3.1 Approche numérique

La théorie de Langevin linéaire sous faible champ magnétique est utilisée pour décrire la dépendance de l'aimantation du ferrofluide avec la température :

$$M = \chi(T)H \tag{6.1}$$

avec $\chi$ la susceptibilité magnétique du ferrofluide donnée par :

$$\chi(T) \ = \frac{\phi\ \mu_0\ \pi\ d^3 M_{s,p}(T)^2}{18\ k_B\ T} \tag{6.2}$$

où $\phi$ est la fraction volumique de matériau magnétique, $d$ est le diamètre moyen des particules, $M_0$ est l'aimantation à saturation de la particule dépendante de la température, $k_B$ est la constante de Boltzmann, et $\mu_0$ est la perméabilité magnétique du vide ($\mu_0 = 4\pi.10^{-7} H.m^{-1}$).

Les équations de la ferrohydrodynamique (Navier-Stokes, Énergie et Magnétostatique) sont utilisées pour résoudre le problème de couplage multiphysique :

$$\begin{cases}
\rho c \partial_t T + \rho c \tilde{\mathbf{u}} \cdot \nabla T - \nabla\cdot(\lambda \nabla T) = P_v & \text{dans } \Omega \\
-\lambda \nabla T \cdot \mathbf{n} = h(T - T_0) & \text{sur } \partial\Omega_{\text{lat,dessus}} \\
-\lambda \nabla T \cdot \mathbf{n} = 0 & \text{sur } \partial\Omega_{\text{dessous}} \\
T|_{t=0} = T_0 & \text{dans } \Omega \\
\partial_t \mathbf{u} + (\nabla\times\mathbf{u}) \times \mathbf{u} + \nabla\left(\frac{p}{\rho_0}\right) - \nabla\cdot(2\nu\nabla^s \mathbf{u}) = \alpha(T - T_0) g \mathbf{e}_z - \frac{\mu_0 H^2}{2\rho_0}\nabla\chi(T) & \text{dans } \Omega_\text{f} \\
\nabla\cdot\mathbf{u} = 0 & \text{dans } \Omega_\text{f} \\
\mathbf{u} = 0 & \text{sur } \partial\Omega_\text{f} \\
\mathbf{u}|_{t=0} = 0 & \text{dans } \Omega_\text{f} \\
\nabla\times\mathbf{H} = \mathbf{j} & \text{dans } \Omega \\
\nabla\cdot(\mu\mathbf{H}) = 0 & \text{dans } \Omega \\
\mathbf{H} \times \mathbf{n} = 0 & \text{sur } \partial\Omega
\end{cases}$$

Notations : $\tilde{\mathbf{u}} = \mathbf{u}$ dans $\Omega_\text{f}$, $\tilde{\mathbf{u}} = \mathbf{0}$ dans $\Omega \setminus \Omega_\text{f}$; $\nabla^s \mathbf{u} = \frac{1}{2}\left(\nabla\mathbf{u} + (\nabla\mathbf{u})^T\right)$

$P_v$ est la puissance thermique volumique dissipée dans le solénoïde ($P_v = 6.14 \times 10^5\ W/m^3$ et les termes en couleur à droite de l'équation de Navier-Stokes sont les termes des Forces de Boussinesq et de Helmholtz. On utilise ici l'approximation de Boussinesq avec un fluide newtonien incompressible.

### 6.3.2 Comparaison des résultats numériques et expérimentaux

La bobine d'essai correspond à un conducteur bifilaire en cuivre. Lorsque les directions du courant dans les deux fils sont les mêmes, un champ magnétique non nul est produit par le solénoïde. Dans ce cas, la force magnétique et l'effet Joule sont activés. Si les directions du courant sont opposées, seul l'effet Joule est actif. On peut ainsi montrer l'effet de la force magnétique sur le transfert de chaleur pour une configuration expérimentale.

La force magnétique de Helmholtz est ainsi périodiquement activée puis désactivée sur une période de 7200 s. À $t = 0\ s$, cette force est active. L'évolution temporelle de la température est montrée dans la figure (6.1). Les résultats numériques et expérimentaux s'accordent qualitativement et quantitativement, et montrent que les conditions du problème étudié sont respectées.

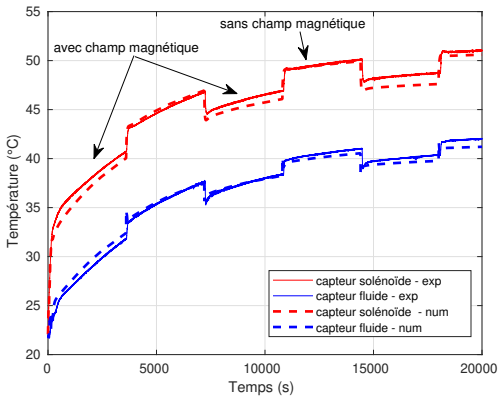


Figure 6.1: Résultats numériques et expérimentaux de la température avec/sans force magnétique.

Les distributions spatiales de température et de vitesse à $t = 16800\ s$ (lorsque la force de Helmholtz est activée) et à $t = 19800\ s$ (lorsque la force de Helmholtz est désactivée) sont montrées dans les figures (6.2) et (6.3).

Les résultats de la figure (6.2) prouvent que la force de Helmholtz influe sur les panaches de température. Si la force magnétique est activée, le panache de température est dévié dans l'espace au dessus du solénoïde, bien qu'il soit centré sur l'axe de symétrie lorsque cette force est désactivée. Cette déviation est due à une recirculation au dessous de la bobine qui pousse le fluide chaud loin de l'axe (voir figure ((6.3)a)). En l'absence de la force de Helmholtz, cette recirculation n'apparaît pas.

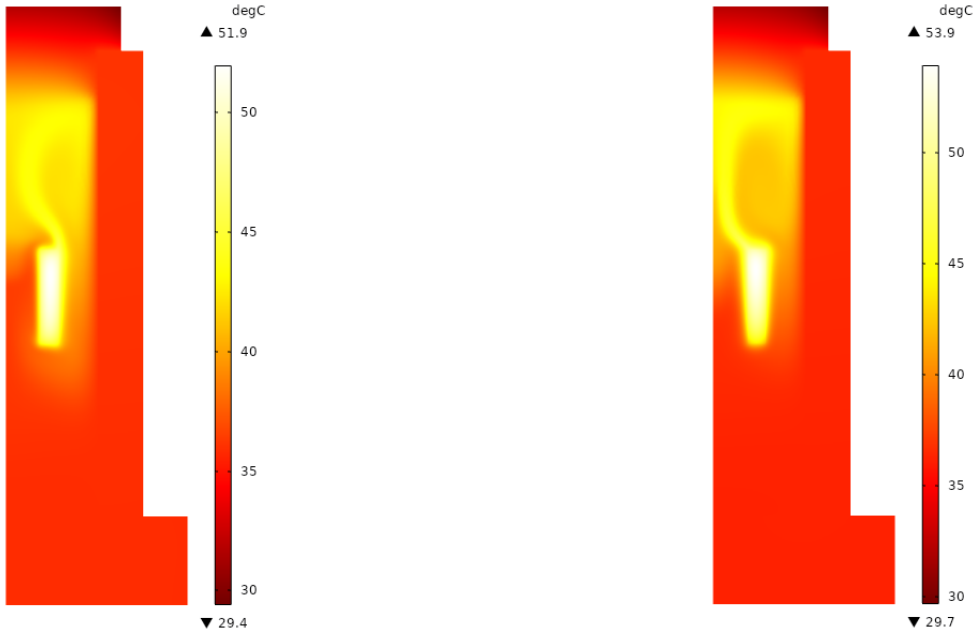


(a) Force magnétique activée (b) Force magnétique désactivée

Figure 6.2: Cartographies de la température en (°C) avec et sans force magnétique.

La température maximale du solénoïde diminue de $1.8\,°\mathrm{C}$ lorsque la force de Helmholtz est activée, et l'effet de la convection thermomagnétique est ainsi vérifié.

## 6.4 Amélioration de la convection thermomagnétique

### 6.4.1 Influence de la température de Curie des nanoparticules

Afin de vérifier l'intérêt des matériaux ferromagnétiques à faible température de Curie, la loi de Bloch est prise en compte pour considérer l'aimantation à saturation des nanoparticules :

$$M_{s,p}(T) = \begin{cases} M_{s,p}(0)(1 - (\frac{T}{T_c})^{1.5}) & \text{si } T \leq T_c, \\ 0 & \text{si } T \geq T_c \end{cases} \tag{6.3}$$

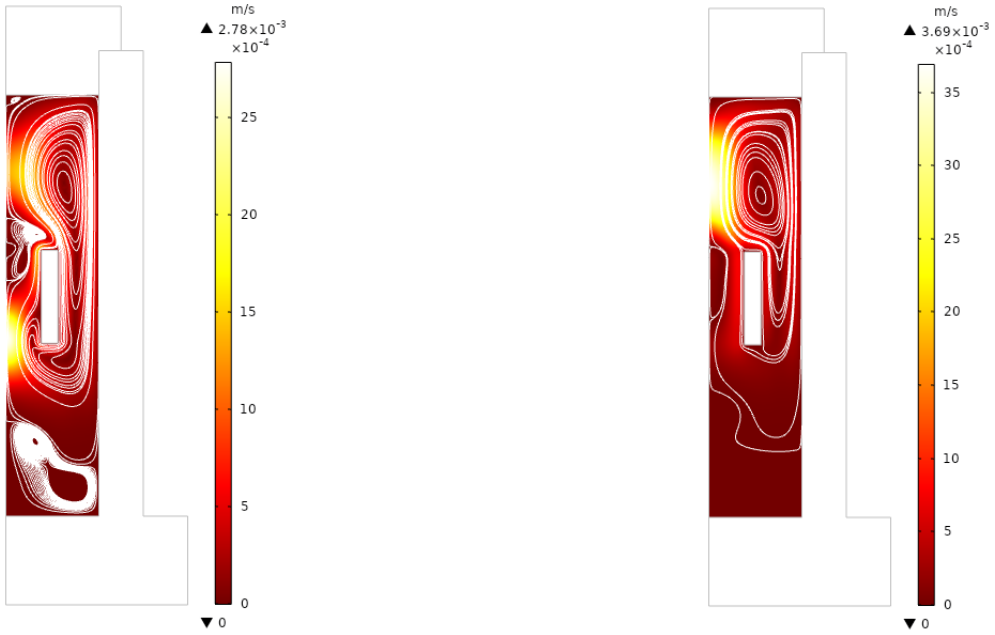


(a) Force magnétique activée (b) Force magnétique désactivée

Figure 6.3: Cartographies de la vitesse en $\mathrm{m\,s^{-1}}$ avec et sans force magnétique.

avec $T_c$ la température de Curie. Selon cette loi, plus $T_c$ est faible, plus l'intensité de l'aimantation à saturation du ferrofluide est importante.
Le calcul numérique montre que la température du dessus du solénoïde (0.01, 0.08) en régime permanent est d'autant plus faible que la température de Curie diminue (voir figure ((6.4)b)). Ce résultat est en accord avec les tests réalisés dans [13], dans le contexte d'amélioration de la convection thermomagnétique avec les ferrofluides.

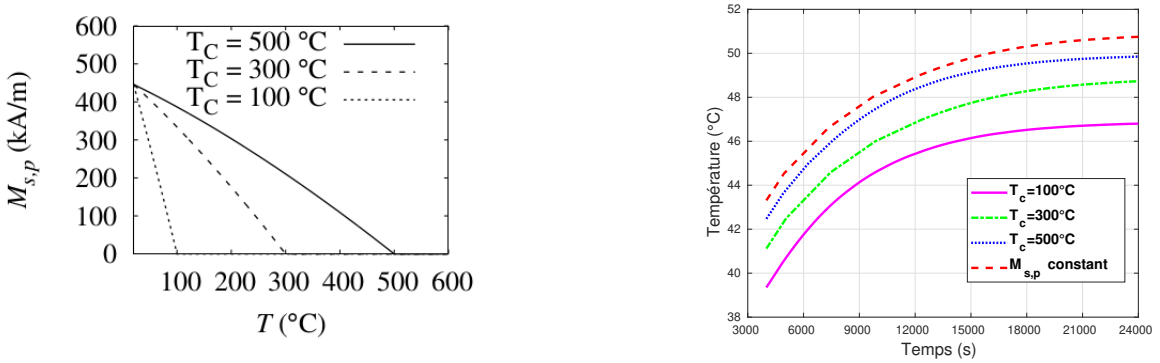


(a) Loi de Bloch (b) Température à la surface du solénoïde

Figure 6.4: Impact de la température de Curie sur le refroidissement.

### 6.4.2 Impact d'un aimant auxiliaire sur le refroidissement

L'étude proposée dans la suite s'intéresse à l'impact de l'ajout d'un aimant annulaire placé à l'extérieur du dispositif sur le refroidissement. Différentes configurations ont été analysées à l'aide du modèle numérique, avec comme paramètres la position de l'aimant et l'orientation de son aimantation rémanente [97]. La première partie présente le dispositif expérimental et le modèle régissant le couplage multiphysique. Dans la deuxième partie, des mesures expérimentales sont comparées aux résultats de la simulation numérique pour valider l'apport de l'aimant dans le refroidissement du système.

#### Dispositif expérimental et couplage multiphysique

Le système étudié est un solénoïde en cuivre immergé dans un ferrofluide à base de ferrite de cobalt. Il est placé dans une cuve en aluminium, fermée par le dessus par un bouchon de PVC comme le montre la figure (6.5). Un aimant torique de section carrée est placé contre la cuve pour étudier l'impact du champ extérieur fourni par ce dernier. Les dimensions du dispositif expérimental sont données dans la table (6.2). Le ferrofluide utilisé est considéré comme étant un fluide Newtonien incompressible, homogène et continu.

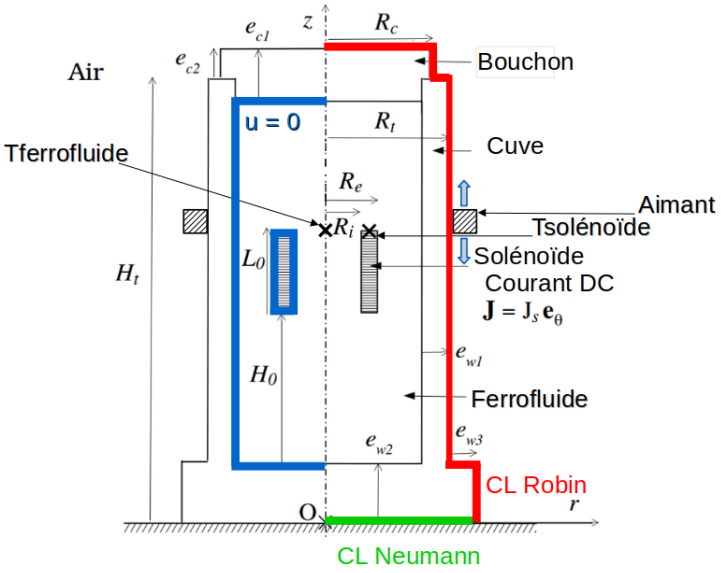


Figure 6.5: Dispositif expérimental, hauteur de la cuve $H_t = 12,5\ cm$.

Les équations de Navier-Stokes décrivant le mouvement du fluide s'expriment par :

$$\begin{cases} \nabla{\cdot}\mathbf{u} = 0, \\ \rho_l \dfrac{D\mathbf{u}}{Dt} + \nabla p - \nabla{\cdot}\mathbb{e}(T,\mathbf{u}) = \rho_l \beta g (T - T_0)\mathbf{e_z} + \mathbf{F}, \end{cases} \tag{6.4}$$

où $\mathbf{u}$ est le vecteur vitesse, $\frac{D}{Dt}$ la dérivée matérielle, $p$ la pression, $\mathbb{e}(T,\mathbf{u}) = \eta(T)(\nabla\mathbf{u} + (\nabla\mathbf{u})^{\mathsf{T}})$ avec $\eta$ la viscosité dynamique (variant en $\eta(T) = Af(\phi)\exp(BT^{-1})$ avec $A = 1,3 \times 10^{-6} Pa.s$, $B = 3,1 \times 10^3\ K$ et $f(\phi)$ donné par le modèle de Rosensweig (voir [13], p. 105), $\rho_l$ la densité,

| Paramètre | $H_t$ | $R_t$ | $e_{w1}$ | $e_{w2}$ | $e_{w3}$ | $H_0$ |
|---|---|---|---|---|---|---|
| Valeur (cm) | 12,5 | 3,1 | 1 | 2 | 1 | 3,9 |
| Paramètre | $L_0$ | $R_i$ | $R_e$ | $R_c$ | $e_{c1}$ | $e_{c2}$ |
| Valeur (cm) | 2,1 | 0,8 | 1,175 | 2,6 | 2 | 1 |

Table 6.2: Dimensions du dispositif expérimental

$\beta$ le coefficient d'expansion thermique, et $g$ l'accélération de pesanteur. Les deux termes à droite de l'équation de la quantité de mouvement sont respectivement la force de Boussinesq et la force magnétique.
Le transfert de chaleur dans le ferrofluide et avec le milieu extérieur est décrit par l'équation d'énergie :

$$\rho_l C_p \frac{DT}{Dt} = \nabla \cdot (\lambda \nabla T) + Q, \tag{6.5}$$

où $C_p$ est la capacité calorifique à pression constante, $\lambda$ la conductivité thermique et $Q$ la source de chaleur volumique dissipée par effet Joule dans le cuivre et donnée par $\frac{1}{\sigma} J_s^2$ (où $\sigma$ est la conductivité électrique du cuivre, et $J_s$ la densité de courant dans le solénoïde).
Le champ magnétique appliqué est statique et l'aimantation du ferrofluide est supposée instantanément alignée avec le champ magnétique. Les équations de la magnétostatique pour le ferrofluide sont données par :

$$\boldsymbol{\nabla} \times H = \mathbf{J}, \quad \nabla \cdot (\mu \mathbf{H}) = 0, \quad \mu = \mu_0 (1 + \chi(T_0)), \tag{6.6}$$

où **J** = $J_s \mathbf{e}_\theta$ et $\mu$ est la perméabilité magnétique du ferrofluide.
Pour le calcul numérique magnétique, une couche d'air est ajoutée autour de la cellule d'essai pour assurer la fermeture des lignes du champ magnétique conforme à la réalité. La condition limite magnétique imposée sur les parois de l'air est $\mathbf{A} \times \mathbf{n} = \mathbf{0}$, **A** étant le potentiel vecteur magnétique, et une condition de non glissement $\mathbf{u} = \mathbf{0}$ est appliquée sur les parois du domaine fluide. Thermiquement, une condition limite de type Robin est imposée sur les parois supérieure et latérale de la cuve, afin de modéliser le transfert de chaleur avec l'air ambiant :

$$-\lambda \nabla T \cdot \mathbf{n} = h(T - T_0), \tag{6.7}$$

où $h$ est le coefficient d'échange thermique et **n** le vecteur unitaire sortant et normal à la cuve. Une condition de type Neumann homogène est appliquée sur la frontière inférieure de la cuve $\partial_z T = 0$. Les conditions initiales sont $\mathbf{u} = \mathbf{0}$ et $T = T_0$.
Les propriétés physiques utilisées dans les équations de Navier-Stokes et de chaleur sont données dans la table (6.3). Le coefficient de transfert de chaleur est fixé à $h = 6,5\ W/m^2.K$. Les autres paramètres sont $\phi = 5,4\ \%$, $d = 16\ nm$, $M_0 = 3,87 \times 10^5\ A/m$, $T_c = 793\ K$. Le courant électrique dans le solénoïde est $I = 8\ A$ avec une densité de courant $J_s = 3,35 \times 10^6\ A/m^2$, la conductivité électrique $\sigma = 5,998 \times 10^7\ S/m$ et le nombre de spires $N = 33$.

| Propriétés | Cu | Al | PVC | Solénoïde | Ferrofluide |
|---|---|---|---|---|---|
| Densité (kg/m$^3$) | 8933 | 2.70e3 | 1.40e3 | 3.964e3 | 1.045e3 |
| Expansion therm. (/K) | - | - | - | - | 7.0004e-4 |
| Capacité calorifique (J/K·kg) | 385 | 945 | 1e3 | 616 | 1.775e3 |
| Cond. therm. (W/m·K) | 401 | 201 | 0.16 | 0.388 | 0.1785 |
| Viscosité dyn. (Pa.s) | - | - | - | - | 0.0703 |

Table 6.3: Propriétés physiques utilisées en simulation numérique.

**Résultats et comparaison**

Plusieurs configurations de position d'aimant et d'orientation de son aimantation rémanente ont alors été modélisées, et cette partie présente la solution qui semble la plus intéressante pour le processus de refroidissement. Un aimant annulaire ($\Phi$ 140 $\times$ 63 $\times$ 17 $mm$) ayant une induction rémanente axiale $B_z = 0,2T$ est ainsi placé contre la cuve à une hauteur optimale de 65 $cm$ par rapport au fond de la cuve. Deux thermocouples sont utilisés pour mesurer la température en surface du solénoïde et dans le fluide (voir figure 1), la température ambiante étant pour cette expérience $T_0 = 288\ K$. En parallèle de la partie expérimentale, un calcul numérique a été lancé pour enregistrer les évolutions de la température aux mêmes points de mesure. Les résultats des deux tests sont présentés dans la figure (6.6).

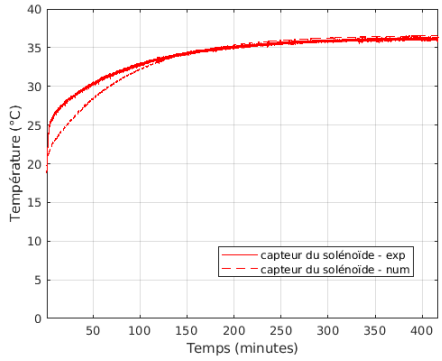


(a) Températures au niveau du solénoïde, $B_z = -0,2\ T$

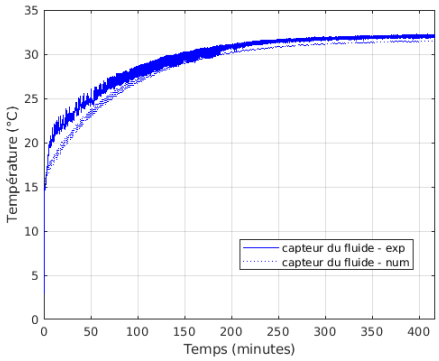


(b) Températures au niveau du fluide, $B_z = -0,2\ T$

Figure 6.6: Comparaison numérique et expérimentale en présence de l'aimant.

Une différence de constante de temps en régime transitoire est observée, avec un temps de diffusion thermique plus rapide en expérimental qu'en numérique, peut-être lié au modèle thermique homogénéisé de la bobine. Les températures en régime permanent sont par contre très proches pour les deux points de mesure. Pour évaluer l'impact des aimants auxiliaires sur le processus de refroidissement, deux essais expérimentaux ont été comparés : le premier en présence de l'aimant axial, et l'autre en absence de ce dernier. Les courbes de température sont présentées dans le graphe de la figure (6.7).

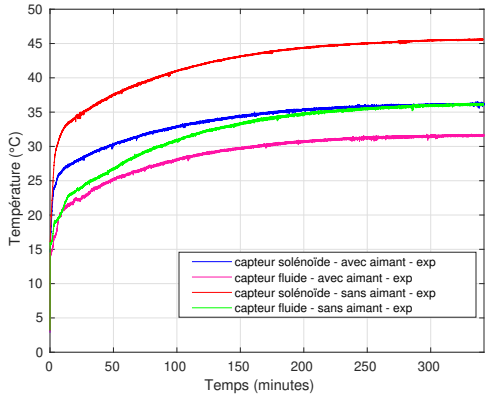


Figure 6.7: Mesures de température, comparaison avec/sans aimant axial.

On remarque que, dans le cas où l'aimant axial est présent, la température de surface du solénoïde est diminuée de $9\,°\mathrm{C}$ environ. Ceci s'explique par l'intensification des flux magnétiques dans le ferrofluide, ce qui amplifie l'amplitude de la force magnétique, et maximise l'écoulement du fluide autour du bobinage. Les échanges thermiques avec l'extérieur sont ainsi directement favorisés.

### Cartographies de vitesse et de température

Deux calculs numériques ont été lancés dans deux configurations différentes : la première en présence d'un aimant axial, la seconde en son absence. Les cartographies de champ magnétique, de vitesse et de la température à $t = 25000\ s$ sont présentées sur les figures (6.8), (6.9) et (6.10) respectivement pour chacun des deux cas.

(a) Intensité du champ magnétique $(A/m)$, sans aimant

(b) Intensité du champ magnétique $(A/m)$, $B_z = -0,2\ T$

Figure 6.8: Distributions du champ magnétique

La comparaison des champs de vitesse et de température à $t = 25000\ s$ confirme la modification de la circulation du fluide autour du solénoïde, et par conséquent l'effet apporté par l'aimant

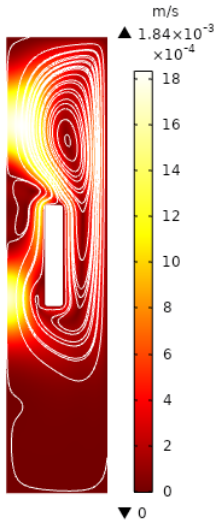


(a) Intensité de la vitesse avec lignes de courant, sans aimant

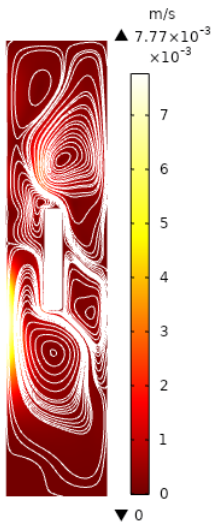


(b) Intensité de la vitesse avec lignes de courant, $B_z = -0,2\ T$

Figure 6.9: Distributions de la vitesse

extérieur sur le refroidissement. Lorsque l'aimant n'est pas ajouté (voir figure ((6.8)a)), seul le champ magnétique du solénoïde est présent. Les circulations du fluide (de la figure ((6.9)a)) sont dues à la présence de la force magnétique s'exerçant sur le ferrofluide en plus de la force de Boussinesq d'origine thermique. La figure ((6.10)a) montre que le panache de température émerge du solénoïde, se rapproche de l'axe de symétrie (bord gauche de la figure), puis se courbe vers l'extérieur.

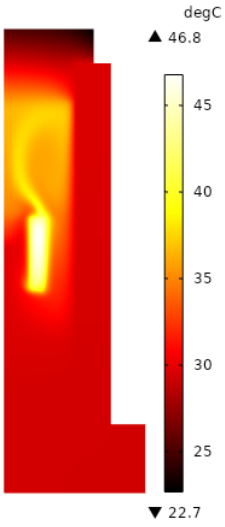


(a) Température, sans aimant

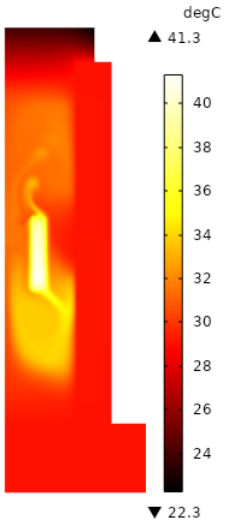


(b) Température, $B_z = -0,2\ T$

Figure 6.10: Distributions de la température

En présence de l'aimant axial $B_z = -0,2\ T$ (voir figure ((6.8)b)), des modifications dans les

circulations du fluide apparaissent dans la partie située sous le solénoïde (voir figure ((6.9)b)) qui amplifient l'évacuation de la chaleur. La vitesse est augmentée. Ceci est causé par la modification des lignes de champ et l'intensification des flux magnétiques dans le fluide. Un nouveau panache thermique apparaît se déplaçant vers le bas et l'extérieur comme cela est montré sur la figure ((6.10)b) : il est entraîné par les deux cellules inférieures de circulation du fluide. Un autre panache ascendant et moins actif est présent dans la partie supérieure de la cuve. Il suit les contours des cellules de convection supérieures.
En conséquence de ces nouvelles circulations du fluide, la température maximale du solénoïde est abaissée de $5.5\,°\mathrm{C}$. L'impact positif de l'ajout d'un aimant auxiliaire sur le refroidissement du solénoïde est vérifié.

Concernant les évolutions temporelles, les courbes de la figure (6.11) permettent d'observer la température en des points définis respectivement à la surface du solénoïde et dans le fluide dans les deux configurations : la première lorsque le champ magnétique du solénoïde est seul présent, la seconde concerne le cas où l'aimant extérieur est présent.

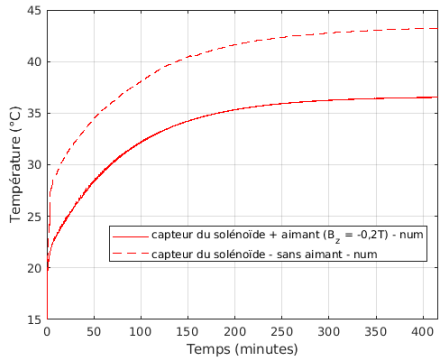


(a) Températures au niveau du solénoïde

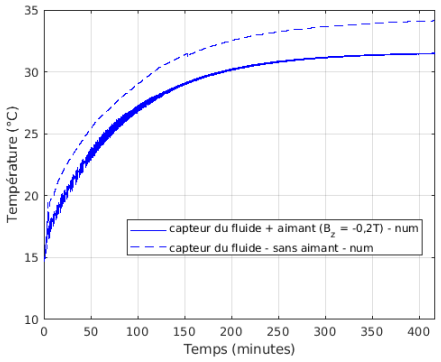


(b) Températures au niveau du fluide

Figure 6.11: Comparaison des évolutions temporelles de la température.

Les courbes de température atteignent un régime stationnaire après environ $25000\ s$ que ce soit pour le fluide ou le bobinage. Pour le bobinage, une diminution de $7\,°\mathrm{C}$ est à noter en présence de l'aimant. Pour le fluide, une diminution moins importante de la température de l'ordre de $3\,°\mathrm{C}$ est enregistrée. Des oscillations sur la courbe de température du fluide sont présentes pendant le régime transitoire pour une durée de $7500\ s$ environ lorsque l'aimant est ajouté.

## 6.5 Modélisation d'un transformateur 40 kVA

L'une des applications industrielles intéressantes qui pourrait intégrer l'emploi des ferrofluides comme liquide de refroidissement afin de réduire l'échauffement excessif des composants, est le transformateur de puissance.
En général, ce dernier est refroidi par de l'huile minérale, dont les effets biologiques néfastes et la disparition progressive sont les principaux inconvénients. Des essais avec de l'huile végétale associée à des particules ferromagnétiques permettent d'envisager des diminutions de température des bobinages lorsque ce genre de suspensions est soumis à un champ magnétique.

Dans ce contexte, nous essayons de modéliser un transformateur de puissance de 40 kVA, de 0.46 m de hauteur, et en structure 2D.

Les principales caractéristiques du transformateur modélisé sont résumées dans le tableau de la figure (6.12).

| | Tension (V) | Courant (A) | Nombre de spires |
|---|---|---|---|
| Primaire | 20 000 | 2 | 10000 |
| Secondaire | 400 | 100 | 200 |

Figure 6.12: Caractéristiques du transformateur modélisé.

Nous considérons une structure très simple du transformateur ((6.13)a) dans le plan (r, z), et dont le maillage choisi est donné en figure ((6.13)b).

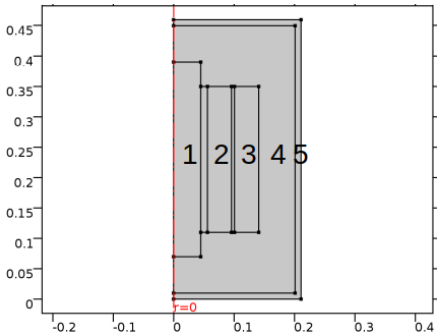


(a) Modèle du transformateur

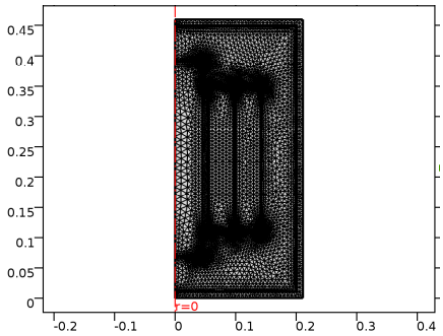


(b) Maillage fin du modèle

Figure 6.13: Modèle COMSOL du transformateur 40 kVA.

Les numéros attribués aux éléments de géométrie du schéma représentatif de la figure ((6.13)a) réfèrent chacun aux éléments constituant la structure du transformateur:

1. le coeur ferromagnétique en fer de perméabilité magnétique $\mu_r = 4000$ ;
2. le circuit secondaire en cuivre engendrant une densité de courant $j_0 = -2\ A.mm^{-2}$;
3. le circuit primaire en cuivre engendrant une densité de courant $j_0 = 2\ A.mm^{-2}$;
4. l'huile magnétique (huile végétale Midel + ferrite de cobalt) avec une fraction volumique de nanoparticules $\phi = 1\%$;
5. la cuve en acier.

Les propriétés thermophysiques des matériaux du modèle sont présentées dans le tableau de la figure (6.14).

| | Masse volumique (kg/m³) | Capacité thermique (J/kg.K) | Conductivité thermique (W/m.K) | Viscosité dynamique (Pa.s) |
|---|---|---|---|---|
| Acier | 7850 | 475 | 44.5 | - |
| Cuivre | 8933 | 385 | 401 | - |
| Fer | 7870 | 447 | 80 | - |
| Ferrofluide | 965 | 1898 | 0.171 | 0.065 |
| Huile classique | 922 | 1970 | 0.166 | A exp(B/T) |

Figure 6.14: Propriétés thermophysiques des matériaux du transformateur modélisé.

La viscosité dynamique de l'huile classique varie fortement avec la température suivant la loi d'Andrade $\mu(T) = A\ exp(\frac{B}{T})$, avec $A \simeq 1,3.10^{-6} Pa.s$ , $B \simeq 3,1.10^3 K$.
Les conditions limites et initiales appliquées au modèle du transformateur sont identiques à celles utilisées pour le modèle de la bobine, et sont représentées dans la figure ((6.15)a).

Pour le choix de la structure du modèle, nous simulons la partie extérieure du transformateur 3D (voir figure ((6.15)b), vue de dessus [86]), sans tenir compte des jambes extérieures du circuit magnétique. Pour notre modèle, nous choisissons un coefficient h = 150 $W.m^{-2}.K^{-1}$ simulant la présence des ailettes de refroidissement, et favorisant l'échange convectif libre de la chaleur cuve-air.

### 6.5.1 Comparaison des résultats numériques

Des simulations numériques ont été lancées lorsque le liquide refroidisseur est de l'huile classique, puis avec du ferrofluide, afin de discerner les changements induits par le choix du type de fluide, et de connaître le gain de température lié au phénomène de la convection thermomagnétique.

Nous essayons dans un premier temps de comparer les courbes de température obtenues aux centres des deux conducteurs interne et externe en fonction du temps. Le régime permanent est atteint

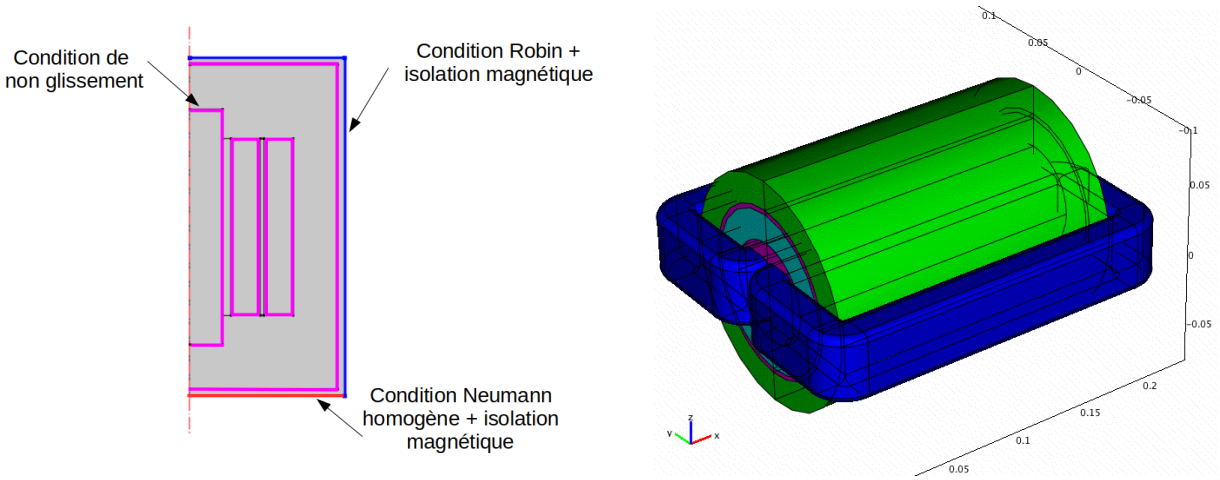


(a) Conditions aux limites (b) Structure 3D du transformateur [86]

Figure 6.15: Conditions aux limites et géométrie 3D.

après environ 3 heures (10000 s).
Pour le conducteur primaire externe (voir figure ((6.16)a)), on remarque une évolution plus rapide de la température avec l'huile magnétique qu'avec l'huile classique, au bout de 6000 s environ (1h 40 min). Au delà de 6000 s, la température monte légèrement avec l'huile classique avec une différence de température de $1.8\,°C$.
Cela indique que la convection thermomagnétique, bien qu'elle soit moins intense que dans le cas précédent, joue un certain rôle dans l'évacuation de la chaleur du système, en profitant de la présence des particules magnétiques en suspension, soumises au champ de fuite.

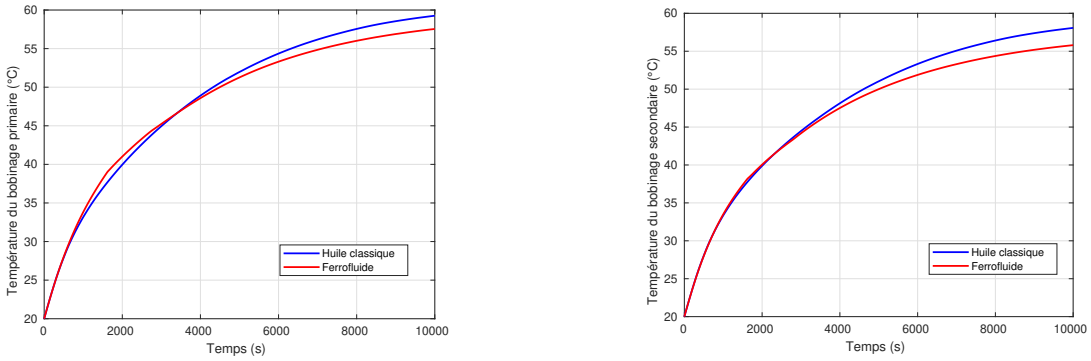


(a) Conducteur primaire (b) Conducteur secondaire

Figure 6.16: Evolutions temporelles de la température aux centres des bobinages.

Regardons maintenant les mêmes évolutions de la température pour le conducteur secondaire interne (voir figure ((6.16)b)). On voit une évolution quasiment identique sur le régime transitoire. En régime permanent, la température avec l'huile magnétique est bien inférieure à celle obtenue en présence de l'huile classique. Cette différence de température de 2.2 °C montre que le conducteur interne est bien refroidi par rapport au conducteur externe, révélant ainsi un gain de température très intéressant dans les domaines industriels. En effet, une diminution de $6\,°C$ de la température

du transformateur permettrait de doubler la durée de vie de ce dernier.

### 6.5.2 Distributions de température et de vitesse

L'analyse des distributions de température relatives à la présence de chaque type de fluide est importante, afin de pouvoir détecter les zones les plus chaudes dans l'entourage des bobinages, et de prévoir la relation entre les caractéristiques thermophysiques de ces liquides magnétiques et le refroidissement du processus. De même, l'étude des champs de vitesse est indispensable à la compréhension du comportement du liquide magnétique lors de son échauffement, pour quantifier l'influence de la convection thermomagnétique sur le changement des cartographies de vitesse en passant de l'huile vers le ferrofluide. Les distributions de température sont représentées à l'aide du logiciel Paraview dans la figure (6.17).

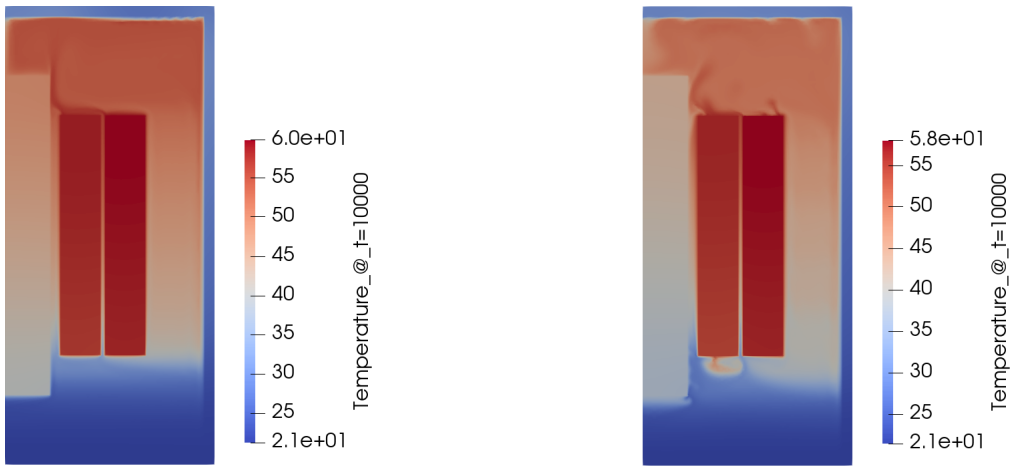


(a) Huile classique (b) Huile magnétique ($\phi = 1\%$)

Figure 6.17: Distribution de la température en (°C) à $t = 10\,000\,\mathrm{s}$.

Un abaissement de la température maximale de 1.8 °C est enregistré en remplaçant l'huile classique par le fluide magnétique, ce qui vérifie l'impact de la convection thermomagnétique sur le processus de refroidissement. Des panaches thermiques apparaissent en bas des bobinages en présence du liquide magnétique, et cela montre une modification de la diffusion de la chaleur dans le liquide, et par la suite un refroidissement plus efficace.

Les distributions de vitesse sont montrées dans la figure (6.18). De nouvelles cellules de convection sont ici aussi décelées avec le ferrofluide, permettant ainsi un mouvement plus rapide du liquide magnétique, et un refroidissement plus rapide des bobinages.
La vitesse maximale atteinte en régime permanent est inférieure dans le cas où la convection thermomagnétique agit (avec l'huile magnétique). Ceci peut être expliqué par la différence de température maximum en régime stationnaire: avec l'huile magnétique, la température atteinte est de $58\,^{\circ}\mathrm{C}$, alors que l'on obtient $59.8\,^{\circ}\mathrm{C}$ avec l'huile classique. Donc un gradient de température plus intense sera présent dans l'huile classique, laissant place à une vitesse plus importante.

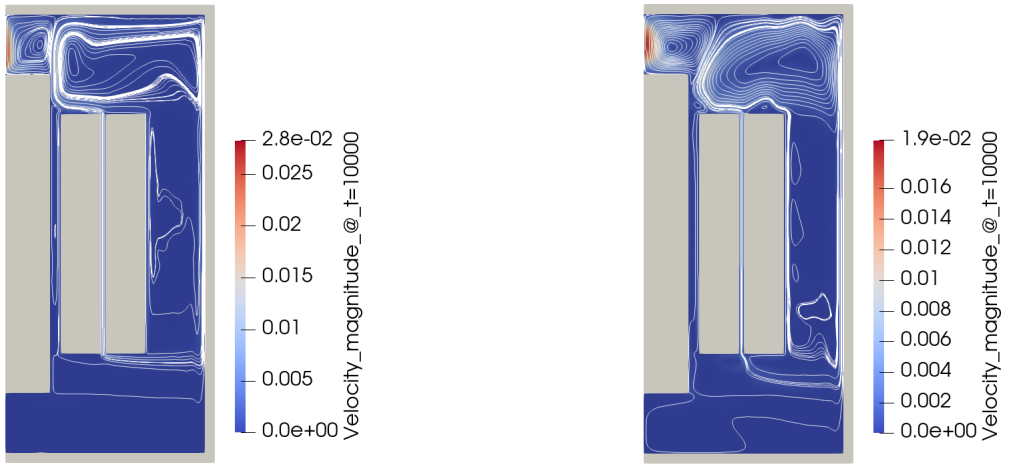


(a) Huile classique (b) Huile magnétique ($\phi = 1\%$)

Figure 6.18: Distribution de la vitesse en ($\mathrm{m\,s^{-1}}$) à $t = 10\,000\,\mathrm{s}$.

## 6.6 Modélisation d'un transformateur 3 kVA

Cette partie présente notre méthodologie pour réaliser le couplage fluide-thermique-magnétique sur un modèle 3D d'un transformateur $3\mathrm{kVA}$. Nous étudions l'efficacité du refroidissement à l'intérieur du modèle de transformateur de puissance en utilisant la méthode des éléments finis.

Tout d'abord, nous considérons la géométrie réelle du modèle 3D présenté dans la figure ((6.19)a). Nous divisons ensuite la structure du transformateur en quatre parties. Le champ magnétique, la vitesse et la température sont calculés numériquement à l'aide de COMSOL Multiphysics dans un quart du modèle afin d'économiser les ressources de calcul, voir la figure ((6.19)b). Dans cette figure, les chiffres indiqués désignent respectivement de droite à gauche : (1) le noyau ferromagnétique, (2) l'enroulement secondaire, (3) l'enroulement primaire, (4) le domaine du ferrofluide, et (5) le réservoir en acier avec une perméabilité magnétique $\mu_r = 100$.

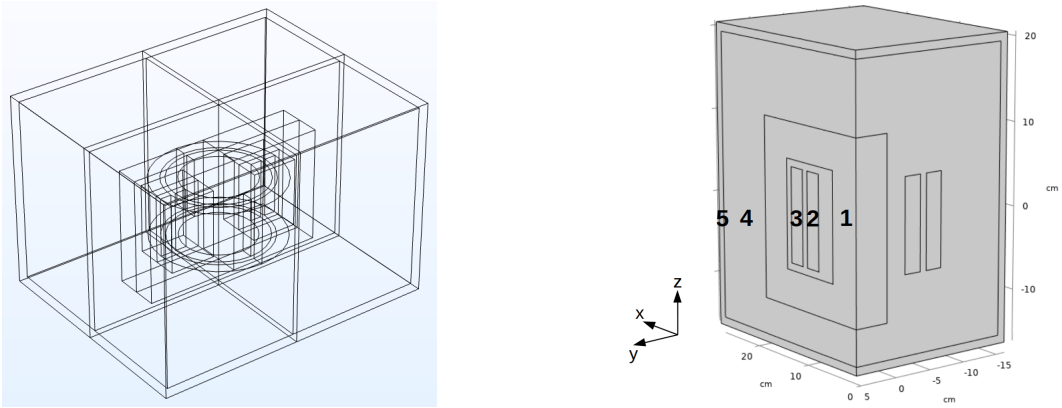


(a) Structure 3D du modèle de transformateur $3\mathrm{kVA}$. (b) Quart du modèle de transformateur $3\mathrm{kVA}$.

Figure 6.19: Structures 3D du transformateur de puissance $3\mathrm{kVA}$.

Le coefficient de transfert thermique est fixé à $h = 150\ \mathrm{W.m^{-2}K^{-1}}$ dans le problème de transfert thermique. Les densités de courant nominales injectées dans les enroulements primaire et secondaire sont ici augmentées de $j_0 = 2\,\mathrm{A.mm^{-2}}$ à $j_0 = 5\,\mathrm{A.mm^{-2}}$ pour maximiser l'échauffement du cuivre à l'intérieur du transformateur de puissance. En fonction de cette augmentation, les valeurs des densités de courant efficaces injectées dans chaque conducteur et les pertes Joule volumiques associées sont données dans la table (6.4).

| Entrée | valeur |
|---|---|
| $J_{1eff}$ | $2.46 \times 10^6\,\mathrm{A/m^2}$ |
| $Q_1$ | $196\,593\,\mathrm{W/m^3}$ |
| $J_{2eff}$ | $-2.46 \times 10^6\,\mathrm{A/m^2}$ |
| $Q_2$ | $193\,127\,\mathrm{W/m^3}$ |

Table 6.4: Paramètres d'entrée pour le couplage ferrohydrodynamique respectivement dans les bobinages primaire (1) et secondaire (2).

L'évolution temporelle de la température est enregistrée lorsque la force magnétique de Helmholtz est activée ou non. Pour ces deux cas, les courbes de température calculées au niveau de deux capteurs localisés au sommet de chaque enroulement sont présentées sur la figure (6.20). En comparant les deux séries temporelles, on peut noter une diminution de la température locale des deux capteurs de $10\,^{\circ}\mathrm{C}$ environ lorsque la force magnétique est activée.

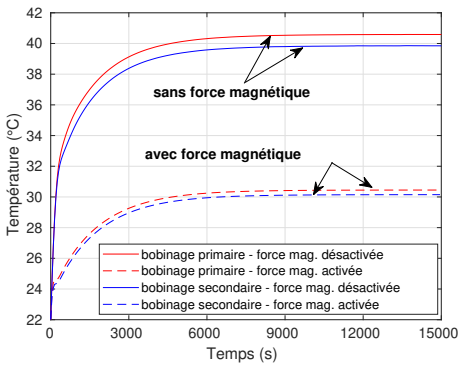


Figure 6.20: Évolution temporelle de la température des bobinages dans les deux cas hydrodynamique et ferrohydrodynamique.

Des distributions spatiales de l'intensité de la vitesse à $t = 15\,000\,\mathrm{s}$ sont présentées sur la figure (6.21) pour deux cas : le cas hydrodynamique où la force magnétique n'est pas appliquée, et le cas ferrohydrodynamique où la force magnétique influence l'écoulement du ferrofluide. Sans force magnétique (voir figure ((6.21)a)), une grande cellule de circulation apparaît vers la partie supérieure du volume de fluide. Si la force magnétique est appliquée (voir figure ((6.21)b)), l'amplitude maximale de la vitesse est localisée dans l'interstice entre les deux enroulements, ainsi qu'au sommet de leur surface. Une nouvelle cellule de convection, qui n'est pas présente dans le cas hydrodynamique, apparaît entre le noyau et la partie inférieure des enroulements. Ainsi, la

circulation du fluide est modifiée entre le noyau et le bobinage interne et amplifie l'évacuation de la chaleur de l'interstice entre les bobinages. En conséquence, la température des enroulements est abaissée. Ceci prouve une fois de plus l'effet bénéfique du phénomène de convection thermomagnétique.

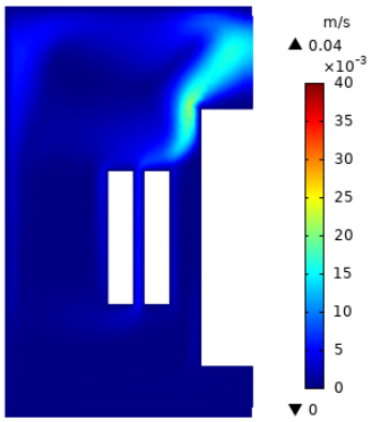


(a) Cas hydrodynamique.

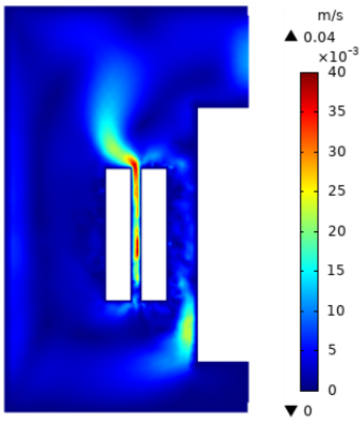


(b) Cas ferrohydrodynamique.

Figure 6.21: Distributions de l'intensité de la vitesse (en $\mathrm{m.s^{-1}}$) dans le plan $(y, z)$ et à $x = 0$ après un régime quasi-permanent $t = 15\,000\,\mathrm{s}$.

Comparons maintenant la température dans les deux conducteurs. La figure (6.22) montre les distributions de la température à un état quasi-stationnaire ($t = 15\,000\,\mathrm{s}$) lorsque la force magnétique (voir figure ((6.22)b)) est présente ou non (voir figure ((6.22)a)).

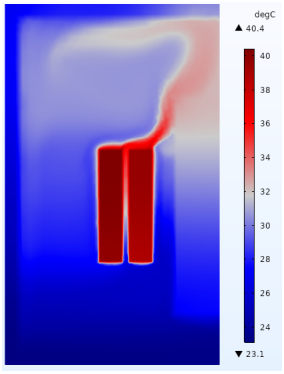


(a) Cas hydrodynamique.

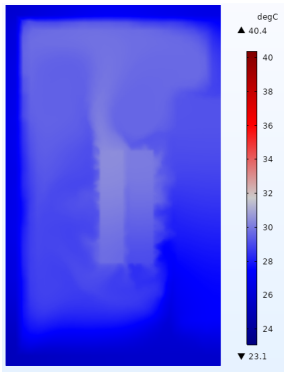


(b) Cas ferrohydrodynamique, échelle modifiée.

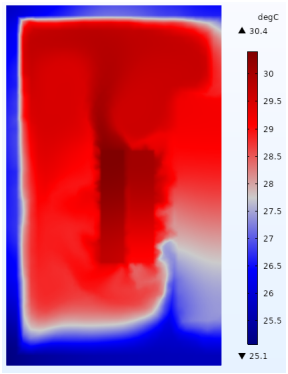


(c) Cas ferrohydrodynamique, échelle réelle.

Figure 6.22: Distributions de la température (en °C) dans le plan $(y, z)$ et à $x = 0$ après un régime quasi-permanent $t = 15\,000\,\mathrm{s}$.

Lorsque la force magnétique n'est pas appliquée, seule la force de Boussinesq peut avoir un impact sur le mouvement du ferrofluide. Le panache thermique (voir figure ((6.22)a)) né au sommet des deux enroulements suit la trajectoire de la cellule de convection montrée sur la figure ((6.21)a)). Il atteint le coin du noyau puis dévie à gauche près du bord supérieur de la cuve. L'enroulement

primaire atteint $40.4\,^{\circ}\mathrm{C}$ à $t = 15\,000\,\mathrm{s}$. En revanche, lorsque la force magnétique est présente (voir figure ((6.22)b)), le panache thermique, dévié par la cellule de convection émergeant entre les conducteurs (voir figure ((6.21)b)), s'élève verticalement depuis le sommet de l'enroulement primaire et se répand ensuite dans la partie supérieure du domaine de ferrofluide. Un autre panache thermique monte au bas des deux enroulements, étant affecté par la nouvelle cellule de convection qui apparaît dans la partie inférieure du réservoir entre le noyau et le bas des enroulements. Le flux de ferrofluide est renforcé entre les conducteurs, ce qui permet un refroidissement efficace des enroulements. L'enroulement primaire atteint $30.4\,^{\circ}\mathrm{C}$ à $t = 15\,000\,\mathrm{s}$. Par conséquent, la température maximale dans les conducteurs est réduite de $10\,^{\circ}\mathrm{C}$ grâce à la convection thermomagnétique.

# 6.7 Conclusions

## 6.7.1 Modélisation numérique

### Modélisation 2D-axisymétrique

Nous avons d'abord considéré le problème du transfert de chaleur dans un système électromagnétique simple. Il s'agit d'une bobine de cuivre immergée dans un ferrofluide. Nous avons utilisé deux codes, COMSOL Multiphysics et SFEMaNS, pour modéliser la convection thermomagnétique dans ce système. Les résultats numériques ont montré un très bon accord après comparaison et ont validé l'intérêt du ferrofluide pour améliorer le transfert de chaleur. La température maximale dans la bobine a été réduite de $2\,^{\circ}\mathrm{C}$ grâce à l'effet de la convection thermomagnétique.
Nous avons également réalisé deux tests afin d'améliorer la convection thermomagnétique dans le système du solénoïde. Le premier test concerne le ferrofluide avec des nanoparticules à basse température de Curie. Les résultats numériques ont montré que l'utilisation de nanoparticules magnétiques à faible température de Curie réduit la température de la bobine. Le second test concerne l'ajout d'un aimant pour modifier la distribution du champ magnétique généré par la bobine dans le ferrofluide et pour étudier son effet sur le processus de refroidissement. Les résultats associés ont confirmé l'intérêt de l'utilisation d'un aimant pour abaisser la température maximale dans la bobine, en fonction de la configuration de l'aimant : direction et intensité de l'aimantation et emplacement.

### Modélisation 3D non-axisymétrique

Nous avons proposé d'étudier une structure plus réaliste en considérant un modèle 3D-non axisymétrique d'un transformateur $3\,\mathrm{kVA}$ immergé dans un ferrofluide. Nous avons étudié les performances de refroidissement dans ce transformateur, et avons constaté une diminution importante de la température maximale des enroulements ($10\,^{\circ}\mathrm{C}$).

## 6.7.2 Expérience

Un dispositif expérimental a été développé au laboratoire GeePs pour étudier le transfert thermique d'un solénoïde immergé dans un ferrofluide et pour valider l'approche numérique. Les mesures de température ont d'abord validé l'impact du champ magnétique sur la température de la bobine. Ensuite, les mesures expérimentales ont été comparées aux mesures numériques, et elles

ont présenté un très bon accord (l'erreur relative était d'environ 0,7 %). Un test expérimental a été réalisé avec un aimant annulaire pour vérifier son impact sur le transfert de chaleur. La température de la bobine a montré une diminution due à l'ajout de l'aimant. La validation croisée numérique/expérimentale a également confirmé l'impact induit par l'aimant. L'expérience a finalement confirmé notre choix du modèle et des conditions aux limites appliquées dans la modélisation.

### 6.7.3 Perspectives

Ce travail a permis de répondre à de nombreuses questions qui se posaient au début de l'étude, mais certains points restent à approfondir.

Concernant la modélisation, nous avons vérifié l'impact de la convection thermomagnétique sur le transfert thermique, et avons obtenu une forte diminution de la température maximale des bobines de l'ordre de $10\,^{\circ}\mathrm{C}$ lorsque la force magnétique est active. Cependant, un calcul ferrohydrodynamique doit être effectué avec un maillage plus fin du modèle de transformateur 3D pour confirmer ces résultats encourageants.

D'un point de vue expérimental, des mesures de température sur un prototype réel de transformateur $3\ \mathrm{kVA}$ doivent être effectuées pour une validation croisée des résultats numériques et expérimentaux. Alors que la modélisation confirme l'avantage de la convection thermomagnétique dans le transformateur, nous devons vérifier ce résultat avec une expérience sur un transformateur réel et si la solution proposée est viable pour un déploiement industriel.

Il semble également intéressant d'étudier le problème multiphysique en considérant la théorie de Langevin dans sa forme classique. Cela signifie que nous allons considérer la non-linéarité du comportement magnétique pour étudier son influence sur le transfert de chaleur. Il est encore difficile de savoir quelle expression de la force magnétique doit être utilisée lorsqu'on considère la non-linéarité du matériau magnétique.

Un dernier point doit être clarifié. Nous avons prouvé l'impact des aimants sur le processus de refroidissement de la bobine. L'aimant ajouté augmente le flux de fuite magnétique dans le ferrofluide et améliore ainsi le refroidissement dans le système solénoïde. Cependant, dans un transformateur de puissance, nous avons tendance à contrôler la valeur du flux de fuite et à concentrer le flux magnétique dans le noyau pour réaliser une meilleure conversion entre les enroulements. Si la convection thermomagnétique nécessite une augmentation du flux de fuite dans le transformateur de puissance, l'efficacité énergétique de ce dispositif pourrait être réduite en raison de la fuite du flux magnétique. Nous devrions trouver un compromis entre la performance de refroidissement du transformateur en terme de réduction de sa température maximale et son efficacité énergétique d'un point de vue électrique.

# Appendix A

# Magnetic relaxation

Literature [6, 10] presents two mechanisms through which a ferrofluid can alter its magnetization once the applied magnetic field is changed. The first mechanism concerns the "magnetically hard particles", i.e., when the magnetic moment is fixed to the particle crystal structure. In this case, the relaxation occurs by a rotation of the whole particle in the liquid. The second mechanism concerns "magnetically weak particles", where the magnetic moment vector within the particle may rotate.
These two relaxation processes are characterized by two respective relaxation times. Ferrofluids relax through the fastest process, which is determined by the lowest relaxation time. If the particle rotation is possible, a Brownian rotational diffusion time $\tau_B$ with hydrodynamic origin can describe the relaxation process (Brown, 1963):

$$\tau_B = 3\frac{\widetilde{V}\eta_0}{k_b T} \tag{A.1}$$

where $\eta_0$ is the dynamic viscosity of the carrier liquid, and $\widetilde{V}$ is the particle volume taking into account the surfactant thickness $s$.
Ferromagnetic particles exhibit two possible magnetizations, i.e., two equilibrium positions when no magnetic field is applied. If the magnetic moment vector within the particle should rotate from one orientation to another, the thermal energy of the particle must overcome an energy barrier. If particles satisfy $K_1 V \ll k_b T$, thermal energy can induce variations in the magnetization of the particle during a characteristic time $\tau_N$ called Néel time (Néel, 1949):

$$\tau_N = \frac{1}{f_0}\exp\left(\frac{K_1 V}{k_b T}\right) \tag{A.2}$$

where $f_0$ denotes the Larmor frequency of the magnetization vector ($f_0 \approx 10^9 \mathrm{Hz}$).
If $\tau_N \ll \tau_B$, Néel relaxation predominates, and the material is said to have intrinsic superparamagnetism. If $\tau_B \ll \tau_N$, relaxation occurs by the Brownian mechanism, and the material has extrinsic superparamagnetism [7]. As a result, both Brownian and Néel mechanisms in a colloidal ferrofluid contribute to an equilibrium state by relaxation processes. These two relaxation times lead to a superparamagnetic behavior of particles, described in the previous section by the classical Langevin's theory.

**Discussion** Note that the Brownian diffusion time $\tau_B$ depends on the hydrodynamic volume of the particle $\widetilde{V}$, including the surfactant layer $s$. On the other hand, Néel relaxation time $\tau_N$ depends on the volume of the magnetic core of the particle [10].
As seen in equations (A.1) and (A.2), both relaxation times depend on the particle volume, i.e., on the particle size $d$. Note that the Brownian time $\tau_B$ increases linearly with the particle diameter. In contrast, Néel time $\tau_N$ grows exponentially when the particle size increases. Figure (A.1) shows a comparison between both times $\tau_B$ and $\tau_N$ for the magnetization of a magnetite-based ferrofluid. According to figure (A.1), for small particle size, the Néel mechanism predominates ($\tau_N \ll \tau_B$), and the relaxation occurs by magnetic vector rotation in the particle domain. The two relaxation curves cross at the critical particle size, from which particles become magnetically hard. Thus a Brownian mechanism occurs ($\tau_B \ll \tau_N$), and the whole particle rotates in the liquid. It is convenient to mention that this critical diameter depends on the anisotropy constant of particles $K_1$, the viscosity of carrier liquid and the surfactant layer $s$ [10].

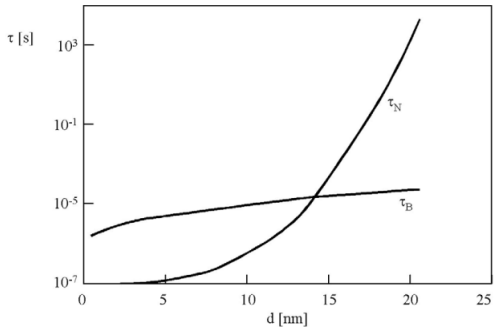


Figure A.1: Brownian and Néel relaxation times ($\tau_B$, $\tau_N$) for the magnetization of magnetite-based ferrofluid ($d$ denotes the diameter, the surfactant thickness is $s = 2$ nm, and kinematic viscosity is $\nu = 100\ \mathrm{mm}^2.\mathrm{s}^{-1}$) [10].

# Appendix B

# Transformer design

## B.1 Characteristic dimension of the transformer

We consider the schematic sketch of the ferromagnetic core in figure (B.1) to calculate $L$.

$$V_1 = n_1 \omega B L^2, \tag{B.1}$$

where $\omega = 2\pi f$.

$$\begin{cases} S = V_1 I_1 = V_2 I_2, \\ S = V_1 J_0 s_1 = V_2 J_0 s_2, \end{cases} \tag{B.2}$$

where $J_0$ is the nominal current density in the primary winding ($J_0 = 2\,\mathrm{A.mm^{-2}}$) and $s_1$ an $s_2$ the sections of wires in the primary and secondary windings ($s_1 = 3.75\,\mathrm{mm^2}$, $s_2 = 6.52\,\mathrm{mm^2}$).

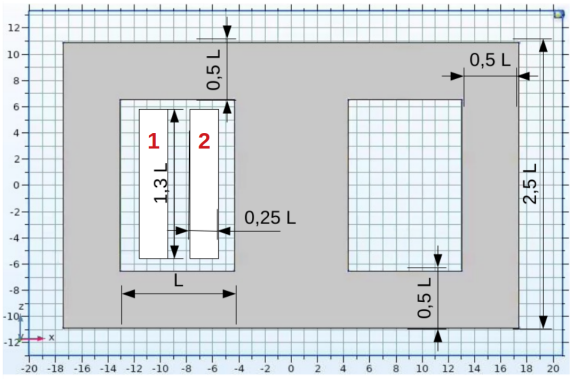


Figure B.1: Ferromagnetic core in $(x, z)$ plane.

The filling coefficient of copper considered in this modeling is $k_b = 0.5$.

$$K_b S_b = n_1 s_1 + n_2 s_2 \simeq 2 n_1 s_1, \tag{B.3}$$

where $S_b$ is the section of the winding and $n_1$ and $n_2$ are respectively the number of turns in the primary and the secondary coils.

Equation (B.3) leads to:

$$n_1 = \frac{K_b S_b}{2 s_1} = \frac{0.5 \times 0.5L \times 1.3L}{2 s_1}, \tag{B.4}$$

Injecting (B.2) in (B.4) leads to:

$$n_1 = \frac{0.1625 L^2}{s_1} = \frac{0.1625 L^2 \times V_1 J_0}{S_b}, \tag{B.5}$$

Equation (B.1) leads to:

$$V_1 = \frac{0.1625 L^4 V_1 J_0 \omega B}{S_b}, \tag{B.6}$$

Equation (B.6) leads to $L = 8.7\,\mathrm{cm}$.

## B.2 Number of turns in the windings

$V_1$ and $V_2$ are the voltages at the bounds of the primary and secondary windings ($V_1 = 400\,\mathrm{V}$ and $V_2 = 230\,\mathrm{V}$).

$$n_1 = \frac{V_1}{\omega B L^2}, \tag{B.7}$$

Equation (B.7) leads to $n_1 = 336$ spires.

$$n_1 = \frac{n_1 V_2}{V_1}, \tag{B.8}$$

Equation (B.8) leads to $n_1 = 193$ spires.

## B.3 Coils resistance

We calculate the resistance connected to each coil using:

$$R = n \frac{\rho l}{s} = n \frac{\rho 2\pi r}{s}, \tag{B.9}$$

Equation (B.9) leads to:

$$\begin{cases} R_1 = n_1 \dfrac{\rho 2\pi 1.275 L}{s_1}, \\ R_2 = n_2 \dfrac{\rho 2\pi 0.925 L}{s_2}, \end{cases} \tag{B.10}$$

Equation (B.10) leads to $R_1 = 1.04\,\Omega$ and $R_1 = 0.25\,\Omega$.

## B.4 Nominal currents

Let us denote by $i_1$ and $i_2$ the nominal currents in the primary and secondary windings.

$$\begin{cases} i_1 = \dfrac{P}{V_1}, \\ i_2 = i_1 \dfrac{n_1}{n_2}, \end{cases} \tag{B.11}$$

These equations lead to $i_1 = 7.5\,\mathrm{A}$ and $i_2 = 13.1\,\mathrm{A}$.

## B.5 Current densities for magnetostatic calculation

$$\begin{cases} J_1 = n_1 \dfrac{I_1}{S_1}, \\ J_2 = n_2 \dfrac{I_2}{S_2}, \end{cases} \tag{B.12}$$

where $S_1$ ans $S_2$ are the sections of the primary and the secondary windings ($S_1 = S_2 = 2.46 \times 10^{-3}\,\mathrm{m}^2$). Equation (B.12) leads to $J_1 = 0.983 \times 10^6\,\mathrm{A/m}^2$ and $J_2 = 0.973 \times 10^6\,\mathrm{A/m}^2$.

# Appendix C

# Additional numerical results

The following figures present the meridian views of the velocity and temperature fields in $(y, z)$, $(x, z)$ and $(x, y)$ planes for each of the three meshes considered and in different regions of the transformer structure.

## C.1 Velocity and temperature distributions in (y,z) plane

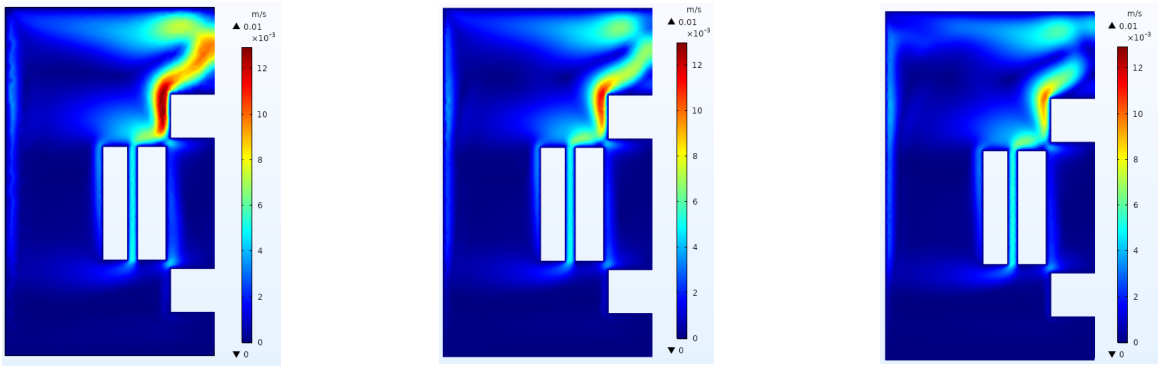

(a) Mesh 0. (b) Mesh 1. (c) Mesh 2.

Figure C.1: Velocity magnitude (in $\mathrm{m.s^{-1}}$) distributions in $(y, z)$ plane and $x = 5$ at a steady state $t = 15\,000\,\mathrm{s}$.

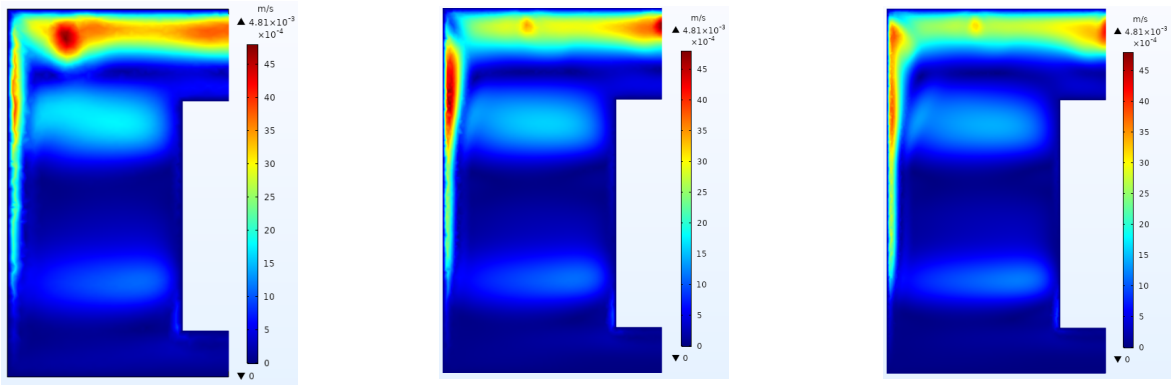

(a) Mesh 0. (b) Mesh 1. (c) Mesh 2.

Figure C.2: Velocity magnitude (in $\mathrm{m.s^{-1}}$) distributions in $(y, z)$ plane and $x = 15$ at a steady state $t = 15\,000\,\mathrm{s}$.

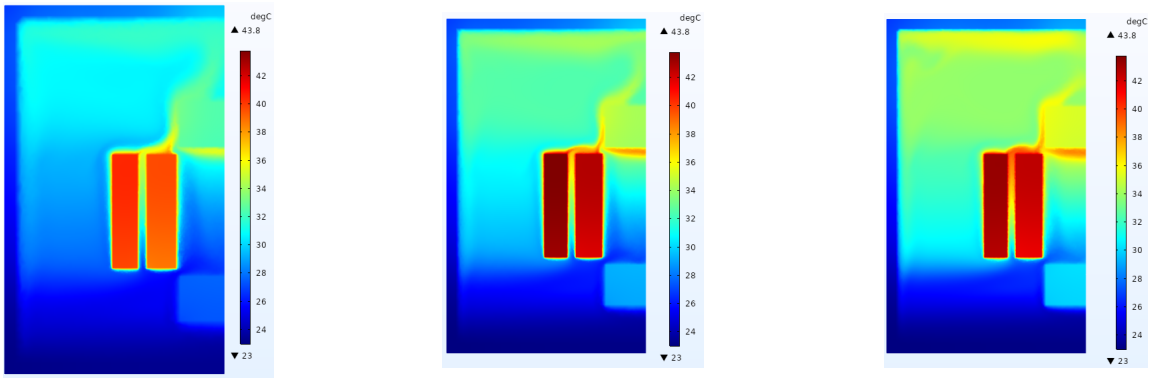

(a) Mesh 0. (b) Mesh 1. (c) Mesh 2.

Figure C.3: Temperature (in °C) distributions in $(y, z)$ plane and $x = 5$ at a steady state $t = 15\,000\,\mathrm{s}$.

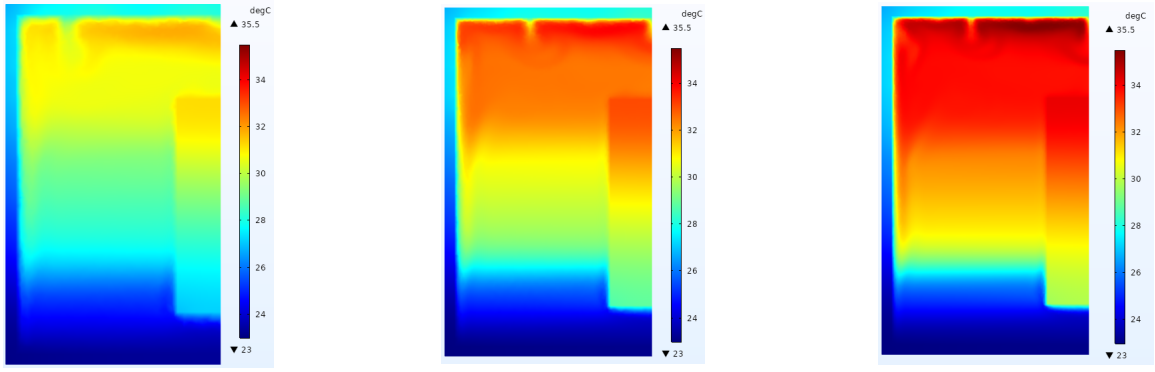

(a) Mesh 0. (b) Mesh 1. (c) Mesh 2.

Figure C.4: Temperature (in °C) distributions in $(y, z)$ plane and $x = 15$ at a steady state $t = 15\,000\,\mathrm{s}$.

## C.2 Velocity and temperature distributions in (x,z) plane

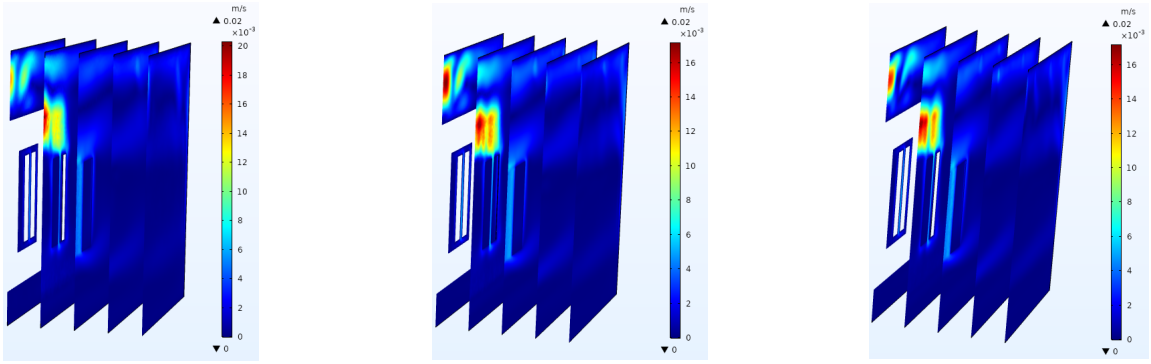

(a) Mesh 0. (b) Mesh 1. (c) Mesh 2.

Figure C.5: Velocity magnitude (in $\mathrm{m.s^{-1}}$) distributions in $(x, z)$ plane at a steady state $t = 15\,000\,\mathrm{s}$.

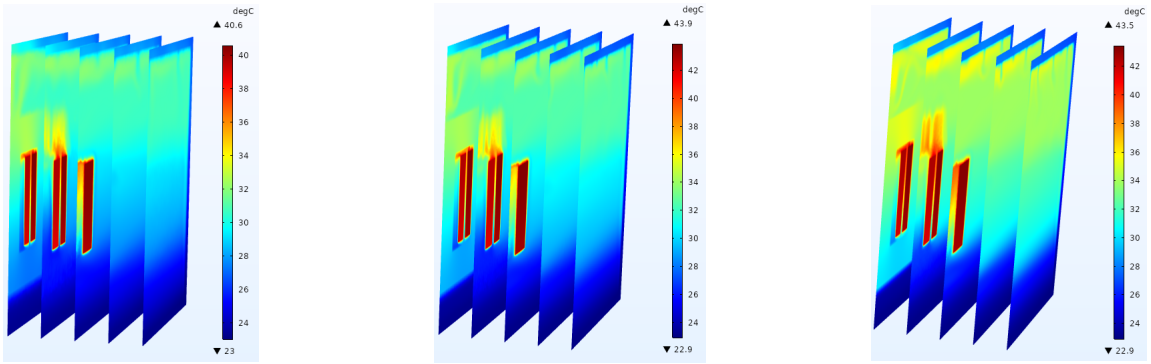

(a) Mesh 0. (b) Mesh 1. (c) Mesh 2.

Figure C.6: Temperature (in °C) distributions in $(x, z)$ plane at a steady state $t = 15\,000\,\mathrm{s}$.

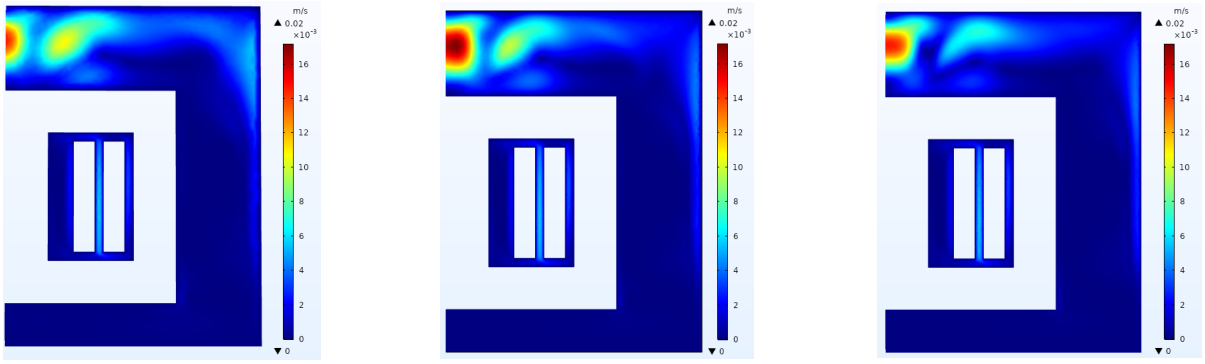

(a) Mesh 0. (b) Mesh 1. (c) Mesh 2.

Figure C.7: Velocity magnitude (in $\mathrm{m.s^{-1}}$) distributions in $(x, z)$ plane and $y = 5$ at a steady state $t = 15\,000\,\mathrm{s}$.

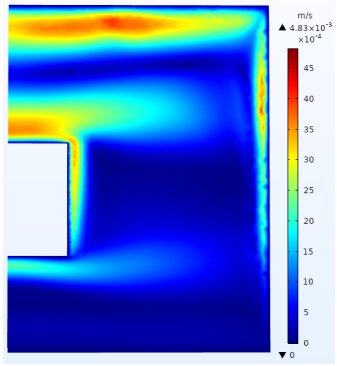

(a) Mesh 0.

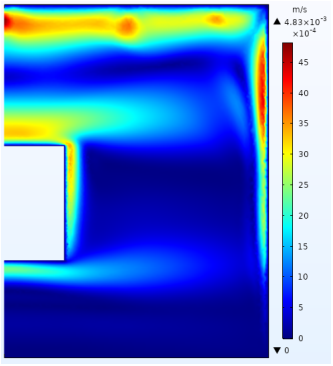

(b) Mesh 1.

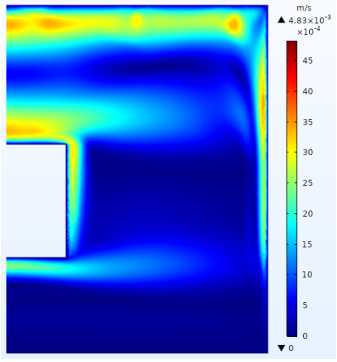

(c) Mesh 2.

Figure C.8: Velocity magnitude (in $\mathrm{m.s^{-1}}$) distributions in $(x, z)$ plane and $y = -5$ at a steady state $t = 15\,000\,\mathrm{s}$.

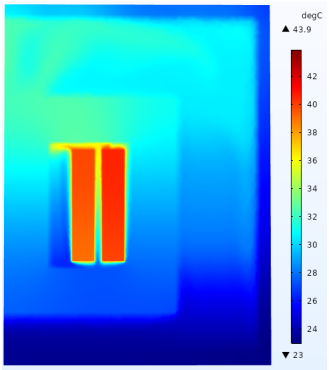

(a) Mesh 0.

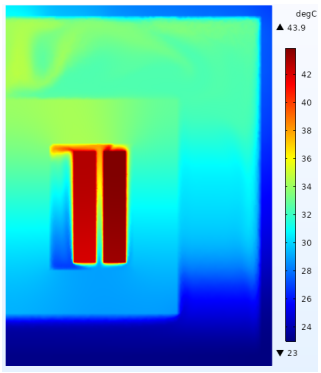

(b) Mesh 1.

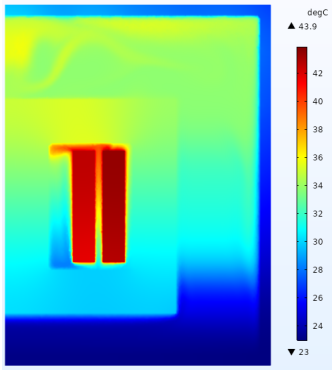

(c) Mesh 2.

Figure C.9: Temperature (in °C) distributions in $(x, z)$ plane and $y = 5$ at a steady state $t = 15\,000\,\mathrm{s}$.

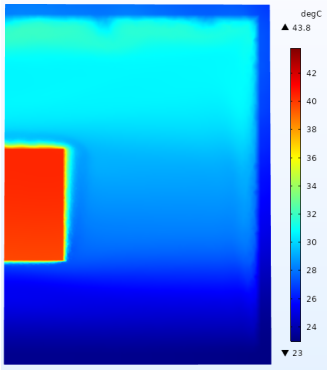

(a) Mesh 0.

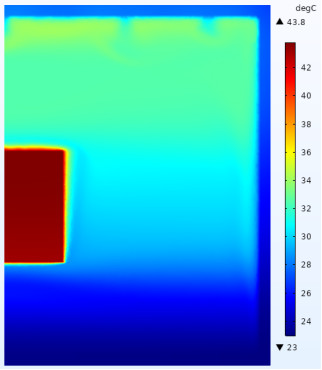

(b) Mesh 1.

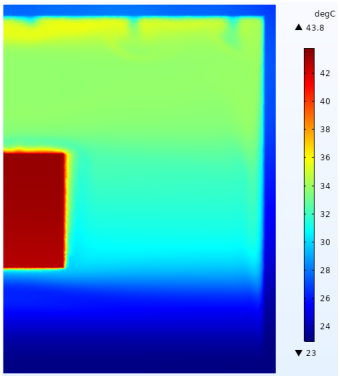

(c) Mesh 2.

Figure C.10: Temperature (in °C) distributions in $(x, z)$ plane and $y = -5$ at a steady state $t = 15\,000\,\mathrm{s}$.

## C.3 Velocity and temperature distributions in (x,y) plane

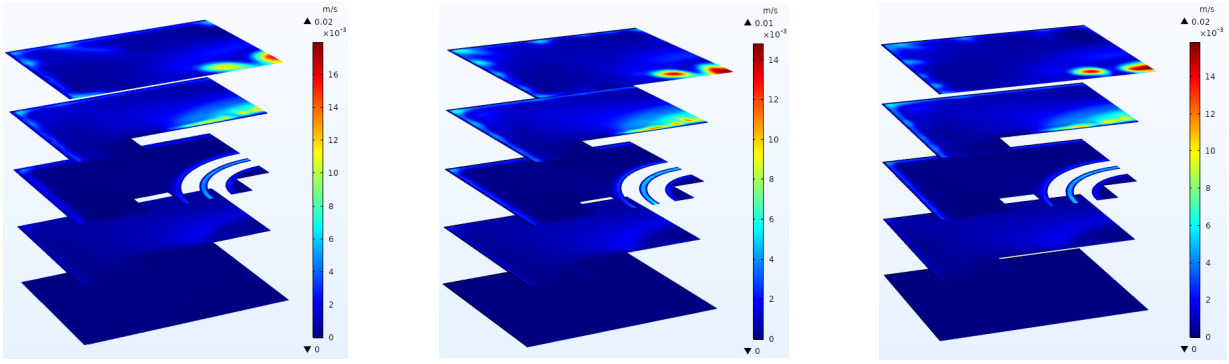

(a) Mesh 0. (b) Mesh 1. (c) Mesh 2.

Figure C.11: Velocity magnitude (in $\mathrm{m.s^{-1}}$) distributions in $(x, y)$ plane at a steady state $t = 15\,000\,\mathrm{s}$.

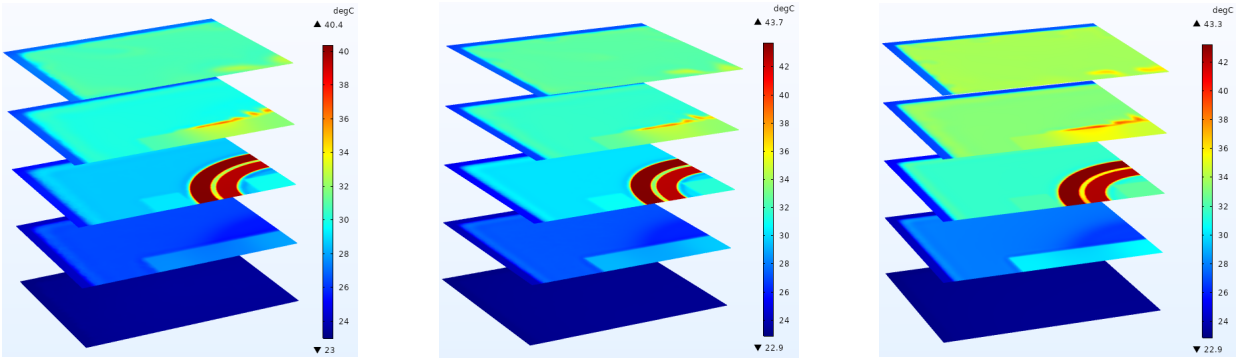

(a) Mesh 0. (b) Mesh 1. (c) Mesh 2.

Figure C.12: Temperature (in °C) distributions in $(x, y)$ plane at a steady state $t = 15\,000\,\mathrm{s}$.

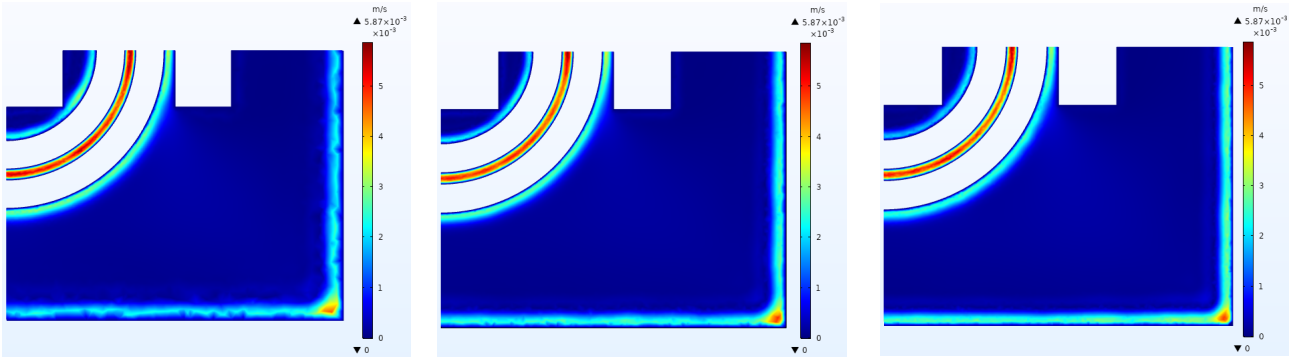

(a) Mesh 0. (b) Mesh 1. (c) Mesh 2.

Figure C.13: Velocity magnitude (in $\mathrm{m.s^{-1}}$) distributions in $(x, y)$ plane and $z = 0$ at a steady state $t = 15\,000\,\mathrm{s}$.

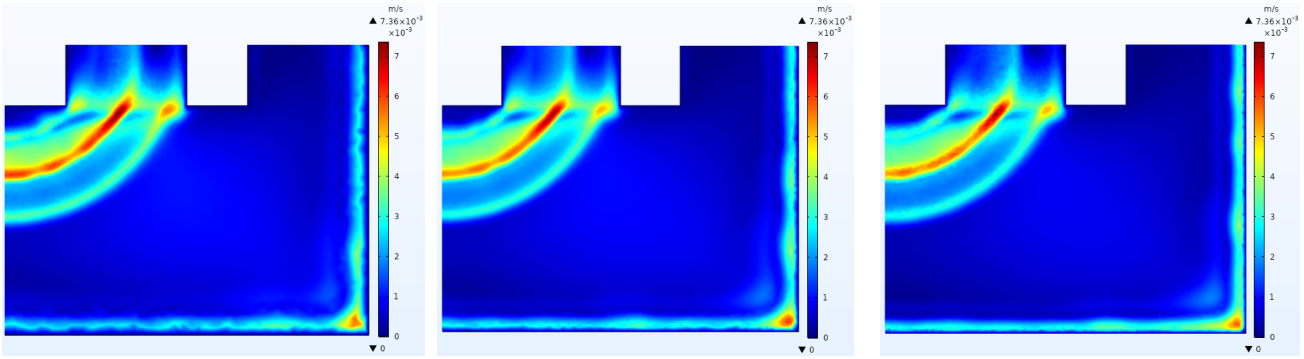

(a) Mesh 0. (b) Mesh 1. (c) Mesh 2.

Figure C.14: Velocity magnitude (in $\mathrm{m.s^{-1}}$) distributions in $(x, y)$ plane and $z = 6$ at a steady state $t = 15\,000\,\mathrm{s}$.

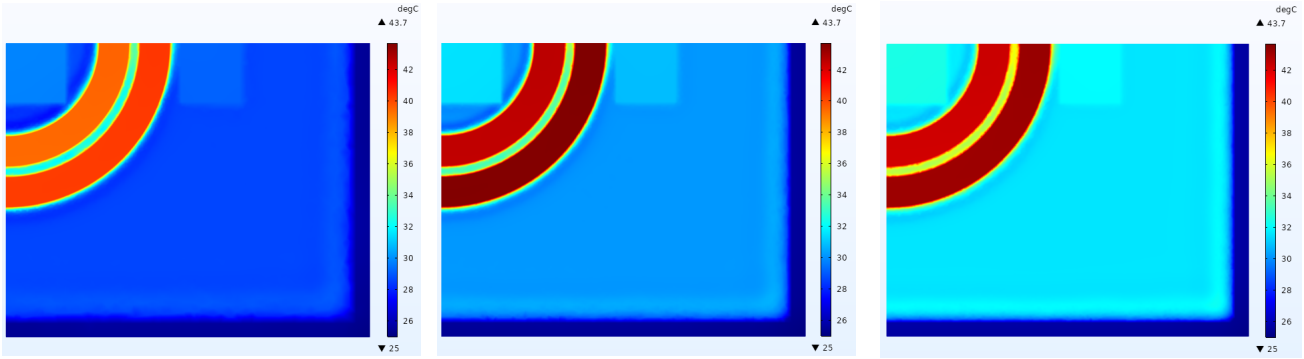

(a) Mesh 0. (b) Mesh 1. (c) Mesh 2.

Figure C.15: Temperature (in °C) distributions in $(x, y)$ plane and $z = 0$ at a steady state $t = 15\,000\,\mathrm{s}$.

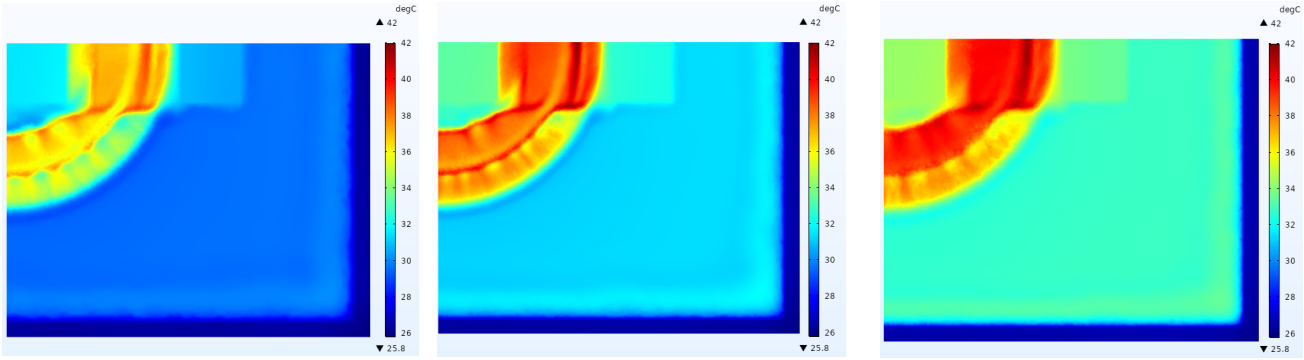

(a) Mesh 0. (b) Mesh 1. (c) Mesh 2.

Figure C.16: Temperature (in °C) distributions in $(x, y)$ plane and $z = 6$ at a steady state $t = 15\,000\,\mathrm{s}$.

# Appendix D

# Publications

# Impact of Magnets on Ferrofluid Cooling Process: Experimental and Numerical Approaches

Sleimane Nasser El Dine[1], Xavier Mininger[1], Caroline Nore[2], Raphaël Zanella[1,2,3], Frédéric Bouillault[1], and Jean-Luc Guermond[3]

[1]GeePs, CNRS, CentraleSupélec, Univ. Paris Sud, Université Paris-Saclay, Sorbonne Université, 91192 Gif-sur-Yvette, France
[2]LIMSI, CNRS, Univ. Paris Sud, Université Paris-Saclay, 91405 Orsay, France
[3]Department of Mathematics, Texas A&M University, College Station, TX 77843 USA

**The cooling performance of vegetable oil seeded with ferromagnetic nanoparticles is tested on a prototype electric transformer coil. The system is investigated both experimentally and numerically. The numerical simulations are done with finite elements assuming axisymmetry. The experimental and numerical results match very well with each other. The numerical tool is also used to investigate the impact of an annular magnet enclosing the setup. The orientation of the remanent magnetic induction of the magnet is observed to play a significant role in determining the cooling efficiency.**

*Index Terms*— **Cooling, ferrofluid, finite-element method, magnet, thermomagnetic convection.**

## I. Introduction

EXCESSIVE heating of power transformers is known to compromise the longevity of these devices. A possible solution to this problem consists of using ferrofluids as cooling agents to enhance the heat-transfer rate. A ferrofluid is a stable colloidal suspension of ferromagnetic nanoparticles dispersed in a non-magnetic carrier liquid. In this article, we study the heat-transfer properties of a ferrofluid composed of Midel vegetable oil seeded with cobalt ferrite $CoFe_2O_4$ nanoparticles. At constant magnetic field, the magnetic permeability of a hot ferrofluid is smaller than that of a cold one [1]. The relation between the ferrofluid magnetization and magnetic field is taken into account by using the assumption of a linear magnetic material for ferrofluids [2]

$$\mathbf{M} = \chi(T)\mathbf{H} \tag{1}$$

where $\mathbf{M}$ is the ferrofluid magnetization, $T$ the temperature, and $\mathbf{H}$ is the magnetic field. Here, $\chi$ is the magnetic susceptibility of the ferrofluid and, as shown in the following, it depends on a number of parameters:

$$\chi(T) = \frac{\phi\mu_0\pi d^3 M_{s,p}^2(T)}{18k_B T}, \quad \frac{M_{s,p}(T)}{M_0} = 1 - \left(\frac{T}{T_c}\right)^{\frac{3}{2}} \tag{2}$$

where $\phi$ is the volume fraction of magnetic material, $\mu_0$ the vacuum magnetic permeability, $d$ the particle average diameter, $M_{s,p}(T)$ the temperature-dependent particle magnetization, $k_B$ the Boltzmann's constant, $M_0$ the particle magnetization at saturation and at 0 K, and $T_c$ the Curie temperature of the cobalt ferrite nanoparticles. The magnetic force added to the thermal buoyancy force changes the flow pattern in the tank. The heated ferrofluid loses its magnetization near the transformer windings and is pushed up by the magnetic and relatively cooler fluid from the surroundings. After losing its heat, the magnetic fluid regains its magnetization. This process helps transfer the heat from the transformer windings to the external shell of the transformer, where the heat is eventually exchanged with ambient air [3]. This mechanism is called thermomagnetic convection. The magnetic force can be modeled by the Helmholtz force (in N/m$^3$)

$$\mathbf{F} = -\mu_0 \frac{H^2}{2} \nabla\chi(T) \tag{3}$$

where $H = \|\mathbf{H}\|$. This force connects the variations in the magnetization with the thermal gradient. Therefore, if effective, one expects that the thermomagnetic convection can help avoid using external mechanical pumping systems.

This article is organized as follows. We first present in Section II the experiment investigated in this article and review the equations modeling the system. The setup is composed of a coil immersed in a ferrofluid. Then, we describe in Section III the finite-element code that is used to solve the coupled thermo-magnetohydrodynamics system. The numerical results and experimental ones are compared in Section IV. After cross-validating the experimental and the numerical results, we numerically study the impact of an annular magnet on the cooling process.

## II. Experimental Setup and Governing Equations

### A. Experimental Setup

The experimental setup under study consists of a copper coil immersed in a ferrofluid contained in a cylindrical tank made of aluminum. The tank is closed at the top by a polyvinyl chloride (PVC) cap as shown in Fig. 1. An annular magnet enclosing the tank can be added at different heights in order to study its impact on the cooling process. The setup dimensions are given in Table I.

Manuscript received August 1, 2019; revised October 4, 2019; accepted October 17, 2019. Date of current version December 20, 2019. Corresponding author: S. Nasser El Dine (e-mail: sleimane.nassereldine@geeps.centralesupelec.fr).

Color versions of one or more of the figures in this article are available online at http://ieeexplore.ieee.org.

Digital Object Identifier 10.1109/TMAG.2019.2949362

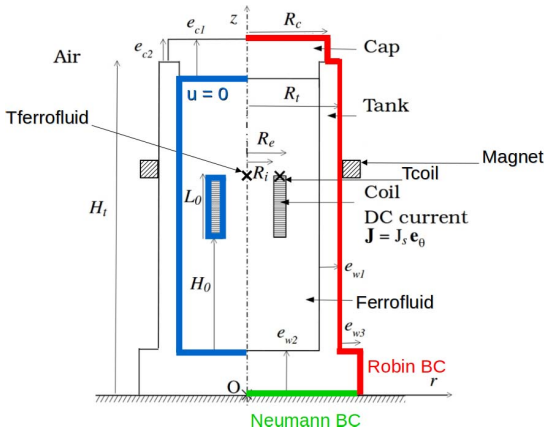


Fig. 1. Experimental setup using ferrofluid cooling.

TABLE I
EXPERIMENTAL SETUP DIMENSIONS

| Parameter | $H_t$ | $R_t$ | $e_{w1}$ | $e_{w2}$ | $e_{w3}$ | $H_0$ |
|---|---|---|---|---|---|---|
| Value (cm) | 12.5 | 3.1 | 1 | 2 | 1 | 3.9 |
| Parameter | $L_0$ | $R_i$ | $R_e$ | $R_c$ | $e_{c1}$ | $e_{c2}$ |
| Value (cm) | 2.1 | 0.8 | 1.175 | 2.6 | 2 | 1 |

### B. Governing Equations

The magnetic fluid is considered as a homogeneous continuous medium with incompressible Newtonian fluid behavior. The study of the thermal exchanges through the cooling device requires the knowledge of the velocity field, which we assume to be well modeled by the Navier–Stokes equations

$$\begin{cases} \nabla\cdot\mathbf{u} = 0 \\ \rho_l \frac{D\mathbf{u}}{Dt} + \nabla p - \nabla\cdot\mathbb{e}(T,\mathbf{u}) = \rho_l \beta g (T - T_{\text{ext}})\mathbf{e_z} + \mathbf{F} \end{cases} \tag{4}$$

where $\mathbf{u}$ is the velocity vector, $\mathbb{e}(T,\mathbf{u}) = \eta(T)(\nabla\mathbf{u} + (\nabla\mathbf{u})^{\mathrm{T}})$, $D/Dt$ the material derivative, $p$ the pressure, $\eta$ is the dynamic viscosity (given by $\eta(T) = Af(\phi)\exp(BT^{-1})$ with $A = 1.3\times10^{-6}$ Pa · s, $B = 3.1\times10^{3}$ K and $f(\phi)$ given by Rosensweig's model, see [4, p. 105]), $\rho_l$ the density, $\beta$ the thermal expansion coefficient, $g$ the gravity, $T$ the temperature, and $T_{\text{ext}}$ the reference temperature. The last two terms on the right-hand side of the momentum equation are, respectively, the buoyancy force and the magnetic force. The heat-transfer process that occurs in the ferrofluid is described by the heat equation

$$\rho_l C_p \frac{DT}{Dt} = \nabla\cdot(\lambda\nabla T) + Q \tag{5}$$

where $C_p$ is the specific heat capacity at constant pressure, $\lambda$ the thermal conductivity, and $Q$ the volumic heat source dissipated by Joule effect at the coil and given by $(1/\sigma)J_s^2$ (where $\sigma$ is the copper electrical conductivity, and $J_s$ the current density in the coil).

The computed electromagnetic field is assumed to be steady, and the ferrofluid magnetization is considered as instantaneously aligned with the magnetic field [4, pp. 22–23]. The pyromagnetic coefficient is neglected. The magnetostatic equations are given by

$$\nabla\times\mathbf{H} = \mathbf{J}, \quad \nabla\cdot(\mu\mathbf{H}) = 0, \quad \mu = \mu_0(1+\chi(T_{\text{ext}})) \tag{6}$$

where $\mathbf{J} = J_s\mathbf{e}_\theta$ and $\mu$ is the magnetic permeability of the ferrofluid. Recall that $\chi$ is given by (2) and $\mu_0$ is the magnetic permeability of vacuum.

Numerically, the PVC-aluminum tank is enclosed in a larger cylinder of radius 0.1 m and height 0.2 m and is therefore surrounded by a specific volume of ambient air. At the boundaries of this cylinder, the boundary condition for the magnetic problem $\mathbf{H}\times\mathbf{n} = \mathbf{0}$ is enforced. The non-slip boundary condition $\mathbf{u} = \mathbf{0}$ is applied at the boundary of the fluid domain (see blue lines in Fig. 1). The air convection at the top and on the lateral wall of the PVC-aluminum tank is modeled by using a Robin boundary condition on the temperature

$$-\lambda\nabla T\cdot\mathbf{n} = h(T - T_{\text{ext}}) \tag{7}$$

where $h$ is the convection coefficient and $\mathbf{n}$ is the outer unit normal vector (see red lines in Fig. 1). The homogeneous Neumann boundary condition $\partial_z T = 0$ is enforced at the bottom of the tank (see green line in Fig. 1). The initial conditions are $\mathbf{u} = \mathbf{0}$, $T = T_{\text{ext}}$, and $\mathbf{H} = \mathbf{0}$.

## III. SFEMaNS Code

We use the code SFEMaNS (the acronym stands for spectral/finite elements for the Maxwell and Navier–Stokes equations) for solving the coupled system of the aforementioned equations. We use a Fourier decomposition in the azimuthal $\theta$-direction and continuous finite elements in the meridian section (piecewise linear Lagrange elements for the pressure and piecewise quadratic Lagrange elements for the velocity, the magnetic field, and the temperature). For instance, the approximate temperature field has the following representation:

$$T = \sum_{m=0}^{m_{\max}-1} T_m^c(r,z,t)\cos(m\theta) + \sum_{m=1}^{m_{\max}-1} T_m^s(r,z,t)\sin(m\theta) \tag{8}$$

where $T_m^c(r,z,t)$ and $T_m^s(r,z,t)$ are scalar-valued finite-elements functions and $m_{\max}$ is the number of (complex) Fourier mode used in the discretization. All of the fields, either vector-valued or scalar-valued, are represented as shown in (8). Modulo the computation of non-linear terms using FFTW, the handling of the Fourier modes in the meridian plane, $(r,z)$, can be done in parallel. The divergence of $\mu\mathbf{H}$ is controlled by a technique using a negative Sobolev norm that guarantees convergence under minimal regularity. SFEMaNS has been thoroughly validated on numerous analytical solutions and against other magnetohydrodynamics codes [5], [6]. All of the computations reported in this article are done assuming axisymmetry, i.e., $m_{\max} = 1$.

## IV. Results and Comparisons

### A. Experiment Versus Numerics for the Coil Experiment

The copper coil that we use is doubly winded in order to form two coaxial resistors. When the direction of the

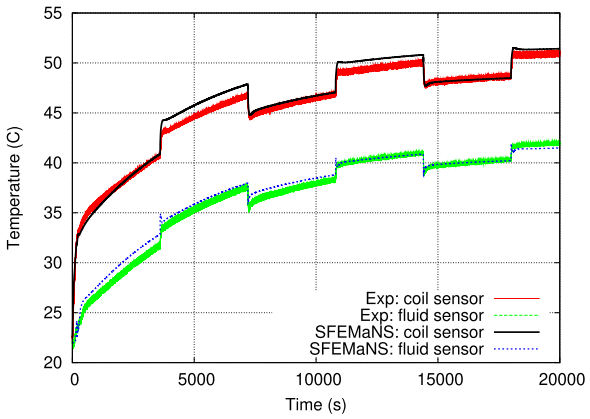


Fig. 2. Experimental and numerical temperature measurements with alternating magnetic force: the Helmholtz force is operative for $0 \leq t < 3600$ s and switched off for 3600 s $\leq t < 7200$ s with a total period of 7200 s.

TABLE II
PROPERTIES USED IN THE SIMULATIONS

| Property | Cu | Al | PVC | Coil | Ferrofluid |
|---|---|---|---|---|---|
| Density (kg/m$^3$) | 8933 | 2.70e3 | 1.40e3 | 4.00e3 | 1.115e3 |
| Therm. expansion (/K) | - | - | - | - | 6.62e-4 |
| Heat capacity (J/K·kg) | 385 | 945 | 1e3 | 612.82 | 1.685e3 |
| Therm. cond. (W/m·K) | 401 | 201 | 0.16 | 0.404 | 0.186 |
| Dyn. viscosity (Pa.s) | - | - | - | - | 0.0787 |

current $I$ is the same in the two windings (the magnetic field produced by the coil is non-zero), both the Joule effect and the Helmholtz force are operative. When the direction of the current is opposite in the windings, only the Joule effect is operative. We can therefore highlight the action of the Helmholtz force in the same experimental configuration.

Temperatures are continuously measured at two locations: on the coil and in the fluid on the symmetry axis (see the symbols "Tcoil" and "Tferrofluid" in Fig. 1). The Helmholtz force is periodically switched on and off with a total period of 7200 s, starting with an active force at $t = 0$ s. The time evolution on the two sensors is shown in Fig. 2.

The physical properties used for the Navier–Stokes and heat equations are listed in Table II. The ambient air is characterized by the exterior temperature $T_{\text{ext}} = 295.15$ K and the heat-transfer coefficient $h = 6.5$ W/m$^2$K. The other parameters are $\phi = 5.4\%$, $d = 16$ nm, $M_0 = 3.87 \times 10^5$ Am$^{-1}$, and $T_c = 793$ K. The electrical current in the coil is $I = 8$ A with the density $J_s = 3.35 \times 10^6$ Am$^{-2}$, electrical conductivity $\sigma = 5.998 \times 10^7$ Sm$^{-1}$, and the number of windings $N = 33$. The meridian mesh contains 118 451 nodes. The time step 0.025 s is used over $9 \times 10^5$ iterations (about 25 wall-clock hours using 64 processors for the domain decomposition on the cluster IBM x3750-M4 from GENCI-IDRIS).

Some uncertainties on the values of the physical parameters exist. However, the agreement between the experimental measurements of the temperatures on the two sensors and the numerical computations is excellent and therefore validates our ferrofluid modeling. Snapshots of the numerical velocity and temperature fields at $t = 16\,000$ s (when the Helmholtz force is active) and $t = 20\,000$ s (when the Helmholtz force is inactive) are shown in Figs. 3 and 4. Fig. 3 shows that the Helmholtz force has an impact of the thermal plume. When the Helmholtz force is active, the plume is deviated in the bulk above the coil, whereas it is centered on the symmetry axis when the Helmholtz force is switched off. This deviation is due to a recirculation localized near the bottom of the coil which pushes the hot fluid away from the axis [see Fig. 4(a)]. This lower recirculation does not exist when the Helmholtz force is inactive: the buoyancy force alone generates a single recirculation in the top part of the tank [see Fig. 4(b)]. Notice that the maximum value of the vertical velocity is the same with or without the Helmholtz force, but the maximum value of the temperature is lowered by 2 K when the Helmholtz force is operative. This proves that the thermomagnetic convection mechanism is beneficial in this case.

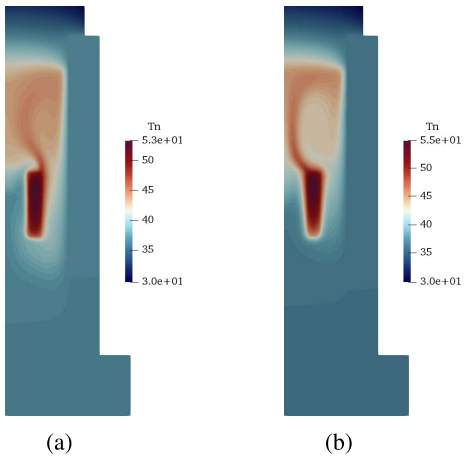


(a) (b)

Fig. 3. Temperature field (in Celsius) with alternating magnetic force. The symmetry axis ($Oz$) is on the left. (a) Helmholtz force at $t = 16\,000$ s. (b) No Helmholtz force at $t = 20\,000$ s.

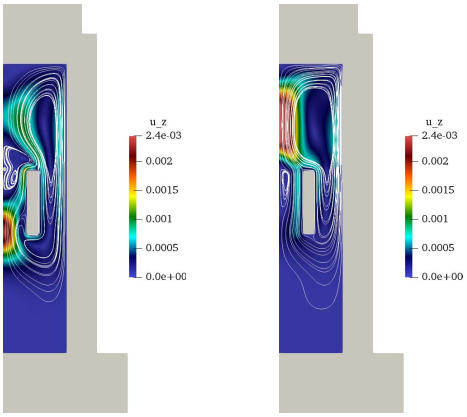


(a) (b)

Fig. 4. Color maps of the vertical velocity (in ms$^{-1}$) and velocity streamlines with alternating magnetic force. The symmetry axis ($Oz$) is on the left. The PVC-aluminum tank is shown in gray. (a) Helmholtz force at $t = 16\,000$ s. (b) No Helmholtz force at $t = 20\,000$ s.

### *B. Numerical Results for the Ferrofluid Experiment With Coil and Magnet*

We now numerically study the impact of an annular magnet with a remanent induction amplitude of 0.3 T. The magnet is localized alongside the PVC-aluminum tank. The objective is

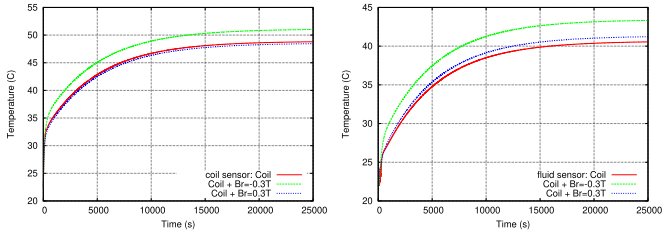


Fig. 5. Comparison of the temperatures computed at the two sensors for the three cases: only coil (red line), coil and $B_r = -0.3\ T$ (green line), and coil and $B_r = +0.3\ T$ (blue line).

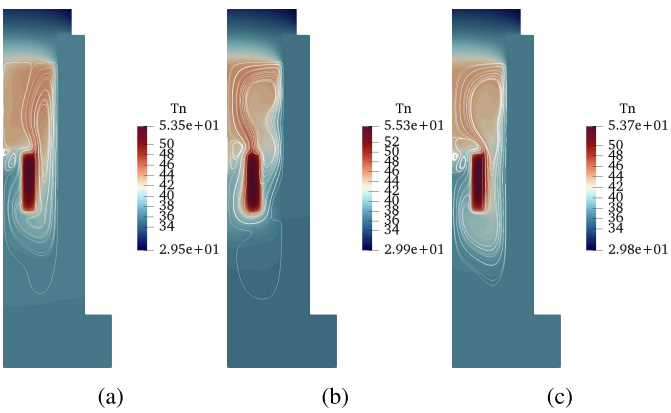


Fig. 6. Temperature field (in Celsius) and velocity streamlines at $t = 25\,000$ s for the three cases. (a) Only coil. (b) $B_r = -0.3\ T$ and coil. (c) $B_r = +0.3\ T$ and coil.

to use the magnet to improve the cooling by changing the distribution of the magnetic field induced by the coil.

*1) Magnet With a Radial Remanent Induction Field:* We test the action of an annular magnet of rectangular cross section with $B_r = \pm 0.3$ T, inner radius $r_i = 3.1$ cm, outer radius $r_o = 3.6$ cm, and height 1 cm. The bottom inner corner is localized at $r = 3.1$ cm and $z = 8$ cm (see Fig. 1). Fig. 5 shows the time evolution of the temperature at the two sensors. Using $B_r = +0.3$ T produces very little changes, whereas using $B_r = -0.3$ T increases the temperature at both sensors by approximately 3 K. Fig. 6 shows the temperature field in the saturated regime for the three cases. Hence, adding an annular magnet with a radial remanent induction does not decrease the maximum temperature reached in the coil.

*2) Magnet With a Vertical Remanent Induction Field:* We now test the action of an annular magnet with $B_z = \pm 0.3$ T using the same geometry and location of the magnet as in Section IV-B1. Fig. 7 shows the time evolution of the temperature at the two sensors. Using $B_z = -0.3$ T leads to an oscillating state (with a period of 22 s for $t < 9000$ s and 44 s for $t \geq 9000$ s). Using $B_z = +0.3$ T yields a steady state with a strong decrease of the temperature at the coil sensor. In fact, the maximum temperature observed in Fig. 8(b) is larger than the maximum temperature obtained with the coil alone by 1.7 K [see Fig. 6(a)].

To conclude, the temperature and velocity fields are strongly impacted by an annular magnet with a $\pm 0.3$ T remanent induction field. Optimization of the location, strength, and orientation of the magnet will be done in the near future. We

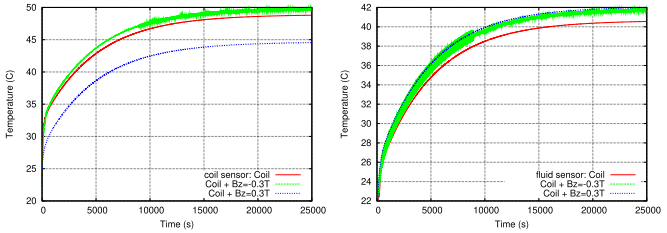


Fig. 7. Comparison of the temperatures computed at the two sensors for the three cases: only coil (red line), coil and $B_z = -0.3\ T$ (green line), and coil and $B_z = +0.3\ T$ (blue line).

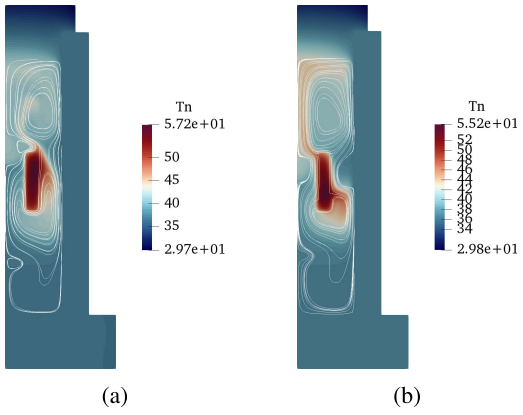


Fig. 8. Temperature field (in Celsius) and velocity streamlines at $t = 25\,000$ s with the coil and annular magnet $B_z = \pm 0.3$ T. (a) $B_z = -0.3\ T$ and coil. (b) $B_z = +0.3\ T$ and coil.

are also going to extend our investigations to more realistic configurations of power transformers like in [4, pp. 127–154].

## ACKNOWLEDGMENT

The high performance computer (HPC) resources for SFEMaNS were provided by Grand Equipement National de Calcul Intensif-Institut du Développement et des Ressources en Informatique Scientifique (GENCI-IDRIS) (grant 2018-0254) in France and by the Texas AM University Brazos HPC cluster. Support from the National Science Foundation under grants DMS 1620058, DMS 1619892 is acknowledged.

## REFERENCES

[1] M. Petit, A. Kedous-Lebouc, Y. Avenas, W. Cherief, and E. Rullière, "Etude expérimentale d'un système statique de génération de pression magnétothermique," in *Proc. Symp. de Génie Électrique*, Jul. 2014, pp. 1–6.

[2] R. Zanella, C. Nore, F. Bouillault, J.-L. Guermond, and X. Mininger, "Influence of thermomagnetic convection and ferrofluid thermophysical properties on heat transfers in a cylindrical container heated by a solenoid," *J. Magn. Magn. Mater.*, vol. 469, pp. 52–63, Jan. 2019.

[3] J. Patel, K. Parekh, and R. V. Upadhyay, "Prevention of hot spot temperature in a distribution transformer using magnetic fluid as a coolant," *Int. J. Therm. Sci.*, vol. 103, pp. 35–40, May 2016.

[4] R. Zanella, "Thermomagnetic convection in ferrofluids: Finite element approximation and application to transformer cooling," Ph.D. dissertation, Univ. Paris Saclay, Saint-Aubin, France, 2018.

[5] C. Nore, H. Zaidi, F. Bouillault, A. Bossavit, and J.-L. Guermond, "Approximation of the time-dependent induction equation with advection using Whitney elements," *COMPEL-Int. J. Comput. Math. Elect. Electron. Eng.*, Vol. 35, no. 1, pp. 326–338, 2016.

[6] A. Giesecke *et al.*, "Influence of high-permeability discs in an axisymmetric model of the Cadarache dynamo experiment," *New J. Phys.*, vol. 14, no. 5, May 2012, Art. no. 053005.

# Amélioration de la Convection Thermomagnétique par Ajout d'un Aimant Auxiliaire

Sleimane Nasser El Dine[1], Xavier Mininger[1], Caroline Nore[2]
[1]Université Paris-Saclay, CentraleSupélec, CNRS, Laboratoire de Génie Electrique et Electronique de Paris, 91192, Gif-sur-Yvette, France.
[1]Sorbonne Université, CNRS, Laboratoire de Génie Electrique et Electronique de Paris, 75252, Paris, France
Sleimane.Nassereldine@geeps.centralesupelec.fr, Xavier.Mininger@geeps.centralesupelec.fr
[2]Université Paris-Saclay, CNRS, LIMSI, 91400 Orsay, France
Caroline.Nore@limsi.fr

**RESUME – Ces travaux s'intéressent à la possibilité d'utiliser un ferrofluide pour l'évacuation de la chaleur liée aux pertes d'un système électromagnétique. Le système simple étudié ici est un solénoïde immergé dans un ferrofluide, auquel est ajouté un aimant en forme d'anneau entourant le dispositif. L'objectif principal est d'analyser dans quelle mesure l'addition du champ magnétique statique de l'aimant permet d'améliorer le transfert thermique. Les approches numérique et expérimentale pour l'étude de ce couplage entre magnétostatique, thermique et écoulement de fluide sont décrites. Le modèle numérique s'appuie sur la méthode des éléments finis en géométrie axisymétrique. Les résultats numériques et expérimentaux montrent que l'addition du champ de l'aimant à celui du solénoïde impacte la distribution des forces magnétiques. En conséquence, l'écoulement du ferrofluide autour du solénoïde est modifié, et l'évacuation de la chaleur peut dans certaines configurations être améliorée.**

***Mots-clés – Ferrofluide, convection thermomagnétique, refroidissement, méthode des éléments finis, force magnétique***

## 1. INTRODUCTION

Afin de refroidir les transformateurs de puissance, ces derniers peuvent être plongés dans un bain d'huile améliorant entre autres l'évacuation de la chaleur due aux pertes du système. Des études ont montré que des huiles végétales naturelles ou synthétiques apparaissent comme une alternative prometteuse aux huiles minérales, dont la pérennité à moyen terme n'est pas assurée. Des chercheurs ont étudié l'impact de l'insertion de particules ferromagnétiques dans ces huiles végétales sur les performances du refroidissement, modifiées d'une part par le changement des propriétés du fluide, mais aussi par la présence d'une force magnétique s'appliquant sur les particules. Ces fluides magnétiques, appelés ferrofluides, sont donc des suspensions colloïdales de particules monodomaines ferromagnétiques, comme la magnétite, placées dans un liquide porteur non magnétique [1]. Un surfactant couvrant ces particules évite leur agglomération.
Sous l'action d'un champ magnétique extérieur, l'aimantation des particules en suspension dans le fluide s'aligne avec les lignes du champ. La force magnétique qui s'exerce sur ces particules a alors tendance à attirer vers le solénoïde les parties froides du ferrofluide, plus perméables au champ magnétique [2]. En se rapprochant de la bobine, le fluide se réchauffe et son aimantation diminue. La dépendance entre la magnétisation du ferrofluide et le champ magnétique est exprimée par la théorie de Langevin pour un matériau magnétique linéaire [3] :

$$\mathbf{M} = \chi(T)\mathbf{H}, \tag{1}$$

où $\mathbf{M}$ est la magnétisation du ferrofluide, $T$ la température, et $\mathbf{H}$ le champ magnétique. $\chi$ est la susceptibilité magnétique du ferrofluide et dépend de plusieurs paramètres :

$$\chi(T) = \frac{\phi\mu_0\pi d^3 M_{s,p}^2(T)}{18k_BT},\ \frac{M_{s,p}(T)}{M_0} = 1 - \left(\frac{T}{T_c}\right)^{\frac{3}{2}}, \tag{2}$$

où $\phi$ est la fraction volumique des particules magnétiques, $\mu_0$ la perméabilité magnétique du vide, $d$ le diamètre moyen des particules, $M_{s,p}(T)$ la magnétisation des particules dépendant de la température, $k_B$ la constante de Boltzmann, $M_0$ la magnétisation des particules à la saturation et à 0K, et $T_c$ la température de Curie du matériau magnétique (ferrite de cobalt pour cette étude). Une force magnétique s'ajoute alors à la force thermique de Boussinesq. Cette force magnétique peut être modélisée par l'expression de Kelvin qui, dans l'hypothèse où $\mathbf{M}$ et $\mathbf{H}$ sont colinéaires, peut se mettre sous la forme [4] :

$$\mathbf{F} = \mu_0(\chi(T) - \chi(T_0))\nabla\frac{H^2}{2}, \tag{3}$$

où $H = \|\mathbf{H}\|$, et $\chi(T_0)$ est la susceptibilité magnétique du ferrofluide à la température extérieure $T_0$.

Cette force entraîne l'apparition d'une convection qui s'ajoute à la convection naturelle du fluide, et qui n'est présente qu'à la condition d'avoir la présence simultanée d'un gradient de champ magnétique et d'un gradient de température. Cette convection magnétothermique a pour conséquence une modification de l'écoulement autour du système électromagnétique qui peut, dans certaines configurations, améliorer le transfert thermique avec l'environnement [5]. Ainsi, l'ajout d'une pompe mécanique pour faire circuler le fluide pourrait être évité.
L'étude proposée s'intéresse à l'impact de l'ajout d'un aimant annulaire placé à l'extérieur du dispositif sur le refroidissement. Différentes configurations ont été analysées à l'aide du modèle numérique avec, comme paramètres, la position de l'aimant et l'orientation de son aimantation rémanente [6]. La première partie de cet article présentera le dispositif expérimental et le modèle régissant le couplage multiphysique. Dans la deuxième partie, des mesures expérimentales seront comparées aux résultats de la simulation numérique pour valider l'apport de l'aimant dans le refroidissement du système.

## 2. DISPOSITIF EXPÉRIMENTAL ET COUPLAGE MULTIPHYSIQUE

Le système étudié est un solénoïde en cuivre immergé dans un ferrofluide à base de ferrite de cobalt. Il est placé dans une cuve en aluminium, fermée par le dessus par un bouchon de PVC comme le montre la figure 1. Un aimant torique de section carrée est placé contre la cuve, pour étudier l'impact du champ

extérieur fourni par ce dernier. Les dimensions du dispositif expérimental sont données dans le tableau 1. Le ferrofluide utilisé est considéré comme étant un fluide Newtonien incompressible, homogène et continu.

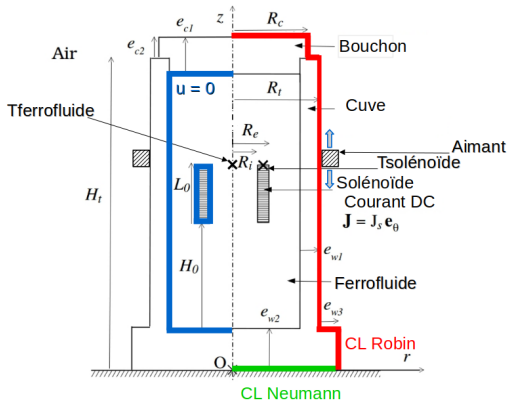


Fig. 1. Dispositif expérimental, hauteur de la cuve $H_t = 12,5\ cm$

| Paramètre | $H_t$ | $R_t$ | $e_{w1}$ | $e_{w2}$ | $e_{w3}$ | $H_0$ |
|---|---|---|---|---|---|---|
| Valeur (cm) | 12,5 | 3,1 | 1 | 2 | 1 | 3,9 |
| Paramètre | $L_0$ | $R_i$ | $R_e$ | $R_c$ | $e_{c1}$ | $e_{c2}$ |
| Valeur (cm) | 2,1 | 0,8 | 1,175 | 2,6 | 2 | 1 |

Tableau 1. Dimensions du dispositif expérimental

Les équations de Navier-Stokes décrivant le mouvement du fluide s'expriment par :

$$\begin{cases} \nabla\cdot\mathbf{u} = 0, \\ \rho_l \dfrac{D\mathbf{u}}{Dt} + \nabla p - \nabla\cdot e(T,\mathbf{u}) = \rho_l \beta g (T - T_0)\mathbf{e_z} + \mathbf{F}, \end{cases} \tag{4}$$

où $\mathbf{u}$ est le vecteur vitesse, $\frac{D}{Dt}$ la dérivée matérielle, $p$ la pression, $e(T,\mathbf{u}) = \eta(T)(\nabla\mathbf{u} + (\nabla\mathbf{u})^{\mathsf{T}})$ avec $\eta$ la viscosité dynamique (variant en $\eta(T) = Af(\phi)\exp(BT^{-1})$ avec $A = 1,3\times10^{-6} Pa.s$, $B = 3,1\times10^3\ K$ et $f(\phi)$ donné par le modèle de Rosensweig (voir [4], p. 105), $\rho_l$ la densité, $\beta$ le coefficient d'expansion thermique, et $g$ l'accélération de pesanteur. Les deux termes à droite de l'équation de la quantité de mouvement sont respectivement la force de Boussinesq et la force magnétique.
Le transfert de chaleur dans le ferrofluide et avec le milieu extérieur est décrit par l'équation d'énergie :

$$\rho_l C_p \frac{DT}{Dt} = \nabla\cdot(\lambda\nabla T) + Q, \tag{5}$$

où $C_p$ est la capacité calorifique à pression constante, $\lambda$ la conductivité thermique et $Q$ la source de chaleur volumique dissipée par effet Joule dans le cuivre et donnée par $\frac{1}{\sigma}J_s^2$ (où $\sigma$ est la conductivité électrique du cuivre, et $J_s$ la densité de courant dans le solénoïde).
Le champ magnétique appliqué est statique et la magnétisation du ferrofluide est supposée instantanément alignée avec le champ magnétique. Les équations de la magnétostatique sont données par :

$$\nabla\times H = \mathbf{J}, \quad \nabla\cdot(\mu\mathbf{H}) = 0, \quad \mu = \mu_0(1+\chi(T_0)), \tag{6}$$

où $\mathbf{J} = J_s\mathbf{e}_\theta$ et $\mu$ est la perméabilité magnétique du ferrofluide.
Pour le calcul numérique magnétique, une couche d'air est ajoutée autour de la cellule d'essai pour assurer la fermeture des lignes du champ magnétique. La condition limite magnétique imposée sur les parois de l'air est $\mathbf{A}\times\mathbf{n} = \mathbf{0}$, $\mathbf{A}$ étant le potentiel vecteur magnétique, et une condition de non glissement $\mathbf{u} = \mathbf{0}$ est appliquée sur les parois du domaine fluidique. Thermiquement, une condition limite de type Robin est imposée sur les parois supérieure et latérale de la cuve, afin de modéliser le transfert de chaleur avec l'air ambiant :

$$-\lambda\nabla T\cdot\mathbf{n} = h(T - T_0), \tag{7}$$

où $h$ est le coefficient d'échange thermique et $\mathbf{n}$ le vecteur unitaire sortant et normal à la cuve. Une condition de type Neumann homogène est appliquée sur la frontière inférieure de la cuve $\partial_z T = 0$. Les conditions initiales sont $\mathbf{u} = \mathbf{0}$, $T = T_0$, et $\mathbf{H} = \mathbf{0}$.
Les propriétés physiques utilisées dans les équations de Navier-Stokes et de chaleur sont données dans le tableau 2. Le coefficient de transfert de chaleur est fixé à $h = 6,5\ W/m^2.K$. Les autres paramètres sont $\phi = 5,4\ \%$, $d = 16\ nm$, $M_0 = 3,87\times10^5\ A/m$, $T_c = 793\ K$. Le courant électrique dans le solénoïde est $I = 8\ A$ avec une densité de courant $J_s = 3,35\times10^6\ A/m^2$, la conductivité électrique $\sigma = 5,998\times10^7\ S/m$ et le nombre de spires $N = 33$.

| Propriétés | Cu | Al | PVC | Solénoïde | Ferrofluide |
|---|---|---|---|---|---|
| Densité (kg/m$^3$) | 8933 | 2.70e3 | 1.40e3 | 3.964e3 | 1.045e3 |
| Expansion therm. (/K) | - | - | - | - | 7.0004e-4 |
| Capacité calorifique (J/K·kg) | 385 | 945 | 1e3 | 616 | 1.775e3 |
| Cond. therm. (W/m·K) | 401 | 201 | 0.16 | 0.388 | 0.1785 |
| Viscosité dyn. (Pa.s) | - | - | - | - | 0.0703 |

Tableau 2. Propriétés physiques utilisées en simulation numérique

## 3. RÉSULTATS ET COMPARAISON

Plusieurs configurations de position d'aimant et d'orientation de son aimantation rémanente ont alors été modélisées, et cette partie présente la solution qui semble la plus intéressante pour le processus de refroidissement. Un aimant annulaire ($\Phi$ 140 $\times$ $63\times17\ mm$) ayant une induction rémanente axiale $B_z = 0,2T$ est ainsi placé contre la cuve à une hauteur optimale de 65 $cm$ par rapport au font de la cuve. Deux thermocouples sont utilisés pour mesurer la température en surface du solénoïde et dans le fluide (voir figure 1), la température ambiante étant pour cette expérience $T_0 = 288\ K$. En parallèle de la partie expérimentale, un calcul numérique a été lancé pour enregistrer les évolutions de la température aux mêmes points de mesure. Les résultats des deux tests sont présentés ci-dessous :

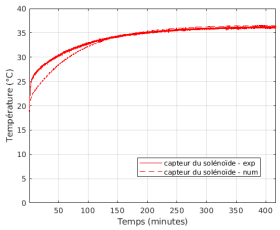


Fig. 2. Températures au niveau du solénoïde, $B_z = -0,2\ T$

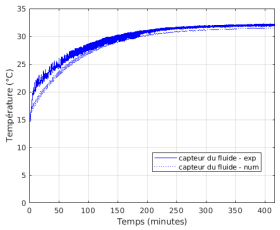


Fig. 3. Températures au niveau du fluide, $B_z = -0,2\ T$

Une différence de constante de temps en régime transitoire est observée, avec un temps de diffusion thermique plus rapide

en expérimental qu'en numérique peut-être liée au modèle thermique homogénéisé de la bobine. Les températures en régime permanent sont par contre très proches pour les deux points de mesure. Pour évaluer l'impact des aimants auxiliaires sur le processus de refroidissement, deux essais expérimentaux ont été comparés : le premier en présence de l'aimant axial, et l'autre en absence de ce dernier. Les courbes de température figurent ci-dessous :

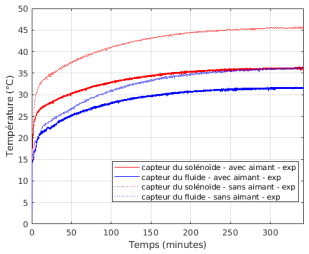


Fig. 4. Mesures de température, comparaison avec/sans aimant axial

On remarque que, dans le cas où l'aimant axial est présent, la température de surface du solénoïde est diminuée de 9 $K$ environ. Ceci s'explique par l'intensification des flux magnétiques dans le ferrofluide, ce qui amplifie l'amplitude de la force magnétique, et maximise l'écoulement du fluide autour du bobinage. Les échanges thermiques avec l'extérieur sont ainsi directement favorisés.

## 4. CARTOGRAPHIES DE VITESSE ET DE TEMPÉRATURE

Deux calculs numériques ont été lancés dans deux configurations différentes : la première en présence d'un aimant axial, la seconde en son absence. Les cartographies de champ magnétique, de vitesse et de la température à $t = 25000\ s$ sont présentées sur les figures 5,6,7,8,9 et 10 respectivement pour chacun des deux cas :

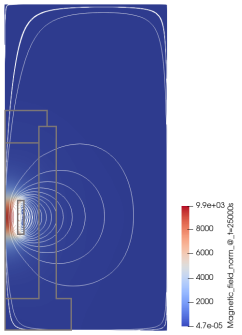

Fig. 5. Intensité du champ magnétique $(A/m)$, sans aimant

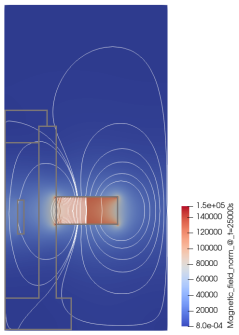

Fig. 6. Intensité du champ magnétique $(A/m)$, $B_z = -0,2\ T$

La comparaison des champs de vitesse et de température à $t = 25000\ s$ confirme la modification de la circulation du fluide autour du solénïde, et par conséquent l'effet apporté par l'aimant extérieur sur le refroidissement. Lorsque l'aimant n'est pas ajouté (voir figure 5), seul le champ magnétique du solénoïde est présent. Les circulations du fluide (de la figure 7) sont dues à la présence de la force magnétique s'exerçant sur le ferrofluide en plus de la force de Boussinesq d'origine thermique. La figure 9 montre que le panache de température émerge du solénoïde, se rapproche de l'axe de symétrie (bord gauche de la figure), puis se courbe vers l'extérieur.

En présence de l'aimant axial $B_z = -0,2\ T$ (voir figure 6), des modifications dans les circulations du fluide apparaissent dans la partie située sous le solénoïde (voir figure 8) qui amplifient l'évacuation de la chaleur. La vitesse est augmentée. Ceci est causé par la modification des lignes de champ et l'intensification des flux magnétiques dans le fluide. Un nouveau panache thermique apparaît se déplaçant vers le bas et l'extérieur comme montré sur la figure 10 : il est entraîné par les deux cellules inférieures de circulation du fluide. Un autre panache ascendant et moins actif est présent dans la partie supérieure de la cuve. Il suit les contours des cellules de convection supérieures.
En conséquence de ces nouvelles circulations du fluide, la température maximale du solénoïde est abaissée de $5,5\ K$. L'impact de l'ajout d'un aimant auxiliaire sur le refroidissement du solénoïde est vérifié.

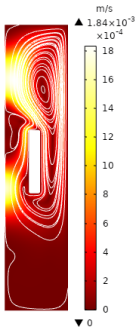


Fig. 7. Intensité de la vitesse avec lignes de courant, sans aimant

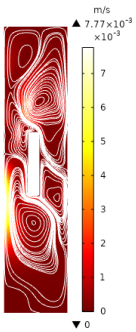


Fig. 8. Intensité de la vitesse avec lignes de courant, $B_z = -0,2\ T$

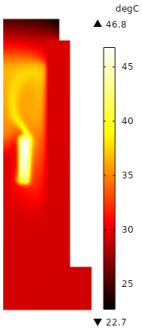


Fig. 9. Température, sans aimant

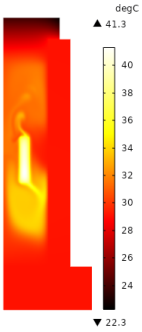


Fig. 10. Température, $B_z = -0,2\ T$

Concernant les allures temporelles, les figure 11 et 12 permettent d'observer la température en des points définis respectivement à la surface du solénoïde et dans le fluide dans les deux configurations : la première lorsque le champ magnétique du solénoïde est seul présent, la seconde concerne le cas où l'aimant extérieur est présent.

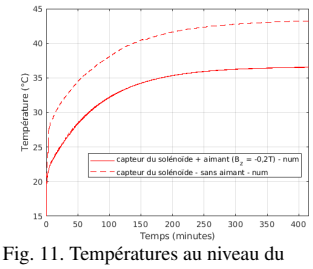


Fig. 11. Températures au niveau du solénoïde

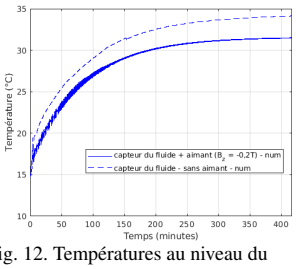


Fig. 12. Températures au niveau du fluide

Les courbes de température atteignent un régime stationnaire après environ $25000\ s$ que ce soit pour le fluide ou le bobinage. Pour le bobinage, une diminution de 7 $K$ est à noter en présence de l'aimant. Pour le fluide, une diminution moins importante de la température de l'ordre de 3 $K$ est enregistrée. Des oscillations

sur la courbe de température du fluide sont présentes pendant le régime transitoire pour une durée de $7500\ s$ environ lorsque l'aimant est ajouté.

## 5. ESSAIS AVEC UN COEUR FERROMAGNÉTIQUE

Dans cette partie, l'idée consiste à insérer un coeur ferromagnétique placé sur l'axe de symétrie pour se rapprocher de la structure réelle d'un transformateur de puissance. Un aimant axial $B_z = 0,3\ T$ est alors fixé sur la partie supérieure du cœur pour augmenter et modifier les flux magnétiques au voisinage du solénoïde en vue d'augmenter l'évacuation de chaleur du système. En lien avec ces deux configurations, deux calculs numériques ont été lancés : le premier concerne le modèle du solénoïde auquel le coeur ferromagnétique est ajouté, et le second correspond au cas où un aimant auxiliaire est placé au-dessus du coeur ferromagnétique. La température initiale pour cette simulation est $T_0 = 295.15\ K$. Les profils du champ magnétique à $t = 10000\ s$ pour chacun des deux cas sont présentés ci-dessous :

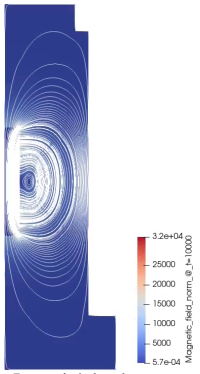


Fig. 13. Intensité du champ magnétique $(A/m)$, sans aimant

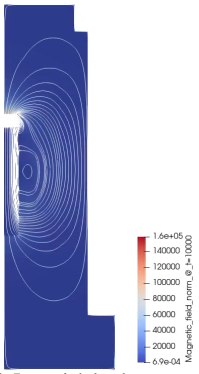


Fig. 14. Intensité du champ magnétique $(A/m)$, $B_z = 0,3\ T$

Dans la figure 13, le coeur ferromagnétique ajouté permet de mieux canaliser les lignes de champ $H$ en concentrant ces lignes sur l'axe de symétrie à l'intérieur du bobinage. Lorsqu'un aimant axial est ajouté sur la surface du coeur (voir figure 14), la distribution des lignes de champ $H$ est modifiée. En effet, une intensification de ces lignes apparaît au niveau de l'aimant et l'intensité du champ magnétique est maximisée. Cela se traduit par une augmentation de la force magnétique vers la partie supérieure du système. Les cartographies de vitesse et de température à $t = 10000\ s$ correspondant aux différentes distributions du champ magnétique sont montrées ci-après.

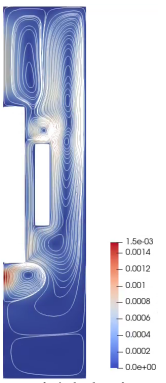


Fig. 15. Intensité de la vitesse $(m/s)$ avec lignes de courant, sans aimant

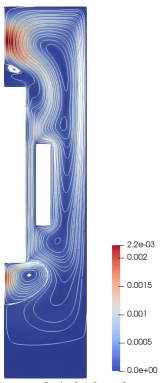


Fig. 16. Intensité de la vitesse $(m/s)$ avec lignes de courant, $B_z = 0,3\ T$

L'écoulement du ferrofluide autour du solénoïde et dans la cuve est fortement modifié après l'ajout de l'aimant. Dans la figure 16, une nouvelle cellule de convection apparaît au-dessus du coeur ferromagnétique entraînant une modification de la circulation du fluide par rapport à son comportement dans la figure 15 lorsque l'aimant est absent. Le ferrofluide acquiert alors une vitesse plus grande et favorise la dissipation de la chaleur à travers la cuve par son écoulement modifié.

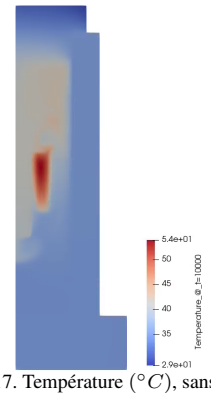


Fig. 17. Température $(°C)$, sans aimant

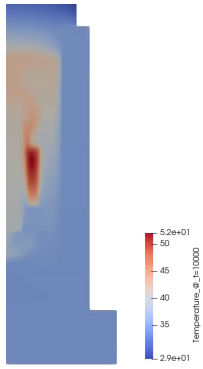


Fig. 18. Température $(°C)$, $B_z = 0,3\ T$

L'analyse des panaches thermiques des deux cas montre l'effet apporté par l'aimant axial sur le refroidissement. Une diminution significative de la température maximale de $2\ K$ est enregistrée. Les volutes des panaches à $t = 10000\ s$ pour le cas avec aimant (figure 18) montrent une évacuation de chaleur renforcée au-dessus du bobinage. Dans cette configuration, l'effet bénéfique de l'aimant sur le processus d'échange de chaleur est à nouveau confirmé.

## 6. CONCLUSIONS

Des résultats numériques et expérimentaux ont montré que l'ajout d'un aimant peut modifier l'écoulement du ferrofluide autour du système électromagnétique, et renforcer ainsi son refroidissement à moindre coût. Les cartographies de vitesse et de température du système étudié permettent de valider l'impact apporté par un champ magnétique auxiliaire. Les circulations du fluide dans la cuve et autour du bobinage sont renforcées et les panaches thermiques montrent que l'échange de chaleur via la convection thermomagnétique est favorisé. Des essais d'optimisation avec insertion d'un coeur ferromagnétique ont montré également un abaissement significatif de la température maximale du solénoïde selon la configuration magnétique adoptée de l'aimant.

## 7. RÉFÉRENCES


[1] R. E. Rosensweig. Magnetic Fluids. *Annual Reviews of Fluid Mechanics*, 19 :437–463, 1987.

[2] M. Petit, A. K-Lebouc, Y. Avenas, W. Cherief, and E. Rullière. Etude expérimentale d'un système statique de génération de pression magnétothermique. In *Symposium de Génie Électrique*, July 2014.

[3] Raphaël Zanella, Caroline Nore, Frédéric Bouillault, Jean-Luc Guermond, and Xavier Mininger. Influence of thermomagnetic convection and ferrofluid thermophysical properties on heat transfers in a cylindrical container heated by a solenoid. *Journal of Magnetism and Magnetic Materials*, 469 :52 – 63, 2019.

[4] R. Zanella. *Thermomagnetic convection in ferrofluids : finite element approximation and application to transformer cooling*. PhD thesis, Université Paris Saclay, 2018.

[5] J. Patel, K. Parekh, and R. V. Upadhyay. Prevention of hot spot temperature in a distribution transformer using magnetic fluid as a coolant. *International Journal of Thermal Sciences*, 103 :35–40, 2016.

[6] S. Nasser El Dine, X. Mininger, C. Nore, R. Zanella, F. Bouillault, and J. Guermond. Impact of magnets on ferrofluid cooling process : Experimental and numerical approaches. *IEEE Transactions on Magnetics*, 56(1) :1–4, Jan 2020.

# Bibliography


[1] Y. Bertrand and Patrick Lauzevis. Low viscosity insulating liquid based on natural esters for distribution transformers. In *22nd International Conference on Electricity Distribution*, pages 374–377, 06 2013.

[2] Y. Bertrand. Development of a low viscosity insulating fluid based on vegetable oil. *2012 IEEE International Symposium on Electrical Insulation*, pages 413–418, 2012.

[3] Y. Bertrand and L.C. Hoang. Vegetal oils as substitute for mineral oils. In *Proceedings of the 7th International Conference on Properties and Applications of Dielectric Materials (Cat. No.03CH37417)*, volume 2, pages 491–494 vol.2, 2003.

[4] John Philip, Shima P Damodaran, and Baldev Raj. Nanofluid with tunable thermal properties. *Applied Physics Letters*, 92:043108–043108, 01 2008.

[5] R. Zanella, C. Nore, F. Bouillault, L. Cappanera, I. Tomas, X. Mininger, and J. Guermond. Study of magnetoconvection impact on a coil cooling by ferrofluid with a spectral/finite-element method. *IEEE Transactions on Magnetics*, 54(3):1–4, 2018.

[6] Ronald E. Rosensweig. *Ferrohydrodynamics*. Dover Publications, 2018.

[7] R. E. Rosensweig. Magnetic Fluids. *Annual Reviews of Fluid Mechanics*, 19:437–463, 1987.

[8] Irena Milosevic, Laurence Motte, and Frédéric Mazaleyrat Résumé. Ferrofluides - nanoparticules superparamagnétiques. *Techniques de l'Ingénieur*, 33, 2011.

[9] W. Cherief. *Etude des ferrofluides et de leurs applications à l'intensification des transferts de chaleur par convection forcée*. PhD thesis, Université de Grenoble Alpes, 2015.

[10] Stefan Odenbach. *Magnetoviscous Effects in Ferrofluids*. Springer-Verlag, 2002.

[11] S Odenbach. Recent progress in magnetic fluid research. *Journal of Physics: Condensed Matter*, 16(32):R1135–R1150, aug 2004.

[12] M. Petit. *Contribution à l'étude des systèmes de refroidissement basés sur le couplage magnétothermique dans les ferrofluides à faible température de Curie : mise en place d'outils de caractérisation et de modélisation*. PhD thesis, Université de Grenoble, 2012.

[13] R. Zanella. *Thermomagnetic convection in ferrofluids : finite element approximation and application to transformer cooling*. PhD thesis, Université Paris Saclay, 2018.

[14] H. C. Hamaker. The london–van der waals attraction between spherical particles. *Physica*, IV(10):1058–1072, 11 1937.

[15] Abdelhamid Elaissari. Ferrofluides et particules magnétiques pour applications biomédicales. *Techniques de l'Ingénieur*, 33, 2015.

[16] R. Chantrell, J. Popplewell, and S. Charles. Measurements of particle size distribution parameters in ferrofluids. *IEEE Transactions on Magnetics*, 14(5):975–977, 1978.

[17] Lucian Pîslaru-Dănescu, Gabriela Telipan, Floriana D. Stoian, Sorin Holotescu, and Oana Maria Marinică. *Nanofluid with Colloidal Magnetic Fe3O4 Nanoparticles and Its Applications in Electrical Engineering*. IntechOpen, 2017.

[18] René Massart, Jean-Claude Bacri, and Régine Perzynski. Liquides magnétiques ou ferrofluides. *Techniques de l'Ingénieur*, D2180 V1, 1995.

[19] J. L. Neuringer and R. E. Rosensweig. Ferrohydrodynamics. *The Physics of Fluids*, 7(12):1927–1937, December 1964.

[20] Shahriar Afkhami, Yuriko Renardy, M. RENARDY, J. RIFFLE, and Timothy St Pierre. Field-induced motion of ferrofluid droplets through immiscible viscous media. *Journal of Fluid Mechanics*, 610:363 – 380, 09 2008.

[21] Ashkan Vatani, Peter Lloyd Woodfield, Nam-Trung Nguyen, Ayoub Abdollahi, and Dzung Viet Dao. Numerical simulation of combined natural and thermomagnetic convection around a current carrying wire in ferrofluid. *Journal of Magnetism and Magnetic Materials*, 489:165383, 2019.

[22] Ashkan Vatani, Peter Lloyd Woodfield, Nam-Trung Nguyen, and Dzung Viet Dao. Onset of thermomagnetic convection around a vertically oriented hot-wire in ferrofluid. *Journal of Magnetism and Magnetic Materials*, 456:300–306, 2018.

[23] Peter S.B. Szabo, Miloš Beković, and Wolf-Gerrit Früh. Using infrared thermography to investigate thermomagnetic convection under spatial non-uniform magnetic field. *International Journal of Thermal Sciences*, 116:118 – 128, 2017.

[24] Peter S.B. Szabo and Wolf-Gerrit Früh. The transition from natural convection to thermomagnetic convection of a magnetic fluid in a non-uniform magnetic field. *Journal of Magnetism and Magnetic Materials*, 447:116 – 123, 2018.

[25] Majid Ashouri and Mohammad Behshad Shafii. Numerical simulation of magnetic convection ferrofluid flow in a permanent magnet–inserted cavity. *Journal of Magnetism and Magnetic Materials*, 442:270–278, 2017.

[26] J. R. Melcher. *Continuum Electromechanics*. MIT Press, Cambridge, MA, 1981.

[27] A. Bossavit. On forces in magnetized matter. *IEEE Transactions on Magnetics*, 50(2):229–232, 2014.

[28] *Convective Heat Transfer Enhancement in Nanofluids: Real Anomaly or Analysis Artifact?*, volume ASME/JSME 2011 8th Thermal Engineering Joint Conference of *ASME/JSME Thermal Engineering Joint Conference*, 03 2011.

[29] Ridho Irwansyah, Christian Cierpka, and Christian Kähler. On the reliable estimation of heat transfer coefficients for nanofluids in a microchannel. *Journal of Physics: Conference Series*, 745:032078, 09 2016.

[30] Y. Raja Sekhar, K.V. Sharma, R. Thundil Karupparaj, and C. Chiranjeevi. Heat transfer enhancement with al2o3 nanofluids and twisted tapes in a pipe for solar thermal applications. *Procedia Engineering*, 64:1474–1484, 2013. International Conference on Design and Manufacturing (IConDM2013).

[31] Yimin Xuan and Wilfried Roetzel. Conceptions for heat transfer correlation of nanofluids. *International Journal of Heat and Mass Transfer*, 43(19):3701–3707, 2000.

[32] S.A. Angayarkanni and John Philip. Review on thermal properties of nanofluids: Recent developments. *Advances in Colloid and Interface Science*, 225:146–176, 2015.

[33] N.S. Susan Mousavi and Sunil Kumar. Effective heat capacity of ferrofluids – analytical approach. *International Journal of Thermal Sciences*, 84:267–274, 2014.

[34] Xiang-Qi Wang and Arun Mujumdar. A review on nanofluids - part i: Theoretical and numerical investigations. *Brazilian Journal of Chemical Engineering*, 25:613–630, 12 2008.

[35] Hidetoshi Masuda, Akira Ebata, Kazunari Teramae, and Nobuo Hishinuma. Alteration of thermal conductivity and viscosity of liquid by dispersing ultra-fine particles. *Netsu Bussei*, 7(4):227, 1993.

[36] S.M.S. Murshed, K.C. Leong, and C. Yang. Enhanced thermal conductivity of tio2—water based nanofluids. *International Journal of Thermal Sciences*, 44(4):367–373, 2005.

[37] S.M.S. Murshed, K.C. Leong, and C. Yang. Investigations of thermal conductivity and viscosity of nanofluids. *International Journal of Thermal Sciences*, 47(5):560–568, 2008.

[38] Elena Timofeeva, Alexei Gavrilov, James McCloskey, Yuriy Tolmachev, Samuel Sprunt, Lena Lopatina, and Jonathan Selinger. Thermal conductivity and particle agglomeration in alumina nanofluids: Experiment and theory. *Physical review. E, Statistical, nonlinear, and soft matter physics*, 76:061203, 01 2008.

[39] Innocent Nkurikiyimfura, Yanmin Wang, and Zhidong Pan. Heat transfer enhancement by magnetic nanofluids—a review. *Renewable and Sustainable Energy Reviews*, 21:548–561, 2013.

[40] Seung Won Lee, Sung Dae Park, Sarah Kang, In Cheol Bang, and Ji Hyun Kim. Investigation of viscosity and thermal conductivity of sic nanofluids for heat transfer applications. *International Journal of Heat and Mass Transfer*, 54(1):433–438, 2011.

[41] Ashkan Vatani, Peter Lloyd Woodfield, and Dzung Viet Dao. A survey of practical equations for prediction of effective thermal conductivity of spherical-particle nanofluids. *Journal of Molecular Liquids*, 211:712–733, 2015.

[42] Maryam Abareshi, Elaheh K. Goharshadi, Seyed Mojtaba Zebarjad, Hassan Khandan Fadafan, and Abbas Youssefi. Fabrication, characterization and measurement of thermal conductivity of fe3o4 nanofluids. *Journal of Magnetism and Magnetic Materials*, 322(24):3895–3901, 2010.

[43] Bruce Finlayson. Convective instability of ferromagnetic fluids. *Journal of Fluid Mechanics*, 40:753 – 767, 03 1970.

[44] Jacob Eapen, Roberto Rusconi, Roberto Piazza, and Sidney Yip. The classical nature of thermal conduction in nanofluids. *Journal of Heat Transfer*, pages 1–24, 07 2010.

[45] Qiang Li, Yimin Xuan, and Jian Wang. Experimental investigations on transport properties of magnetic fluids. *Experimental Thermal and Fluid Science*, 30(2):109–116, 2005.

[46] H. C. Brinkman. The viscosity of concentrated suspensions and solutions. *The Journal of Chemical Physics*, 20(4):571–571, 1952.

[47] T. S. Lundgren. Slow flow through stationary random beds and suspensions of spheres. *Journal of Fluid Mechanics*, 51(2):273–299, 1972.

[48] G. K. Batchelor. The effect of brownian motion on the bulk stress in a suspension of spherical particles. *Journal of Fluid Mechanics*, 83(1):97–117, 1977.

[49] A. Einstein. Eine neue bestimmung der moleküldimensionen. *Annalen der Physik*, 324(2):289–306, 1906.

[50] David C. Venerus, Jacopo Buongiorno, Rebecca Christianson, Jessica Townsend, In Cheol Bang, Gang Chen, Sung Jae Chung, Minking Chyu, Haisheng Chen, Yulong Ding, Frank Dubois, Grzegorz Dzido, Denis Funfschilling, Quentin Galand, Jinwei Gao, Haiping Hong, Mark Horton, Linwen Hu, Carlo S. Iorio, Andrzej B. Jarzebski, Yiran Jiang, Stephan Kabelac, Mark A. Kedzierski, Chongyoup Kim, Ji-Hyun Kim, Sukwon Kim, Thomas McKrell, Rui Ni, John Philip, Naveen Prabhat, Pengxiang Song, Stefan Van Vaerenbergh, Dongsheng Wen, Sanjeeva Witharana, Xiao-Zheng Zhao, and Sheng-Qi Zhou. Viscosity measurements on colloidal dispersions (nanofluids) for heat transfer applications. *Applied Rheology*, 20(4), 2010.

[51] John P. McTague. Magnetoviscosity of magnetic colloids. *The Journal of Chemical Physics*, 51(1):133–136, 1969.

[52] W. F. Hall and S. N. Busenberg. Viscosity of magnetic suspensions. *The Journal of Chemical Physics*, 51(1):137–144, 1969.

[53] Mark Shliomis. Effective viscosity of magnetic suspensions. *Sov. Phys. JETP*, 34:1291–1294, 01 1972.

[54] S. Odenbach and S. Thurm. Magnetoviscous Effects in Ferrofluids. *Lecture Notes in Physics*, pages 185–201, January 2008.

[55] Chandrasekhar Subrahmanyan. *Hydrodynamic and hydromagnetic stability / by S. Chandrasekhar...* Dover Publications, New York, impr. 1981, 1961.

[56] Mickaël Petit, Afef Kedous-Lebouc, Yvan Avenas, Wahid Cherief, and Elisabeth Rullière. Etude expérimentale d'un système statique de génération de pression magnétothermique. In *Symposium de Génie Electrique - SGE2014*, Cachan, France, July 2014.

[57] Harald Engler and S. Odenbach. Parametric modulation of thermomagnetic convection in magnetic fluids. *Journal of physics. Condensed matter : an Institute of Physics journal*, 20:204135, 05 2008.

[58] Elmars Blums, Andrejs Cebers, and M. M. Maiorov. *Magnetic Fluids*. De Gruyter, 2010.

[59] Ranjan Ganguly, Swarnendu Sen, and Ishwar K. Puri. Thermomagnetic convection in a square enclosure using a line dipole. *Physics of Fluids*, 16(7):2228–2236, 2004.

[60] Adrian Lange and Stefan Odenbach. Thermomagnetic convection in magnetic fluids subjected to spatially modulated magnetic fields. *Physics Procedia*, 9:171–175, 2010. 12th International Conference on Magnetic Fluids (ICMF12).

[61] M. Heckert, L. Sprenger, A. Lange, and S. Odenbach. Experimental determination of the critical rayleigh number for thermomagnetic convection with focus on fluid composition. *Journal of Magnetism and Magnetic Materials*, 381:337–343, 2015.

[62] H. Aminfar, M. Mohammadpourfard, and Y. Narmani Kahnamouei. Numerical study of magnetic field effects on the mixed convection of a magnetic nanofluid in a curved tube. *International Journal of Mechanical Sciences*, 78:81–90, 2014.

[63] D Zablockis, V Frishfelds, and E Blums. Numerical investigation of thermomagnetic convection in a heated cylinder under the magnetic field of a solenoid. *Journal of Physics: Condensed Matter*, 20(20):204134, may 2008.

[64] M.S Krakov and I.V Nikiforov. To the influence of uniform magnetic field on thermomagnetic convection in square cavity. *Journal of Magnetism and Magnetic Materials*, 252:209–211, 2002. Proceedings of the 9th International Conference on Magnetic Fluids.

[65] Raphaël Zanella, Caroline Nore, Frédéric Bouillault, Jean-Luc Guermond, and Xavier Mininger. Influence of thermomagnetic convection and ferrofluid thermophysical properties on heat transfers in a cylindrical container heated by a solenoid. *Journal of Magnetism and Magnetic Materials*, 469:52–63, 2019.

[66] L. Schwab, U. Hildebrandt, and K. Stierstadt. Magnetic bénard convection. *Journal of Magnetism and Magnetic Materials*, 39(1):113–114, 1983.

[67] L. Schwab and K. Stierstadt. Field-induced wavevector-selection by magnetic bénard-convection. *Journal of Magnetism and Magnetic Materials*, 65(2):315–316, 1987.

[68] L. Schwab. Thermal convection in ferrofluids under a free surface. *Journal of Magnetism and Magnetic Materials*, 85(1):199–202, 1990.

[69] Morteza Hangi and Mehdi Bahiraei. A two-phase simulation for ferrofluid flow between two parallel plates under localized magnetic field by applying lagrangian approach for nanoparticles. *European Journal of Mechanics - B/Fluids*, 74:252–259, 2019.

[70] M. Ghasemian, Z. Najafian Ashrafi, M. Goharkhah, and M. Ashjaee. Heat transfer characteristics of fe3o4 ferrofluid flowing in a mini channel under constant and alternating magnetic fields. *Journal of Magnetism and Magnetic Materials*, 381:158–167, 2015.

[71] M. Yarahmadi, H. Moazami Goudarzi, and M.B. Shafii. Experimental investigation into laminar forced convective heat transfer of ferrofluids under constant and oscillating magnetic field with different magnetic field arrangements and oscillation modes. *Experimental Thermal and Fluid Science*, 68:601 – 611, 2015.

[72] K. Raj and R. Moskowitz. Ferrofluid-cooled electromagnetic device and improved cooling method, 1995. US Patent 5462685.

[73] M. Yang, R. O'Handley, and Z. Fang. Modeling of ferrofluid passive cooling system. In *Excerpt from the Proceedings of the COMSOL Conference 2010 Boston Modeling*, number 1, 2010.

[74] Qi Liu, Saad F. Alazemi, Mohammed F. Daqaq, and Gang Li. A ferrofluid based energy harvester: Computational modeling, analysis, and experimental validation. *Journal of Magnetism and Magnetic Materials*, 449:105 – 118, 2018.

[75] Varun Chaudhary, Zhiping Wang, Ayan Ray, Idapalapati Sridhar, and Raju Ramanujan. Self pumping magnetic cooling. *Journal of Physics D: Applied Physics*, 50:03LT03, 01 2017.

[76] V. Segal, K. Linsley, A. Hjortsberg, and A. Rabinovich. Ac $60hz$ and impulse breakdown strength of a colloidal fluid based on transformer oils and magnetite nanoparticles, international symposium, electrical insulation. In *IEEE CONFERENCE RECORD OF IEEE INTERNATIONAL SYMPOSIUM ON ELECTRICAL INSULATION, Electrical insulation, International symposium, Electrical insulation*, volume 2, pages 619–622. IEEE;, 1998.

[77] Arthur Charles Franklin and David Peter Franklin. *The J and P transformer book: a practical technology of the power transformer; 11th ed.* Butterworths, London, 1983.

[78] Juraj Kurimský, Michal Rajňák, Pavol Bartko, Katarína Paulovičová, Roman Cimbala, Dušan Medveď, Mária Džamová, Milan Timko, and Peter Kopčanský. Experimental study of ac breakdown strength in ferrofluid during thermal aging. *Journal of Magnetism and Magnetic Materials*, 465:136 – 142, 2018.

[79] Michal Rajňák, Milan Timko, Peter Kopčanský, K. Paulovičová, Jozef Kuchta, Marek Franko, Juraj Kurimsky, Bystrík Dolník, and Roman Cimbala. Transformer oil-based magnetic nanofluid with high dielectric losses tested for cooling of a model transformer. *IEEE Transactions on Dielectrics and Electrical Insulation*, 26(4):1343–1349, 2019.

[80] J. Patel, K. Parekh, and R.V. Upadhyay. Prevention of hot spot temperature in a distribution transformer using magnetic fluid as a coolant. *International Journal of Thermal Sciences*, 103:35–40, 2016.

[81] L. Pîslaru-D˘anescu, A. M. Morega, J. B. Dumitru, M. Morega, N. C. Popa, F. D. Stoian, D. Susan-Resiga, S. Holotescu, and M. Popa. Miniature Planar Spiral Transformer With Hybrid, Ferrite, and Magnetic Nanofluid Core. *IEEE Transactions on Magnetics*, 54(10), 2018.

[82] V. M. Jimenez-Mondragon, R. Escarela-Perez, E. Melgoza, M. A. Arjona, and J. C. Olivares-Galvan. Quasi-3-D Finite-Element Modeling of a power Transformer. *IEEE Transaction on Magnetics*, 53:4–7, 2017.

[83] Y. B. Zhang, Y. L. Xin, T. Qian, X. Lin, W. H. Tang, and Q. H. Wu. 2-d coupled fluid-thermal analysis of oil-immersed power transformers based on finite element method. In *2016 IEEE Innovative Smart Grid Technologies - Asia (ISGT-Asia)*, pages 1060–1064, 2016.

[84] W. Guan, M. Jin, Y. Fan, J.Chen, P. Xin, Y. Li, K. Dai, H. Zhang, T. Huang, and J. Ruan. Finite Element Modeling of Heat Transfer in a Nanofluid Filled Transformer. *IEEE Transactions on Magnetics*, 50(2):2942–2951, 2014.

[85] L. Pîslaru-Dănescu, A. M. Morega, G. Telipan, M. Morega, J. B. Dumitru, and V. Marinescu. Magnetic Nanofluid Applications in Electrical Engineering. *IEEE Transactions on Magnetics*, 49(11):5489–5497, 2013.

[86] A. M. Morega, M. Morega, L. Pislaru-Danescu, V. Stoica, F. Nouras, and F. D. Stoian. A Novel, Ferrofluid-Cooled Transformer. Electromagnetic Field and Heat Transfer by Numerical Simulation. In *12th International Conference on Optimization of Electrical and Electronic Equipment, OPTIM 2010*, pages 140–146, 2010.

[87] Yunpeng Zhang, S.L. Ho, Weinong Fu, Xinsheng Yang, and Huihuan Wu. Numerical study on natural convective heat transfer of nanofluids in disc-type transformer windings. *IEEE Access*, 7:51267–51275, 01 2019.

[88] M. Kosterec, J. Kurimský, R. Cimbala, Zsolt Conka, L. Kruelák, M. Rajňák, M. Timko, P. Kopanský, and B. Vargová. Analysis of thermal field in mineral transformer oil based magnetic fluids. *Acta Physica Polonica A*, 131:937–939, 2017.

[89] Iliana Marinova and Valentin Mateev. Thermo-electro-magnetic convection in electrically conductive ferrofluids. In *2019 22nd International Conference on the Computation of Electromagnetic Fields (COMPUMAG)*, pages 1–4, 2019.

[90] S. S. Papell and O. C. Faber Jr. *Zero- and Reduced-gravity Simulation on a Magnetic-colloid Pool-boiling System*. NASA TECHNICAL NOTE D-3288, WASHINGTON, 1966.

[91] C. Nore, H. Zaidi, F. Bouillault, A. Bossavit, and J.-L. Guermond. Approximation of the time-dependent induction equation with advection using Whitney elements. *COMPEL: The International Journal for Computation and Mathematics in Electrical and Electronic Engineering*, 35(1):326–338, 2016.

[92] A. Giesecke, C. Nore, F. Stefani, G. Gerbeth, J. Léorat, W. Herreman, F. Luddens, and J.-L. Guermond. Influence of high-permeability discs in an axisymmetric model of the Cadarache dynamo experiment. *New Journal of Physics*, 14(053005):1–16, 2012.

[93] Alain Bossavit. Virtual power principle and maxwell's tensor: Which comes first? *COMPEL-the International Journal for Computation and Mathematics in Electrical and Electronic Engineering*, 30:1804–1814, 11 2011.

[94] A. Bossavit. A nonlinear and symmetric maxwell tensor. *European Journal of Electrical Engineering*, 18(3-4):169 – 177, 01 2016.

[95] J. Patel, K. Parekh, and R.V. Upadhyay. Performance of Mn-Zn ferrite magnetic fluid in a prototype distribution transformer under varying loading conditions. *International Journal of Thermal Sciences*, 114:64–71, 2017.

[96] Hasna Louahlia and Sébastien Yon. *«Dissipation dans les composants/systèmes électroniques, un enjeu pour la fiabilité des Composants/Systèmes électroniques, Quelles solutions technologiques ?», AREELIS Technologies -LUSAC (Laboratoire Universitaire des Sciences Appliquées de Cher-bourg).* 27/07/2015.

[97] S. Nasser El Dine, X. Mininger, C. Nore, R. Zanella, F. Bouillault, and J. Guermond. Impact of magnets on ferrofluid cooling process: Experimental and numerical approaches. *IEEE Transactions on Magnetics*, 56(1):1–4, 2020.

[98] Victor Vargas, Ronald Brenes, and Gabriel Gonzales. *«Les Ferrofluides Comment expliquer de quelle manière un Ferrofluide peut être utilisé pour dépurer les substances oléiques de l'eau ?», Lycée franco-costaricien, Olympiades De Physique, France.* Olympiades De Physique, France, 2017.

[99] Stephan Lampert and Cynthia Talon. *«Ferrofluide un liquide attirant», Lycée Louis Massignon, Olympiades De Physique, France.* Olympiades De Physique, France, 2014.

[100] C. Scherer and A. M. Figueiredo Neto. Ferrofluids: properties and applications. *Brazilian Journal of Physics*, 35:718 – 727, 09 2005.

[101] Hussein Sleiman. *Systèmes de suspension semi-active à base de fluide magnétorhéologique pour l'automobile*. Theses, Arts et Métiers ParisTech, June 2010.

[102] Wahid Cherief. *Etude des ferrofluides et de leurs applications à l'intensification des transferts de chaleur par convection forcée*. Theses, Université Grenoble Alpes, December 2015.

[103] Mehdi Bahiraei and Morteza Hangi. Flow and heat transfer characteristics of magnetic nanofluids: A review. *Journal of Magnetism and Magnetic Materials*, 374:125 – 138, 2015.

[104] Stefan Odenbach and Steffen Thurm. *Magnetoviscous Effects in Ferrofluids*, pages 185–201. Springer Berlin Heidelberg, Berlin, Heidelberg, 2002.

[105] Mohand Laïd Idoughi. *Extraction de modèles thermiques simplifiés des machines électriques à partir d'un calcul du champ de températures*. Theses, Université Paris Sud - Paris XI, December 2011.

[106] A. M. Morega, M. Morega, L. Pîslaru-Dănescu, V. Stoica, F. Nouraş, and F. D. Stoian. A novel, ferrofluid-cooled transformer. electromagnetic field and heat transfer by numerical simulation. In *2010 12th International Conference on Optimization of Electrical and Electronic Equipment*, pages 140–146, 2010.

[107] G. Y. Jeong, S. P. Jang, H. Y. Lee, J. C. Lee, S. Choi, and S. H. Lee. Magnetic-thermal-fluidic analysis for cooling performance of magnetic nanofluids comparing with transformer oil and air by using fully coupled finite element method. *IEEE Transactions on Magnetics*, 49(5), 2013.

[108] H. S. Choi, T. I. Sung, and Y. S. kim I. H. Park. Buoyancy Force Evaluation on Nonmagnetic Solid Object Submerged in Magnetic Liquid Subjected to Non-uniform Magneto-static Field. *IEEE*, Manuscript received December 22 2009.

[109] Z. L. Lu, P. Z. Gao, R. X. Ma, J. Xu, Z. H. Wang, and E. V. Rebrov. Structural, magnetic and thermal properties of one-dimensional CoFe2O4 microtubes. *Journal of Alloys and Compounds*, pages 428–434, 2016.

[110] P. B. Kharat, J. S. Kounsalye, M. V. Shisode, and K. M. Jadhav. Preparation and Thermophysical Investigations of CoFe2O4-based Nanofluid: a Potential Heat Transfer Agent. *Journal of Superconductivity and Novel Magnetism*, pages 1–11, 2018.

[111] I. Milosevic, L. Motte, and F. Mazaleyrat. Ferrofluides - Nanoparticules superparamagnétiques. *Techniques de l'Ingénieur*, 33, 2011.

[112] A. M. Morega, L. Pislaru-Dănescu, and M. Morega. A novel microactuator device based on magnetic nanofluid. In *Proceedings of the International Conference on Optimisation of Electrical and Electronic Equipment, OPTIM*, pages 1100–1106, 2012.

[113] L. J. Love, J. F. Jansen, T. E. McKnight, Y. Roh, and T. J. Phelps. A magnetocaloric pump for microfluidic applications. *IEEE Transactions on NanoBioscience*, 3(2):101–110, June 2004.

[114] S. Lee and H. Lee. Numerical and experimental validation to the ability of magnetoconvection to cool vegetable-based transformer oil with magnetic nanoparticles. *IEEE Transactions on Magnetics*, 55(7):1–5, July 2019.

[115] B. Assadsangabi, M. H. Tee, and K. Takahata. Electromagnetic microactuator realized by ferrofluid-assisted levitation mechanism. *Journal of Microelectromechanical Systems*, 23(5):1112–1120, 2014.

[116] Vladimir Segal and K. Raj. An investigation of power transformer cooling with magnetic fluids. *Indian Journal of Engineering and Materials Sciences*, 5(6):416–422, 1998.

[117] Yuefan Du, Yuzhen lv, Chengrong Li, Mutian Chen, Yuxiang Zhong, Jianquan Zhou, Xiaoxin Li, and You Zhou. Effect of semiconductive nanoparticles on insulating performances of transformer oil. *IEEE Transactions on Dielectrics and Electrical Insulation - IEEE TRANS DIELECT ELECTR IN*, 19:770–776, 06 2012.

[118] M. Lappa. *Thermal Convection: Patterns, Evolution and Stability*. John Wiley Sons Ltd, 2010.

ÉCOLE DOCTORALE
Physique et ingénierie : Electrons, Photons, Sciences du vivant (EOBE)

**Titre :** Modélisation multiphysique du refroidissement de transformateurs de puissance plongés dans un ferrofluide

**Mots clés :** Mécanique des fluides, Électromagnétisme, Transfert de chaleur, Couplage multiphysique, Transformateurs, Refroidissement, Éléments finis

**Résumé :** Des considérations écologiques amènent à utiliser des huiles végétales ensemencées par des nanoparticules magnétiques comme une alternative aux huiles issues du pétrole au sein des transformateurs de puissance. Cependant, les propriétés physiques macroscopiques de ces suspensions et les forces qui en découlent sont mal connues. Pour les étudier, nous proposons une approche couplée, numérique et expérimentale, de ce problème multiphysique alliant des effets thermique, magnétique et fluidique. Le problème multiphysique nécessite l'utilisation des équations de Navier-Stokes dans l'approximation de Boussinesq, de l'équation de conservation de l'énergie, et des équations de la magnétostatique. Les simulations sont d'abord réalisées avec deux codes éléments finis pour vérifier l'impact de la convection thermomagnétique sur le refroidissement d'un solénoïde immergé dans un ferrofluide. Les résultats numériques ont montré une diminution de 2°C de la température de la bobine. Les résultats numériques ont été comparés à des mesures expérimentales et ont montré un très bon accord. Ensuite, nous avons effectué deux tests pour améliorer la convection thermomagnétique dans le modèle de solénoïde. Le premier test vise à étudier l'effet de nanoparticules magnétiques à faible température de Curie. Le second test évalue l'impact d'un aimant annulaire placé à un emplacement optimisé pour maximiser le flux de fuite dans le ferrofluide. Nous avons également inséré un noyau ferromagnétique dans ce système comme première approche vers un transformateur de puissance afin d'augmenter le transfert de chaleur à l'intérieur du réservoir. Nous avons également effectué une validation 3D du système de solénoïde comme transition vers la modélisation 3D. Un modèle axisymétrique 2D d'un transformateur de puissance monophasé de 40 kVA, 20kV/400V est ensuite étudié. L'impact de la convection thermomagnétique sur le processus de transfert de chaleur est vérifié. La diminution maximale de la température dans les enroulements est évaluée à 2°C en utilisant le ferrofluide. Nous avons réalisé une étude 3D pour le même modèle de transformateur simplifié lorsqu'il est immergé dans de l'huile végétale. Les résultats ont montré un accord relativement bon. Enfin, nous avons modélisé un transformateur de puissance monophasé non axisymétrique de 3 kVA, 400/230V. Les résultats numériques ont montré une diminution significative de la température maximale des enroulements de 10°C lorsque la force magnétique est présente.

Maison du doctorat de l'Université Paris-Saclay
2ème étage aile ouest, Ecole normale supérieure Paris-Saclay
4 avenue des Sciences,
91190 Gif sur Yvette, France

ÉCOLE DOCTORALE
Physique et ingénierie : Electrons, Photons, Sciences du vivant (EOBE)

**Title :** Multiphysics modeling of cooling of power transformers immersed in a ferrofluid

**Keywords :** Fluid mechanics, Electromagnetism, Heat transfer, Multiphysics coupling, Transformers, Cooling, Finite elements

**Abstract :** Ecological considerations lead to the use of vegetable oils seeded with magnetic nanoparticles as an alternative to petroleum oils in power transformers. However, the macroscopic physical properties of these suspensions and the resulting forces are poorly known. To study them, we propose a coupled approach, both numerical and experimental, of this multi-physical problem combining thermal, magnetic, and fluidic effects. The multiphysics problem consists of the Navier-Stokes equations with Boussinesq approximation, the energy conservation equation, and the magnetostatic equations. The simulations are performed first with two finite element codes to verify the impact of the thermomagnetic convection in a solenoid immersed in a ferrofluid. Numerical results have shown a decrease by 2°C of the temperature of the coil. In parallel, the numerical results have been compared to experimental ones and have shown a very good agreement. Then, we have made two tests to improve the thermomagnetic convection in the solenoid model. The first test consists of studying the effect of magnetic nanoparticles with low Curie temperature. The second test investigate the impact of an annular magnet at an optimized location to maximize the leakage flux in the ferrofluid. We have also inserted a ferromagnetic core in the coil system as a first approach for the power transformer to increase the heat transfer inside the tank. We have also performed a 3D validation of the solenoid system as a transition to the 3D modeling. A 2D axisymmetric model of a 40 kVA, 20kV/400V single-phase power transformer is then studied. The impact of the thermomagnetic convection on the heat transfer process is verified. The maximum temperature decrease in the windings is evaluated to 2°C when using ferrofluid. We have performed a 3D study for the same model of the simplified transformer when it is immersed in regular oil. Results have shown a relatively good agreement. Finally, we have modeled a 3 kVA, 400/230V non-axisymmetric single-phase power transformer. The numerical results have shown a significant decrease in the maximum temperature of the windings by 10°C when the magnetic force is present.

Maison du doctorat de l'Université Paris-Saclay
2ème étage aile ouest, Ecole normale supérieure Paris-Saclay
4 avenue des Sciences,
91190 Gif sur Yvette, France